CLIMATE CHANGE IMPACT ASSESSMENT UNDER DATA SCARCITY

—

IMPROVED HYDROLOGICAL MODEL PARAMETRIZATION USING FIELD MONITORING TECHNIQUES AND GEOSTATISTICS

Dissertation
an der Fakultät für Geowissenschaften der Ludwig-Maximilians-Universität München

vorgelegt von

Swen Meyer
Aus Oldenburg

München, 2016

Supervisor:	**Prof. Dr. Ralf Ludwig,** Department of Geography, LMU Munich
2nd Supervisor:	**Prof. Dr. Rainer Duttmann,** Department of Geography, CAU Kiel

Tag der mündlichen Prüfung: **08.07.2016**

PREFACE

This work is the result of a long journey that actually started with leaving the city of Kiel, where I studied and graduated in physical geography, and by moving to Munich. I left Kiel with very mixed feelings, since I lived my whole former life in the north of Germany. On the one hand I was afraid of leaving my comfort zone of a well-known environment, good friends and the Baltic Sea, where I enjoyed going windsurfing. On the other I felt exited to explore a new environment, with new people, to learn about a different German culture and last but not least to start working in science.

I thank **Prof. Dr. Ralf Ludwig** for asking me to work with him scientifically in the EU funded project "Climate Induced Changes on the Hydrology of Mediterranean Basins" (CLIMB) at the LMU Munich. I really enjoyed being part of this project, even if working in such a project is not always an easy task. Seeing that it became a success story at the end of the day, is a great paycheck for the energy, effort and time I invested. I also like to thank **Prof. Dr. Rainer Duttmann**, **Dr. Michael Blaschek** and the team of the Department of Geography at the CAU Kiel, for planning together the soil sampling campaigns on Sardinia, for the scientific exchange, the good collaboration within CLIMB. I like to thank **my colleagues** of the Department of Geography, the AG-Ludwig and especially the GLOBAQUA team. I really enjoyed the good collaboration, exchange and discussions, which included much more than just work related topics. I thank **Vera Erfurth** for managing all the bureaucracy with the administration. Very special thanks go to my friend and colleague **Dr. Philip Marzahn**, for endless hours of constructive discussions, joking, lunch and coffee breaks and finally for your support in finishing this thesis. I thank my American friend **Jeff Wong**, for being a good drinking and snowboard buddy, friend and for reviewing and editing this thesis language wise. The biggest thanks go to **my family**, who always supported me with their positive thinking, good advices and love.

The journey of this thesis has ended and I'm looking forward to new exiting journey in the near future.

ABSTRACT

According to current climate projections, Mediterranean countries are at high risk for an even pronounced susceptibility to changes in the hydrological budget and extremes. These changes are expected to have severe direct impacts on the management of water resources, agricultural productivity and drinking water supply. The different regions of the Mediterranean landscape are already experiencing and expecting a broad range of natural and man-made threats to water security. Current projections of future hydrological change, based on regional climate model results and subsequent hydrological modeling schemes, are very uncertain and poorly validated. The Rio Mannu di San Sperate Basin, located in Sardinia, Italy, is one test site of the CLIMB project. The catchment has a size of 472.5 km^2. The catchment was already affected by multi-drought periods (1990-2000) (Piras et al. 2014).

The process-based Water Simulation Model (WaSiM) was set up to model current and future hydrological conditions. The availability of measured meteorological and hydrological data is poor as it is common for many Mediterranean catchments. The lack of available measured input data hampers the calibration of the model setup and the validation of model outputs. A soil sampling campaign was conducted together with the department of Geography of the University of Kiel to assess more precisely the physical properties of the top soil (30cm depth) at 239 locations in the Rio Mannu catchment. Different deterministic and hybrid geostatistical regionalization methods like Multi-Linear Regression, Inverse Distance Weighting, Ordinary Kriging and Regression Kriging (Odeh et al. 1995) were used to calculate spatially distributed maps of particular lab-analyzed soil information. The applied regionalization methods were then tested on the prediction performance. The best performing prediction method was used to calculate a new classified soil texture map for the catchment. Soil hydrological properties were assigned to the soil texture classes by pedo-transfer functions.

WaSiM was then parameterized in 2 different settings. One setting (WASiM-ARU) used the standard available soil information of Aru et al. (1990) and the other (WASiM-RKS) the improved new soil information. The WaSiM-ARU setting was used for calibration and validation. WaSiM-ARU was calibrated and validated with spatially distributed evapotranspiration rates derived with the triangle method (Jiang and Islam, 1999) and soil

moisture records, due to missing adequate gauging information in the catchment. The modeled evapotranspiration result girds using WaSiM-RKS setup with the improved soil model setup show a better fit especially for the growing season to those derived from remote sensing without further calibration. Both WaSiM setups were driven with the meteorological forcing taken from 4 different ENSEMBLES climate projections for a reference (1971-2000) and a future (2041-2070) times series. The climate change impact was assessed based on differences between reference and future time series and with climate change indices like the standardized difference precipitation index, the evapotranspiration index and by the number of consecutive flow conditions. Furthermore long-term annual and monthly mean changes were analyzed.

The simulated results show a reduction of all hydrological quantities in the future. Furthermore simulation results reveal an earlier onset of dry conditions in the catchment. The comparison of modeling results shows that the quality of the soil model setup has a major impact on the spatial distribution of modeling outputs.

Finally runoff modeling results of both WaSiM setups were compared to other modeling results which were processed with other hydrological models in the test site within CLIMB. Those models used a very similar setup as WaSiM-ARU. The comparison shows a significant uncertainty in the processed results based on to the applied hydrological model. Especially in ungauged catchments like the Rio Mannu those uncertainties need to be considered in the climate change impact assessment analysis, the resulting adaption strategies and for the policy decision making. However, findings also show that the quality of soil input and parametrization creates uncertainties when using WaSiM that are in the same range as the uncertainties produced by the different applied hydrological models.

The study shows that the combination of sophisticated climate model downscaling and bias correction techniques, improved hydrological model parametrization with improved soil information, and validation with in-situ and remote sensing measurements, has a high potential to improve environmental impact assessment in data scarce regions.

CONTENTS

LIST OF FIGURES:

List of figures:

List of figures:

List of figures:

LIST OF TABLES:

List of tables:

1. INTRODUCTION

The Fifth Assessment Report of the Intergovernmental Panel on Climate Change (IPCC) summarizes an increasing air temperature throughout the 21st century. Those projections are a robust feature across climate models and the temperature increase is nearly the same for all Representative Concentration Pathway (RCP) scenarios (Collins et al. 2013).

Higher uncertainties are expected for the projected future change of precipitation sums, distributions and intensities. However, there is a scientific consensus that precipitation patterns and sums are expected to change by the end of the century (Christensen et al. 2007). In contrast to the great number of climate change and climate model downscaling studies that have been published in recent time, the amount of studies focusing on regional hydrological impact assessment of climate change is manageable (Raposo et al. 2013). Climate change is expected to have a distinct impact on the European continent. Many studies, summarized in the IPCC report 2007, indicate a strong north-south impact gradient for Europe.

It is likely that winter temperatures will increase more in northern Europe than in central and southern Europe. In contrast to that summer temperatures are projected to increase more in the Mediterranean and central Europe (Christensen et al. 2013). While for northern Europe an increase of precipitation, runoff, and floods is projected with a medium confidence, southern Europe is expected to be more severely affected by droughts due to a warmer and drier climate (Alacamo et al. 2007, Christensen et al. 2013). In a climate analysis of 20 GCMs using up to 3 IPCC emission scenarios (A1B, A2, B1), Giorgi (2006) found that the Mediterranean area is one of the most prominent “hot-spots” with regards to climate change by the end of 21st century. Christensen et al. (2013) shows that the recent (1981-2012) trends in annual mean air temperature raise in the Mediterranean area exceed the global mean land trend. The uncertainty assessment of a large ensemble of regional and general climate models (RCM & GCM) in this

region shows that the temperature response of the models is robust even for the 2021-2051 time frame (Déqué et al. 2012).

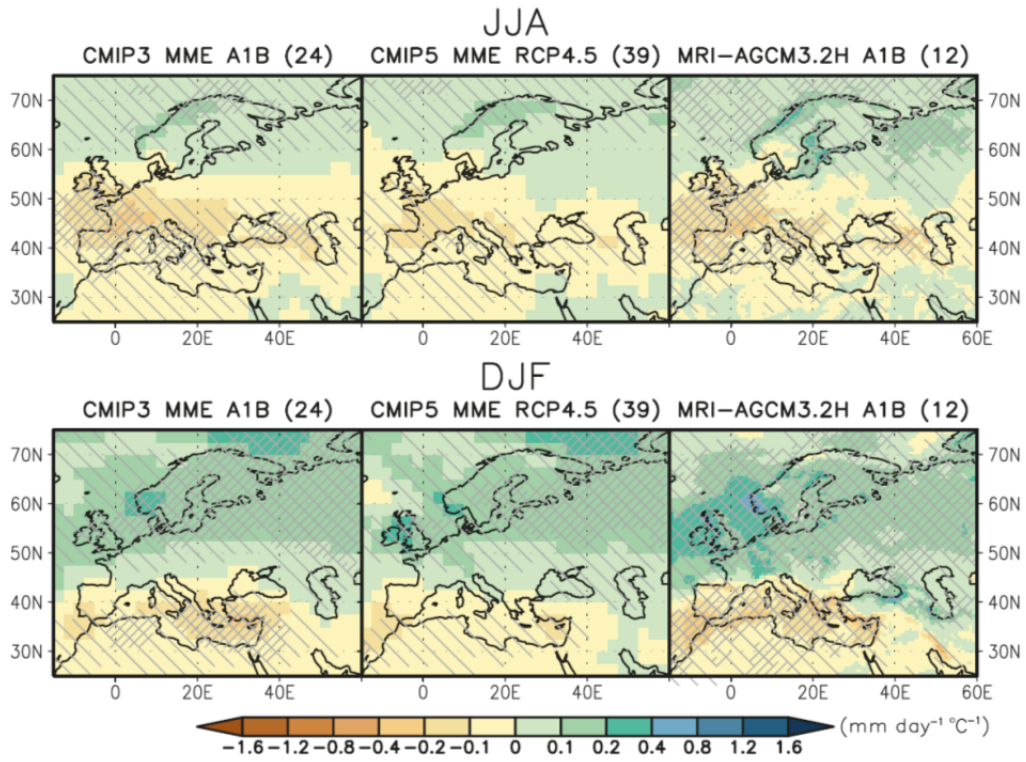

Figure 1: Maps of precipitation changes for Europe and Mediterranean in 2080–2099 with respect to 1986–2005 in June to August (above) and December to February (below) in the SRES A1B scenario with 24 CMIP3 models (left), and in the RCP4.5 scenario with 39 CMIP5 models (middle). Right figures are the precipitation changes in 2075–2099 with respect to 1979–2003 in the SRES A1B scenario with the 12 member 60 km mesh Meteorological Research Institute (MRI)-Atmospheric General Circulation Model 3.2 (AGCM3.2) multi-physics, multi-sea surface temperature (SST) ensembles (Endo et al., 2012). Precipitation changes are normalized by the global annual mean surface air temperature changes in each scenario. Light hatching denotes where more than 66% of models (or members) have the same sign with the ensemble mean changes, while dense hatching denotes where more than 90% of models (or members) have the same sign with the ensemble mean changes (Fig. source: Christensen et al. 2013).

Thus there are strong signs that longer lasting dry periods, will lead to an increased risk of droughts, interrupted by extreme intense precipitation (Christensen et al. 2007, Zollo et al. 2012, and Raposo et al. 2013). Arnell (1999), Alacamo et al. (2007), Falloon & Betts (2010) and other authors showed that for the Mediterranean countries a significant

reduction of precipitation, runoff and ground water recharge is projected. Raposo et al. (2013) found that the recharge of water bodies may concentrate in the winter season and dramatically decrease in the summer–autumn season leading to an increased dry season duration, which is exacerbating the current problems in water supply. In summary there is a high confidence in model predictions of mean air temperature in this region and is very likely that temperatures will continue to increase throughout the 21st century (Christensen et al. 2013).

Temporal water scarcity is on the one hand a natural phenomenon in semi-arid regions, which forced people long time ago to adapt the agricultural activity to those temporal conditions. Over exploitation of water resources and climate change impacts on the other hand already imply a threat to agricultural productivity, with a possible increasing trend in the future. The Italian island of Sardinia is one example for a region that is already facing temporal water scarcity problems. Sardinia was recently affected by water shortage, due to very dry conditions in the second half of the year 2014. L'Ente acque della Sardegna (ENAS) reported that the water reservoirs of the island were only filled by 56.3% in the beginning of 2015. Due to this fact water supply for agriculture irrigation was prohibited in the time of 19.02.-30.04.2015 in the northern part of the island. The recent water resource issues are not only a consequence of the recent very dry climate conditions, in fact the quantity of fresh water resources is affected furthermore by a combination of factors like eutrophication, water losses due to a poor infrastructure system (storage capacity and efficiency of networks) and fragmented water management (Sannitu 2006). Furthermore the Water Plan presented under Sardinian Renewable Program in 1988 shows that there is a large mismatch between water supply and water demand leading to a water deficit of -280 million m^3/a in southern Sardinia and -543 million m^3/a for the whole island. The total demand of southern Sardinian is 511 mio. m^3/a, from which the agricultural sector claims the highest quota (346 mio. m^3/a) followed by domestic users (140 mio. m^3/a) and industry (25 mio. m^3/a). The average yearly supply on the other hand is only 232 mio. m^3/a. The resource availability is further reduced by a drop in rain fall of 50-60% within the last 20 years (Sannitu 2006). The severe fresh water resource situation might be even more exacerbated by climate change. To face current and future water resource problems in the region a holistic water management, which implies the quantification of future climate change impacts is needed.

In order to quantify climate change effects on a catchment scale, Xu et al. (2005) suggests performing the following three steps:

1. Choose the outputs of different climate projections from GCMs or RCMs.
2. Find and apply downscaling techniques to the GCMs & RCMs outputs, to match those with the scales needed for the impact assessment modeling.
3. Apply the downscaled data into a hydrological model, to model and study future changes in the hydrological budgets in the study area.

With this procedure a spatial feasibility for hydrological impact modeling can be achieved, but it comes together with the confinement that the uncertainties of the modeling results will increase. For a more precise assessment of current and future hydrological conditions on the climatological timescale, a complex modeling chain is required (Muerth et al. 2012).

In a hydrological climate impact assessment study of the French coastal catchments, Lespinas et al. (2014) simulated a mean reduction of discharge by 55% (A2) and 46% (B2) for the summer season of the time series 2070-2100, by forcing the hydrological model GR2M with different PRUDENCE RCMs. In contrast to the work of Lespinas et al. (2014) and Raposo et al. (2013), most of the few studies that have been published on regional hydrological climate change impact assessment in the Mediterranean, use simple average annual climate data (Molina-Navarro et al. 2014). Furthermore projections of future hydrological changes based on regional climate modeling results are very uncertain and modeling schemes often poorly validated (Ludwig et al. 2010a). In many Mediterranean catchments long-term time series of recorded discharge and climate variables that are needed to calibrate and validate process-based hydrological models are not available. The lack of information is one reason why the amount of studies focusing on regional hydrological impact assessment of climate change is low (Raposo et al. 2013). Thus, in order to meet the needs of policy makers and stakeholders for the adaptation to climate change, hydrological modeling capabilities must be adapted and improved to overcome existing limitations, (Ludwig et al. 2010a).

Process-based hydrological models require numerous soil (-hydraulic), terrain and vegetation parameters in an appropriate spatial and temporal resolution. Although it is known that the response of those models is sensitive to the quality of soil data, ade-

quate soil information is missing in many cases. Spatially explicit data of soil properties are needed to link catchment characteristics and distributed hydrological model parameterization (Götzinger & Bardossy 2007), as well as understanding and predicting plant water responses to changing climate conditions (Browning & Duniway 2011). The inquiry of soil properties based on field surveys is time consuming and costly, but on the other hand there is a worldwide increasing demand of high resolution soil data to meet the data requirements of sophisticated environmental and hydrological models. The main limiting factor of the modeling projection quality is the quality model input data which is especially true for spatially highly distributed soil information (Sumfleth 2008). Commonly available high-resolution soil maps have a resolution of 1:25.000 to 1:50.000, but the resolution is often much coarser, thus hampering the spatially modeling quality and increases uncertainties in modeled projections. Behrens & Scholten (2006) and Duttmann & Sumfleth (2007) agree that the development of new cost effective, soil property regionalization techniques is meaningful. Hydrologist can benefit from those developments and might want to integrate those existing and solid regionalization techniques to improve the quality of model input soil data. Solid regionalization techniques that have been tested by soil scientists on their prediction performance in many studies are multilinear regressions (MLR), inverse distance weighting (IDW), ordinary kriging (OK) and regression kriging (RK) (Piccini et al. 2014, Yoa et al. 2013, Adhikari et al. 2013, Eldeiry & Garcia 2010, Herbst et al. 2006).

1.1 Motivation

The lack of knowledge on climate change impacts on the hydrology in the Mediterranean region is a common problem for present and future water management. Physically based hydrological models, like the Water balance Simulation Model (WaSiM) presented in section 5, are needed to simulate the non-linear climate change impacts on the hydrological quantities catchment scale. Thus, the analysis of those simulations can help to improving the knowledge of future hydrological impacts and is a prerequisite for a sophisticated water management, as well for adaption strategies and policy making. The lack of spatially distributed soil information needed for a solid model parametrization hampers the quality of hydrological modeling results and might cause high differences (uncertainties) in the produced simulation results. The reduction or at least the identifi-

cation of uncertainties that are coming from different sources is important to improve and value the quality of modeling results. Especially in ungauged catchments a sophisticated model setup is needed, since a normal case calibration and validation with recorded discharge data cannot be executed. The survey of such soil information is on the one hand costly but can be on the other executed in rather a short time compared to long-term discharge monitoring. Different and easy to apply regionalization schemes, like MLR, IDW, OK and RK, have the potential to improve the hydrological modeling results or at least show a range of uncertainties that are related to soil model parametrization of physically based spatially distributed hydrological models like WaSiM.

Thus, the following hypothesizes will be tested in this thesis:

I. Hydrological resources and the agricultural production are endangered by climate change impacts in the Mediterranean semi-arid area.

II. A solid soil physical parametrization of physically based fully distributed hydrological models hydrological models is crucial to simulate reliable modeling results for the spatial and temporal domain.

III. Different regionalization methods applied to soil physical data will lead to different spatial distributions of soil textures in the catchment.

IV. Setting up WaSiM's soil model with soil information coming from different sources will have a considerable impact on the hydrological modeling results.

V. The hydrological climate change impact assessment implies high uncertainties coming from different sources, like climate model input meteorology, the structural setup and the architecture of different hydrological models.

1.2 Work flow

The European FP-7 project CLIMB aimed to project climate induced changes on the hydrology of the Mediterranean Basins by investigating 7 test sites located in the countries Italy, France, Turkey, Tunisia, Gaza, and Egypt. CLIMB employed a combination of novel geophysical field monitoring concepts, remote sensing techniques and integrat-

ed hydrological modeling to improve process descriptions and understandings and to quantify existing uncertainties in climate change impact analysis (http://www.climb-fp7.eu).

The presented study was conducted in one CLIMB study site named Rio Mannu di San Sperate on the Italian island of Sardinia; a catchment located approximately 30km north of the island's capital Cagliari. The catchment was already affected by multi-drought periods between 1990 and 2000 (Piras et al. 2014). Due to water scarcity, a water plan was developed under the "Sardinia Renewable Program" and presented in 1988.

Long-term records of hydrologic quantities like discharge as well as reliable soil texture information were not available for the catchment. This lack of observed data hampers a solid setup and parameterization of process-based hydrologic models and increases uncertainties in the modeling results. A prediction of hydrological quantities in un-gauged basins is one of the grand challenges in hydrology. To tackle this challenge hydrological modeling needs to accept and integrate multi-scale heterogeneity of climate, vegetation, soil and topography within the basin and needs to learn about interactions of those parameters from field observations and patterns behind the data Sivapalan (2003).

For this study the following workflow was applied:

(i) A soil sampling campaign was conducted in the Rio Mannu (large scale) to gain knowledge about soil properties and heterogeneity within the basin.

(ii) Different deterministic and hybrid geostatistical interpolation methods like Multi-Linear Regression, Inverse Distance Weighting, Ordinary Kriging, and Regression Kriging (Odeh et al. 1995) tested for the predicted performance of the different regionalization models.

(iii) The best performing interpolation model was used to calculate a classified soil texture map for the catchment to better represent the true soil heterogeneity.

(iv) The climate change impacts were analyzed on the water resources in the catchment by driving the process-based fully distributed hydrologi-

cal model WaSiM (Schulla 2012) with a downscaled bias-corrected RCM ensemble that consists of 4 different GCM-RCM combinations (Deidda et al. 2013) for the time series 2041-2070.

(v) WaSiM was run with two different soil model setups and the sensitivity to modeling outputs was tested.

(vi) Finally, spatial grids of actual evapotranspiration from remote sensing data were calculated with the Triangle-Method (Jiang & Islam 1999) to validate WaSiM's actual evapotranspiration output grids.

(vii) Hydrological climate change impact indices like evapotranspiration index (ETI), change of soil water (CSM) and number of consecutive low flow days were calculated and compared.

(viii) Hydrological climate change impact on discharge was compared to modeling results coming from different hydrological models to estimate model architecture and model input applied uncertainties.

1.3 State of the art regionalization of soil properties

Due to the constantly increasing computational speed within the last 25 years, different approaches and methods have been developed to regionalize soil surface properties. Those deterministic and (geo-) statistic methods are named with different synonyms, which imply Digital Soil Mapping (Mc Bratney 2003), Pedometric Mapping, and Predictive Soil Mapping (Scull et al. 2003) and are summarized with the name Pedometrics (McBratney et al. 2000, Webster 1994). Up to date there is no explicit definition for the term Pedometrics. The best approach to define Pedometric in one sentence is given by Heuvelink (2003): *"Pedometrics is the application of mathematical and statistical methods for the study of the distribution and genesis of soils."* In this scientific field various approaches are used to predict soil properties or classes including univariate and multi-variate statistical, geostatistical and hybrid methods and process-based models (Grundwald 2010). Hengl et al. (2002) generally understand Pedometric Mapping as a quantified inventory of soil attributes expressed over continuous spatial fields.

Jenny's equation (Jenny 1941) is one out of many ways to quantify soil information and still is the conceptual prerequisite to many soil regionalization methods. In this approach a single soil property is described as a conceptualized function of environmental factors which imply climate (CL), organisms (O), relief (R), its parent material (P), and time (T) (CLORPT). The CLORPT-approach was modified by McBratney et al. (2003) and applied to digital soil mapping to explain relationships of soil properties and other spatially distributed environmental quantities (co-variables) (Moonjun et al. 2010). In the SCORPAN model McBratney et al. (2003) added the factors S: Soil, T was replaced by A: Age and N: Space, spatial position. With this modification the prediction was made temporally and geographically explicit (Grunwald 2010). These spatially distributed quantities or co-variables are normally available in higher spatial resolutions than the surveyed soil samples. A model that implies a solid relationship between a target variable (sampled soil properties) and spatially high distributed co-variables allows a continuously distributed prediction of soil properties at unsampled locations in the spatial resolution of the co-variable and with a certain degree of significance. Improving the relationship of target and co-variables is still a state of the art research field in Digital Soil Mapping. Grunwald (2010) gives an overview of commonly used co-variables, which imply Digital Elevation Model (DEM), primary and secondary terrain attributes (deviations of the DEM), like Slope, Aspect, Analytical Hill shading, Topographic Wetness Index etc., satellite and air borne, active and passive remote sensing products (optical and microwave remote sensing), as well as products from ground based geophysical remote sensing applications like electromagnetic induction (EMI) and gamma ray emission sensors. Hengl (2009) summarized three groups of statistical models based on correlations between target and co-variables, which imply classification-based models (Boolean or Fuzzy classification rules), tree-based models (decision tree), and regression models (Generalized Linear Models and General Additive Models).

Pure mathematical approaches like inverse distance weighting (IDW) splines and kriging do not consider functional relationships between soil properties and soil forming environmental factors. Kriging has been a synonym for geostatistical interpolation for many decades (Hengl 2009). Kriging is a geostatistical method that was introduced by Krige in 1951 and further improved by Matheron (1963). Kriging is a linear predictor that uses the spatial autocorrelation of a target variable. Those models estimate the values by a weighted averaging of nearby samples (Ahmed et al. 2010) by a semi-variogram model. Kriging is an exact and robust interpolation method and was used in many

studies. The advantage of kriging compared to other pure mathematically based soil prediction methods is that it is an unbiased prediction method (predicted values are the same as target variable values at sampled locations) and that it provides a spatially distributed measure of uncertainty based on the prediction variance i.e. the estimated variance of the prediction error (Hengl 2009). The most commonly used method in digital soil mapping is Ordinary kriging (OK) (Adhikari et al. 2013). A disadvantage of purely mathematical interpolation models is that predicted maps often show patterns that appear unnatural. Kriging tends to under-estimate large values and overestimate small values at unsampled locations (Oliver & Webster 2015).

A solution to avoid these problems is to use multivariate prediction techniques that include co-variables in the geostatistical prediction model (Adhikari et al. 2013). So-called hybrid methods are able to overcome disadvantages of pure mathematically based or pure CLORPT & SCORPAN based models and are able to combine advantages of both. Examples of multivariate geostatistical models used for the prediction soil properties are for example cokriging used by Gallichand & Marcotte (1993), Odeh et al. (2003), Eldeiryand & Garcia (2010), neural networks used by Zhao et al. (2009), and regression kriging (RK) applied by von Knotters et al. (1995), Odeh et al. (1995), Dobos et al. (2000), Odeh & McBratney (2000), Hengl et al. (2004), Ahmed et al. (2010), Adhikari et al. (2013) and Stockmann et al. (2015). The terms cokriging, regression kriging and kriging with external drift refer to a family of hybrid regionalization methods that are only slightly different. Other methodologies used are neural network (Behrens et al. 2005, Malone et al. 2009 and Guo et al. 2013, Blaschek 2015), imply genetic programming, simulation of gaussian fields, Markov Chain Random Fields or mechanistic models, but require a profound mathematical expertise (Grunwald 2010). Minasy & McBratney (2007) summarize that RK appears to be a robust technique to predict soil properties in various soil regions and suggest this method for practical applications. RK is a combination of a multivariate deterministic regression model and the stochastic kriging model, was first introduced by Odeh et al. (1995) and is also called kriging with external drift. RK involves various combinations of different regression and kriging models (Ahmed et al. 2010). The so called regression kriging approach of Odeh et al. (1995) uses a multi linear regression model to predict the target variable based on the applied co-variables. In a second step the residuals of sampled locations will be applied into an Ordinary Kriging (OK) approach. In the last step both resulting maps will be summed up. A major limitation, however, of these (MLR and RK) approaches is that the relationship between target

and covariates is assumed to be stationary across the space (Kumar 2015). This assumption might lead to misleading information especially if the target variable shows a spatial trend. Seo et al. (2015) found that hybrid regionalization models including RK outperform pure stochastic approaches like OK, simple kriging and universal kriging.

1.4 State of the art hydrological modeling

Climate change impacts on water resources are assessed by hydrologist by applying a variety of different hydrological models (Leavesley 1999). According to Moradkhani and Sorooshian (2008) all Rainfall-Runoff models and hydrological models represent a simplified characterization of the real world. These models are used to understand and predict system behavior and various hydrological processes (Devia et al. 2015). It can be defined as a coherent bundle of equations which helps to estimate runoff as a function of various parameters used for describing watershed characteristics (Devia et al. 2015). Models use and have parameters, which are numerical measures of a property or characteristics that are constant under certain conditions (Wheater et al. 2007). Most important input data sets for those models are climate records, for a defined drainage area, along with the characteristics of the watershed, like soil properties, vegetation cover and its characteristics, topography, and soil moisture content (Devia et al. 2015).

Hydrological models can be grouped into various categories upon the modeling approaches used (Daniel et al. 2011). They can be distinguished for example on their spatial (lumped over semi-distributed to fully distributed watershed discretization), temporal (event based to continuous time steps) and physical (empirically to physically based) and mathematical (deterministic or stochastic) complexity. The differences and the field of application of those hydrological models has been discussed and reviewed in many scientific publications for example in Devia et al. (2015), Sood and Smakhtin (2015), Golmohammadi et al. (2014), Daniel et al. (2011), Rochester (2010), Beckers et al. (2009), Moradkhani and Sorooshian (2008), Wheater et al. (2007) and many more.

In areas where hydrological records are lacking hydrologists may favor to use less complex lumped and/or empirical models (Daniel et al. 2011). Those data driven models try to find a function relationship between inputs and outputs, based on regressions and/or correlation, without considering the features and processes in a hydrological

system Devia et al. (2015). Due to that they are only valid within defined boundaries. Modeling detailed hydrological processes can be challenging since it involves highly non-linear processes, complex interactions and high spatial variabilities within the basin (Islam 2011). However, as soon as more detailed results are needed, a fully distributed and/or physically based hydrological model might be necessary and it may be necessary to collect detailed data to apply the model Beckers et al. (2009).

The Rio Mannu catchment in Sardinia Italy is the test site used for this study and was one major test site of the CLIMB project. This Mediterranean catchment is characterized by complex hydrological response due to the non-uniform and seasonal variation of precipitation events and strong inter-annual variability (Moussa et al. 2007). The terrain is furthermore characterized by highly heterogeneous land and surface properties (Mascaro et al. 2013) such as complex soil type and geological distribution, which is described in more detail in section 2. Those features have a controlling process and may include a strong non-linear dependency on antecedent wetness. Based on those initial conditions, storm events with the same quantity and intensity of precipitation can either produce a major flood or just a few millimeters of runoff (Beven et al. 2002). Modeling such complex systems in a continuous fashion to manage and plan water resources as well as to predict hydrological extremes is a difficult task (Mascaro et al. 2013) and due to that asking for the application of physically based fully distributed hydrological models.

Physically-based models are a mathematically idealized representation (Devia et al. 2015) of real hydrological system. In such models mass, transfer, momentum and energy are simulated using differential equations. Those equations are solved using various numerical methods such as the Richards equation for the unsaturated zone flow or the Penman-Monteith equation for the evaporation Daniel et al. (2011). Those models are capable to quantify the vertical and lateral water fluxes for continuous time steps in a spatially explicit manner (Mascaro et al. 2013). As a result physically based hydrological models are more capable to represent the strongly non-linear precipitation-runoff relationship of the hydrological system.

For this study the physically based fully distributed hydrological model WaSiM (Water Simulation Model) Version2 Richard-equation (Schulla 1997) was applied.

State of the art research fields using physically based hydrological models are the improvement of input data and parametrization of such models, by using remote sensing techniques and products, field survey, generic and geostatistical interpolation approaches and GIS applications. Beckers et al. (2011) stated that the better quantification of climate change impact on hydrology is one key area of computational improvements in hydrological modeling.

For example Daniel et al. (2011) points out that the distribution of soil types and its linked hydrological properties need to be improved by using remote sensing techniques, GIS applications and genetic algorithms. Rötzer et al. (2014) used WaSiM to compare modeled and upscale soil moisture content with derived soil moisture of (SMOS and ASCAT) radar remote sensing products.

WaSiM was applied successfully for many hydrological climate change impact assessment studies, for example by Gampe et al. (2015), Meyer et al. (2016), Cornelissen et al. (2013), Gädecke et al. (2013), Muerth et al. (2013), Ott et al. (2013), Velázquez, et al. (2013) and many more. Those studies showed successfully that WaSiM is capable to reproduce non-linear hydrological surface processes and that it is an up to date physically based fully distributed hydrological model. Therefore it was chosen to study the non-linear impacts of climate change on the hydrology in the Rio Mannu basin.

2. STUDY SITE CHARACTERIZATION

The presented study was conducted in the Rio Mannu di San Sperate catchment, located in the southern part of the Italian island Sardinia. This catchment is, as already mentioned in the introduction, affected by temporarily water scarcity conditions based on its semi-arid climate and the drop of rainfall of 50-60% in the last 20 years (Sannitu 2006) indicates that the hydrology of this catchment is already affected by climate change. The CLIMB-Project partner institution AGRIS Sardegna runs an agricultural research facility located close to the village Ussana, in the south western part of the catchment. Since in the CLIMB-Project hydrological quantities were investigated on different scales the basin was found to be an ideal test site and used for more intensive research than others test sides within CLIMB.

2.1 Rio Mannu di San Sperate

The basin drains an area of approximately 472.5 km² (Figure 2). The Rio Mannu has its headwaters in the north of the catchment. The basins outlet is close to the city Monastir. Here a dam was constructed in the nineteen-sixties. Since that time the Rio Mannu fills this artificial reservoir (10000m³). The basin ranges in elevation from 67m to 966 m above sea level with an average of 295m. The catchment is characterized by a mountainous region in the eastern part and a plain valley area (campidano plain) in the south-western part. The headwater of the main river channel is located in the mountains of Sette Fratelli (south-east of the basin), an area with higher elevation (up to 800 m.a.s.l.) and rugged terrain. The lower areas, closer to the outlet, have more gentle topography and are part of the Campidano plain. The flat downstream areas have been drained artificially through a system of channels since the 20th century. This was done to convert the former swampy land into fertile agricultural fields (Mascaro et al. 2013).

Intensive agricultural activity is still the main economic activity in this region (De Girolamo et al. 2010).

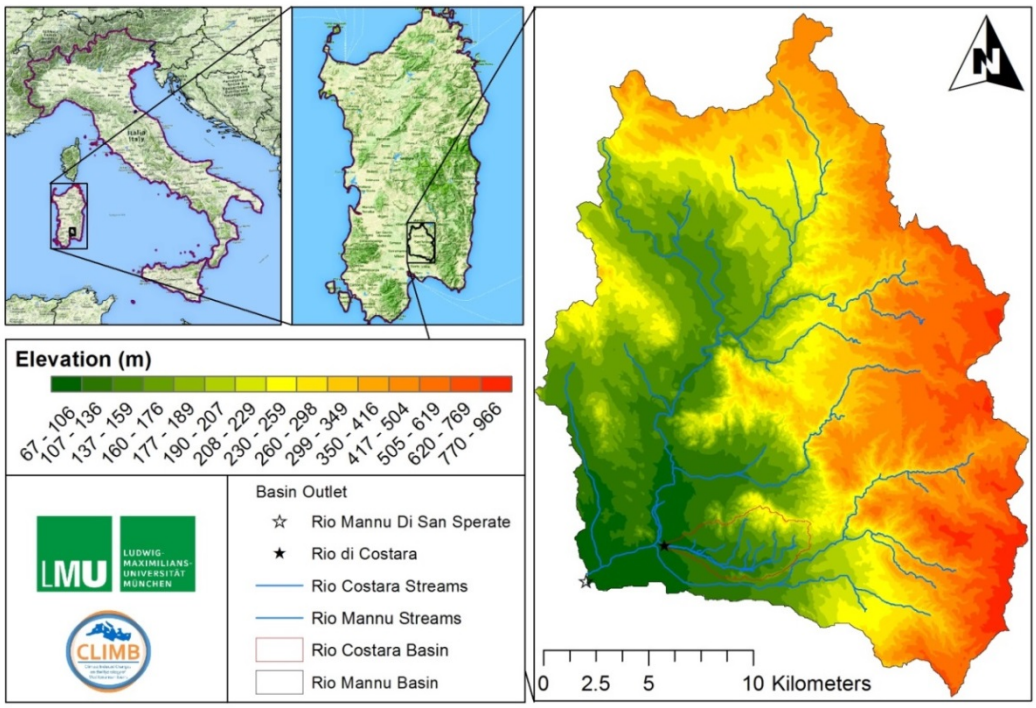

Figure 2: Location of the Rio Mannu di San Sperate catchment with locations of streams and information.

2.1.1 Land use

Figure 3 reports the land use in the Rio Mannu catchment based on CORINE 2006 (EEA 2007) land use land cover information. The most important crops grown are wheat (durum wheat), corn silage, aslike clover, beans and artichokes, which are cultivated in these flat valley areas. These areas are classified in the CORINE 2006 land use map as non-irrigated arable land and dominate the campidano plain. The eastern mountainous areas of the catchment are covered by grass land, vineyards, olive trees, broad leaf forest, and coniferous forest and in higher elevations by Sclerophyllous vegetation (maquis shrub land or Macchia mediterranea). Due to a project internal model harmonization strategy land use classes were aggregated to 6 main land use classes for the hydrological modeling (methodologies section 5.2.3.1).

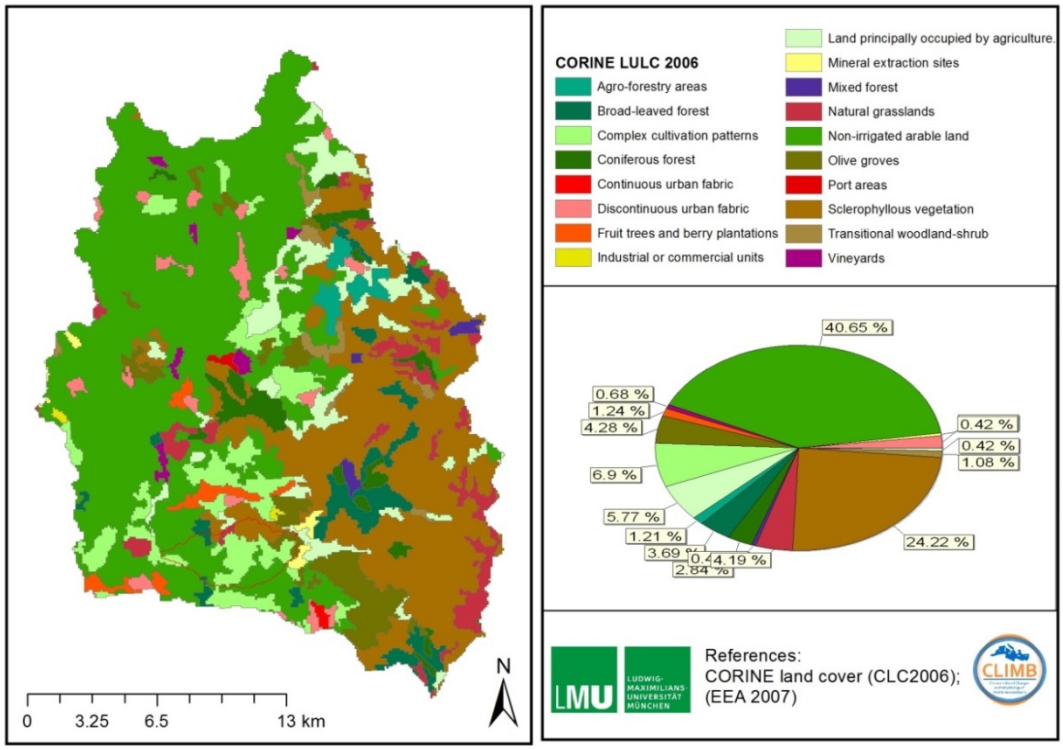

Figure 3: CORINE 2006 land use map of the Rio Mannu catchment.

2.1.2 Geology

Plate tectonics is the primary control on the geodynamic evolution of the Western Central Mediterranean (Carmignani et al. 2015). The geological structure of Sardinia is linked to the collision of Africa, Eurasia and the smaller Adriatic and Iberian plates active since the Mesozoic (Casula et al. 2001). Sardinia is the only sector of the outcropping Hercyian orogeny in Italy that is not superimposed by Alpine or Apennistic thrust belt (Doglioni & Flores 1997). It was part of a large Pallaeozoic mountain system, which was built 480-250 Ma ago from the diachronic collision of two continents (Laurentia–Baltica to the NW and Gondwana to the SE). Sardinia is part of the Amorica micro continent that was detached from Gondwana docked onto Laurentia and Baltica (Rossi et al. 2009). During the Mesozoic and Paleocene Sardinia separated from the European plate and drifted into its current position during the Burdigalian in a counter-clockwise rotation together with Corsica (Casula et al. 2001).

Figure 4 reports the simplified geological structure of southern part Sardinia together with the location of the Rio Mannu catchment. The main geological units, reported in Carmignani et al. (2015), in whole of Sardinia and in the southern part of the island are:

1. The Variscan basement composed of anchizonal to high grade meta-morphic rocks and Permo-Carboniferous batholith.

2. The Permian to Oligocene sedimentary succession, which was built when Sardinia was part of southern Europe, with a deposition of a widespread carbonate platform and clastic and marine deposition of small out crops of Lower Eocene limestones.

3. The Oligocene to Miocene volcano-sedimentary succession deposited in several basins of the so called Sardinian Rift.

4. The Campidano half graben, which developed during Tortonian and Messinian times from a carbonate-mixed siliciclastic deposition in shallow marine and transitional environments.

The Rio Mannu catchment covers all four main geological units. The south-western part of the catchment covers the Campidano, which is predominantly characterized by Plio-Quaternary continental deposit. The Campidano plain is a graben area up to 600m deep that was filled most recently with post-Variscan quaternary and tertiary sediments (Doglioni & Flores 1997). The mountainous eastern parts of the catchment are part of the Paleozoic or Variscan basement and are characterized by Paleozoic substratum and related Mesozoic-Eocene marine sedimentary covers. The Miocene marine deposits in the center of the catchment are surrounded by the former two geological units in a north-western direction from the city Cagliari to the city Oristano. The smallest unit in the catchment in the southern part of the catchment is characterized as Plio-Quaternary alkaline volcanic (compare Murru et al. 2015).

Based on the geological map 1:25,000 map published by the geoportal of the Autonomous Region of Sardinia the main geological features can be identified: In the most northern part of the catchment predominantly sandstones and conglomerates of the burdigalian are present and followed by an area in the south-west characterized by alternating layers of silty marls and sandstone developed from coarse to fine volcanic sediments. The Gerrei area, in the eastern mountainous part of the catchment (Figure

4), is characterized by metasandstones and metasiltstones from the middle Cambrian. The transition of the former two geological units consists of Holocene deposits of sand with underling silts and clays. Close to the present stream network, coarse to medium alluvial deposits of Holocene graves are dominant. Based on the Ussana formation main geological processes that took place in the Rio Mannu catchment in history can be illustrated.

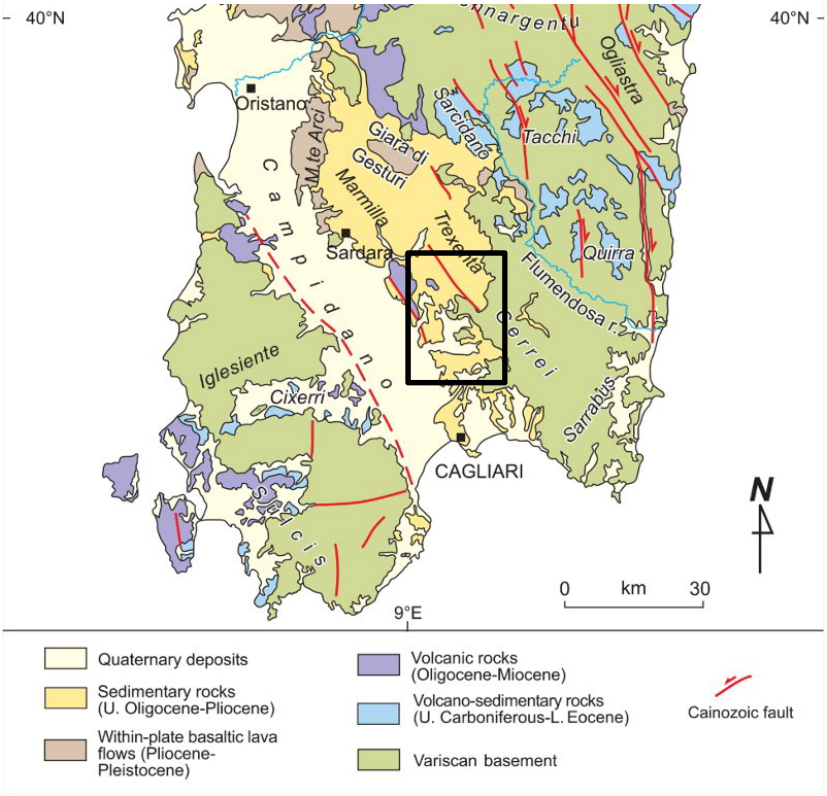

Figure 4: Simplified geological features of southern Sardinia (source: Carmignani et al. (2015) changed, the black rectangle shows the geological features of the Rio Mannu catchment).

Casula et al. 2001 describes the historical process during the Burdigalian horsts, grabens and titled blocks formed controlled by tectonics and volcanic morphology. The uplift occurred along the campidano margins and was linked to strong erosion with the development of mega-breccias, breccias and continental conglomerates clasts (Casula et al. 2001). Those formed deposits of a red violaceous, sandy clayey matrix at the foot of the fault escarpments with a centimeter to several meter thickness. The Ussana formation is covered by a layer of mainly fine-grained sediment succession (Mancosu

2013). No significant Pliocene erosion occurred in the southern Campidano. In the Pliocene the Samassi Formation developed by the erosion of redeposited Miocene sediments from the eastern flanks. The Samassi formation consists of continental marls and silts, with occasional sand and pebble beds in layers of clay. This sedimentation process continued until the Quaternary (Casula et al. 2001). The geology in this area is rather complex and certain geodynamic settings and structural evolutions, like Miocene volcano-sedimentary succession are still debated in literature (Carmignani et al. 2015). This shows that the Sardinian landscape morphology is rather complex and its development processes are not fully understood up to now.

2.1.3 Soil information

The so called Mediterranean soils will by definition form under a Mediterranean climate (Verheye de la Rosa 2006). This forming climate is characterized by wet winters with some months of excess rainfall over evapotranspiration and by dry and hot summers, with decreased soil moisture content (Yaalon 1997). The second important soil forming factor is the parent material, which is in the case study not easy to determine as shown in section 2.1.2.

In the Mediterranean the soil forming process is characterized by an effective dissolution and leaching of calcium carbonate and other soluble elements. This process is most active in the rainy winter time (Verheye & de la Rosa 2006). Most important parent materials in the Mediterranean are carbonaceous rock, which are dominated by relatively soluble $CaCO_3$ fraction. Verheye & de la Rosa 2006 indicate that the speed of the development of Mediterranean soils over limestone is strongly influenced by: (I) the dilution speed of the carbonate fraction; (II) the amount of precipitation that infiltrates into the soil and (III) the initial $CaCO_3$ content. Those soils when developing over lime stone have a reddish color (Terra Rossa) and a high content of clays and silty-clay material (Durn 2003). Terra Rossa in the Mediterranean are characterized by silica enrichment and by clay mineral assemblages which are often dominated by less weathered clay minerals such as smectite (Lucke 2014). The development of many soils in the Mediterranean area is also affected significantly by dust that coming from the Sahara desert. It was proven by using stable isotopes that most of the fine silt fractions in the climax soils developed over Terra Rossa are of aeolian origin (Yaalon 1997). The more

hilly landscapes are stronger affected to erosional processes, which is leading to rejuvenated soils on slopes and accumulation of soil material at lower positions (Blaschek 2015).

The spatial distribution of soil properties varies strongly within the catchment and influenced by the parent rock material and in fertile areas by the 1000 year lasting agricultural activity (Fanni et al. 2004). Following the FAO classification ambisols, regosols, and vertisols or marls, sandstones and conglomerates characterize the soils in the valley part of the catchment, while cambisols and lithosols on crystalline schists and quartzite are present in the rocky mountainous region. In the area close to the village Ussana, regic anthrosols and calcaric regosols are present with slightly alkaline conditions. The flood plain consists mainly of alluvial soils, predominantly gravelly or sandy gravelly (Aru et al. 1990). Following the USDA classification major soil types in the catchment are typic dystrict, Lithic Xerorthents (clay-loam, deep), Lithic Xerochrepts (sandy-loam to loamy-clay, deep), and Lithic Xerorthents (sandy-loam, to loamy clay, shallow) (De Girolamo et al. 2010, Aru et al. 1990).

In a field campaign together with a team from the University of Kiel (CAU) 3 soil profiles were investigated at the Azienda di San Michele in March 2011. The Azienda San Michele is an agricultural research farm that is operated by the CLIMB-Project partner ARGIS. Two more soil profiles were investigated by the CAU at the Azienda di San Michele in March 2013 additionally. The profiles were classified following the German soil classification system of the soil mapping manual of Sponagel (2005) (AG Boden 2005). The 5 soil profiles were classified and described in Blaschek (2015). The five bullet points below are a summary of this description. A detailed description of those profiles is given in Blaschek (2015)

1. Calcaric Regosol (Ap, Ck1, Ck2, Ck3) located on top of a hill, significantly affected by erosion. In the first 100cm the soil textures class is clay and has high calcium carbonate ($CaCO^3$) content. The soil developed over calcareous sand stone.

2. Calcaric Regosol (Ap, Ck1, Ck2, Ck3), located at a lower position, but also affected by erosion. The soil formed over calcareous sand stone. Like in profile 1, the upper layers are classified as clay, and change to clay loam in the Ck3 horizon.

3. Regic Anthrosol (Ap1, Ap2, Bw1, Bw2) located at a different field close to a weather station that was installed during the CLIMB-Project. The first two layers are strongly influenced by anthropogenic erosion (Ap1, Ap2). The underlying Bw1 and Bw2 horizons are well developed with high CaCO3 content. The soil texture of all horizons was classified as clay-loam.

4. Chromic Cambisol (Ap1, Ap2, Bw1, Bw2). This profile was located in a small depression and due to that less affected by erosion. Compared to the other horizons, no clear clay migration is visible in the Bw1 and Bw2 and most horizons are classified as sandy-clay-loam. The soil has a reddish color due to iron oxidization, which is stronger developed in the upper horizons.

5. Haplic Luvisol (Ap, E, Bt1, Bt2, Btk, C). This mature soil shows a strong clay illuviation in the tree Bt horizons. All horizons except for the last Bt are almost $CaCO^3$ free. In the last Bt $CaCO^3$ reaches a value of 56%. The first horizons are classified as sand clay loam. The clay illuviation results in a clay classified texture for the Bt2 and Btk horizons. The profile formed dominantly by alluvial deposits up to a depth of 160cm and contains pebbly components from the surrounding metamorphic granitic Paleozoic hills. A detailed description is given in Blaschek (2015).

2.2 Historical data precipitation and runoff data

The investigated area is characterized by a semi-arid climate, with a cold winter period from October to April and very dry and hot summer months. The mean annual air temperature is 17 °C. The annual precipitation ranges from about 400 to 700 mm (Figure 5) and occurs almost entirely in the winter season (Vacca et al. 2000). Delitala et al. (2000) show that the yearly mean precipitation sums can vary highly on the Sardinian island and show a clear correlation of wet and dry years with the NAO (North Atlantic Oscillation). Rainfall events are unevenly distributed, as they are rather short but intense and exert a great amount of influence on the flow regime (De Girolamo et al. 2010). Besides the temporal variance, precipitation sums can vary highly within short distances

on the island.

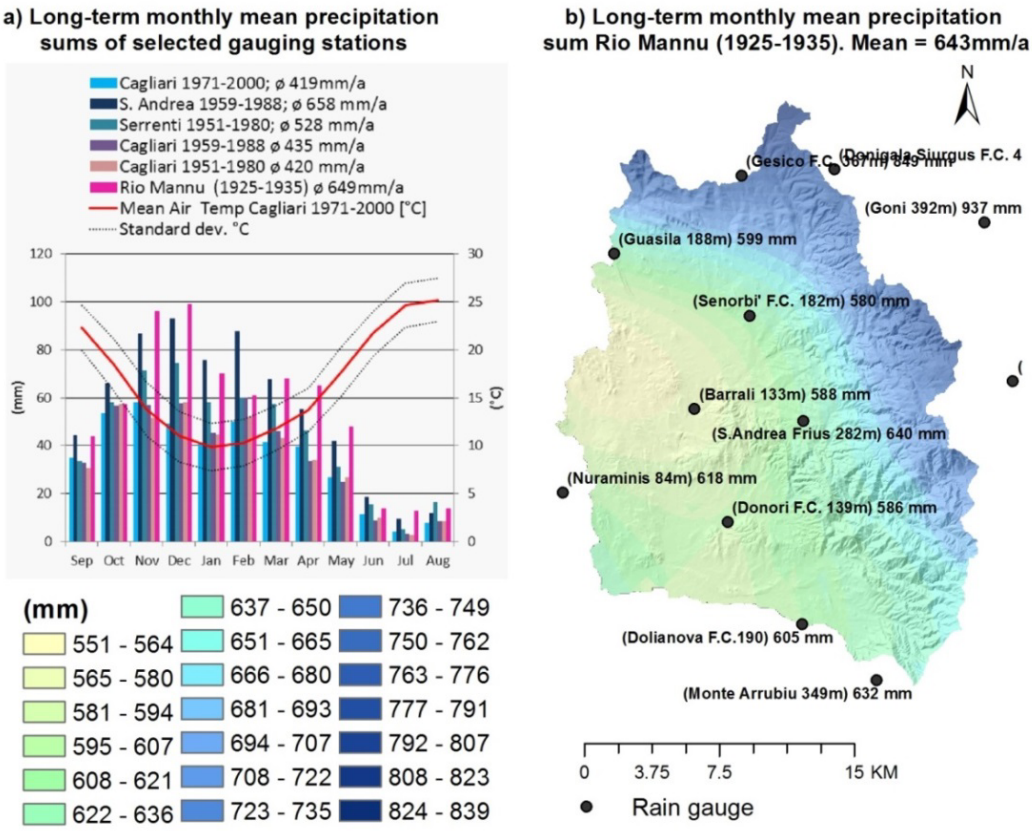

Figure 5: a) Recorded long-term monthly mean precipitation sums of selected gauging stations and b) precipitation map interpolated from recorded long-term annual precipitation sums of 12 gauging stations for the time series 1925 to 1935 using inverse distance weighting. The map was overlaid with a transparent hill shading layer to give an impression of the topography.

The identification and collection of available geographical, hydrological, and climatological data of each CLIMB case study and the distribution of this data to CLIMB partners was one of the first working steps at the beginning of the project.

A set with daily precipitation rates of 76 rain gauging stations of southern Sardinia during the period from 1922 to 1996, a dataset with maximum and minimum air temperatures for Cagliari and recorded discharge of the Rio Mannu di San Sperate Basin (RMB) at the Monastir gauging station for the time series 1925-1935 was delivered by the CLIMB partner CINFAI.

The daily mean precipitation dataset unfortunately contained long lasting data gaps. Only 12 gauging stations were consistent for time series >10 years and only two gauging stations in Serrenti and S. Andrea de Frius recorded a nearly consistent time series of 30 years. Figure 5a reports the long-term monthly mean precipitation rates of these two stations in comparison with monthly mean precipitation rates of Cagliari (30km south of the case study) for the equivalent time series and the CLIMB reference time series 1971-2000 (downloaded from KNMI climate explorer 2013). The monthly mean precipitation rates of the three stations show a strong deviation. While in S. Andrea des Frius annual mean of 658mm was recorded for the time series 1959-1988, only 80% of this rate (528mm/a) were recorded in Serrenti for the Time series 1951-1989. The gauging station located in Cagliari recorded 419mm/a for the CLIMB reference time series 1971-2000. This is only 64% of the value of S. Andrea de Frius. This strong deviation in recorded precipitation is most likely explainable due to the differences in elevation of the two gauging stations. Sannitu (2006) pointed out that the precipitation rate in southern Sardinia was reduced by 50-60% in the last 20 years. This reduction is at least not visible in the recorded annual precipitation sums for Cagliari until the year 2000.

Figure 5b reports the inverse distance weighting interpolated recorded data of 12 gauging stations for the time series 1925-1935. The map was overlaid on a Hill shading layer to give an impression of the catchments topography. The map shows a clear trend of lower precipitation rates in the valley area in the western part of the catchment to strongly increasing precipitation rates in the mountainous eastern part of the catchment. The daily precipitation data of 1925-1935 were aggregated to long-term monthly mean sums to get an impression of how precipitation is transformed into discharge.

Figure 6 reports the long-term monthly mean and median discharge of the Rio Mannu catchment for the time series 1925-1935. This time series was the only discharge information that was available in a daily mean temporal resolution.

Highest discharge is generated in the months December to February, with a mean peak in January and a median peak in February. The strong deviation between mean and median values indicates that mean high flow conditions are affected by single short time extreme events and that the histogram of discharge is heavily left skewed for this time of the year. The median value of February for example reaches only 47% of the mean discharge. The months March to June and November are transition months in which the

discharge curve is dropping and increasing strongest. Lowest flows are present from July to October. Median and mean discharge values show only minor deviation from May to October. This indicates that the discharge is only slightly affected by extreme precipitation event in this time of the year.

2.2.1 Flow duration curve and number of flow conditions of the recorded historical discharge in the Rio Mannu di San Sperate Basin

Flow duration curves (FDC) were calculated from the historical recorded discharge of 1925-1936. A flow duration curve measures in X-axis direction from high to low flow and the Y-axis gives the discharge quantity for each percent exceedance value (1-100%). Based on the derived FDCs of the recorded discharge as well as for the hydrological modeling discharge results, threshold values for the different flow conditions were determined. A detailed overview of this method is given in section 5.3.1.

Figure 6 reports the average number of low, dry, mid-range, wet and high flow condition days per month, based on the thresholds of the FDC in Figure 25.

Low flows are defined as 90%-100% flow exceedance percent (0.0349-0 m^3/s), dry conditions are in the range 90%-60% flow exceedance percent (0.035-0.299 m^3/s), mid-range flows are in the range 60%-40% flow exceedance percent (0.3-0.619 m^3/s), wet conditions are in the range 40%-10% flow exceedance percent (3.38-0.62 m^3/s) and high flow conditions are in the range 0%-10% flow exceedance percent ($Q > 3.39$ m^3/s).

In the recorded discharge time series dry conditions with more than 15 days per month are dominant from July to October. The transition months from March to May are dominated by days with wet conditions. As soon as the mid-range flow conditions are increasing discharge is significantly dropping in May. The small number (<5 days) of high flow conditions in March and April has a significant impact on the mean discharge, which is about 1.5m^3/s higher compared to May, where days with wet conditions are about the same.

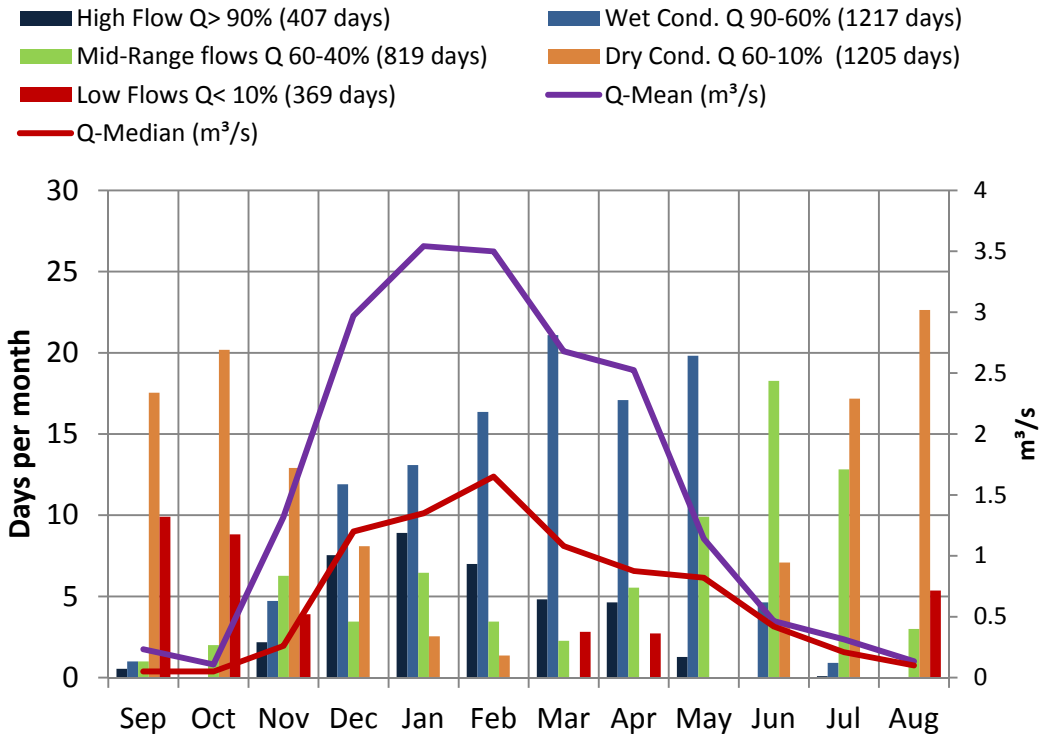

Figure 6: Long-term monthly mean and median of recorded discharge data and mean number of days with low, dry, mid-range, wet and high flow in the Rio Mannu di San Sperate catchment (Gauging station Monastir 1925-1935). The total number of days for 1925-1935 is presented in the brackets.

In January and February the mean discharge has the highest values, those month are mainly characterized by days with wet conditions and high flows. Note that the analysis of the flow conditions also shows some errors in the recorded time series in March and April, where days with low flows are present but no dry conditions. The recorded discharge drops from 28.02.1928 to 01.03.1928 from 0.89 m^3/s to 0 m^3/s. The value stays at the 0 m^3/s level for the total March and April 1928 and at 1st of May 1928 increases to 1.1 m^3/s. This is obviously an error or gap in the recorded time series.

3. METHODOLOGIES OF THE REGIONALIZATION OF SOIL PROPERTIES

3.1 Soil information and soil sampling campaign

The quality of the hydrological model setup of WaSiM is strongly dependent on the available soil information (Rieger et al. 2010). WaSiM has to be set up in this version by linking grid values of the soil texture map with lookup tables, which describe the hydrological properties of each soil texture class. This means that distributed soil information of good quality is crucial to the successful setup of the hydrological model.

The available soil texture information of Aru et al. (1990) in the catchment was rather unreliable, since its spatial units do not represent a unique classification of soil texture classes. Instead the spatial units of the soil map represent ranges of soil texture classes. Using this kind of soil information to setup a hydrological model is a problematic obstacle, since for example the determination of hydrological properties based on pedotransfer function is nearly impossible. However, it was used for the official hydrological modeling in the CLIMB-project. In the CLIMB-Project three different hydrological models were applied in the Rio Mannu catchment. Not all of those applied models were able to handle high resolution soil information. The available regional soil map (Aru et al. 1990) was aggregated to 6 classes for the standard hydrological model setup. In this map, soil texture information was still present in ranges of soil texture classes per soil region polygon. Due to this, a distinct linking of soil type and soil grid value of the soil map was not possible. Since, every class still included a range of different soil texture classes; the weighted average soil texture of every class was used. With this procedure it was

possible to set up the soil model lookup tables in WaSiM with six unique soil texture classes following the German classification system of Sponagel (2005).

First hydrological modeling tests backed the assumption that the Aru et al. (1990) soil information seemed rather inaccurate, additional soil texture information was surveyed by collecting a total of 239 soil samples in the catchment during two field campaigns. Soil samples were taken following a design-based, stratified, two-stage sampling (de Gruijter et al. 2006) in early October 2010 and in March 2011. The selection sampling locations was done by University of Kiel. The stratification was based on quantiles of the two land-surface parameters, topographic wetness index and potential incoming solar radiation, which were derived from a Digital Elevation Model (DEM) as well as the four main geological units coming from a 1:25000 geological map. The random selection of target polygons for each strata has been repeated ten times and was only permitted for polygons greater than one hectare.

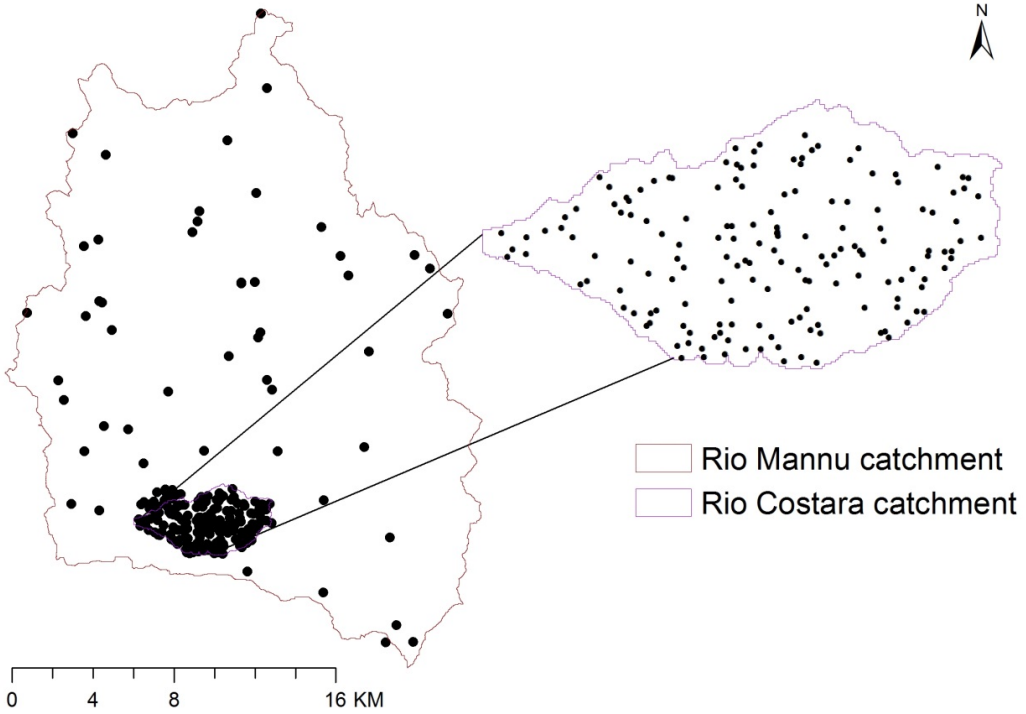

Figure 7: Soil sampling location Rio Mannu (N=239) catchment and Rio Costara sub-catchment (N=168).

The final sampling scheme was chosen in a way that the geographical spread was maximal. The sampling was done on two scales. A spatially very dense sampling approach for a 16km² sub-basin (Rio di Costara catchment) within the Rio Mannu catchment were chosen to sample small scale variability. This information was used by hydrological models that were applied on a very fine scale (30m) in this sub-basin and was used in the doctoral thesis of Michael Blaschek who developed, applied and tested Neural Network interpolation approach to regionalize the soil properties of this sub-catchment. A number of 50 additional soil samples were collected for the larger Rio Mannu catchment. Both sample sets, small and large scale were used to provide spatial soil information for the hydrological modeling on the large scale. Composite soil samples from a depth of 30cm were taken using a gouge auger of the type Pürckhauer. An overview on sampling designs as well as a detailed description of the sampling approach is given in his thesis Blaschek (2015).

3.2 Laboratory analysis

At certain sampling locations bulk density and soil moisture was determined using sample rings with a volume of 100cm³, which were weighed field fresh, dried 24hours at 105°C and weighted again. This was done at the laboratories of the Azienda San Michele research facility in Italy.

All other lab-analysis was done by the Department of Geography of the University of Kiel. Soil samples were analyzed for grain size distribution, calcium carbonate content ($CaCO_3$), organic content, Soil pH, exchangeable cations, available potassium and phosphorus content, free iron oxides and amorphous iron oxides.

The main interest of this study is the grain size distribution, the bulk density and the organic content at sampling location. Those soil properties were regionalized (section 4) and applied into a pedo-transfer function to derive the soil hydraulic properties for the hydrological model WaSiM (section 5.2.3.4).

The grain size distribution was analyzed based on the sieve-pipette method of Köhn (din standard; DIN ISO 11277). For this study soil samples were dried and sieved to fraction smaller 2mm to eliminate gravel fractions. The resulting fine fractions of the samples

were treated with different chemicals to eliminate organic matter, iron oxides and carbonate and to remove coatings of the soil particles. The treated samples were dispersed using sodium pyrophosphate ($Na_4P_2O_7$) and the sand fractions were separated using the wet sieving method to classes of (2000-630, 630-200 and 200-63 µm). The final step was the separation of the silt and clay classes. A defined amount of the diluted fraction smaller 63µm gets extracted after certain sedimentation time steps. The extracted amount of liquid was after dried. The different silt fractions (63-20, 20-6.3 and 6.3-2µm) and the clay fraction (<2µm) were after determined by weighing the dried extractions. Finally seven fractions of sand, silt and clay content were available in weight percent. The single fraction of sand and silt were afterwards aggregated to single classes, to finally have a dataset with the sand silt and clay distribution for each location.

The C/N ratio was analyzed using the EURO EA Element Analyzer, which is a gas chromatograph from the HEKA-tech company. The SOC was determined from the disparity of total and the inorganic carbon content of the CaCO3. A detailed description of the lab-analysis of soil properties which were not used in this study, can be found in Blaschek (2015)

All sample point locations were georeferenced using a Trimble Juno SB handheld with a positional accuracy of about 2-5 m and identified by a unique id. For the regionalization of the soil properties on the Rio Mannu scale, position accuracy was neglected.

3.3 DEM data and digital terrain analysis

One set of auxiliary variables was extracted from a digital elevation model of 10m resolution (published under the Italian Open Data License in version 2 by the geoportal of the Autonomous Region of Sardinia). The DEM was resampled to a pixel resolution of 208m for the Rio Mannu catchment, following the approach of Hengl (2006):

$$px = \sqrt{obs * A * \frac{10^6}{n}} * 100 + 0.0005\,, \qquad (1)$$

where A is the catchment area in km², n is the number of samples and obs equals 2.5 observations per cm² on the map Hengl (2006)

Terrain attributes were computed in SAGA-GIS by a 3*3 window. First the primary terrain attributes aspect (A), Slope (β [rad]), plan curvature (Ch), profile curvature (Cv), divergence/convergence index (CDI), specific catchment area (SCA), and afterwards the secondary terrain attributes stream power index (Ω), topographic wetness index (TWI), and the SAGA wetness index (SWI) were processed using terrain analysis modules of SAGA GIS (SAGA User Group Association 2011). Each calculated variable represents terrain attributes that can be linked to the intensity of natural processes that are influencing the soil forming processes, which means more specific:

The β quantifies the maximum rate of change from each cell to its neighbor in the DEM and controls overland subsurface flow velocity as well as runoff rate. Increasing β angles normally increase the runoff speed, which results in higher erosion rates in those areas (Scheffer & Schachtschabel 2002). The β has a major impact on the thickness of soil horizons, the nutrient availability, as well as the soil texture composition. Areas with high β angles are often characterized by a thin soil horizons thickness, a poor nutrient availability and coarser soil texture composition. Low angles indicate deep soil layers, a higher nutrient availability and finer soil texture compositions (Gessler et a. 2000, Schauppenlehner 2008). The spatial distribution of the slope angle in the catchment is presented in Figure 10. The slope angle in this figure was recalculated to degree (°) to increase the readability.

Aspect (A) defines the cardinal direction in 0-360° that a surface is facing. The A of a slope can influence the local (micro)-climate (exposure to sun light, precipitation and wind etc.), and often shows correlations with soil moisture content, the distribution of vegetation, soil organic matter and soil texture compositions. In the northern hemisphere south-facing slopes (south aspects) are normally warmer and drier due to a higher solar radiation than north-facing slopes (north aspects). The warmer temperatures on south facing slopes speed up most chemical reactions and increases soil genesis and the evaporation of water from the soil profiles (USDA 2015).

The curvature of a slope can be described in horizontal and vertical direction. The profile curvature (Cv) is rate at which surface slope changes in the vertical direction. Cv in geomorphometry defines curvatures as negative for concavities and positive for convexities. Plan curvature (Ch) is the rate at which flow direction changes following a contour line. Ch is negative for valleys and positive for ridges (Peckham 2011).

The curvature affects the run off direction and erosion potential and by that the soil moisture patterns of a slope (Souza et al. 2006).

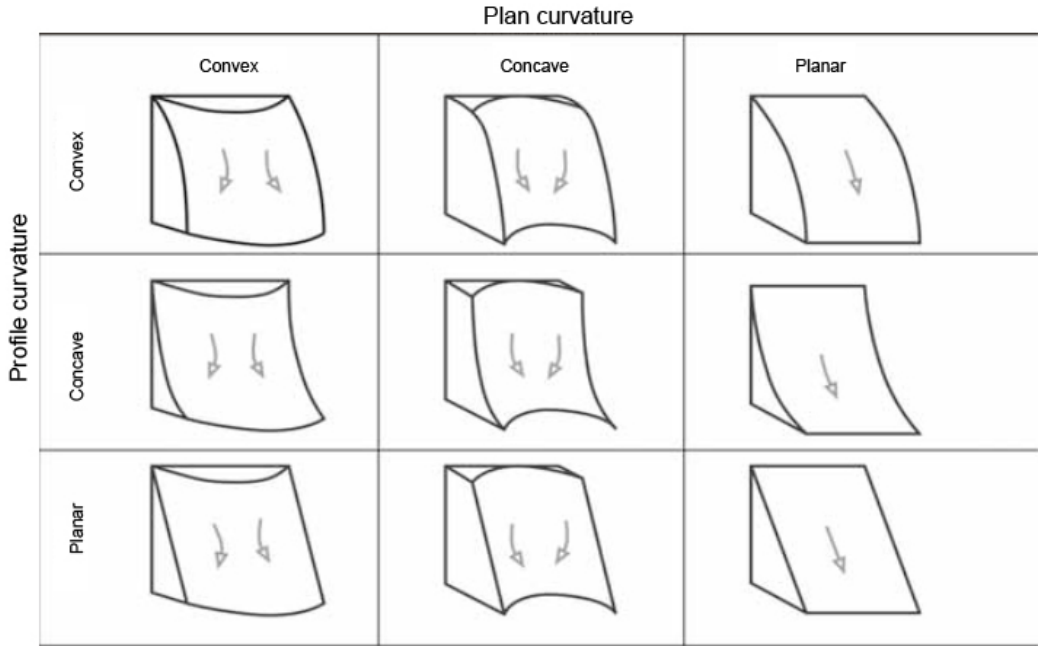

Figure 8: Slope described by combinations of profile and plan curvature (Schauppenlehner 2008 (modified)).

The convergence divergence index (CDI) is a relative measure in percent of flow direction vectors of neighboring pixels that point into the direction or away from the central pixel. A CDI of 100% means complete divergence (all neighboring pixels point away from the central pixel, Figure 9a), while a CDI of -100% means complete convergence (like a sink, all neighboring pixels point into the direction of the central pixel, Figure 9c). A CDI of 0% would say that the same number of vectors that point into the direction of the central point away from it (Figure 9b).

For the channel network base level the vertical distance to the local channel network base level is calculated. The channel base level is the elevation at the channel bottom at the point where all runoff from the watershed leaves the watershed. The algorithm calculates the CNBL two major steps: First the channel network base level elevation is interpolated, and afterwards this base level is subtracted from the original elevations (Conrad 2002).

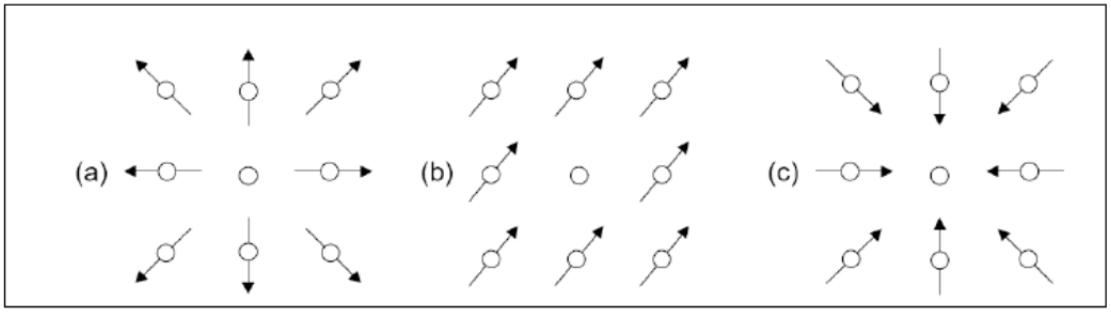

Figure 9: Convergence / Divergence Index (Köthe & Lohmeier 1993).

SAGA uses the multiple flow direction algorithm of Freeman (1991) to calculate specific catchment area (SCA).This algorithm calculates for every pixel the up slope drainage area. It is a prerequisite to calculate the SAGA wetness index.

The TWI (Beven and Kirkby 1979) was derived by the equation TWI = ln(α/tan β), where α is local upslope contributing area and β is the local slope. It is commonly used to quantify topographic controlled hydrological processes (Sørensen et al. 2006). In this case for each grid cell the catchment area is defined as the discharge contributing upslope area of each grid cell. The specific catchment area, defined as the corresponding drainage area per unit contour width, was computed using the multiple flow direction method (Böhner et al. 2006). The index is used to identify soil moisture patterns within a catchment, which have a strong relation to soil forming processes. However, in rather flat areas of a catchment differences in altitude cause random like flow pattern, which distinctly limit the predictive capacity. The SAGA wetness index modifies the specific catchment area SCA_M of each grid cell in iterations as a function of slope angle β and the neighboring maximum values SCA_{max} unless results remain unchanged (Böhner et al. 2006)

$$SCA_M = SCA_{max}\left(\frac{1}{15}\right)^{\beta\exp(15^{\beta})} \text{ for } SCA < SCA_{max}\left(\frac{1}{15}\right)^{\beta\exp(15^{\beta})} \quad (2)$$

The SAGA wetness index is then computed as a tangent function of slope and SCA_M (Böhner et al. 2006).

$$SWI = ln\left(\frac{SCA_M}{\tan\beta}\right) \quad (3)$$

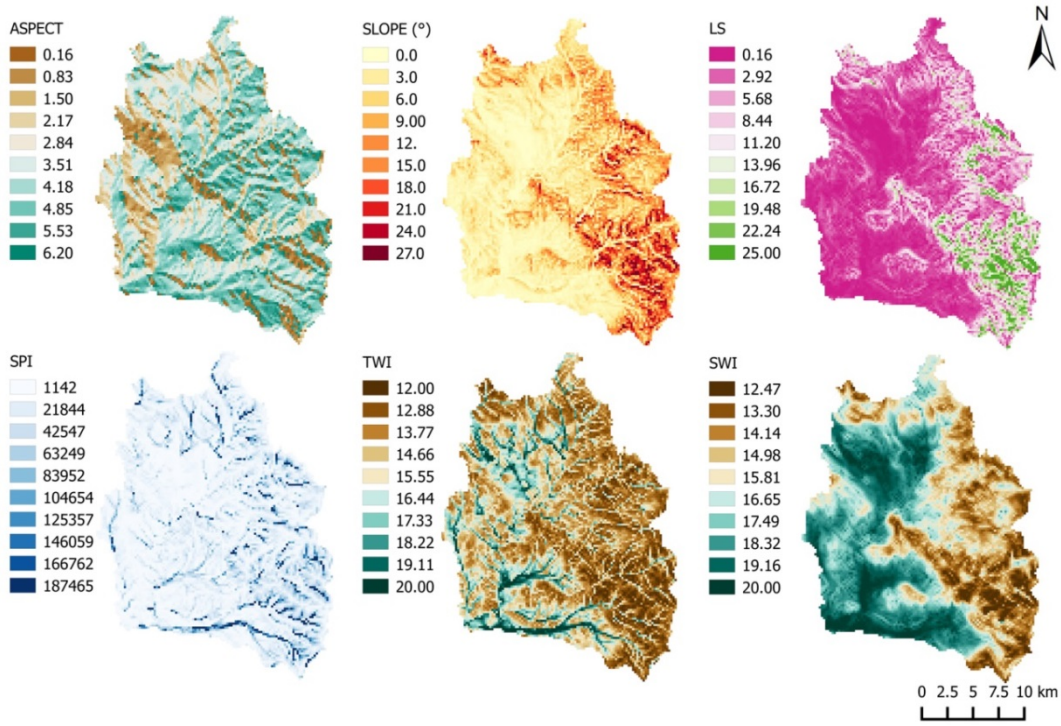

Figure 10: Selection of applied terrain attributes (Co-Variables).

Figure 10 reports the calculated TWI and SWI for the Rio Mannu catchment. Both indices characterize the valley part consequently with a higher wetness index. The patterns of the TWI are clearer drawn and differences in the index are strongly related to the distance to streams. The SWI on the other hand is characterized by more smooth patterns. Detailed information regarding the terrain analysis procedure of SAGA GIS can be found in Olaya (2004), Conrad (2006) and Hengl (2009).

3.4 Data handling

The GPS information and the ID identifier of the soil samples (section 3.1) were used to create a geo-database and lab-analyzed information about grain size distribution and organic content.

Regionalization methods like Multi-Linear-Regressions, Regression Kriging use secondary information (e.g. DEM, SLOPE, ASPCET etc.) to predict the target variable at unknown locations. This is often done by a linear regression model, which is developed based on the relationship of target variable and secondary information at sampled locations, as illustrated in sections (1.3, 3.5 and 3.7). The R-gstat library (Pebesma 2004) was used to read out and apply the pixel values of the terrain attributes (section 3.3) for each soil sampling location. The geo-database was the basis to proceed with the (geo-) statistical analysis and interpolation of soil physical properties.

3.5 Applied deterministic soil regionalization models

3.5.1 Multiple linear regression (MLR)

The multi linear regression is a widespread statistical analytical method to predict a target variable Z by one or a set of independent coefficients or co-variable(s), by the assumption that the conditional mean function is linear.

$$Z(S_0) = \beta_0 + \beta_1 \beta X_1(S_0) + \cdots + \beta_q \beta X_q(S_0) + \epsilon, \quad (4)$$

where β_0 is the intercept, $\beta_1, \ldots, q$ are the regression coefficients for the independent information (explanatory factors) and ϵ is the residual error.

The multiple linear regression equations were determined by applying the data of the soil physical data and the terrain attributes into the MLR model:

$$\hat{Z}_{OLS}(S_O) = \sum_{k=0}^{p} \hat{\beta}_k q_k(s_0) \quad (5)$$

Where $q_k(s_0)$ are the values of the p covariates and β_k are coefficients that have to be estimated using the Ordinary Least Squares (OLS) with,

$$\hat{\beta} = (q^T * q)^{-1} * q^T * z, \quad (6)$$

where *q* is the matrix of predictors *(n*p+1)* and z is the vector of sampled observation. The prediction error (residuals) was calculated by determining the mean square error (*MSE*) around the regression line (Hengl 2009).

In order to estimate Z with a minimum number of independent co-variables getting in the appropriate final regression equations, a backward stepwise procedure was used. Only those auxiliary variables that were significantly correlated with any particular target variable regarding spearman rank correlation coefficients have been considered as initial regressors.

3.5.2 Inverse Distance Weighting (IDW)

As a second interpolation method an inverse distance weighting (IDW) interpolation model (Shepard 1968) was applied to the soil physical properties. This technique has been widely used in the past and is probably one of the oldest spatial prediction methods (Hengl 2009). In an IDW interpolation model the weighted average is used to derive the value of a target variable at new location:

$$\hat{z}(s_0) = \sum_{i=1}^{n} \lambda_i (s_0) * z(S_i) \quad (7)$$

Where λ_i is the weight of neighbor i. The interpolation is unbiased as long as the sum of weights sum up to one. The inverse distances of all sample points relative to the new point are used to determine the weights:

$$\lambda_i(s_0) = \frac{\frac{1}{d^{\beta}(S_o,S_i)}}{\sum_{i=0}^{n}\frac{1}{d^{\beta}(S_o,S_i)}};\ \beta > 1 \quad (8)$$

Where $d(S_o, S_i)$ is the distance between sampled points and β is the coefficient that is used to adjust the weights. By this method sampled points that are close to the unknown location will obtain high weights, while those points that are far away will influence the interpolated value only with small weights. The term β, in some literature referred as power, is used to emphasize spatial similarity. A popular choice of β is two (Webster and Oliver, 2007) β but should be adjusted in the way, that it reflects the true strength of the autocorrelation of the feature space (Hengl 2009).

3.6 Geostatistical interpolation models (Kriging)

Geostatistics have its origin in the gold mining industry and got popular with the research of the engineer Krige (1951), who developed a stochastic approach to predict gold deposits. Since that time this basic (Kriging) approach was further developed, modified and improved along with the evolution of computational performance. This field of applied mathematics deals with the description and prediction of natural phenomena in space and time (Akin & Siemes 1988). Today different geostatistical kriging approaches are applied widely and with increasing sophistication in petroleum engineering, mining and geology, meteorology, hydrology, soil science, precision agriculture, pollution control, public health, fishery, plant and animal ecology, and remote sensing (Webster & Oliver 2015).

The value of a natural variable z can change in space and time completely random or discontinuous or more or less continuous. This fact reveals the problem that a complete and true mathematical description of the variance of z is neither possible by statistics nor by a deterministic formula. However, a functional description of local variance can be made, by the fact that in natural systems values of neighboring points are normally more common than those at larger distances. Matheron (1965) improved the idea of Krige (1951) by treating the variation of *z* as though it were random. In this case z at the location *x (z(x))* is one realization of infinity values of a random variable *Z(x)*. The set of random values at all such places, again infinity in number, in a region is a random process, and also denoted *Z(x).* The random variable is spatially correlated at some scale (Webster & Oliver 2015). Since a set of measured values are only single realization of the total process, one cannot calculate statistics for a certain point. A model of local variance can be formulated anyway by the assumption of the stationarity process and the intrinsic hypothesis. The assumption of stationarity is fulfilled if,

I. a variable with an expected mean *(μ)* exists and is not dependent from the location *(x),*

II. the covariance exists for every pair of random variables,

III. the covariance is only dependent on the distance of points.

The covariance cannot exist when the mean is not constant, which leads to the assumption of the intrinsic hypothesis of Matheron (1965). Here the covariance is replaced by half of the variance of differences the so called semi-variance. This function of distance is described mathematically as:

$$\gamma(h) = \frac{1}{2} E[\{Z(x) - Z(x+h)\}^2] \quad (9)$$

Where h is the separation in both distance and direction, *Z(x)* and *Z(x+h)* are the values of *Z* at places *x* and *x+h* and E denotes the expectation. On grounds of the semi-variance function one can calculate the experimental variogram from the sampled data points *z(xi)*:

$$\hat{\gamma}(h) = \frac{1}{2m(h)} \sum_{j=1}^{m(h)} \{z(x_j) - z(x_j + h)\}^2, \quad (10)$$

where m(h) is the number of paired comparisons at lag h. The semi-variances at unknown locations can then be computed by fitting a smoothing curve to the experimental variogram points and create a theoretical variogram model (Figure 11). Now a semi-variance value can be identified for every location in feature space.

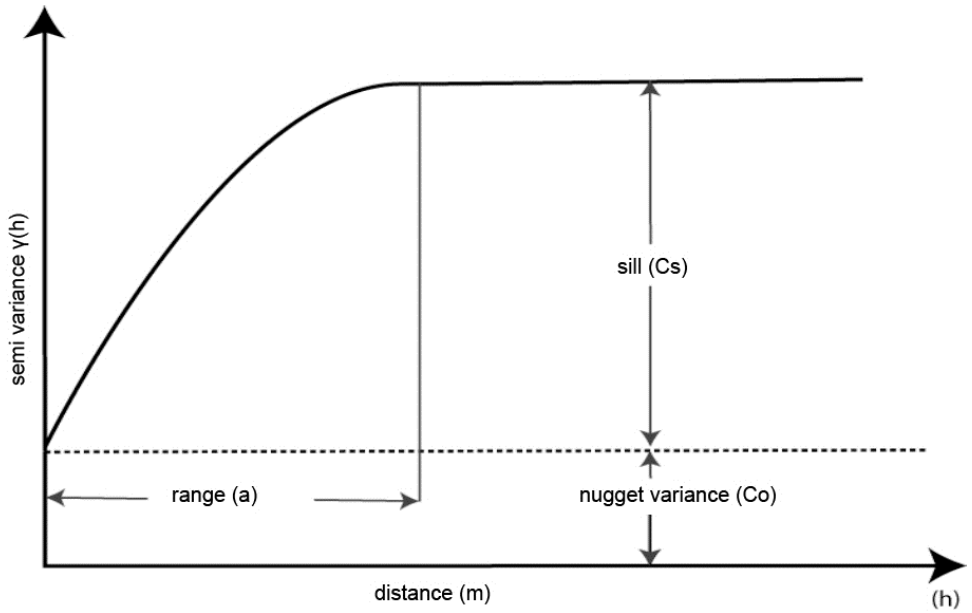

Figure 11: Scheme of a theoretical variogram model.

In this study the theoretically variograms were determined by using the isotropic spherical-plus-nugget model, which is the most popular variogram function (Webster & Oliver 2015).

$$\gamma(h) = C_O + C\left\{\frac{3h}{2a} - \frac{1}{2}\left(\frac{h}{2a}\right)^3\right\} for\ 0 < h \leq r \quad (11)$$

$$= C_O + C\ for\ h > 0 \quad (12)$$

$$= 0\ for\ h = 0 \quad (13)$$

Where $h=|h|$ is the lag distance, C_O the nugget variance, C the spatially correlated variance, and a the range, which is the limit of the spatial correlation.

The total of sampled points of N=239 for Rio Mannu catchment were applied into the variogram analysis as a prerequisite for the applied Ordinary Kriging interpolation (section 3.6.1). The same was done with the residuals of the MLR and is a prerequisite for the Regression Kriging (section3.7). The single soil physical properties and the residuals of the MLR were tested on normal distribution and second order stationarity before. Variogram models were computed automatically using an automated R-script and the R-statistic packages “gstat” (Pebesma 2004) and automap (Hiemstra et al. 2008). Oliver and Webster (2014) strongly recommend to not fit variograms by eye anymore, since the results are unreliable. They instead recommend for the variogram modeling a method that is implement in the automap R-library. The algorithm uses initial values. The initial sill value is estimated as the mean of the max and the median of the semi-variance and the initial range is defined as 0.10 times the diagonal of the bounding box of the data. The “autofitVariogram” function in “automap” iterates over possible variogram models and picks the model that has the smallest residual sum of squares with the sample variogram (Hiemstra 2008). The results of the kriging approaches presented in sections 3.6.1 and 3.7 are heavily dependent on the applied variogram model.

3.6.1 Ordinary Kriging (OK)

Kriging is a generic term for a range of least-squares methods to provide, in terms of minimum variance, the best linear unbiased prediction (BULP) (Webster & Oliver 2015) a

standard version of kriging is Ordinary Kriging (OK) (Matheron 1965), in which the prediction are based on the Model:

$$Z(s) = \mu + \varepsilon'(s) \quad (14)$$

Where μ is the constant stationary function (mean of the total sampled target variable) and $\varepsilon'(s)$ is the spatially correlated stochastic part of the variation. The predictions are made using,

$$\hat{Z}_{OK}(S_0) = \sum_{i=1}^{n} \lambda_i(S_0) * Z(S_i) = \lambda_0^T * Z, \quad (15)$$

Where λ_0^T is the vector of the kriging weights λ_i and Z is the vector of *n* observations at primary location (Hengl 2009).

The weights of the kriging predictor are determined for a point S in the way that the prediction error is zero, the variance of the prediction error in minimal and the sum of weight a (λ_i) is one. The variance error is minimized by introducing the lag-range multiplier which leads to an equation that can be solved:

$$\gamma(h) = \begin{cases} \sum_{i=1}^{n} \lambda_i \gamma(Sj - Si) + \psi(S_0) = \gamma(Sj - S_0) j = 1, \dots, n \\ \sum_{i=1}^{n} \lambda_i = 1 \end{cases} \quad (16)$$

where $\gamma(Sj - Si)$ is the semivariance between data points i and j and $\gamma(Sj - S_0)$ is the semivariance between the target point S_0 and the lag-range multiplier $\psi(S_0)$.

OK is the most popular and referred as the “work horse” of geostatistical interpolation methods since it serves well in most situations with its assumptions easily satisfied. OK solves a set of linear equations in the kriging system, and needs for this the semi-variances that come from the fitted variogram model (Webster & Oliver 2015).

The OK interpolation was applied on the sampled soil properties as well as on the residuals of the MLR and then applied into the Regression Kriging model (section 3.7).

3.7 Hybrid Interpolation Model – Regression Kriging (RK)

A disadvantage of pure deterministic or pure stochastic interpolation models is that predicted maps often show patterns that appear unnatural. Kriging tends to under-estimate large values and overestimate small values at unsampled locations (Oliver & Webster 2015).

A solution to avoid these problems is, to use multivariate prediction techniques that include co-variables in the geostatistical prediction model (Adhikari et al. 2013). So called hybrid methods are able to overcome disadvantages of pure mathematically based or pure CLORPT & SCORPAN based models and are able to combine advantages of both. RK is a combination of a multivariate deterministic regression model and the stochastic kriging model. It was first introduced by Odeh et al. (1995) and is also called kriging with external drift.

Due to inaccurate measurements and limited process knowledge the modeling of spatial data is often based on stochastic considerations. Following the notation of Hengl (2007), it denotes a gaussian spatial process *Z(s)* that can be decomposed in a deterministic part (section 3.5) and a stochastic part (section 3.6), which can be modeled independently. RK is a hybrid method that combines the advantages of the deterministic and stochastic part in model so we obtain:

$$\hat{Z}_{OK}(S_0) = \hat{m}(S_O) + \hat{e}(S_O) = \sum_{k=0}^{p} \hat{\beta}_k * q_k(S_0) + \sum_{i=1}^{n} \lambda_i * e(S_i) \quad (17)$$

where $\hat{m}(S_O)$ is the fitted deterministic part, $\hat{e}(S_O)$ is the interpolated residual, $\hat{\beta}_k$ are estimated deterministic model coefficients ($\hat{\beta}_k$ is the estimated intercept), λ_i are kriging weights determined by the spatial dependence structure of the residual and where $e(S_i)$ is the residual at locations S_i (Hengle 2009).

The regression coefficients $\hat{\beta}_k$ were estimated in this study by a MRL (section 3.5) which was applied to the soil physical properties and the terrain attributes (section 3.3) and fitted using ordinary least squares (OLS) method. A backward stepwise procedure was used to reduce the amount of co-variables and getting an appropriate final regression equation. Only those auxiliary variables that were significantly correlated with the

particular target variable regarding Pearson's correlation coefficients were considered as initial regressors. The applied co-variables of the final regression model were finally tested on multicollinearity (Hengl et al., 2004). The final regression models were determined, by relating the soil properties with the pixel values of the terrain attributes at the sampled location. With this procedure a single deterministic grid *Zpr** for every soil texture was interpolated. The resulting residuals of the final regression models, based on the sampling locations, were applied into a variogram analysis (section 3.6) and finally interpolated using the OK interpolation (section 3.6.1). With this procedure a grid of the MLR residual error *(ε *)* had been interpolated for every soil texture. The final RK prediction result map was calculated by the sum of the *Zpr** and *ε** grid for every soil texture (Figure 12).

The advantage of the RK model compared to the pure deterministic and pure stochastic model is that the deterministic part allows the application of secondary information that is normally available in higher resolution then the target variable. The stochastic part respects and applies the interpolation error of the deterministic model spatially distributed. RK involves various combinations of different regression and kriging models (Ahmed et al. 2010). Seo et al. (2015) found that hybrid regionalization models including RK outperform pure stochastic approaches like OK, simple kriging and universal kriging.

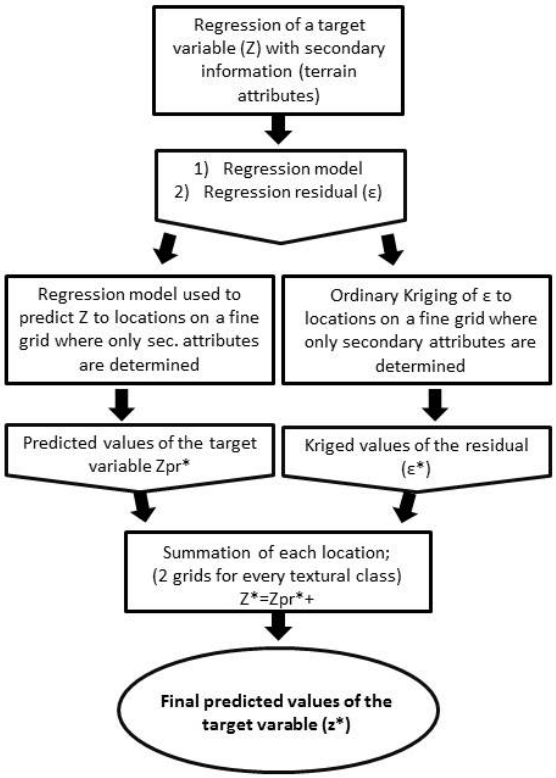

Figure 12: Scheme of the applied regression kriging model (after Odeh et al. 1995).

3.8 Validation of the model performance

The prediction performance of applied interpolation models was tested against the sampled soil physical properties. The model performance was assessed using a leave-one-out cross-validation (Isaaks & Srivastava 1989). Both the root mean square error (RMSE) and the mean absolute error (MAE) are regularly employed in model evaluation studies. But if the error distribution is expected to be Gaussian, than RMSE is more appropriate to represent model performance than the MAE (Chai and Draxler 2014).

Due to that the accuracy of each model run was compared with the Root Mean Square Error $RMSE = [1/n \sum_{i=1}^{n} (\hat{z}_i - z_i)]^{1/2}$, (18)

with $\hat{z}_i$ and z_i being the predicted and measured values, respectively.

4. RESULTS AND DISCUSSION OF THE REGIONALIZED SOIL PHYSICAL PROPERTIES

4.1 Results soil sampling and lab analysis Rio Mannu

The descriptive statistics of the collected 239 soil samples are summarized in Table 1. The sand content is increasing with higher elevation while for clay it is the opposite. The samples show highest clay values of up to 50% in the north-western part of the catchment, while sand fractions are dominant in the middle and eastern part of the catchment. Silt is the dominant fraction in a small area in the southern middle and in the southeastern part of the catchment. The standard deviation (SD) of silt 6.85 is significantly lower compared to sand 13.48.

Table 1: Descriptive statistics of collected and lab-analyzed soil samples; Rio Mannu (N=239).

TARGET	Min	Max	Mean	Median	SD	CV	Skewness	Kurtosis
Rio Mannu, N=239								
CLAY %	5.20	63.19	31.00	31.87	11.29	36.42	0.05	-0.60
SILT %	6.16	50.23	26.32	26.57	6.85	26.01	0.11	0.84
SAND %	6.89	88.64	42.68	40.65	13.48	31.58	0.54	0.69

Figure 13 reports the sampling locations and the classified soil textures following the German KA5 (Sponagel 2005) and the United States Department of Agriculture (USDA) classification system. Note that the class breaks of the German classification system in soil texture triangle are black, while those of the USDA system are red. Sampled soil

textures are dominated by more than 40% clay in the northern-western part and in the denser sampled Riu Costara sub-catchment (KA5 = Lts, Lt3, Tu2, Ts2 and Tl; USDA = Cl). This area is followed in the south by a band directing from northeast to southwest, that is dominated by clay loam, sandy clay loam and loam (USDA = ClLo, SaClLo, Lo). Those soil texture classes are also very dominant close to the basin outlet in the southwest. The mountainous region in the east is whether covered by loam or sany loam (KA5 = Ls3, Ls4, Sl4; USDA = Lo, SaLo).

The relative higher sand content in those exposed areas indicates that finer fractions were already eroded and transported in to the lower areas of the catchment. The rather low variance of silt might be an indication the spatial distribution is strongly influenced by Aeolian processes and as indicated already in section 2.1.3.

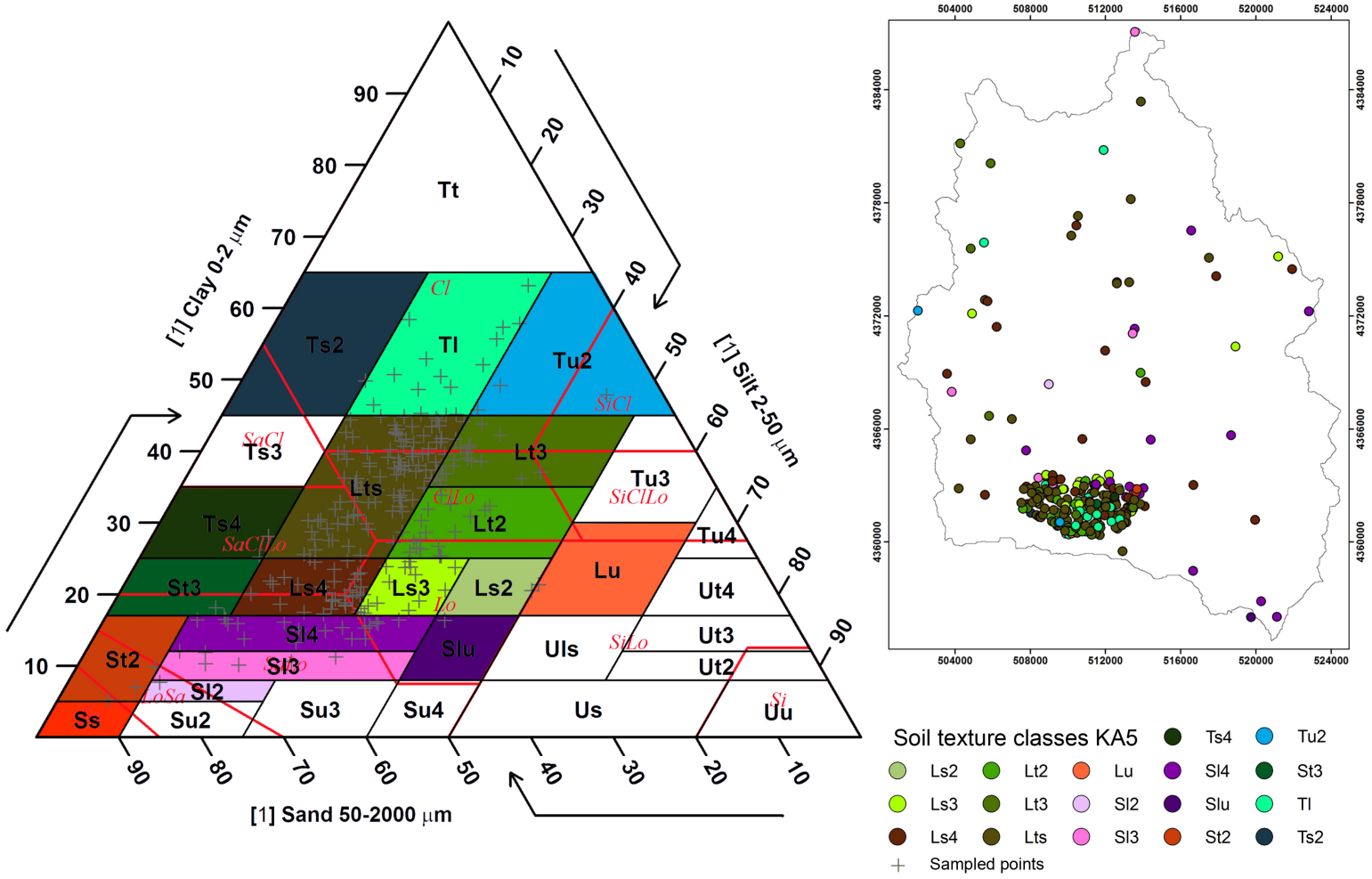

Figure 13: Soil sampling locations in the Rio Mannu di San Sperate, and sampled texture classes classified after the German classification system (KA5 of Sponagel 2005) and the United States Department of Agriculture (USDA) Classbreaks. Black lines represent the German classification system, while the red lines represent the USDA system. Each grey cross in the triangle represents one sampling location.

4.2 Selection of Co-Variables for the Rio Mannu catchment

The relief often has a strong influence on the pedo-genisis since it controls and impacts the local gravity, climate, water and living environment (Scheffer & Schachtschabel 2002). This hypothesis was tested for the sampled soil data by correlating the soil textural fractions with the primariy and secondary terrain attributes presented in section 3.3.

The Pearson coefficients of correlation (*r*) for each soil texture fraction and the co-variables are presented in Table 2. For both methods correlation coefficient are low. Highest values but still low correlations are visible for the fraction sand and clay. Both fractions show highest correlation with digital elevation model (DEM). The positive *r* of sand and the negative *r* of clay with the DEM confirm the influence of the relief on the distribution of soil textural fractions in the catchment.

Table 2: Pearson coefficients of correlation surveyed soil samples and the primary and secondary terrain attributes presented in section 3.3.

Pearson N=239			
Co-Variable	CLAY	SILT	SAND
A	-0.01	-0.15	0.12
β	-0.27	0.08	0.21
CDI	0.03	-0.06	0.03
Ch	0.02	-0.03	0.03
Cv	-0.03	-0.03	0.07
DEM	-0.34	-0.10	0.36
LS	-0.30	0.09	0.24
SPI	-0.22	0.12	0.13
SWI	0.33	-0.08	-0.28
TWI	0.17	-0.04	-0.15

The same, but in an opposite manner, is true for the correlation of both fractions with the Saga-Wetness-Index (SWI). This reveals that at locations with high clay content in the catchment the specific catchment area is larger than at locations with a high sand content. However, the low correlation of all terrain attributes reveal that important

processes which significantly influence the distribution of the soil properties can't be explained by the terrain attributes. This is especially true for the fraction silt. This confirms the assumption that the silt distribution is dominated by other processes like wind deposition. The significantly lower correlation of silt fit to the low coefficients of variation and the low standard deviation presented in Table 1.

The very low correlation of all fractions to the terrain attributes Cv, Ch & CDI reveal the shape of slope does not have a significant influence on the soil forming process. The low correlations to the stream power Index (SPI) indicate that local gully erosion only has minor influence on the distribution of the soil textures clay and sand.

The low correlation might also be a result of the large scale of the case study. Krüger (2008) showed that the correlation coefficients between soil properties and terrain attributes were significantly reduced on the regional scale compared to the field scale. The very strong heterogeneity in the catchment supports the plausibility of this hypothesis.

The co-variables of the terrain attributes were used as predictors in a stepwise (backward and forward) Multi Linear Regression (MLR) and Regression Kriging (RK) model. A maximum of 4 predictors (β_i) were applied into the MLR and RK following Hengl et al. (2007). The derived MLR equations for clay, silt and sand are as followed:

Clay = 7.10 + (-0.02**DEM*) + (0.06**CDI*) +(1.63*SWI); (19)

(R^2=0.2; p ≤ 0.001)

Silt = 22.62 + (0.41**TWI*) + (-0.01**A*) + (18.32**ß);* (20)

(R^2=0.1; p ≤ 0.001)

Sand = 75.00+ (0.03**DEM*) + (-0.07**CDI*) + (-2.13*SWI) + (-32.58**ß*) (21)

(R^2=0.1; p ≤ 0.001)

where *A* is aspect, *ß* is slope, SWI is the SAGA wetness index, *DEM* is the elevation *TWI* is the topographic wetness index and *CDI* is the convergence-divergence-index.

Even though there are no strong correlations visible for the terrain attributes CDI (with clay and sand) and TWI (with silt), surprisingly these terrain attributes found entrance

into the final MLR model. The final MLR equations were used on the grid of the terrain attributes to derive the spatial distribution of the single textures and the resulting residual errors at sampling location were applied into the variogram analysis.

4.3 Variogram analysis

The collected and lab-analyzed soil samples were automatically interpolated following the equations introduced in the sections 3.5 & 3.6 by using the R package "automap" of Hiemstra et al. (2008) (section 3.5). Variogram models were calculated for the target textures clay, silt and sand (Figure 14a) and for the residuals derived from the MLR (4.2) for each texture, respectively (Figure 14b). All variogram models were calculated using the spherical model. Figure 14a presents the experimental and theoretical variogram model of the soil properties clay, silt, sand, and their residuals, while Table 3 reports the derived parameters of the theoretical variogram models.

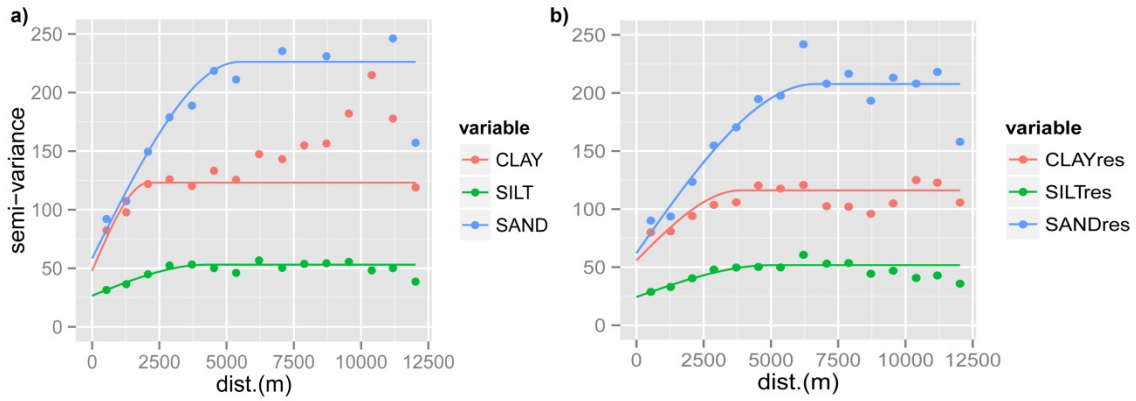

Figure 14: Variogram modeling for a) the soil textures clay, silt and sand and b) the corresponding residuals for each fraction.

The sand fraction shows the highest nugget variance (C_0), partial sill (C_s) and the largest range for the target variable as well as for the residual error of the MLR (Figure 14a).

The nugget to sill ratio enables the comparison of the relative magnitude of the nugget effect of soil properties (Zhao et al. 2012). The theoretical variogram models of soil properties show a medium spatial dependence with a nugget to nugget sill ratio (NSR) of

<25% to >75%. The low NSR of 26% of the sand fraction indicate the strongest spatial dependence. The low NSR and the high semi-variance fit well the findings in sections 4.1 & 4.2. The variogram model of the silt fraction in comparison is rather flat, and the NSR of 51% percent indicates a much lower spatial dependence for this soil property. The same is true for the variogram of residuals of the silt fraction. The shortest ranges are visible for the clay fraction as well as for the clay residuals. The relatively high nugget variance of clay as well as the short range, indicate that this fraction varies strongly in short distances and that a lot of small scale variance is not covered by the collected soil samples. In comparison to that is the NSR of the clay residual lower as for clay.

Table 3: Derived theoretical variogram-model parameters of the target variables clay, silt and sand and the residuals ($clay_{res}$, $silt_{res}$ and $sand_{res}$).

Rio Mannu N=239					
Soil properties	*Theoretical Model*	*Nugget C_0*	*Partial sill C_S*	*Range (m)*	*NSR (%)*
CLAY	Spherical	48	123	2113	39
SILT	Spherical	27	53	4292	51
SAND	Spherical	58	226	5485	26
$CLAY_{res}$	Spherical	56	113	3880	50
$SILT_{res}$	Spherical	24	52	5037	46
$SAND_{res}$	Spherical	62	208	6648	30

The semi-variance in the experimental variogram of the clay fraction is increasing after reaching sill at a range of approximately 5000m to 10000m and then dropping again strongly. Dual scale processes might be present due to the fact that the natural soil texture distribution (large scale) is different by the agricultural management, on the field scale (small scale). An automatic variogram fitting on anisotropy target variables is not possible in the used R-package “automap”. The variogram models of the target variables and of the residuals were applied into an Ordinary Kriging (OK) and Regression Kriging (RK) model (Odeh et al. 1999), respectively.

4.4 Predicted soil physical properties

Figure 17, Figure 16 & Figure 17 report the result maps with the spatial distribution of the soil properties clay, silt and sand using the applied interpolations methods (sections 3.5, 3.6 & 3.7).

The distribution of the target soil properties is roughly similar. The clay fraction (Figure 17) shows higher relative percentages in the north-western part of the catchment and a little spot with increased clay values in the south-western part of the watershed, while the mountainous parts are lower in clay content. The opposite can be recognized from the distribution of the sand fraction, with high values in the eastern part and in the center of the catchment. Especially the result maps of sand and clay derived by OK, look like inverted maps of each other. The silt fraction (Figure 16) shows the lowest range of 30%. Highest values up to 42% can be recognized in a small band that reaches from the southern-center to eastern center and two spots of high silt content are visible at the catchment boundary in the western center and in the southeast.

The local patterns of high and low values of the textures in the predicted maps, on the other hand, are very different. One can clearly recognize that the maps show typical spatial patterns depending on the applied regionalization method.

The result maps derived with the MLR show similar patterns. Here the strongest predictor applied in the regression model dominates the spatial distribution of regionalization results. For clay and sand the pattern of the derived MLR maps follow the DEM, which is the strongest predictor in the MLR equation (section 4.2) and for the MLR silt results can recognize the pattern of the slope grid (Figure 10).

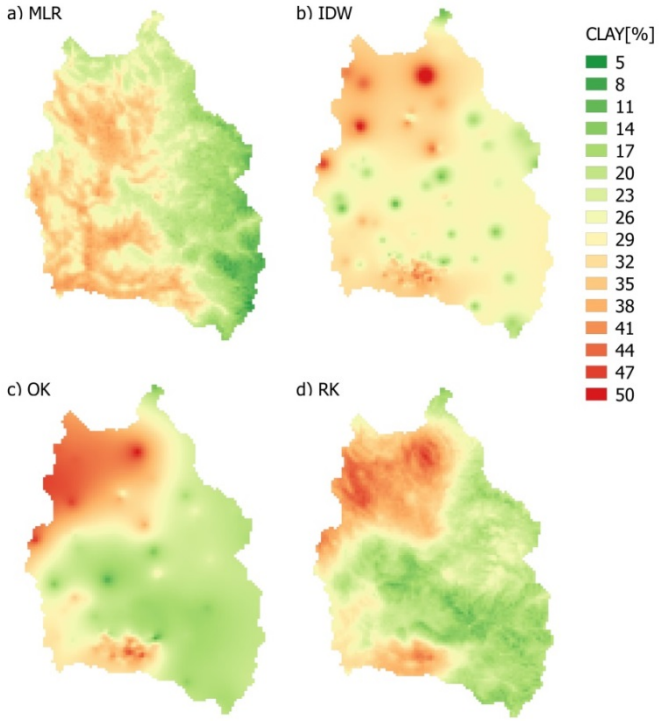

Figure 15: Spatial distributed prediction results of the soil property clay using a a)Multi-Linear Regression, b) Inverse Distance Weighting, c) Ordinary Kriging and d) a Regression Kriging interpolation approach.

The result maps determined with IDW show another extreme spatial distribution. In all IDW maps the typical "bulls eye effect" is visible. These restricted areas are characterized by extreme high or low values within a short range. This well-known effect makes the maps look rather unnatural and patchy. The comparison of the IDW and MLR maps shows the limitations of the MLR method for the soil texture prediction. The MLR silt prediction shows a large patch of high values in the south-eastern part of the catchment which are not visible in the IDW and OK prediction. This patch seems to be wrong and is a result of the rather poor correlations of silt and the applied predictors, as shown in section 4.2. The spatial prediction of MLR silt map follows strongly the positive spatial correlation with the slope grid. The maps of the OK predictions also show the "bulls eye effect" but less strong compared to IDW predictions. The transition of areas with high and low values in the OK predictions appear much smoother compared to IDW. This smoother appearance is a well-known problem of the OK prediction for example reported in Rezaee et al. (2011) and Yamamoto (2005).

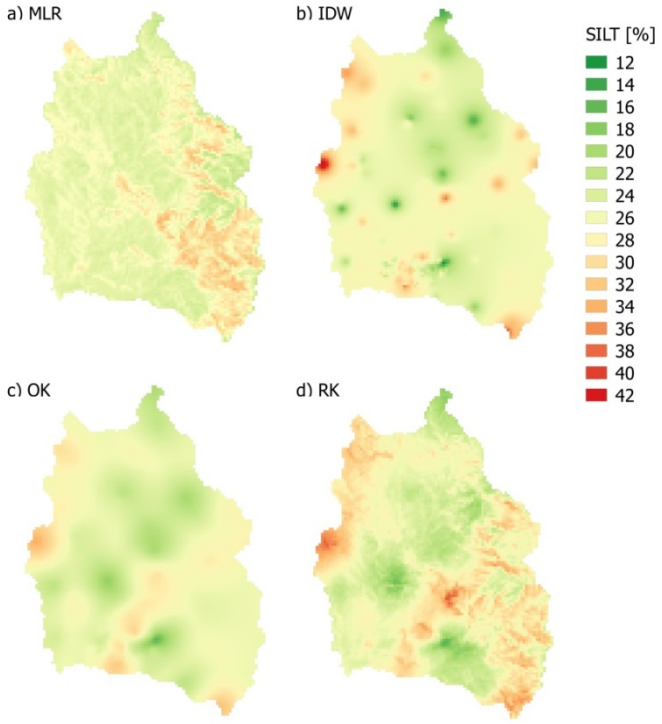

Figure 16: Spatial distributed prediction results of the soil property silt using a) Multi-Linear Regression, b) Inverse Distance Weighting, c) Ordinary Kriging and d) Regression Kriging interpolation approach.

The Regression Kriging maps appear to have the most naturally looking patterns. On the one hand one can clearly identify areas with extreme value as visible in the IDW and OK prediction maps, but on the other also the influence of the MLR prediction. This is quiet subjective impression but the distribution appears to be less artificially constructed.

Table 5 compares the descriptive statistics of the sampled fractions to those of the interpolated soil property maps. Sampled extreme values of all fractions are not represented by any prediction method. For the clay fraction MLR is closest to the minimum value of 5.2% while the OK is closest to the sampled maximum value and IDW fits best the recorded mean and median values. The differences between the sampled mean and median values compared to the interpolation methods are quiet high. For the mean IDW performs best while RK performs worst. This is astonishing, since the Root Mean Square Error (RMSE) presented in Table 5 identifies RK as the best performing prediction

method (RMSE= 8.82), while IDW is less precise and MLR shows the strongest deviation between measured and predicted samples.

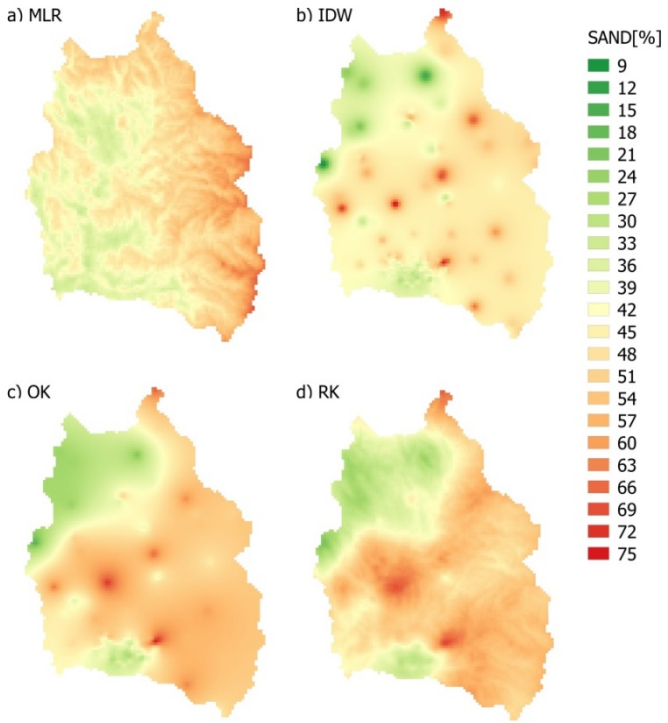

Figure 17: Spatial distributed prediction results of the soil property sand using a a) Multi-Linear Regression, b) Inverse Distance Weighting, c)Ordinary Kriging and d) a Regression Kriging interpolation approach.

The sample mean and median values of the silt predictions are better represented by the different regionalization methods. Deviation of sampled und predicted mean and median are less than 1 Vol.-% for all regionalization methods. The representation of the total sampled range on the other hand is a different story. Here the prediction results of the IDW are closest to the sampled extreme values. The RK regionalization shows again best prediction performance, but is only slightly better than OK.

Table 4: Descriptive statistics of the predicted soil property maps.

CLAY		Sampled	MLR	IDW	OK	RK
	Min.	5.2	6.4	11.4	9.4	10.4
	Max.	63.2	41.2	56.7	50.2	48.2
	Mean	31	26.3	29.8	26.2	25.7
	Median	31.9	26.4	28.9	22.6	23.2
SILT		Sampled	MLR	IDW	OK	RK
	Min.	6.2	21.8	11.6	16.1	15.6
	Max.	50.2	36.0	44.3	35.6	38.9
	Mean	26.3	27.2	25.9	26.3	26.5
	Median	26.6	26.6	26.0	26.4	26.3
SAND		Sampled	MLR	IDW	OK	RK
	Min.	6.9	31.4	8.9	17.1	20.7
	Max.	88.6	69.3	74.9	74.5	69.7
	Mean	42.7	46.5	44.3	47.5	47.8
	Median	40.7	46.5	45.1	51.1	50.5

The lowest RMSE in predicting the sand fraction are achieved by the OK regionalization, even though sampled mean and median are worst represented by this method. The range of sampled values is best represented by IDW. Highest prediction errors of RMSE 10.7-12.8% are visible for the sand fraction, while the RMSE of silt is the lowest of all applied regionalization methods.

Table 5: Cross-validation results of the soil texture regionalization.

	CLAY	SILT	SAND
RMSE MLR	10.21	6.71	12.85
RMSE IDW	9.18	5.96	10.77
RMSE OK	9.02	5.91	10.51
RMSE RK	8.82	5.77	10.68

RMSE=root mean square error, MLR Multi-Linear Regression, IDW=Inverse Distance Weighting, OK= Ordinary Kriging, RK= Regression Kriging

From all applied interpolation techniques the stochastic Ordinary Kriging (OK) model and hybrid Regression Kriging (RK) model showed the best prediction performance with lowest RMSE. But IDW, OK and RK produce nearly the same RMSE results for the silt and sand fraction with only minor differences. RK shows the best performance for the clay

and silt fraction, but the prediction performance is just minor improving the prediction results compared to OK. The opposite result is true for the sand fraction. This indicates that the variance of the target variables is more represented by stochastic total random model and the deterministic explanation is rather small. This hypothesis corresponds to the high (semi-)variances in the variogram models of the residuals of the multi-linear-regressions (MLR) and the high RMSE in the prediction of the MLR model for all target variables (Figure 14 & Table 5).

4.5 Classified soil texture result maps

The three interpolated texture grids of the fractions clay, silt, and sand were used to create new classified soil texture maps for each applied regionalization method. Therefore the German classification system of Sponagel (2005) was applied to the soil texture result maps presented in section 4.4. Figure 18a shows the soil information used in the CLIMB-project based on the soil map of Aru et al. (1990) (ARU map).

Figure 18b-e report the results and differences of the soil maps that were calculated based on the applied interpolation techniques. While in the map of IDW the typical local hotspots or bulls eyes can still be observed, even after the classification, OK shows a smoothing effect. The IDW map appears to be very unrealistic since most of the catchment is heterogeneously covered by sandy-clay-loam (Lts), and only at a few restricted areas different soil texture classes are visible.

In the maps of the MLR typical patterns of the predictor maps are visible (DEM & SLOPE GIRD). The soil maps, that were interpolated based on the soil sampling survey, draw in general a more distinct picture of the spatial soil texture distribution in the catchment compared to the Aru et al. (1990) soil map (ARU map). In the ARU map only 6 soil texture classes are present, while the interpolated maps distinguishes up to 16 soil texture classes. This indicates clearly a more natural spatial representation of soil properties in the catchment, since the composition of soil textures naturally varies highly in spatial extent.

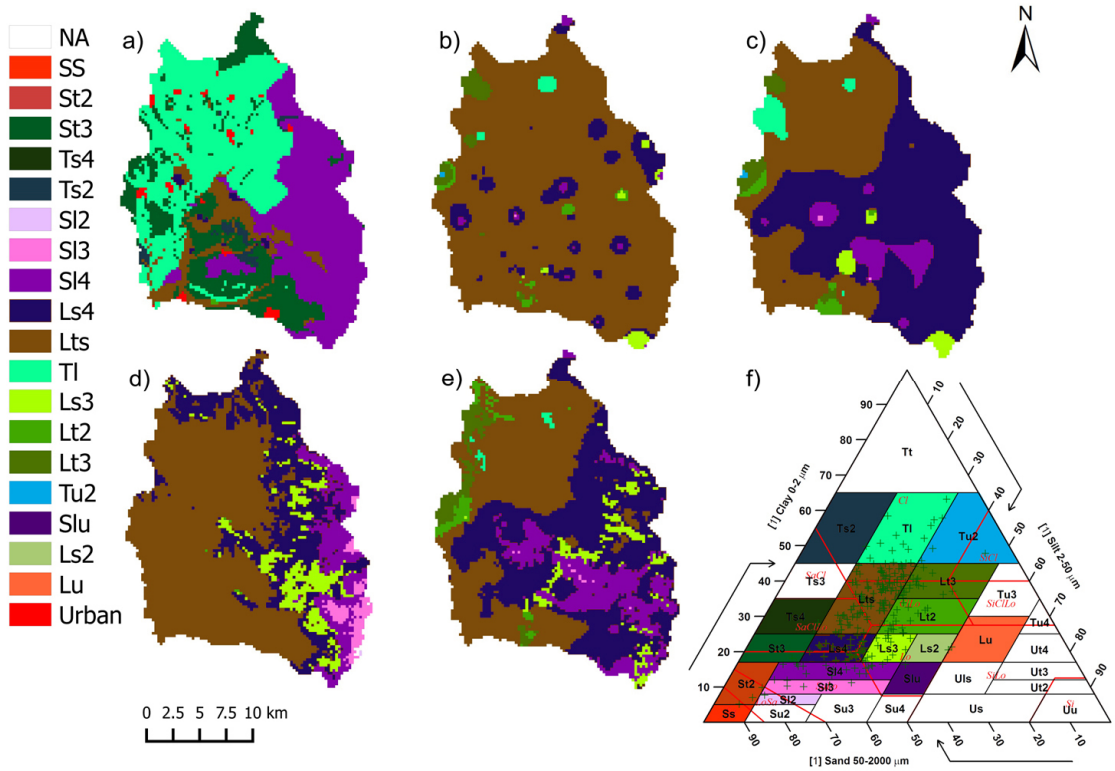

Figure 18: Distribution of soil texture classes in the Rio Mannu catchment a) Official CLIMB soil map based on Aru et al. 1990, b) Inverse Distance Weighting model, c) Ordinary Kriging model, d) Multi-Linear-Regression, e) Hybrid Regression Kriging model and f) Composite soil texture classification triangle following the German and the USDA classification system with sampled textures.

The ARU map seems to overestimate the clay (Tl) fraction in the north western part of the catchment. The regionalized soil maps show in comparison to that only small spots of Tl, while the majority is classified as sandy-clay-loam or Lts. A large area in the south western part of the catchment is classified as sandy loam (Sl4) in the ARU map. This texture class is only visible in small patches in the IDW, OK and RK soil maps, but is relatively large in the MLR map. This indicates the ARU map was maybe derived based on a MLR regionalization approach. In all predicted maps Lts and Ls4 are the most dominant soil textural classes in the catchment. Surprisingly the LTS soil textural class doesn't even appear in the ARU map.

4.6 Closing discussion of the soil texture regionalization

State of the art filed monitoring techniques were used to collect soil texture information and applied geostatistical interpolation models like Regression Kriging (Odeh et al. 1995) to interpolate recorded sampling results at catchment scale.

If the spatial information of soil textural properties were significantly improved compared to available soil information of Aru et al. (1990), cannot be stated since the base sampling information of the Aru et al. (1990) soil map was not available for comparison. But what can be clearly stated is that the patterns of the derived RK soil maps appear much more natural looking, compared to the Aru et al. (1990) map. The quality of the soil texture maps based on the root mean square error (RMSE) is a similar range to other studies. 77 soil samples, of the Rio Mannu data set used in this study, were applied by Ehlers et al. (2015) into a kriging model to predict top soil texture in the test site. The prediction errors of the resulting soil texture maps of this study are in good correspondence or in some cases even outperform their results. The RMSE of the predicted clay texture map RMSE = 8.8 % (Regression Kriging approach) is below the results of Sun et al. (2012) RMSE = 16.1%, Odeh & McBratney (2000) RMSE = 10.2% and Ehlers et a. (2015) RMSE = 9.9% but slightly higher than in McBratney et al. (2000) RMSE = 6.1%. The lowest RMSE for the clay prediction was found in Sumfleth & Duttmann (2008) RMSE = 4.6%. Only two studies where RK was used to predict silt were found in literature. The prediction error RMSE = 5.36% of Sumfleth & Duttmann (2008) is similar to the RMSE of the silt prediction in this study RMSE = 5.8% and outperform the prediction results of Ehlers eta al. (2015) RMSE = 7.4%. The prediction error of the sand fraction RMSE = 10.7% is significantly lower compared to the studies of Ge et al. (2007) (RMSE = 19.8%) and Ciampalini et al. (2012) (RMSE = 16.8%) and Ehlers et al. (2015) RMSE =13.6%.

The high Nugget values of the sand and clay fractions (C0 clay=48 and C0 sand=58 (Table 3)) indicate that a lot of small-scale variability (semi-variance) is not represented in the field data. The Nugget value and the coefficient of variation of the silt fraction are much lower. This is leading to better spatial prediction and lower prediction error. The low NSR of 51% furthermore indicates that the silt fraction has a minor spatial dependence.

The produced maps of the soil physical properties as well as the maps of the classified soil textures show patterns that are strongly influenced by the applied prediction method. From all applied prediction methods OK and RK show the best performance (sections 4.4 and 4.5). The soil texture maps that were processed using RK have the most naturally looking patterns, since this interpolation methods accounts for both, the natural patterns in the deterministic model and the model error in the stochastic part.

On the one hand the RMSE of the applied regionalization models reveal only minor differences in the prediction power of the regionalization methods, but on the other hand if one compares the different soil textural maps (Figure 15, Figure 16 & Figure 17) and the classified maps (Figure 18), significant differences in the spatial distribution of predicted soil properties can be noticed. Applying these different soil maps might cause uncertainties in the hydrological modeling. Since the RK prediction results performed best for two textural classes (clay and silt), the derived textural soil map was used for further investigations and tested in the physically based hydrological model WaSiM. The influence of the soil physical input was investigated using two different WaSiM model setups. One WaSiM model was set up with the Regression Kriging soil map (WaSiM-RKS) and one was setup with the official CLIMB soil physical information derived from the Aru et al. (1990) soil map (WaSiM-ARU). Hydrological simulation results of both soil model setups were compared and changes were assessed (section 5).

5. METHODOLOGIES HYDROLOGICAL MODELING

5.1 Water balance Simulation Model (WaSiM)

The fully distributed process-based Water balance Simulation Model (WaSiM) (Schulla 1997) was applied in the test site to perform the hydrological simulations. WaSiM is available in two different versions. Version 1 uses the more empirical based Topmodel approach to calculate the fluxes within the unsaturated zone, while version 2 uses the more physical based Richards-equation. In this study the WaSiM version 2 (Richards-equation) was applied.

WaSiM was applied successfully for many hydrological climate change impact assessment studies for example by Cornelissen et al. (2013), Gädecke et al. (2013), Muerth et al. (2013), Ott et al. (2013), Velázquez, et al. (2013) and many more. WaSiM is a distributed, deterministic, and mainly physically based hydrological model which runs in constant time steps in a grid-based structure and uses the Richards equation to calculate water flux within the unsaturated zone. WaSiM is composed in sub-modules (Figure 19) which are processed for each time step and one by one for the entire catchment grid (Schulla 2012). The complexity of used sub-modules can be adjusted depending on the catchment characteristics and data availability. The different modules calculate various hydrological variables like interception, discharge, runoff, snow melt, evapotranspiration etc.

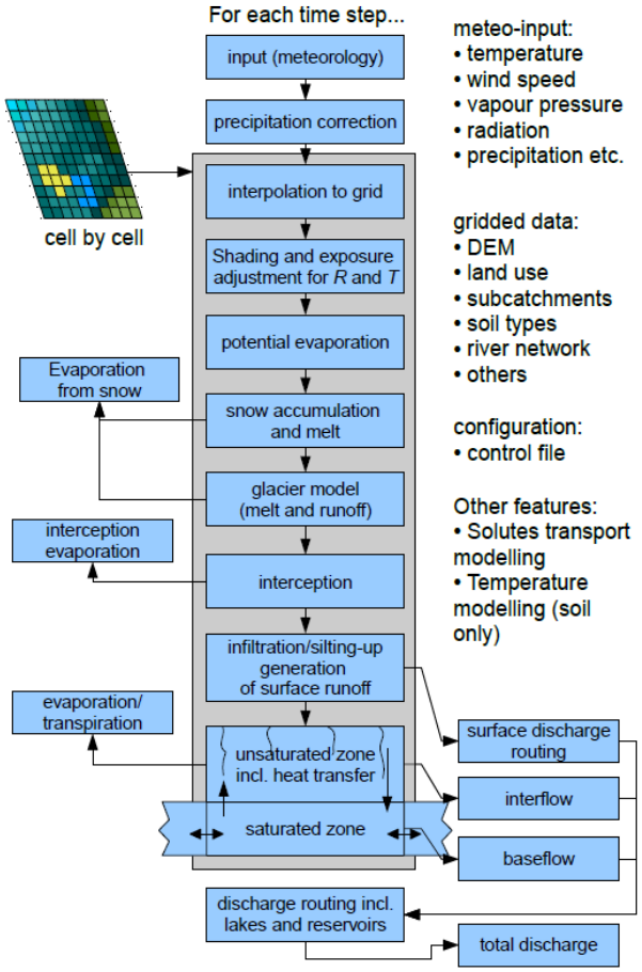

Figure 19: Structure of the hydrological model WaSiM (Schulla 2014).

5.1.1 Water fluxes of the unsaturated zone

The applied WaSiM version uses the RIDCHARDS-equation for modeling fluxes within the unsaturated soil zone. This is done one-dimensional in the vertical direction using a soil with several numerical layers (Schulla 2015). In WaSiM the soil profiles are typically formatted in multiple horizons, of different thicknesses each. If the groundwater module is used in WaSiM, the thickness of these numerical layers has to be larger than the "thickness of the uppermost (first) groundwater aquifer" to avoid the groundwater table from falling below the deepest soil layer.

The continuity equation for this type of problem is given by:

$$\frac{\partial \Theta}{\partial t} = \frac{\partial q}{\partial z} = \frac{\partial}{\partial z}\left(-k(\Theta)\frac{\partial \Psi(\Theta)}{\partial z}\right) \quad (22)$$

with
- Θ water content (m³/³)
- t time (s)
- k hydraulic conductivity (m/s)
- Ψ hydraulic head as sum of the suction Ψ and geodetic altitude h (m)
- q specific flux (m/s)
- z vertical coordinate (m)

The discretized RICHARDS-equation is given by:

$$\frac{\Delta \Theta}{\Delta t} = \frac{\Delta q}{\Delta z} = q_{in} - q_{out} \quad (23)$$

with
- q_{in} inflow into the actual soil layer (m/s)
- q_{out} outflow from the actual soil layer (including interflow and artificial drainage)

The hydraulic properties are dependent on the water content of the soil. In the soil model this is considered in a discrete manner. The flux between 2 numerical layers with indices u (upper) and l (lower) is then given by:

$$q = k_{eff} * \frac{h_h(\Theta_u) - h_h(\Theta_l)}{0.5*(d_u + d_l)} \text{ with } \frac{1}{k_{eff}} = \frac{d_u}{d_l + d_u} * \frac{1}{k(\Theta_u)} + \frac{d_l}{d_l + d_u} * \frac{1}{k(\Theta_l)} \quad (24)$$

with
- q specific flux (m/s)
- k_{eff} effective hydraulic conductivity (m/s)
- h_h hydraulic head, dependent on the water content and given as sum of suction $\Psi(\Theta)$ and geodetic altitude h_{geo} (m)
- d thickness of the layers under consideration (m)

The effective conductivity is the harmonic average of the conductivities of both layers. It is possible to use layers with any thickness in this approach (Schulla 2013).

5.1.2 Calculating real evapotranspiration

Actual evapotranspiration (ETR) is modeled according to available soil water, which is determined by the Richards equation, with the actual capillary pressure as given by the Van Gnuchten parameters. ETR is calculated as a fraction of the potential evapotranspiration (ETP) after Penman-Monteith, if the soil water content undercuts the permanent wilting point and the soil is not saturated. If the actual suction exceeds the permanent wilting point, ETR is set to zero by the model. If the pressure head undercuts the saturated status, ETR is equal to ETP. Besides a reduction as a result of dry soils $\left(\Theta(\Psi) < \Theta_{\Psi g}\right)$ also the impact of too wet soils $(\eta * \Theta_{sat} < \Theta(\Psi) < \Theta_{sat})$is considered.

$$ETR_i = 0 \qquad \Theta(\Psi) < \Theta_{wp} \qquad (25)$$

$$ETR_i = ETP_i * \left(\Theta(\Psi_i) - \Theta_{wp}\right) / \left(\Theta_{\Psi g} - \Theta_{wp}\right) \qquad \Theta_{wp} \leq \Theta(\Psi) \leq \Theta_{\Psi g} \qquad (26)$$

$$ETR_i = ETP_i \qquad \Theta_{\Psi g} \leq \eta * \Theta_{sat} \qquad (26)$$

$$ETR_i = ETP_i * \left(\Theta_{sat} - \Theta(\Psi_i)\right) / (\Theta_{sat} - \eta * \Theta_{sat}) \qquad \eta * \Theta_{sat} < \Theta(\Psi) \leq \Theta_{sat} \qquad (27)$$

with
- i index of the soil layer (5.1.1)
- ETR real evaporation
- ETP potential evaporation
- $\Theta(\Psi)$ actual relative soil water content at suction Ψ(-)
- Ψ(-) actual suction (capillary pressure) (m)
- η maximum relative water content without partly or total anaerobe conditions (≈0.9...0.95)
- Θ_{sat} saturation water content of the soil (-)
- $\Theta_{\Psi g}$ soil water content at a given suction Ψg
- Θ_{wp} water content of the soil at permanent wilting point $(\Psi = 1.5\ \mathrm{MPa} \approx 150\mathrm{m})$

The parameters of the equation above are given as suction for each crop type to respect land use variations. Due to this ETR depends on soil and crop type and can easily be converted into a time dependent parameter as well (Schulla 2015).

A multiple land use table can be implemented. Therefore, the parameterization of vegetation within the model can be arranged in Julian Days. For each defined Julian Day and each crop type, varying stomatal behavior, root depth, leaf area index (LAI) and Albedo can be defined. The days in between two defined Julian Days are automatically linearly interpolated to simulate the full vegetation cycle each year. Sensitivity studies

by Schulla and Jasper (2007) showed that the resistance parameters rs and ra in the Penman-Monteith equation are very sensitive to the resulting evapotranspiration. These two parameters can be calibrated in the land use table, and serve as a fitting parameter within WaSiM, since in situ measurements of stomatal conductance, or resistances in consequence, which are time intensive and hardly transferable at catchment scale.

To run the WaSiM V.2 (Richards-Equation) using the Penman-Monteith evapotranspiration the availability of several climate input parameters in a daily temporal resolution is necessary. These parameters are precipitation, air temperature, humidity, wind speed, & global radiation (Schulla 2015).

5.1.3 Runoff generation

WaSiM generates base flow, interflow and surface flow. Base flow is generated only by exfiltration of ground water into the channel network. The model was applied in this study without using the groundwater model. In this case the base flow is generated similar to the TOPMODEL-approach:

$$Q_B = Q_O * K_s * e^{(h_{GW} - h_{geo,0})/k_B} \quad (28)$$

with

Q_B base flow (m/s)
Q_O scaling factor for base flow (or maximum base flow if the soil is saturated) (-)
K_s saturated hydraulic conductivity (m/s)
h_{GW} groundwater table (m a.s.l.)
$h_{geo,0}$ geodetic altitude of the soil surface (upper limit 1st layer) (m a.s.l.)
k_B recession constant for base flow (m)

The approach is applied to each grid cell of the model modeling domain.

Interflow is generated at soil layer boundaries if the slope angle is > 0 and a drop in hydraulic conductivity is present. Interflow calculation starts from the last completely saturated layer, down to the groundwater layer. Interflow is generated if the suction in a layer holds <3.45m water column. In this condition the maximum possible drainable water content of the actual layer is calculated and interflow as a result of conductivity river density and hydraulic gradient is generated. The smaller result of that calculation

determines the interflow q_{inf}. WaSiM considers also interflow generation by exfiltration into infiltration from rivers and lakes. Interflow is calculated by a one dimensional vertical finite difference scheme. Interflow will be translated by the model to the sub-basin outlet using a flow time histogram (isochronic method). A more comprehensive description of runoff generation is given in Schulla (2015). Finally surface runoff is ether generated if the infiltration rate is below the precipitation rate or if the ground water table rises up to the surface or above (full saturation of the unsaturated zone).

5.2 Setup hydrological model

This section describes the applied climate model simulations and the detailed parametrization and setup of hydrological WaSiM simulations.

5.2.1 Applied regional climate model (RCM) ensemble

In this study WaSiM was operated at a daily time step. To run WaSiM using the Penman-Monteith-equation the meteorological input of five different climate variables is needed (precipitation (mm), air-temperature (°C), relative humidity (%), wind speed (m/s), and global radiation (W/m²)).

The climate variables were provided by different General Climate Model (GCM) – Regional Climate Model (RCM) combinations of the EU FP-6 ENSEMBLES project. One first skill measure of a climate simulation is to reproduce the climatology in a certain area, for example like a hydrological basin. To ensure that the needed climate model inputs fulfill those criteria, Deidda et al. (2013) investigated different hydrological basins of the "EU FP-7 CLIMB-Project" with the ENSEMBLES RCMs in an A1B emission scenario.

IPCC emission scenarios of the A1 family reflect a 21st century future world characterized by a rapid economic growth, a global population growth that peaks in the mid-century and declines thereafter and a rapid introduction of new and more efficient technologies. The A1 scenario family develops into 3 groups that describe alternative directions of technological change in energy systems: The fossil-insensitive (A1FI), non-fossil energy sources (A1T), and a balance across all sources (A1B) (Christensen et al.

2007). In this study the climate projections are based on greenhouse gas and aerosol concentrations from the A1B emission scenario, which are considered the most realistic (Nakićeović et al. 2000), and which are the most complete data sets in the ENSEMBLES data base (Deidda et al. 2013).

CRU E-OBS reference observation datasets were used to test the suitability of the RCMs in representing the climatology in the Rio Mannu di San Sperate catchment and in the other CLIMB test sites. Based on this investigation the four best performing RCMs were chosen. The historical meteorological situation in the RMB, with respect to the state of the art CRU E-OBS reference datasets for the control period of 1951–2010 (Bird et al. 2015), was best reproduced by the ENSEMBLES RCMs ECHAM-5 REMo (ECH-REM), ECHAM-5 RacMO (ECH-RMO), ECHAM-5 RCA 3 (ECH-RCA) and HadleyCM3 RCA (HCH-RCA).

Since even the best performing RMCs showed quite a deviation to the observed climatology, a large scale bias correction of precipitation and air temperature fields was applied to the four chosen RCMs using the E-OBS data sets, by applying the daily translation method (Piras et al. 2014).

The bias correction uses a monthly cumulative distribution function (CDF) of observed (F_{obs}) and simulated (F_{sim}) daily variables. The unbiased daily value for precipitation and temperature were calculated by:

$$x^* = F_{obs}^{-1}[F_{sim}(x)] \tag{29}$$

with
- x^* unbiased value
- x daily biased climate variable value
- F_{obs} CDF of observed daily variable
- F_{sim} CDF of simulated daily variable
- F_{obs}^{-1} is the inverse of F_{obs}

F_{obs} and F_{sim} were derived on a monthly mean basis pooling together all daily observations for each month (Piras et al. 2014).

The E-OBS bias corrected precipitation was downscaled using multifractal cascades starting from areal averages of daily precipitation (Deidda et al. 2013). For the Rio Mannu basin a total of 800 precipitation events were used to derive model parameter and identify the calibration relations as a function of R for the study area. Detailed

information on the applied downscaling methods can be found in Mascaro et al. (2013) and Deidda et al. (2013). Finally remaining local biases were corrected based on the observation data of 13 precipitation gauging stations within the catchment over a period of 1951-2008 Piras et al. (2014). Air temperatures from the ENSEMBLE RCMs were downscaled based on the procedure described in Liston and Elder (2006).

Simulations were performed for a reference time period (REF) (1971-2000) and a projection time period (FUT) (2041-2070).

5.2.2 Modeling scheme

Figure 20 summarizes the scheme of the applied climate change impact modeling chain in the Rio Mannu catchment. Two WaSiM setups (WaSiM-ARU and WaSiM-RKS) were driven with 4 regional climate models (section 5.2.1) for a reference time series (1971-2000) and for a future projection (2041-2070) following the scheme in Figure 20.

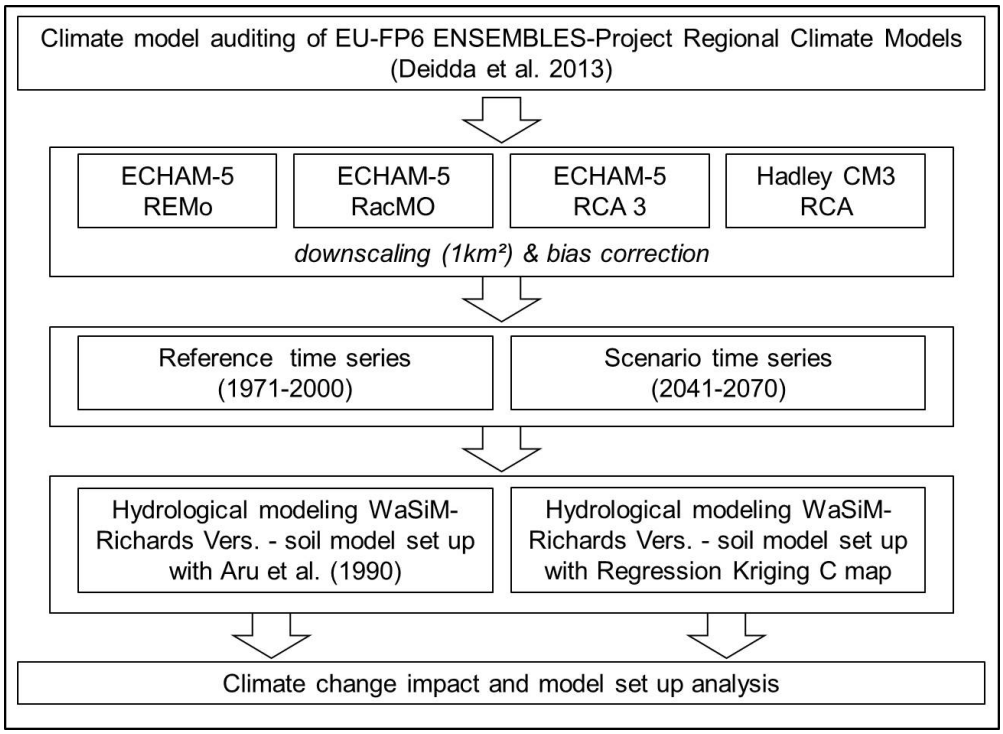

Figure 20: Model parametrization and hydrological climate change impact assessment scheme.

5.2.3 CLIMB model harmonization strategy

Within all seven case study sites of the CLIMB project a variety of hydrological models were used to quantify the impact of climate change and associated risks on hydrological budgets and extremes. In the Rio Mannu catchment the three different hydrological models WaSiM, tRIBS, mGROWA, and SWAT were applied and results compared to investigate model based uncertainties in the hydrological climate impact assessment. To investigate the model internal uncertainties, hydrological model input data as well as the model parametrization of the catchment were harmonized as far as this was possible for the three different model architectures. Models were setup with the same land use information (section 5.2.3.1.) and the same Aru et al. (1990) soil information (section 5.2.3.3). Unique parameters were applied for the land use classes and soil types as far as the different model architectures allowed this.

WaSiM was set up with a grid resolution of 250m, reflecting a compromise to ensure acceptable computational performance, as well as the spatial representation of the landscape heterogeneity. Difficulties in the parametrization of the model can results from too coarse resolutions. Due to that Schulla (2012) suggest using resolutions smaller than 500m to consider variation in surface or soil properties. Topographic features such as catchment delineation, slope, aspect, stream orders, flow distances etc. were derived from the Digital Elevation Model (DEM), aggregated to a 250m resolution.

5.2.3.1 Aggregation and parametrization of land use information

The land use land cover (LULC) map of 2008 (Figure 3) was aggregated to 8 major land use classes: The LULC map was aggregated by the CLIMB partner institution CINFAI following the CLIMB harmonization strategy. The major LULC classes in the aggregated LULC map are agriculture (48%) (comprising main crops like wheat, corn and artichoke), sparse vegetation (26%), olive yards (8%), forest (7%), pastures (5%), urban areas (3%), vine yards (2%), and water bodies (1%). Land use specific model parameters like leaf area index (LAI), root depth, and stomatal resistance were collected from literature (Cermák et al. 2007, Schulla 2007, Villalobos et al. 2005, Winkel & Rabal 1993). Irrigated agriculture is only present in a small north western part of the catchment. Due to

missing information of irrigation water quantities, irrigation was neglected in the model setup.

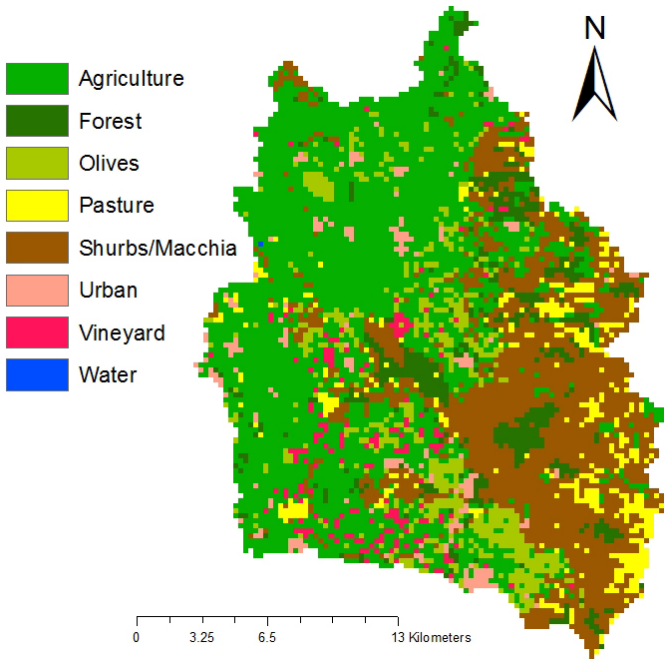

Figure 21: Land use information of the Rio Mannu basin, which was applied in the WaSiM model.

The plant parameters of Table 6 have been parameterized in the WaSiM control file in look up tables based on Julian days (JD). In between two JDs parameters WaSiM interpolates the parameter linear automatically.

For the major land use classes agriculture and pasture low LAI, root depth (RD), vegetation cover fraction (VCF) and aerodynamic roughness (Z0) values are parameterized for the months of July, August, and September, before increasing slowly and reaching the peak in April and May. In comparison to that, Forrest, Olives, Macchia / shrub vegetation, and vineyards, were parametrized with still high LAI, VCF, Z0 and RD. Woody land use classes were parametrized with only little change over the year since due to the deeper root depth plant available water is longer present. Peak values of high LAI, VCF, Z0 and RD are set for the months of August and September, while low values were set from November to the beginning of March.

Table 6: Plant parameters used for modeling in WaSiM.

LULC classes	LAI [m²/m²]	VCF [-]	Rooting depths [m]	Stomata resistance [s/m]	Aerodyn. roughness [m]
Agriculture	0.4 - 3	0.1 - 0.95	0.1 - 0.5	60 - 120	0.3 - 0.4
Forest	3 - 7	0.7 - 0.95	2	50 - 110	1.8
Olives	3.5	0.88	2	116	0.013
Pasture	0.1 - 2.1	0.2 - 0.9	0.2 - 0.4	35 - 80	0.03 - 0.04
Macchia / Shrubs	4 - 5	0.95	2	30 - 150	1.82
Settlements	0	0.3	0	100	100-150
Vineyards	0 - 1.48	0.35 - 0.59	1.2	70 - 155	1.82
Water	0	0	0	0	0.3

5.2.3.2 Parametrization of the soil model

The soil model of the physically based hydrological model WaSiM, uses the RICHARDS-equation to model the water fluxes in the unsaturated soil zone in a one-dimensional vertical direction (Schulla 2012). The parametrization is done using lookup tables for each soil type. Based on soil textural information the van Gnuchten method (van Gnuchten 1976) is applied to calculate the actual water content per modeled time step.

$$\theta = \theta_r + (\theta_s - \theta_r)\left(\frac{1}{1+(\psi\alpha)^n}\right)^m, \qquad (30)$$

where, ψ is the suction (m), α ,n and m are empirical parameters (with m=1-1/n), θ is the actual water content, θr is the residual water content and θs is the saturated water content.

Soil physical properties of WaSiM's soil module, such as saturated hydraulic conductivity (ksat), the residual water content (Φr) and the saturated water content (Φs) and the van Gnuchten parameter n and a, were assigned to the two different soil maps. The parameterization was done using the pedo-transfer-function (PTF) of Wörsten et al. (1999). A constant soil depth of 10m was assumed for the whole catchment, which is indeed not

realistic especially for mountainous regions. This depth was chosen for the different hydrological models (section 5.2.3) applied in the test site within the CLIMB project to investigate hydrological model dependent uncertainties in the climate change impact assessment. To do so, every applied model had to have a setup, with maximum similarity. The different layers within the soil horizons were parameterized uniformly for all layers. The recession parameter k_{rec} controls the reduction of k_{sat} with increasing soil depth. K_{sat} is reduced by k_{rec} in the layers up to a soil depth of 2 m. Below 2 m soil depth k_{sat} stays constant to the value of the 2 m layer. The drainage density (d_r) and k_{rec} control the generation of interflow. WaSiM produces no interflow by setting $d_r = 0$ or by setting $k_{rec} = 1$ (Schulla 2012). A combination of $k_{rec} = 0.8$ and a dr = 10 was found to be best for this study. This is obviously a very simple approach considering real changes in porosity k_{sat} and interflow generation with increasing soil depth, but since soil information was only present for the top soil layer, this appeared to be a practical parametrization approach, also recommended in Schulla (2012). Changes of soil texture composition, bulk density, organic matter, macro pores reduction with increasing soil depth and soil compaction of the plow horizon as done by Rieger et al. (2010) were not considered in the soil model parametrization. An explicit parameter sensitivity assessment of sub-soil parametrization was not considered in this study.

5.2.3.3 Setup of the ARU soil model (WaSiM-ARU)

As already pointed out in section 3.1, the only soil information available in the basin was a soil type map of Aru et al. (1990). This map was aggregated to 6 soil textural classes by the Sardinian CLIMB partner University of Cagliari. The aggregated soil type result map still did not give distinct information about the spatial distribution of soil textural classes in the basin. Each of the 6 soil type polygons consisted of a range of different soil textures. WaSiM soil model needs to be setup with van Gnuchten parameters.

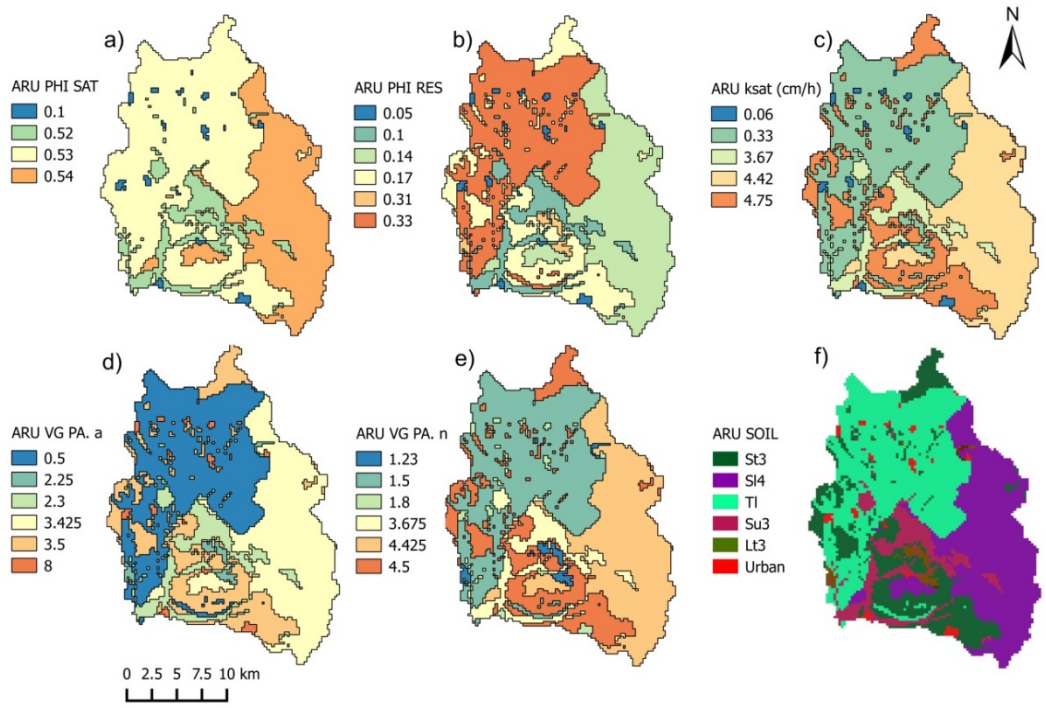

***Figure 22: Van Gnuchten parameters a) "PHI SAT" = saturated water content, b) "PHI RES" = residual water content, c) "Ksat" = hydraulic conductivity, d) "VG Par. A" = Van Gnuchten α, e) "VG Pa. n" = Van Gnuchten* n, which were derived from the ARU soil texture map in f).**

Van Gnuchten parameters can be either determined by literature sources or directly based on so called pedo transfer function PTF, but soil textural information is a necessity either way. The average weighted mean soil texture of the range of soil textural classes for each soil type was taken to determine a distinct soil texture class for polygon in the ARU map. Figure 18a) & Figure 22f) report the ARU soil map with a distinct soil textural classification. With this distinct soil texture information it was possible to determine the van Gnuchten parameters based on literature sources of Sponagel (2005). The determined parameters are presented in Figure 22a-e). The presented hydrological properties of Figure 22a-e) were transferred for each soil texture class into one distinct soil look table for each soil texture class in the WaSiM control files.

The soil model was setup with two horizons. The first horizon (H1) consisted of 5 layers of 0.2 meter thickness for every soil texture class (total of depth 1m). The second horizon (H2) consisted of 5 layers of 1.8 m thickness each (total of 9 m) (Note that the number of layers has to be same for each horizon due to numerical reasons (Schulla

2012)). Based on the CLIMB model harmonization strategy the soil depth was set to 10 meters for all soil texture look up tables. To investigate the model internal uncertainties of the different hydrological models, this rather unnatural soil depth parametrization had been applied to all models which were used in this test site within CLIMB.

5.2.3.4 Setup of the RKS soil model (WaSiM-RKS)

The regionalization of the derived soil samples brought new information on the spatial structure of soil textures in the catchment (4.5). This soil textural map was only applied in the WaSiM-RKS model. WaSiM's parameterization was done by using the pedo-transfer-function (PTF) of Wörsten et al. (1999) and Vereecken et al. (1989). The PTF of Vereecken et al. (1989) was only used to calculate residual soil water content ϑr. This decision was made since in the approach of Wösten et al. (1999) the residual water content is fixed to 1 Vol-% or 2.5 Vol.-%. This very low residual water content value is unrealistic, due to that Vereecken et al. (1989) was applied to calculate ϑr.

$\vartheta s =$ $0.7919 + 0.001691 * C - 0.29619 * dB - 0.000001491 * U^2 + 0.0000821 * Corg^2 + 0.02427 / C + 0.01113 / U + 0.01472 * \log(U) - 0.0000733 * C_{org} * C - 0.000619 * dB * C - 0.001183 * dB * C_{org} - 0.0001664 * 1 * U,$ (Wörsten et al. 1999) (31)

$\vartheta r =$ $0.015 + 0.005 * clay + 0.014 * C_{org},$ (Vereecken et al. 1989)

$k_{sat} =$ $\exp(7.755 + 0.0352 * U + 0.93 * 1 - 0.967 * (dB^2) - 0.000484 * (C^2) - 0.000322 * (U^2) + 0.001 / U - 0.0748 / C_{org} - 0.643 * \log(U) - 0.01398 * dB * C - 0.1673 * dB * C_{org} + 0.02986 * 1 * C - 0.03305 * 1 * U),$ (Wörsten et al. 1999) (32)

$\alpha =$ $\exp(-14.96 + 0.03135 * C + 0.0351 * U + 0.646 * C_{org} + 15.29 * dB - 0.192 * 1 - 4.671 * dB^2 - 0.000781 * C^2 - 0.00687 * C_{org}^2 + 0.0449 / C_{org} + 0.0663 * \log(U) + 0.1482 * \log(C_{org}) - 0.04546 * dB * U - 0.4852 * dB * C_{org} + 0.00673 * 1 * C),$ (Wörsten et al. 1999) (33)

$n =$ $1 + \exp(-25.23 - 0.02195 * C + 0.0074 * U - 0.1940 * C_{org} + 45.5 * dB - 7.24 * dB^2 + 0.0003658 * C^2 + 0.002885 * C_{org} - 12.81 * dB^{-1} - 0.1524 * U^{-1} - 0.01958 * C_{org}^{-1} - 0.2876 * \log(U) - 0.0709 * \log(C_{org}) - 44.6 * \log(dB) - 0.02264 * (dB * C) + 0.0896 * (dB * C_{org}) + 0.00718 * (1 * C)),$ (Wörsten et al. 1999) (34)

where C = clay(%), U = silt(%), S = sand(%), C_{org} = total organic carbon content(%) and dB = bulk density(g/cm³)k_{sat}= saturated hydraulic(cm/h) conductivity, *α & n dimensionless van Gnuchten parameter*

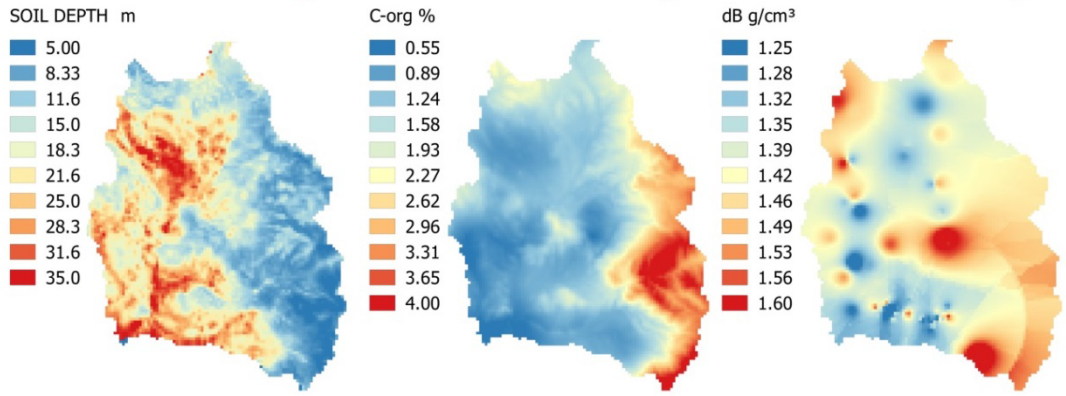

Figure 23: Spatially distributed maps of soil depth (m), C-org = organic carbon content (%) and dB = bulk density (g/cm³).

For each soil textural class of the RK result map (Figure 18d) the median soil textures of clay (Figure 15e), silt (Figure 16e) and sand (Figure 17e), as well as for the soil depth, the organic content (C_{org}), and the bulk density (Figure 23) were calculated and applied in the PTF of Wösten et al. (1999) and Vereecken et al. (1989). Figure 24 reports the hydrological parameters that were applied to the WaSiM soil table.

The soil in WaSiM-RKS was parameterized in 3 horizons. The first horizon was sub-divided into 5 layers; note that the number of layers has to be the same for all each horizon due to numerical reasons (Schulla 2012), with a layer depth ($H1_{layer}$) of 0.2 meter for each layer, so that the total depth is 1m.

$$H2_{layer} = \frac{(\overline{X}(h_{soil}) - 1m)}{n_{layers}}, \tag{35}$$

where n_{layers}ᵣ =layer depth second horizon, h_{soil} = depth of soil per soil texture class and n_{layers} = number of layers in the second soil horizon.

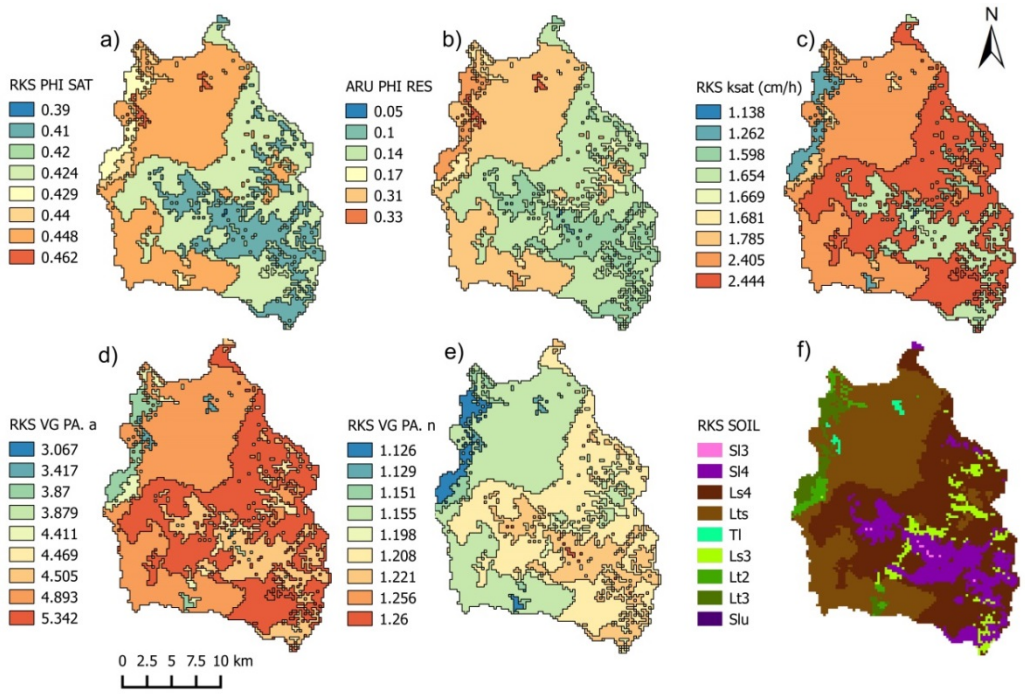

***Figure 24: Van Gnuchten parameters a) "PHI SAT" = saturated water content, b) "PHI RES" = residual water content, c) "Ksat" = hydraulic conductivity, d) "VG Par. α" = Van Gnuchten α, e) "VG Pa. n" = Van Gnuchten* n, which were derived from the Regression Kriging map in f).**

The second horizon consist also of 5 layers, but here again the median depth of each soil textural class was calculated and the depth divided by:

The last horizon consisted of 8 layers with $H3_{layer}$ = 0.5m (total horizon depth = 4m). This Horizon was parameterized as rock, with values taken from the standard soil table of WaSiM.

Except for the parameter described in the sections 5.2.3.3 & 5.2.3.4 the WaSiM setup of the WaSiM-ARU and the WaSiM-RKS were the same.

5.3 Calibration of WaSiM modeling results

5.3.1 Flow duration curve (FDC)

Flow duration curves were calculated from the historical recorded discharge as well as in a later step of this study for the hydrological modeling outputs. Flow duration curves are widely used in different areas of hydrology. A flow duration curve is a cumulative frequency curve showing the percent of time or probability, specific discharges were equal of exceeding a certain value during a given time period (Searcy 1959, USEPA 2011). The flow duration curves were derived as followed:

I. Acquire stream flow data (in this study measured and modeled daily mean discharge),

II. arrange data,

III. rank flow data,

IV. obtain frequency of occurrence (exceedance probability)

The frequency of occurrence is obtained as follows:

$$F = 100 * \frac{R}{N+1} \quad (36)$$

Where,

F is the frequency of occurrence (expressed in % of time a particular flow value is equaled or exceeded), R is the Rank, and N is the Number of observations (USEPA 2011)

A flow duration curve measures in X-axis direction from high to low flow and the Y-axis gives the discharge quantity for each percent exceedance value (1-100%). Based on the derived FDCs of the recorded discharge as well as for the hydrological modeling discharge results, threshold values for the different flow conditions were determined.

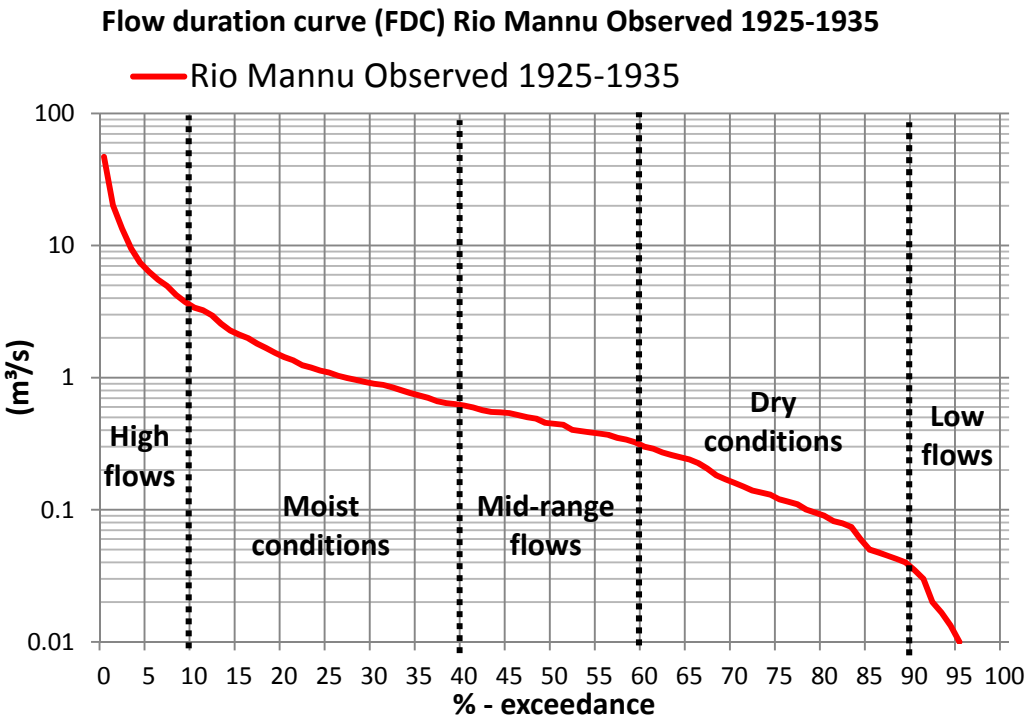

Figure 25: Example of a flow duration curve (FDC). Different discharge behaviors are marked based on the percent-exceedance range.

In this study the WaSiM-ARU setup was used to calibrate WaSiM based on the flow duration curves. Since the recorded discharge is not overlapping with the reference time of the WaSiM inputs runoff calibration was only performed based on the probabilities of flow conditions.

This setup was afterwards transferred to the WaSiM-RKS setup except the soil model parametrization. The mean flow duration curves of the WaSiM-ARU and the WaSiM-RKS ensemble for the reference time series were used to determine the threshold values for high flows-, wet conditions, mid-range flows, dry conditions and low flows. This was done for both the WaSiM-ARU and WaSiM-RKS ensemble reference period.

5.3.2 Comparison of modeled soil water content (SWC) with recorded SWC

Soil moisture content was recorded using Frequency Domain Reflectometry (FDR) with four "ThetaProbe ML2x" probes on a pasture field at the Azienda St. Michele in the Rio Costara catchment (location WGS-84 UTM 32N EAST: 508589, NORTH: 4362827, 150m above sea level). SWC was recorded at two different points (10m distance to each other) for each at 10cm and 20cm depth below surface. SWC recording started on October 5th 2010 and ended on January 5th 2012, with a recording interval of 10 min. The recorded SWC was averaged to monthly mean values and compared to WaSiM SWC modeling results for the pixel at which the SWC probes were located.

5.3.3 Evapotranspiration Patterns

Assimilating remote sensing data is especially important for ungauged catchments (Hrachowitz et al. 2013). For example Mohamed et al. (2006), Winsemius et al. (2008) used evaporation products derived from remote sensing applications to improve the hydrological model parameterization.

In this study spatial patterns of real evapotranspiration (ETR) from optical and thermal satellite imagery were derived using the Triangle Method. The method was introduced by Price (1990) and further developed by Jiang & Islam (1999). The approach is based on the surface energy balance. The actual evapotranspiration is equivalent to the surface latent heat flux. The surface latent heat flux was calculated as followed:

$$\lambda E = R_n - G - H, \quad (37)$$

where λE is the latent heat flux , R_n the net radiation, G the soil heat flux and H the sensible heat.

Since the estimation of *H* and to a lesser extent as well R_n and *G* involves high uncertainties (Huber Garcia 2013), regional grids of ETR patterns as well as EF were calculated by using the simplified Priestley-Taylor formulation (Priestley & Taylor, 1972).

$$\lambda E = \phi(R_n - G) * \frac{\Delta}{\Delta+\gamma}, \quad (38)$$

where ϕ is the Priestley-Taylor parameter [-], Δ is the slope of the saturated vapor pressure at air temperature [kPaK-^{1}]and $\gamma$the psychrometric constant [kPaK-^{1}]

An advantage of this simplified approach is that all variables on the right side of the equation can be calculated independently from remote sensing data and λE can be determined by the evaporative fraction (*EF*) (Tang et al. 2010).

$$EF = \frac{\lambda E}{R_n - G}, \quad (39)$$

and gives

$$EF = \phi * \left[\frac{\Delta}{\Delta+\gamma}\right], \quad (40)$$

The method uses the feature space of land surface temperature plotted against the Normalized Difference Vegetation Index (NDVI) derived from thermal and optical remote sensing data respectively. The resulting triangle NDVI-LST scatterplot is analyzed to determine quantitatively a dry and a wet edge of the feature space, representing the limiting factors of soil water content (Figure 26c). The scatterplot shows the heterogeneity in the catchment, since now for every NDVI pixel (Figure 26a) a range of different LST values (Figure 26b) can be attributed (Jiang & Islam 1999). The variance of LST for each NDVI value is caused by the evaporative cooling effect and is strongly related to plant available soil water content. Thus, the higher the soil water content, the higher the evaporation rate and the lower the LST. Dots close to the blue line in the example scatter plot (Figure 26c) represent pixel with potentially evapotranspiration rates. The dry edge (red line in the scatter plot Figure 26c) is the soil moisture limiting factor. Dots close to this line represent pixels with high temperature. Since temperature is high the evapotranspiration rate is zero. In reality evapotranspiration is barely zero for vegetated pixels as plants can get water from the root zone even the surface soil is dry. (Stisen et al. 2008; Huber Garcia 2013). Due to that zero transpiration is not represented by the dry edge but by the true dry edge (Figure 26c). Based on the borders of the triangle ϕ was scaled. For pixels with the lowest NDVI and highest LST, ϕ_{min} was set to 0 and is representing the global minimum (Huber Garcia 2013). The global maximum ϕ_{max}.was set fixed to 1.26 following the method of Barta eta al. (2006). The dots that are close to

the point where the wet edge intersects the dry edge (Figure 26c) represent the pixels with the highest NDVI and at the same time lowest LST. After the definition of the global ϕ boundary conditions, the Jiang and Islam (1999) interpolation approach slightly modified by Stisen et al. (2008), was applied to obtain ϕ values for each pixel. This is done in a two-step process by determining first the lower bound $\phi \mathrm{i}, \min$ (eq. 42) and after upper bound with (eq. 43). The upper bound of ϕ ($\phi_{i,max}$) corresponds to the wet edge. As it is constant regardless of the land surface, $\phi_{i,max}$ it is equal to $\phi_{,max}$=1:26 independently of the NDVI value (Stisen et al. 2008). By applying a linear equation with the slope of the dry edge and the temperature of the wet edge as y-intercept to the NDVI values, the maximum LST for every NDVI, equal to the dry edge was determined (Huber Garcia 2013). For the calculation of the evaporative fraction (eq. 40) now the slopes of the saturated vapor pressure at air temperature [kPaK-^{1}] Δ and the psychrometric constant γ [kPaK-^{1}] have to be obtained. Where, Δ and γ were determined by the approach of Allen et al. (1998) (eq. 44). This approach is based on the Penman-Monteith equation and is mainly dependent on the air temperature. Since no air temperature observations at the sensors overflight time (always 10-11 a.m.) were available, the mean daily temperature of meteorological station Cagliari at each overflight day was chosen. This data was downloaded from KNMI climate explorer database. To solve eq. 45, the atmospheric pressure (P) needs to be calculated. This was done using eq. 46 of Huber Garcia (2013). This approach is an extension to the one of Wang et al. (2008). P is in this approach, instead of using an average elevation for the total field of observation, calculated for each pixel of the satellite data with a certain elevation taken from a digital elevation model. Air Temperature T was applied similar to eq. 45. To finally solve eq. 38 *Rn* was and applied using an average value for the field of observation. Rn was estimated on a very simple approach in which *Rn* is about 55% of the global radiation (Davies 1967). Global radiation values acquired from the SoDa database (Solar Energy Services for Professionals) were used for each day of available satellite images. *G* was estimated from *Rn* following the approach of Gragoa and Brutsaert (1996) and is about 7% of the global radiation. With the now full set of needed quantities to solve eq. 38 λE was estimated. Further information on the Triangle-Method can be found in Jiang &Islam (1999), Wang et al. (2006), Tang et al. (2010) Huber Garcia (2013) and Gampe et al. (2015).

The processing scheme to determine the evaporative patterns is as follows:

I. Conversion of Landsat TM/ETM radiances in LST (°C or K) for each pixel (Figure 26 yellow box) and calculation of the Normalized Difference Vegetation Index (NDVI)

$$NDVI = \frac{(NIR-Red)}{NIR+Red)} = \frac{(LTM\ Waveband4-LTM\ Waveband3)}{(LTM\ Waveband4+LTM\ Waveband3)}, \quad (41)$$

where LTM waveband 3 = Red (630-690nm) and LTM waveband 4= Very Near-Infrared (760-900nm) in planetary reflections

calculate and scale ϕ with,

$$\phi i, \min = \phi \max \left[\frac{NDVI_i - NDVI_{min}}{NDVI_i - NDVI_{max}}\right]^2 \quad (42)$$

where $NDVI_i$ is the NDVI of the actual pixel $NDVI_{min}$ is the minimum observed NDVI value of vegetation (generally set to 0.1.) and $NDVI_{max}$ the maximum observed value (Figure 26 purple box).

II. Define the boundary conditions with the triangle and calculate ϕi for each pixel (Figure 26 green boxes),with

$$\phi_i = \frac{LST_{i,max} - LST_i}{LST_{i,max} - LST_{i,min}} * \left(\phi_{max} - \phi_{i,min}\right) + \phi_{i,min} \quad (43)$$

III. Calculation of slopes of the saturated vapor pressure at air temperature [kPaK^{-1}] Δ and the psychrometric constant γ [kPaK^{-1}] (Figure 26 grey boxes) with,

$$\Delta = \frac{4098 * \left[0.6108 * exp\left(\frac{17.27 * T}{T+237.3}\right)\right]}{(T+237.3)^2} \quad (44)$$

where T is the air temperature[°C] (Allen et al. 1998). In this study the mean catchment air temperature at observation day was chosen.

$$\gamma = \frac{C_P * P}{\varepsilon * \lambda} \quad (45)$$

where Cp is the specific heat at constant P(1.013*10^{-3} MJ°C^{-1} kg^{-1}), P is the atmospheric pressure [kPa], ε is the ratio between molecular weight of water vapor and dry air (0.662) and λ is latent heat vaporization (2.45 MJkg^{-1}) (Allen et al. 1998)

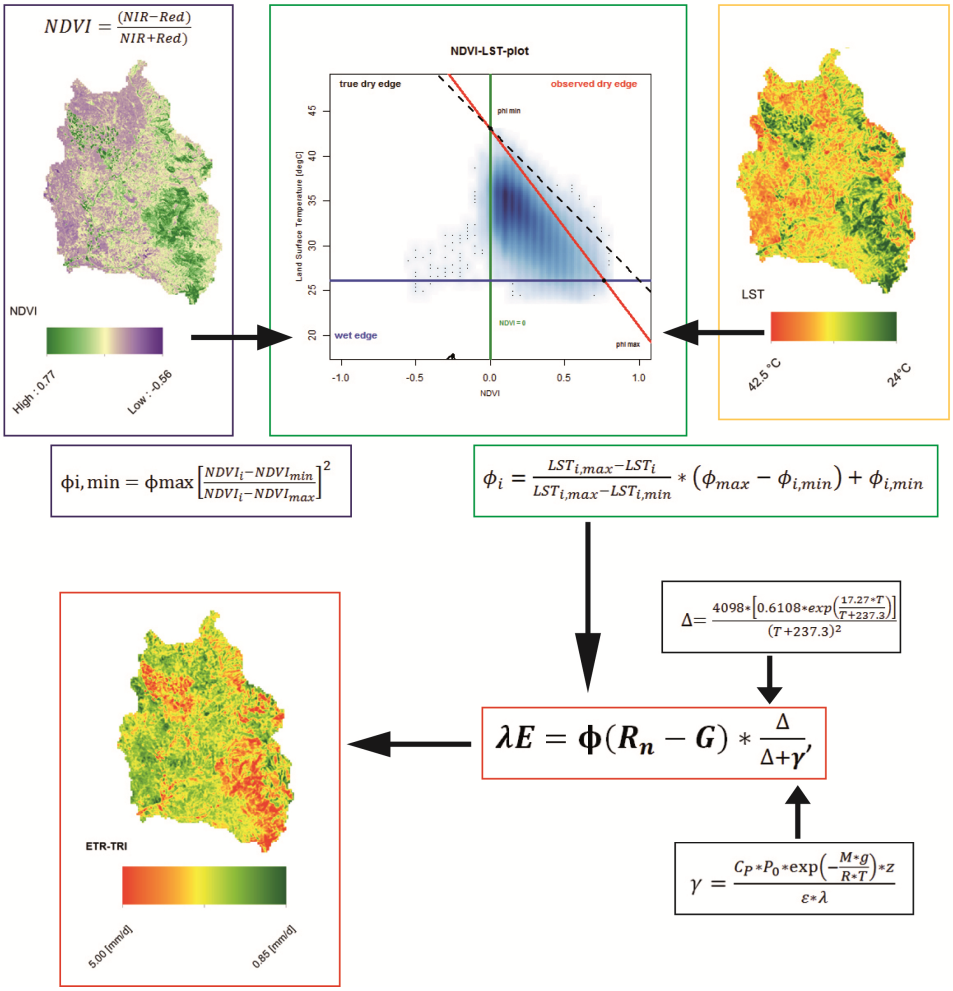

Figure 26: Processing scheme to calculate the remote sensing evapotranspiration patterns.

P was determined by means of a temperature dependent variation of the barometric formula after Roedel (1994)

$$P = P_0 * \exp\left(-\frac{M*g}{R*T}\right) * z \qquad (46)$$

where P_0 is the standard atmospheric pressure at sea level (1013.15 hPa), M is the mean molar mass of the earth's air (28.97 $gmol^{-1}$), g is the mean gravitational acceleration (9:81 ms^2), R is the universal gas constant for air (8.315

$WsK^{-1}mol^{-1}$), T is the air temperature in [K] and z is the elevation a.s.l. [m] (Huber Garcia 2013).

IV. Calculation of the λE for pixel by applying the results of steps I and II for each pixel into using eq. 38 (Figure 26 red boxes)

V. Transformation of λE [W/m²] to [mm/d] for each pixel (Figure 26 red boxes)

VI. Calculation of average evapotranspiration for each month of the year based on available satellite data (Table 7) and upscaling to monthly mean values by multiplication with the number of days per month.

Application to the Landsat satellite images

Evapotranspiration sums derived by the Triangle method will be indicated as (ETR-TRI). The Triangle Method was applied to optical/thermal satellite imagery from LANDSAT 5 Thematic Mapper (TM) and LANDSAT 7 Enhanced Thematic Mapper. Available images covered a period from 1984 to 2003. For each image spatially distributed grids of daily mean ETR (mm/d) were calculated. The grids were normalized by averaging monthly, then multiplying by a number of 28-31 days depending of the length of the particular month. Satellite data coverage was best for summer months, due to the fact that only cloud free scenes are applicable in this procedure. In total 12 Landsat TM and 16 Landsat (ETM) scenes of the catchment were available and used to derive one evapotranspiration grid (ETR-TRI) for every month of the year. For each image evapotranspiration patterns are calculated and images belonging to a certain month of the year were averaged in order to derive mean information for each month of the year in the Rio Mannu catchment.

Table 7 summarizes the available satellite scenes that were used to calculate the daily actual evapotranspiration (ETR). A second validation source for ETR was found in a study of Montaldo et al. (2013). In this study ETR rates over grass land were derived in the neighbor catchment Flumendosa River using the eddy covariance method (Montaldo et al. 2013). Since there are different land use land cover types located in the Rio Mannu catchment and in the model set up the actual evapotranspiration over grassland can only be used as a validation source in a limited manner.

Table 7: Cloud free Landsat TM & ETM satellite scenes available for the Rio Mannu di San Sperate catchment (1984-2010).

MM	Date	LS	Date	LS	Date	LS	Date	LS	No.
JAN	07.01.2002	ETM							1
FEB	02.02.2002	ETM							1
MAR	25.05.2002	ETM	09.03.2003	ETM					2
APR	06.04.1987	TM							1
MAY	21.05.1986	TM							1
JUN	25.06.1987	TM	20.06.2000	ETM	07.06.2001	ETM	18.06.2002	TM	4
JUL	27.07.1987	TM	22.07.2000	ETM	25.07.2001	ETM	07.07.2003	TM	4
AUG	21.08.1999	ETM	26.08.2001	ETM	08.08.2003	TM	24.08.2003	TM	4
SEP	04.09.1984	TM	13.09.1987	TM	08.09.1991	TM	24.09.1991	TM	4
OCT	10.10.2000	ETM	13.10.2001	ETM	16.10.2002	ETM			3
NOV	09.11.1999	ETM	11.11.2000	ETM					2
DEC	19.12.2002	ETM							1

5.4 Indices of the hydrological climate change impact assessment

In the following sub-section three different indices for the climate change impact assessment will be introduced. Those indices were used in the CLIMB-Project on the one hand to better compare climate change impacts among the project's different case studies in the Mediterranean, to assess the uncertainties of results that come from the different applied hydrological models and on the other they were intended to give a more easy to digest information on climate change impacts on the hydrology.

The Standardized Precipitation Index is used to analyze changes in the main hydrological input precipitation. It shows the climate change impact on precipitation in the basin from different temporal points of view. In comparison to the other two indices, changes of this hydrological quantity are only forced by the applied RCM. The range of results and the magnitude of projected climate change impacts are only dependent on the applied RCM.

The other two quantities were determined by using results of the hydrological modeling. The results are influenced by the climate model and the applied hydrological model. The

results of those indices are especially good to analyze the uncertainty that is applied to the results by the hydrological models.

The changes in number of different flow conditions will give information if and if yes how the flow regime and flow extremes are projected to change in the future.

The evapotranspiration index will give spatially distributed information about the plant available water and shows indirectly possible plant water stress.

5.4.1 Standardized Precipitation Index (SPI)

The Standardized Precipitation Index (SPI) developed by Mc Kee et al. (1993; 1995) to improve the representation of abnormal wetness and dryness, is a spatially invariant probability based indicator. It takes respect to the importance of the time scale in the analysis of the water availability and water use (Guttman 1999). Due to its adaptability for the analysis of drought on any given time scale, it can be used to monitor agricultural as well as hydrological drought (Waseem et al. 2015).

The SPI was determined as followed:

I. determine the probability density function of the long term time series of precipitation

II. determine the cumulative probability or the observed precipitation

III. transform the cumulative probability based on equal probability to a normal distribution with mean zero and a standard deviation of one.

One can expect these values to be within one standard deviation approximately 68% of the time, within two standard deviations 95% of the time, and within three standard deviations 99% of the time, because SPI values fit a typical normal distribution. A related interpretation would be that an SPI value of less than -1.0 occurs 16 times in 100 years, an SPI of less than -2.0 occurs two to three times in 100 years, and an SPI of less than -3.0 occurs once in approximately 200 years (Hayes et al. 1999). McKee et al. (1993) suggest the following classification scale of the SPI: +2 and above = (extremely wet), +1.5

to + 1.99 = very wet, +1.0 to +1.49 = moderately wet, -0.99 to +0.99 = near normal, -1.0 to -1.49 = moderately dry, -1.5 to - 1.99 = severely dry and -2 and less = (extremely dry).

The SPI has the advantage that precipitation data is the only input parameter. It can be computed for different time scales (1, 3, 6, 12, 24, 48 month), provides an early warning of drought, helps assessing drought severity and is less complex as for example the Palmer Drought Severity Index and many others (WMO 2012). It has the disadvantage that it only quantifies the precipitation deficit. No soil water-balance component, thus no ratios of evapotranspiration/potential evapotranspiration (ETR/ETP) can be calculated. This is a key limiting factor of this index for climate change analysis, since air temperature is not considered (WMO 2012).

The SPI was calculated in this study for the reference and future precipitation modeling inputs of WaSiM.

5.4.2 Number of days with low flows, dry conditions, mid-range flows, moist conditions and high flows

Discharge can be classified into different conditions from high to low flows based on the exceedance probability (5.3.1). Each modeled daily mean discharge was counted based on this classification (low flows (LF), dry conditions (DC), mid-range flows (MRF), moist conditions (MC) and high flows (HF)) for every modeled hydrological year for the reference (REF) and future time series (FUT). Threshold values for the classification ranges given in Figure 25 were calculated based on the FDC (section 5.3.1) mean values of the REF data sets. For example WaSiM-ARU was driven with 4 different RCM in the REF. For each run a FDC was calculated based daily mean discharge values of the total modeling period. Each FDC has different 90, 90-60, 60-40, etc.-% exceedance discharge values. The mean values of the 4 REF runs were calculated and used to classify low to high flow conditions. Afterwards daily mean discharge values belonging to each class were counted, for every model run and every hydrological year separately for the REF and FUT.

5.4.3 Evapotranspiration Index (ETI)

The ETI, was calculated to derive the real Evapotranspiration (ETR) share in the potential Evapotranspiration (ETP).

$$ETI = \frac{ETR}{ETP}$$

Where, ETR is the actual evapotranspiration and ETP is the potential evapotranspiration.

The index describes the missing percentage to full plant water availability. This index gives an indication about plant water stress at times, when plant cover is present. A value of 1 indicates that plants have perfect water availability and the soil is fully saturated. Values close to zero indicate extreme drought conditions.

5.5 WaSiM parameter sensitivity and calibration approach in the Rio Mannu basin

In this chapter the calibration and validation efforts for the WaSiM model in the Rio Mannu basin are documented. The official CLIMB model calibration and validation procedure was based on two independent observations.

5.5.1 Sensitivity of WaSiM parameters

The soil model of WaSiM version2 has less sensitive parametrization parameters compared to the version 1, due to the more physical based nature of the model and soil properties in particular the porosities should be understood as fixed values that should not be calibrated. Only three parameters of the soil model in WaSiM should be calibrated, which are:

- The recession constant k_{rec} for the saturated hydraulic conductivity K_s with depth
- The interflow drainage density d_r

- For this study the base flow parameters Q_0 and $K_{ELS,Q0}$ since the groundwater module was disabled due to missing information about groundwater levels and groundwater flow directions.

The recession constant k_{rec} considers the decreasing hydraulic conductivity with increasing depth. The value reduces the conductivities downward up to a soil depth of 2m (fixed model internal parameter). Below depth of 2m d_r remains constant with the 2m value (Schulla 2014).

The interflow drainage density d_r considers the stream density per grid cell and is an effective parameter to linearly affect the amount interflow.

The most sensitive parameters of the evapotranspiration model the surface resistance rsc, but this parameter is only effective if resistances are much higher or lower than the optimum value (Schulla 2014).

Since snow fall only occurs very seldom in the mountainous parts of the catchment, the snow model of WaSiM was disabled and calibration parameters of the snow model were not considered for the calibration.

5.5.2 Calibration of WaSiM parameters

From a hydrological perspective the catchments needs to be classified as an ungauged catchment, even though a short time series of recorded discharge data was available. Stream flow data in a daily resolution was measured at the river outlet in Monsatir in the years of 1925-1935, but unfortunately no recorded discharge data was available for the reference period (1971-2000). To run WaSiM V.2 (Richards-Equation) the availability of several climate input parameters in a daily temporal resolution is necessary (section 5.1). Since for the observed discharge time series 1925-1935, those required data were not observed in the test site, it was not possible and meaningful to calibrate and validate WaSiM on recorded discharge data in a daily temporal resolution. Furthermore a dam was installed in the Rio Mannu catchment in the 1960s and the steam network has been heavily modified in the last 80 years. Due to the strong artificial modifications of the steam network it can be expected that the discharge behavior is significantly different nowadays compared to the recorded discharge of 1925-1935. For ungauged catchments

Blöschl (2005) suggested calibrating hydrological models based on recorded data of neighboring catchments. Patil and Stieglitz (2011) showed that good predictability of runoff in ungauged catchments from characteristics of nearby catchments is more likely in humid regions than in dry regions. Perrin et al. (2007) also showed that stable parameterizations are more problematic to obtain in catchments characterized by dry climate than in humid climates.

Since neighboring catchment characteristics, especially the soil properties are known to be significantly different to the Rio Mannu catchment and the catchment is located in a dry evaporation dominated climate, this approach was refused. To overcome the issues described above, WaSiM-ARU was calibrated by driving it with the downscaled and bias corrected climate model forcing of the reference time series (1971-2000) which were delivered by Deidda et al. (2013). WaSiM's computed discharge outputs (1971-2000) were then compared with the recorded discharge of 1925-1935 as long-term monthly means (see Figure 28) and by the calculation of flow duration curves (FDC) (Figure 29).

The parameters d_r and k_{rec}, that control the amount of interflow, were used to calibrate WaSiM's soil model. The parameters dr and K_{rec} are affecting each other. For example no interflow can be generated by whether setting d_r=0 or K_{rec}=1, while setting K_{rec} very close to zero and d_r very high would result in the production of nearly pure direct runoff. Due to this a cross calibration procedure was used to find the best parameter set. This was done manually, since WaSiM does not have an automated calibration algorithm.

The calibration of those parameters was done in a 250m spatial resolution using the outputs for the total Rio Mannu catchment area. The soil model was setup with the soil information of the Aru et al. (1990) soil map. The parameter combination of dr= 10 and Krec =0.8 was found to fit best the observation of 1925-1935 on a long-term monthly mean basis (Figure 28). This parameter set was then transferred to all WaSiM model runs in the Rio Mannu.

The surface resistance parameter r_{sc} of the evapotranspiration module was found to be relatively insensitive to changes. Due to that the parameters were set and left to values that were found in literature. WaSiM's spatial evapotranspiration outputs were compared to spatial reference evapotranspiration that was derived by LANDSAT satellite imagery.

6. RESULTS AND DISCUSSION HYDROLOGICAL MODELING AND PROJECTED CHANGES

6.1 Calibration results of the WaSiM model

This section presents the comparison of recorded field data with hydrological model outputs when driven with the climate model meteorology of the reference time series 1972-2000 (REF) and shows the calibration approaches for the data scarce Rio Mannu di San Sperate catchment.

6.1.1 Comparison of model outputs and recorded discharge data of 1925-1935

Figure 28 reports the long-term monthly mean discharge values of the WaSiM simulations in comparison to the observed long-term monthly mean of 1925-1935. The model outputs were computed using the reference climatology of the 4 regional climate models (RCMs) provided, by Deidda et al. (2013). Daily model outputs were aggregated to long-term monthly mean discharge.

The simulation results in comparison to the observations show, that the general annual distribution of the runoff (high flows from November to February, mean flows in Oct, March-May and low flows from June-September) is well represented in the model outputs using the current model setup with regional climate model forcing.

Also general trends of simulation output errors are visible. While autumn and winter discharge are overestimated in the simulations, spring and summer discharge are underestimated. Those errors in the simulations might occur by different uncertain sources, since the reference climatology of the RCMs cannot be expected to fully represent the climate conditions of the recorded time series of 1925 to 1935.

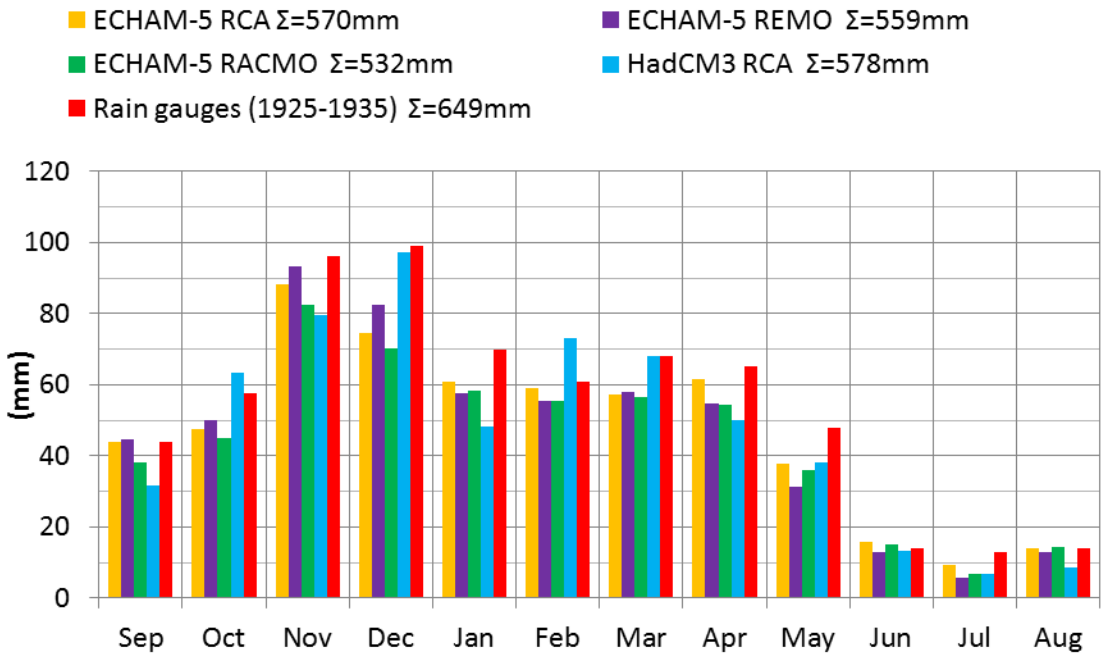

Figure 27: Comparison of long-term monthly mean precipitation rates of the regional climate model inputs for the reference time series (1971-2000) and the recoded gauging station data (1925-1935).

Especially the daily precipitation rates and the discharge behavior of the stream network for the observation time series might be highly different to the ones of the reference period and already strongly impacted by the changing climate. For example Sannitu (2006) pointed out the precipitation rate was reduced by 50-60% within the last 20 years in this region. In Figure 27 long-term monthly mean precipitation sums of the RCMs for the reference time series are compared to the long-term monthly mean precipitation sums recorded by 12 precipitation gauging stations of 1925-1935, which were located in and close to the catchment. The annual precipitation sums of the RCM climate forcing of the reference time series reach only 82%-89% of the interpolated Rio Mannu precipita-

tion sum of 1925-1935 (Figure 5 & Figure 27). The calibration results using the Flow Duration Curves (FDC) (Figure 29) show that the WaSiM outputs represent a good fit of modeled and recorded flows that are above 1m³/s while the reproduction of extreme mid-range to low flows under 1m³/s shows a distinct picture. The dry to low flow conditions under 0.1 m³/s might imply a relative higher measurement error. For those conditions modeling uncertainties seem to be very high. The gap between observed and modeled mid-range flow conditions (0.1-0.6m³/s) might be caused by the difference between precipitation inputs of 1925-1935 and the RCM precipitation inputs of 1971-2000, which meet only 85% of the rate of 1925-1935. To have an approximation of how much runoff should be produced by the catchment, Figure 30 presents the precipitation runoff transformation for different catchments as well as for the total island of Sardinia after Sannitu (2006). Based on the annual climate model ensemble input precipitations, WaSiM's model runoff outputs (73-106 mm per year) fit well the expected runoff from the transformation scheme.

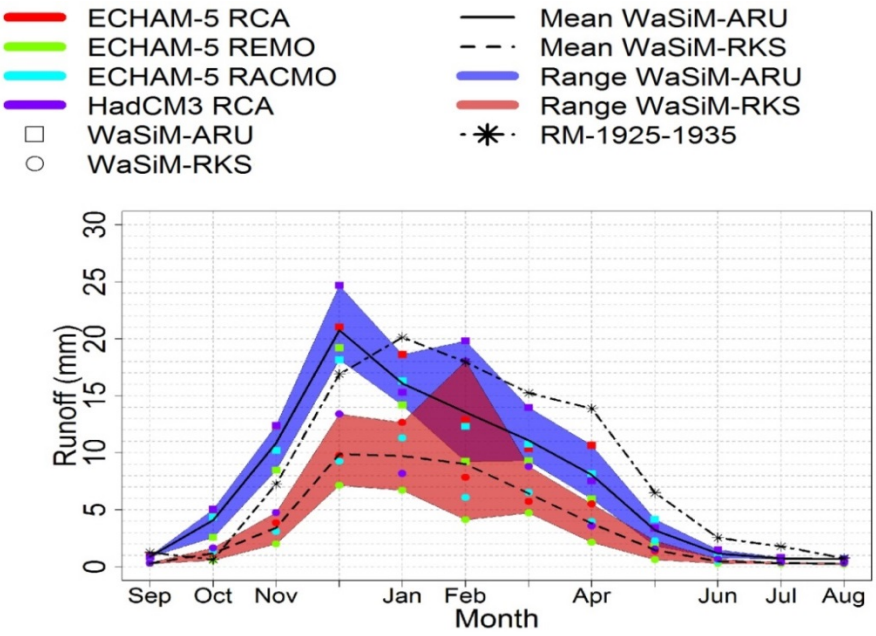

Figure 28: Rio Mannu - Run off observed (1925-1935) vs. WaSiM run off (1971-2000).

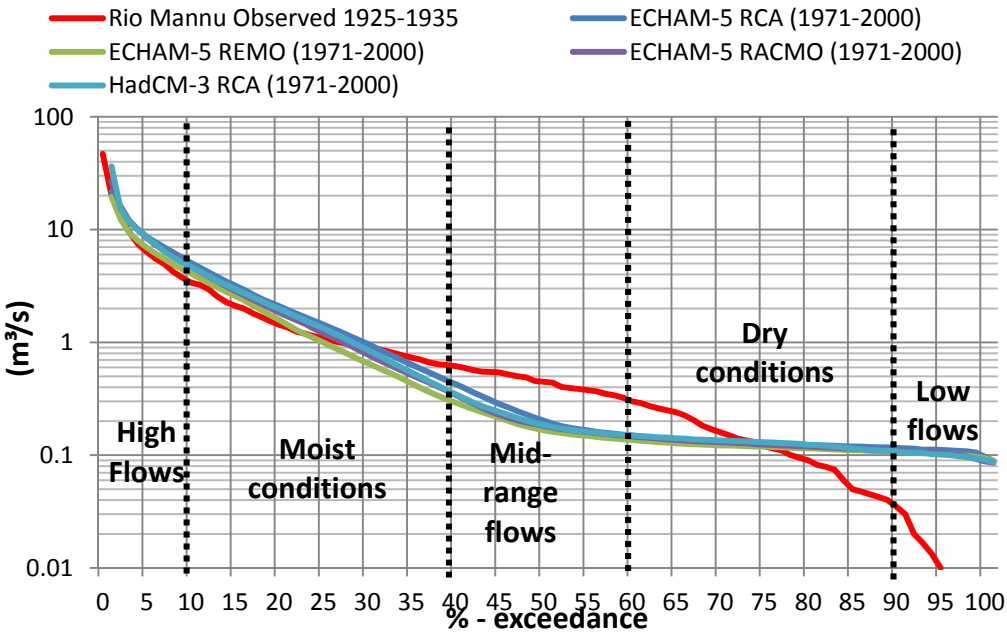

Figure 29: Rio Mannu - Flow duration curves of observations (1925-1935) and WaSiM simulations of the reference time series (1971-2000).

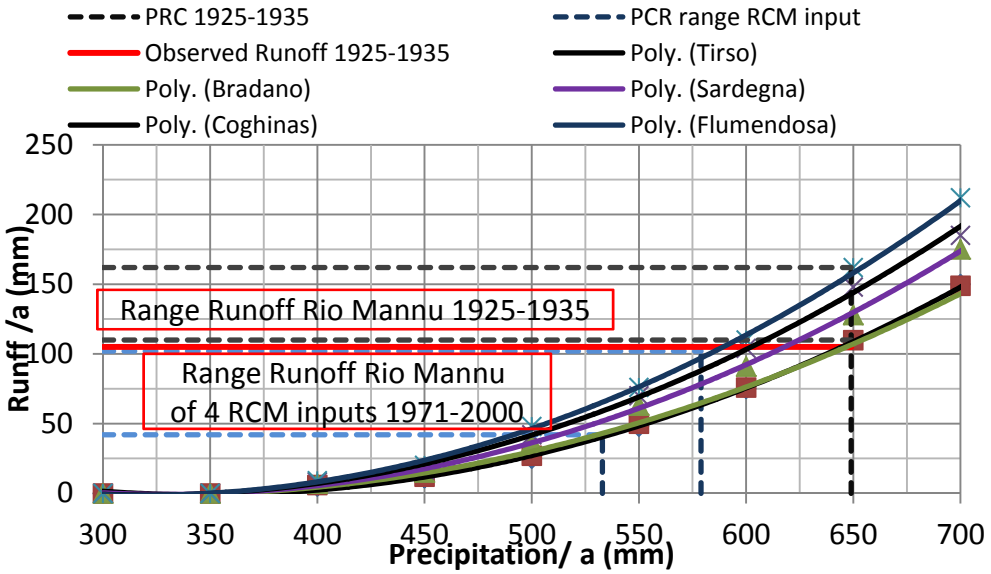

Figure 30: Precipitation runoff transformation for selected catchments in Sardinia and for the total island. (Data source: Sannitu 2006).

In Table 8 the root mean square erros (RMSE) of WaSiM-ARU FDCs in comaprison to the observation FDC of 1925-1935 using the best WaSiM setup forced with regional climate model inputs provided by WP4 are shown.

The root mean square errors are presented following the FDC classification scheme in Figure 29. With the current WaSiM-ARU model setup, best results for high flows were achived using the HadCM3-RCA climate inputs while the ECHAM-5 REMO forcing shows the highest error for high flows. Moist conditions on the other hand have the lowest error for the ECHAM-5 REMO run. The Mid-flow to low flows RMSEs are very similar for all climate model inputs. Especially for the low flow conditions the RMSE is nearly as high as the flow range. This model error might be a consequence of significantly lower climate model precipitation input, compared to the precipitation of 1925-1935, in the season (March-July) where the majority mid to low flows are generated.

After the calibration WaSiM generated plausible discharge and runoff outputs.

Table 8: Root mean square error of WaSiM-ARU simulations (1971-2000) vs. observations (1925-1935).

	ECHAM-5 RCA (1971-2000) (m^3/s)		ECHAM-5 REMO (1971-2000) (m^3/s)		ECHAM-5 RACMO (1971-2000) (m^3/s)		HadCM-3 RCA (1971-2000) (m^3/s)	
	RMSE	flow range	RMSE	flow range	RMSE	flow range	RMSE	flow range
High f.	7.88	21.69-6.27	8.71	19.47-4.93	6.23	26.90-5.8	3.61	36.37-5.67
Moist cond.	0.58	6.26-0.5	0.29	4.92-0.34	0.38	5.79-0.40	0.45	5.66-0.41
Mid-range f.	0.24	0.49-0.16	0.29	0.33-0.14	0.27	0.39-0.15	0.26	0.40-0.15
Dry cond.	0.07	0.16-0.12	0.08	0.14-0.11	0.07	0.15-0.11	0.07	0.15-0.11
Low	0.10	0.12-0.09	0.09	0.11-0.09	0.09	0.11-0.09	0.09	0.11-0.09

6.1.2 Comparison of evapotranspiration model outputs and derived evapotranspiration patterns

The second criterion of the calibration/validation strategy is a comparison of patterns of actual evapotranspiration, which were simulated in the WaSiM model with patterns derived from remote sensing imagery. This step was done on the optimized WaSiM model after the calibration on observed discharge was conducted.

The WaSiM simulation results in the Rio Mannu of the reference are only for certain months in good correspondence with derived act. Triangle evapotranspiration (ETR-TRI) and reference grass evapotranspiration of Montaldo et al. (2013) (Figure 31). Little deviations between reference ETR over grass (Montaldo et a. 2013) and modeling results are visible for the months of January, February, March, August, Sep, Oct, Nov, and Dec. But a high mismatch is visible for the months of April, May, June, and July. The monthly mean sums of the ETR patterns do not fit the modeling results but also do not fit to the reference ETR over grass. The ETR-TRI patterns do fit the monthly mean sums only for the months of March (WaSiM-ARU) and April (WaSiM-RKS). The reference ETR over grass and the ETR-TRI do match also only for the months of June and January.

There are several reasons for differences between simulated and observed evapotranspiration patterns. One reason for the mismatch might occur from the problem that remote sensing imagery features only a short snapshot of a particular situation, which may not display long-term characteristics for this region. This is especially true for the months of December to March where only one remote sensing image per month was available. A better temporal cover was available for the months June to September with 4 satellite images per month, while November and March are covered by two and October by 3 images. The mismatch modeling results might be intensified by the too low precipitation climate model inputs in this season.

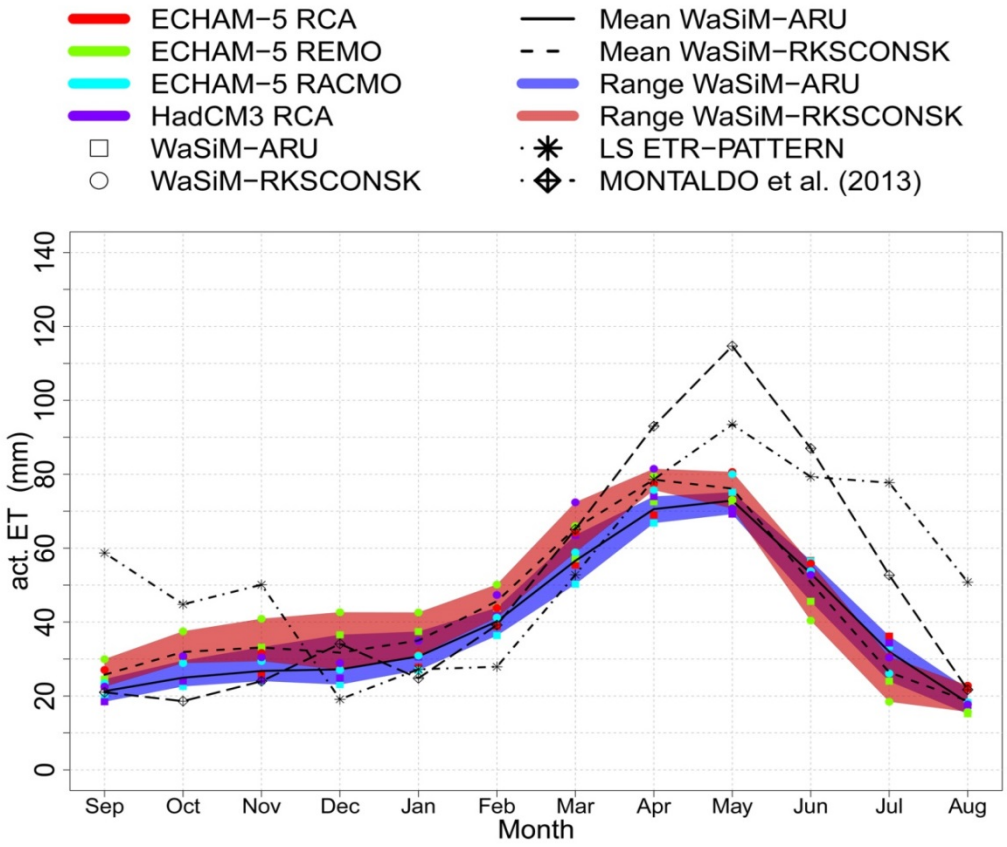

Figure 31: Observed grass evapotranspiration (ETR) after Montaldo et al, (2013) and derived Triangle Method evapotranspiration (ETR-TRI) versus simulated ETR outputs of WaSiM driven with the RCM climatology for the reference time series (1971-2000).

Exemplary derived ETR-TRI patterns as spatially distributed grids in comparison to the WaSiM-ARU and WaSiM-RKS hydrological modeling results are shown in Figure 32, for the months May and June. The derived ETR sums from the ETR-TRI patterns show a mean evapotranspiration sum of 94 mm for May and 79 mm for June. A gradient can be detected from minimum values in the lower southwestern valley areas, where agricultural land use is dominant, to higher values in the more mountainous regions, characterized by olive trees and macchia vegetation.

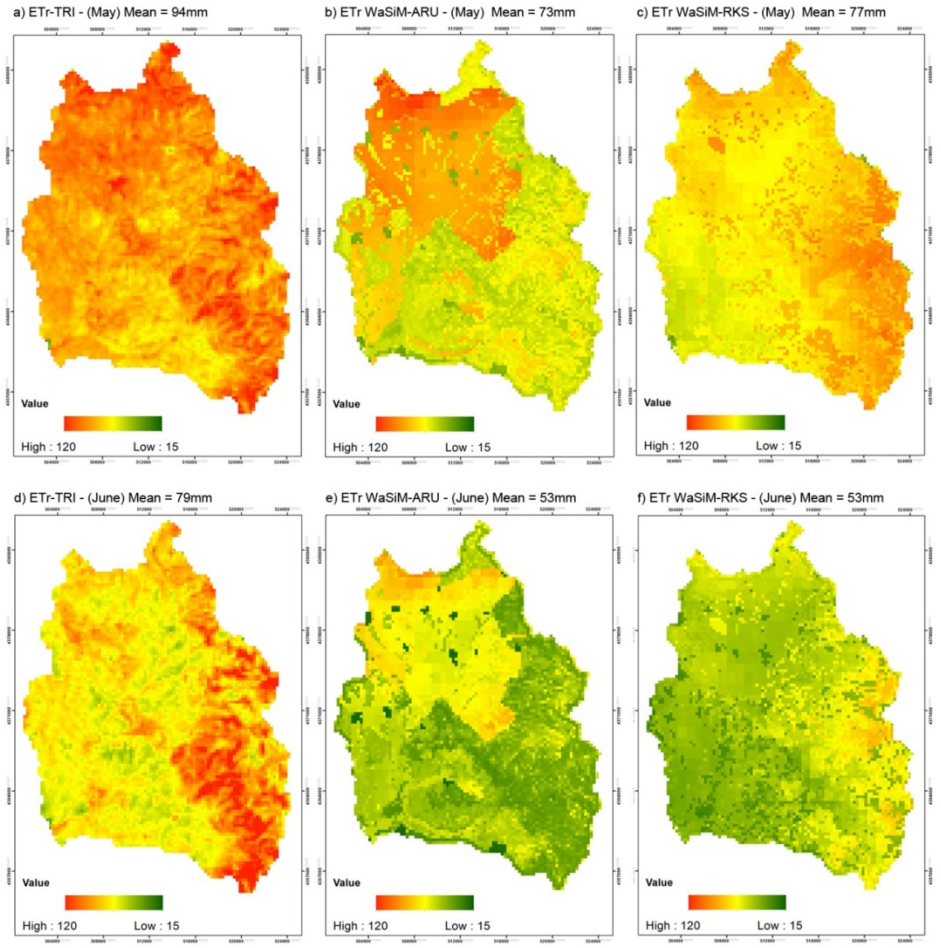

Figure 32: a) & d) Triangle Method Evapotranspiration pattern (ETR-TRI) versus spatially distributed b) & e) ETR results maps of WaSiM-ARU and c) & f) WaSiM-RKS.

The gradient is even larger in June. During this month, many agricultural crops are already harvested (Bird et al. 2015) and it can be assumed that soil moisture content is rapidly dropping to values close to permanent wilting point in the lower valley region. The higher ETR values in the mountainous regions can be explained by the lower air temperatures and higher humidity in higher elevations and by the fact that the dominant land uses – olive trees and macchia plants – can extract water from deeper soil horizons of the unsaturated zone. The comparison of the two WaSiM soil model setups shows that WaSiM-RKS outputs fit better the derived ETR-TRI patterns (Figure 33).

The Aru et al. (1990) soil map also used in the study of Piras et al. (2014) seems to less well represent the true distribution in the catchment. The WaSiM-ARU setups show very high values of ETR in the southwestern part of the Rio Mannu basin (Figure 18b & e). The distinct boundaries of this pattern look untrustworthy, as they relate almost perfectly to the ARU soil texture class loamy clay (Tl) in the Aru et al. (1990) based soil texture map (Figure 18). In the RKS soil model, the same soil texture class is only present as a small spot in the south. As a consequence of the different texture distributions, hydrological model properties are quite different between the two soil model setups in this region. Resulting ETR sums of Piras et al. (2014) are much higher for the months July and August. Another explanation for the underestimated evapotranspiration in the dry months of the year might be that irrigation is not considered in the current WaSiM setup. From the study of the Landsat remote sensing imagery, it gets clear that in the north-eastern part of the catchment irrigation is applied in the dry season, but unfortunately it was not possible to get any information about the length of irrigated days, nor about the total amount of irrigation water used in this region. The scarce information about irrigation activities in the test site made a consideration in the model set up infeasible. For future WaSiM setups this information is vulnerable to improve the fit of observations and simulations.

The R^2 of scatterplot results of WaSiM-RKS in Figure 33ii) & iv) reveal a better match with the derived ETR-TRI patterns. The comparison shows on the one hand for both hydrologic model setups a very low to low R^2, but on the other hand an improved R^2 for WaSiM-RKS setup of 0.06 (250m) & 0.05 (30m) for May and 0.18 (250m) & 0.18 (30m) for June. Nearly no correlation is visible for the WaSiM-ARU setup with very little R^2 of 0.01 (250m & 30m) for May and 0.09 (250m) & 0.09 (30m) for June, in a negative relation.

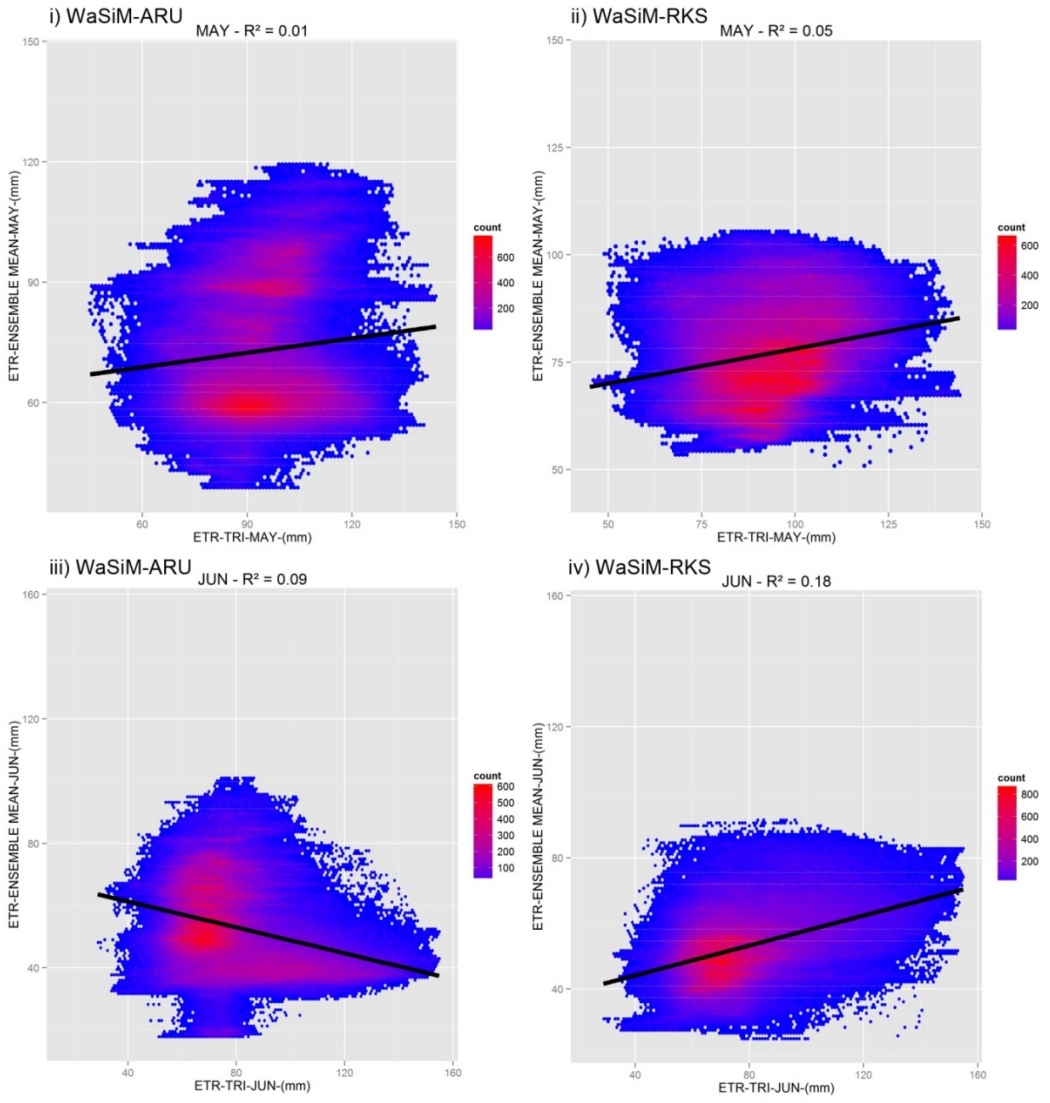

Figure 33: Scatter plot comparison of ETR-TRI and WaSiM-ETR results, i) WaSiM-ARU May referring to Figure 32 a) & b), ii) WaSiM-RKS-May referring to Figure 32 a) & c), iii) WaSiM-ARU June referring to Figure 32 d) & e) and iv) WaSiM-RKS June referring to Figure 32 d) & f).

6.1.3 Modeled vs. recorded soil water content (SWC)

Finally, considering point measurements for validation, WaSiM's SWC model results were compared with recorded soil water content from 2010-2012 (section 5.3.2). In Figure 34 field observed SWC is compared to model results using WaSiM-ARU (a) and

WaSiM-RKS (b). The recorded SWC reaches maximum values in February, with a monthly mean close to 35 vol.-%. SWC reaches minimum values in August but does not drop below 15 vol.-%.

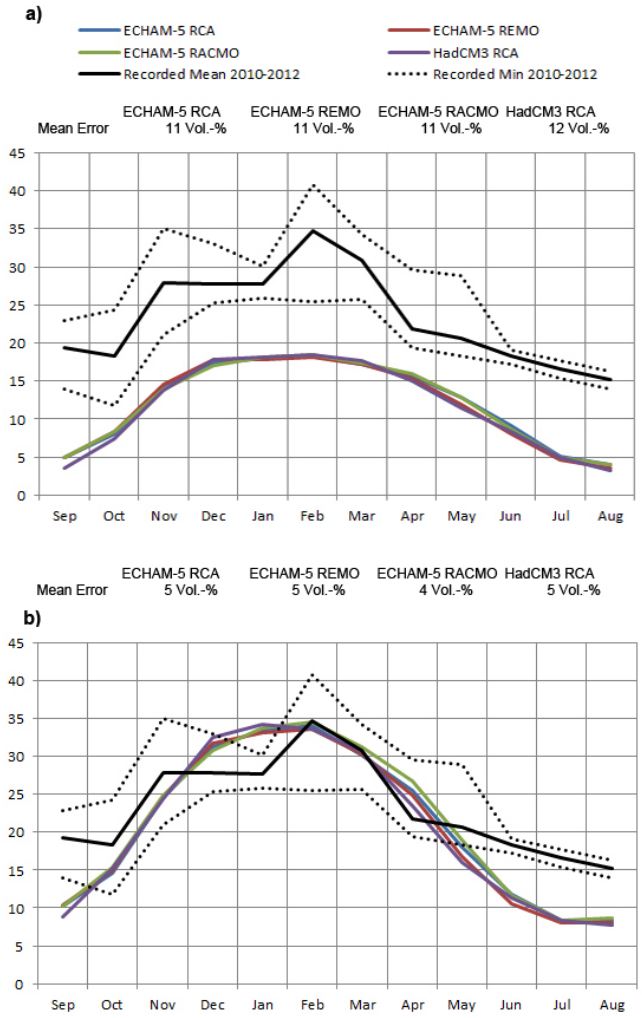

Figure 34: Recorded soil moisture from 2010-2012 in comparison to WaSiM modeling results of a) the WaSiM-ARU model setup, b) the WaSiM-RKS model setup.

Measured minimum values are about 7 vol.-% higher as compared to observations made by Cassiani et al. (2012) using electric resistivity tomography and electromagnetic induction.

The SWC outputs of both soil model setups match, in principle, the seasonal regime of the recorded SWC, however with considerable biases when using the conventional soil map. The WaSiM-ARU SWC stays below the 20 vol.-% all over the year, much too dry even for a semi-arid climate. The absolute monthly means of simulated SWC using the WaSiM-RKS SWC match much better with observations. The deviation between modeled and recorded SWC is below 1 vol.-% in February and March. Higher negative deviations (-9 to -7 vol-%) can be observed in the dry season from June to September and positive deviations of 6 vol.% in January. For the rest of the year, deviations are below 4 vol.%. Those results reveal strong improvements in reproducing SWC behavior using the WaSiM-RKS soil setup. Furthermore it is shown that the soil parametrization is one major source of uncertainty in modeling SWC.

6.2 Modeling results and hydrological climate change impact

In this section the outputs of WaSiM for a reference (1971-2000) and future (2041-2070) time series were compared and analyzed. The comparison was first made based on changes of annual mean hydrological modeling results. This was done for both soil model setups (WaSiM-ARU & WaSiM-RKS). Afterwards inter-annual changes were quantified in a comparison of long-term monthly means. Finally WaSiM's spatial evapo-transpiration output grids were compared with grids of evapotranspiration patterns that were derived from LANDSAT satellite images (section 6.1.2).

6.2.1 Annual hydrological modeling results

Table 9 quantifies the WaSiM outputs for the major water balance components on an annual mean basis for the REF and FUT. Part b) of Table 9 summarizes the annual mean relative changes in the single water balance components for the future time series. Columns 1-3 represent the annual modeling results that are independent from the soil model setup of WaSiM.

For all regional climate forcings, annual precipitation rates are dropping in the future time series. The decline ranges from -39mm or -7% (ECHAM-5 REMO) to -124mm or -21% (HadleyCM3 RCA) per year. The applied RCMs show an increase in air temperature of 1.8°C (ECHAM-5 RCA & RACMO) up to 3.1 °C (HadleyCM3 RCA).

The range of modeled potential evaporation (ETP) outputs fit well the annual value of 1500 mm/as published by the EEA (2013). Highest values for the REF were modeled by WaSiM when applying the ECHAM-5 REMO. All future model outputs show increased ETP values from 182 mm (ECHAM-5 RCA) up to 338 mm (HadleyCM3 RCA) per year. This is mainly caused by rising temperatures. These results show that in terms of climate change impact within the A1B emission scenario the HadleyCM3 RCA is a more pessimistic climate forcing while the ECHAM-5 driven RCMs show a more moderate future climate change projection.

Note that Table 9 shows WaSiM results of the same water balance components (runoff (Q), actual evapotranspiration (ETR) and soil water content (SWC)) using two different soil model setups. Projections show that the hydrological parameters Q, ETR and SWC are expected to decline for at least 3 hydrological projections in the future. The range of changes depends strongly on the applied RCM. While results of WaSiM driven with the (ECHAM-5 RACMO and REMO) show only moderate hydrological changes of Q (-5% to -20%), significant annual changes of up to -37% for WaSiM-ARU and up to -46% for WaSiM-RKS are revealed when driven with the HadleyCM3. WaSiM-RKS driven with ECHAM-5 RACMO shows even a Q increase of 2%.

Table 9: Modeled hydrological a) quantities and b) projected annual changes in the water balance budgets of the Rio Mannu di San Sperate catchment by driving WaSiM-ARU & WaSiM-RKS with the regional climate model ensemble.

a)	Modeled long-term annual hydrological quantaties in the Rio Mannu Basin								
	Soil model setup independent quantaties			Results with Aru soil setup			Regression Kriging C soil setup		
Climate forcing	P (mm)	T (°C)	ET_p (mm)	Q (mm)	ET_r (mm)	SWC (vol.-%)	Q (mm)	ET_r (mm)	SWC (vol.-%)
ECHAM-5 RCA (REF)	570.10	15.90	1308.40	97.50	476.60	17.10	47.90	534.10	21.30
ECHAM-5 REMO (REF)	559.10	15.80	1612.40	73.70	492.00	15.80	28.40	545.50	19.60
ECHAM-5 RACMO (REF)	532.50	15.80	1339.30	87.70	452.90	16.80	43.80	503.90	20.90
HadleyCM3 RCA (REF)	578.70	15.40	1441.90	105.90	476.10	16.60	59.90	528.90	21.00
ECHAM-5 RCA (FUT)	500.90	17.70	1490.40	78.20	428.30	15.50	38.10	477.70	19.70
ECHAM-5 REMO (FUT)	519.80	17.60	1802.30	64.60	460.60	14.70	26.20	506.50	18.50
ECHAM-5 RACMO (FUT)	490.70	17.60	1531.30	83.70	409.80	15.70	44.70	455.50	19.80
HadleyCM3 RCA (FUT)	454.90	18.50	1779.90	66.40	394.60	13.90	32.50	436.60	18.00

b)	Modelled long-term hydrological changes Δ																	
	Soil model setup independent changes						Changes with ARU et al. soil setup						Changes with Regression Kriging soil setup					
	ΔP (mm)	ΔP (%)	ΔT (°C)	ΔT (%)	ΔET_p (mm)	ΔET_p (%)	ΔQ (mm)	ΔQ (%)	ΔET_r (mm)	ΔET_r (%)	ΔSWC (vol.-%)	ΔSWC (%)	ΔQ (mm)	ΔQ (%)	ΔET_r (mm)	ΔET_r (%)	ΔSWC (vol.-%)	ΔSWC (%)
ECHAM-5 RCA (FUT)	-69.20	-12%	1.80	11%	182.10	14%	-19.20	-20%	-48.30	-10%	-1.50	-9%	-9.70	-20%	-56.40	-11%	-1.60	-8%
ECHAM-5 REMO (FUT)	-39.30	-7%	1.80	11%	189.90	12%	-9.10	-12%	-31.50	-6%	-1.10	-7%	-2.20	-8%	-39.00	-7%	-1.10	-6%
ECHAM-5 RACMO (FUT)	-41.70	-8%	1.80	11%	192.00	14%	-4.00	-5%	-43.10	-10%	-1.10	-7%	0.90	2%	-48.40	-10%	-1.10	-5%
HadleyCM3 RCA (FUT)	-123.80	-21%	3.10	20%	338.00	23%	-39.60	-37%	-81.50	-17%	-2.70	-16%	-27.40	-46%	-92.30	-17%	-3.00	-14%

Annual quantities of modeled Q using WaSiM-ARU fit well the results of Piras et al. (2014), who applied the same ARU et al. (1990) soil map and the same regional climate model ensemble to drive the hydrological model tRIBS in the RMB. However, the projected WaSiM-ARU as well as WaSiM-RKS ΔQ is somewhat lower compared with the findings of Piras et al. (2014), who found a Q reduction of -17% to -50%, for the future time series.

The WaSiM-RKS results compared to WaSiM-ARU for Q are significantly lower (41-61% in the REF), while outputs for ETR (11-12%) and SWC (24-27%) are higher in the REF. This shows that the soil setup is less important for projected long-term annual changes, but has a major impact on the modeled total quantities of the main hydrological parameters. Depending on the applied climate forcing, SWC is reduced in a range of -7% to -16% for WaSiM-ARU and -5 to -14% for WaSiM-RKS.

T is projected to increase for all months between 1°C to 3°C in FUT. The fluctuation in T of the applied RCM ensemble shows just a minor variation for REF as well as for the FUT period. Little variation is visible between the different RCMs for the months of March, April, and June. It is not astonishing that P (Figure 36), in contrast, shows a much stronger variation in both REF and FUT. The monthly mean P-sum represents well the Mediterranean nature of the catchment with high P-sums in the winter months and very little P-sums in the summer months. The comparison of the REF and FUT time series shows a slight increase of P-sums for the month January, while for the rest of the year; mean P-sums of the RCM ensemble are projected to decline. The low p-values derived from a T-test between REF and FUT indicate a significant climate change impact for the months March ($p<0.002$), April ($p<0.001$), and May ($p<0.001$).

6.2.2 Monthly mean hydrological modeling results and climate change impacts

WaSiM's hydrological outputs based on long-term monthly means were analyzed to investigate inter-annual changes in the catchment. Furthermore, the sensitivity of modeling results was tested, based on the applied soil model setup. WaSiM's long-term monthly mean air temperature (T) and precipitation (P) inputs for the REF and FUT are compared for hydrological years (September-August) in Figure 35 and Figure 36.

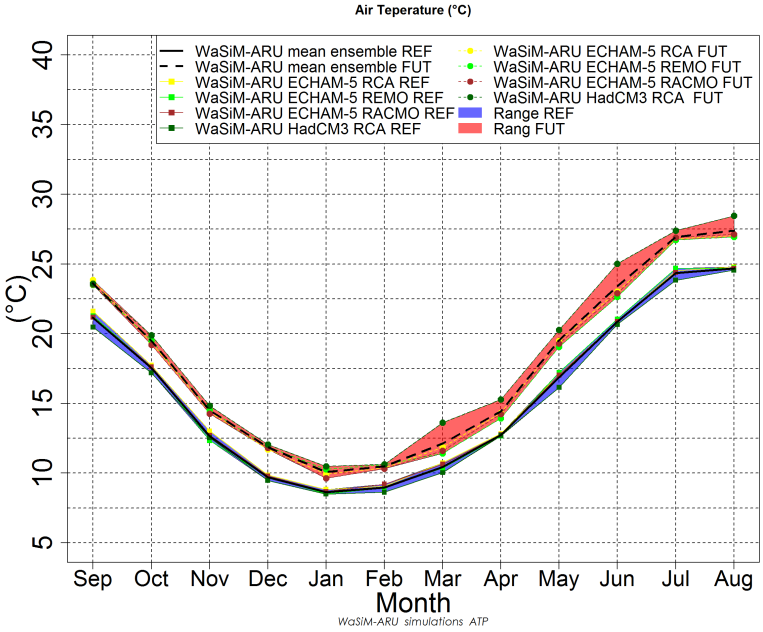

Figure 35: Modeled air temperature (°C) Rio Mannu for the reference (1971-2000) and scenario period (2041-2070).

Spatially distributed WaSiM outputs of P when driven with ECHAM-5 RCA and HadCM3 for the IPCC seasons December, January, February (DJF; winter), March, April, May (MAM; spring), June, July, August (JJA, summer), September, October, November (SON, autumn) are presented in Figure 37 for the REF and FUT. High P sums are present in the mountainous eastern areas of the catchment and lower values are generated in the valley areas, for the FUT as well as for the REF. Only in the summer season no spatial

variability is observable, due to very low P sums in this season. This spatial distribution appears to be plausible.

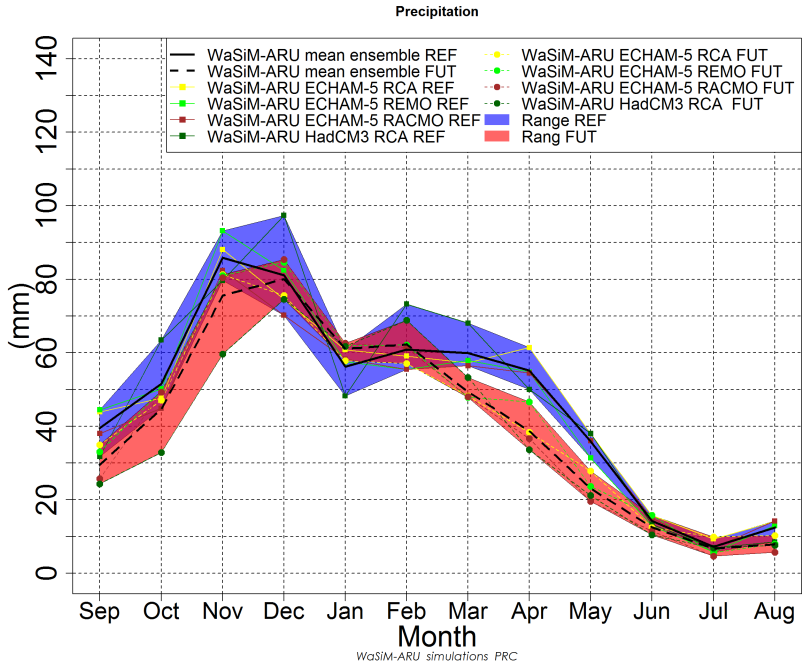

Figure 36: Modeled precipitation (mm) Rio Mannu for the reference (1971-2000) and scenario period (2041-2070).

P sums are projected to decline in the FUT for the spring, summer and autumn seasons and slightly increase in winter. Little deviation (7mm) in the annual total P sums and distribution is visible for both applied RCMs in the REF. In contrast to that is the annual deviation of 47mm highly increased between the two applied RCMs in FUT. The HadCM3 RCA is in comparison to ECHAM-5 RCA the more extreme climate projection since it processes highest P sums in winter and the lowest P sums in summer of all applied RCMS (Appendix 1). Highest deviations of the P sums in the FUT are present in autumn, where HadCM3 RCA is about 30% lower than ECHAM-5 RCA.

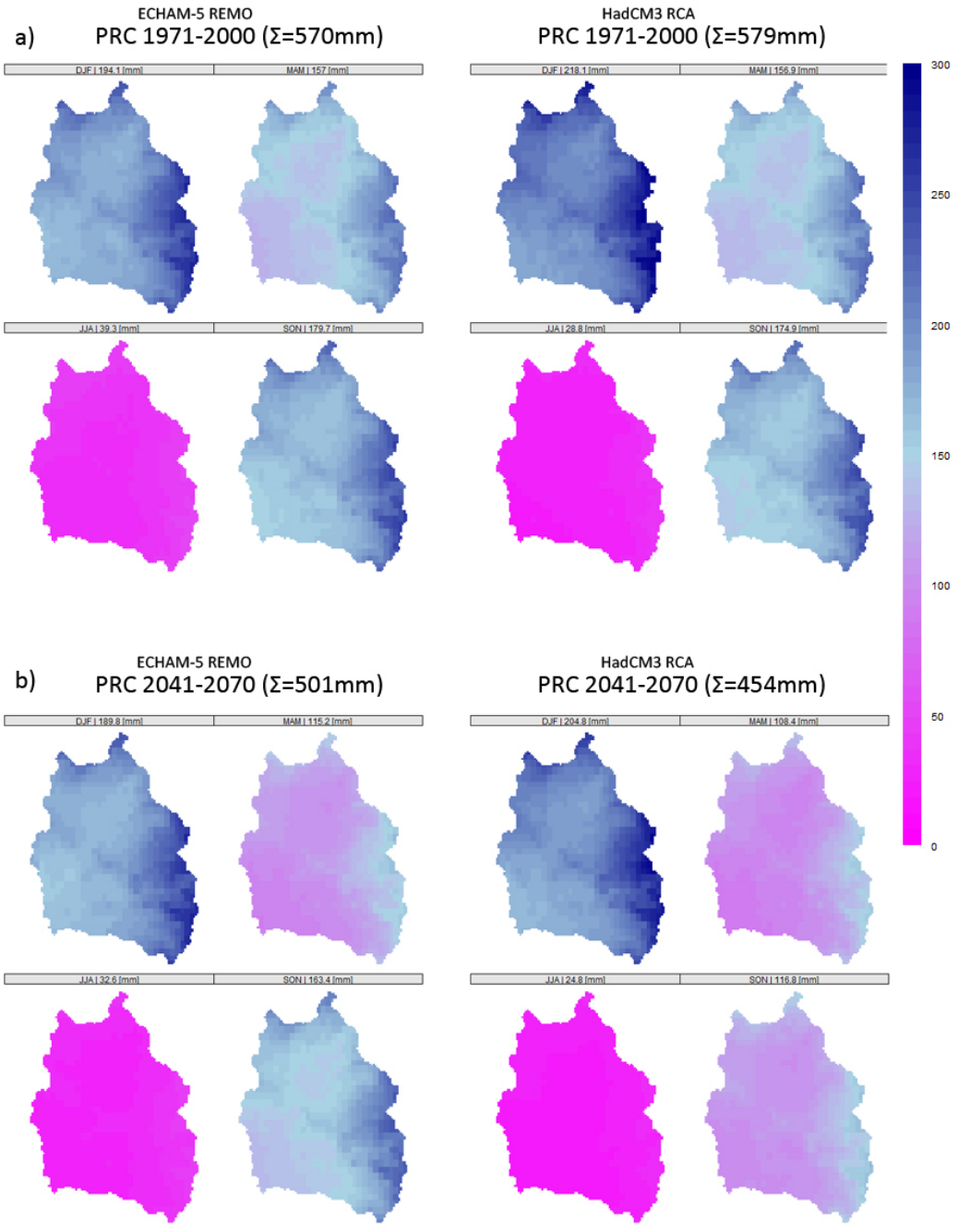

Figure 37: Spatially distributed precipitation of ECHAM-5 RCA and HadCM3 RCA for the IPCC seasons a) REF and b) FUT period.

6.2.3 Standardized Precipitation Index (SPI)

In this study the 6-months SPI (SPI-6) and 12-month SPI (SPI-12) are presented in Figure 38 and Figure 39, respectively. The 4 upper graphs of the figures belong to the REF model precipitation while the lower 4 graphs belong to the precipitation for the FUT of the same climate models. The 6-month SPI compares the precipitation for that period with the same 6 months over the historical record, while the 12-month SPI is the same for 12 consecutive months. The 6-month SPI indicates seasonal to mid-term trends in precipitation. It is supposed to be very effective in showing precipitation over distinct seasons. It is especially good to analyze drought seasons in the very important wet Mediterranean season (October to March). Its information can be associated with the beginning of anomalous stream flows and reservoir levels. The 12-month SPI long-term reflect precipitation patterns. It tends to gravitate towards zero unless a distinct wet or dry trend is taking place (WMO 2012). The behavior can be good observed by comparing the REF of Figure 38 and Figure 39. White space (zero) is much more present in the SPI-12 than in the SPI-6. In both figures the FUT is characterized by a higher number of extremely dry events (value = -2). The ECHAM-5 REMO (ERE) precipitation also shows a higher number of extreme wet events in the FUT. Severely dry and extremely dry periods increase from March to July SPI-6 FUT. Those projection results reveal that the wet seasons (October to March (SPI-6 March)) and the wet to growing seasons (January to July (SPI-6 July)) will be more effected by severe droughts in the future. In those seasons all climate models precipitation inputs point in the same direction of change. Furthermore FUT results show that drought events are supposed to last longer than in the REF. This can be very clearly observed from the HadCM3 RCA (HCH) FUT precipitation where extremely dry conditions projected for the years 2051-2053 and 2064-2067. The latter period is also confirmed in parts (2064-2066) by the ECHAM-5 driven RCMs. The SPI-6 change to more severe droughts in the FUT is significantly confirmed by the SPI-12 increase in Figure 39 and by the increased number of months with severely dry conditions in Figure 40. In the long-term SPI-12 one can find patterns for example in 2055 that are present in all ECHAM-5 driven RCMs. This indicates that the applied RCM does have less importance when observing the long-term drought trends. For the short term analysis on the other hand the RCM seems to have a larger influence and one can see that the drought patterns of the ECHM-5 driven RCM are much more diverse.

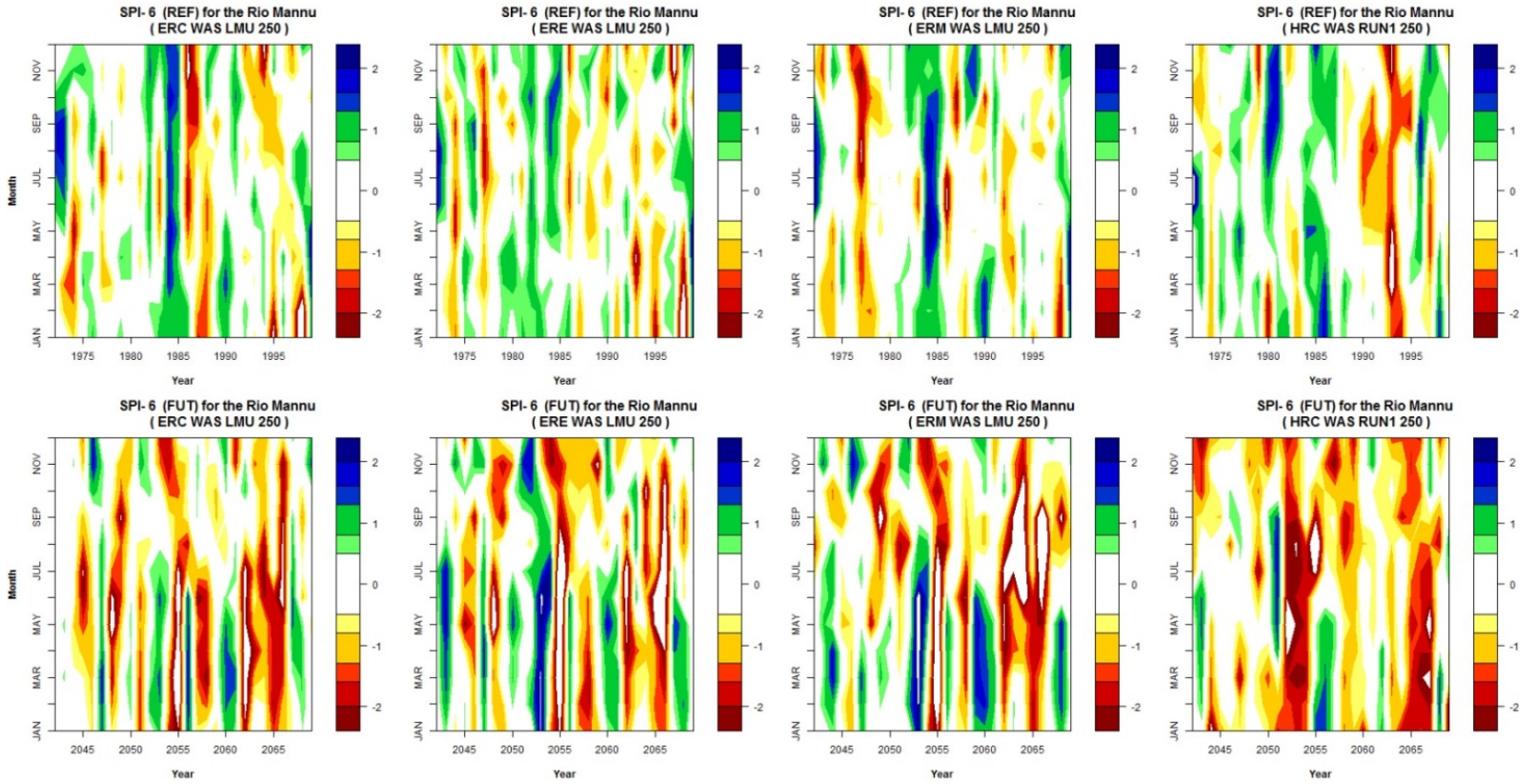

Figure 38: Standardized Precipitation Index for the 06 month interval (SPI 6)of the hydrological modeling inputs for the FUT and REF. RCM abbreviation: ERC = ECHAM-5 RCA, ERE = ECHAM-5 REMo, ERM = ECHAM-5 RACMO and HRC = HadleyCM3 RCA. The values represent: +2 and above = (extremely wet), +1.5 to + 1.99 = very wet, +1.0 to +1.49 = moderately wet, -0.99 to +0.99 = near normal, -1.0 to -1.49 = moderately dry, -1.5 to - 1.99 = severely dry and -2 and less = (extremely dry).

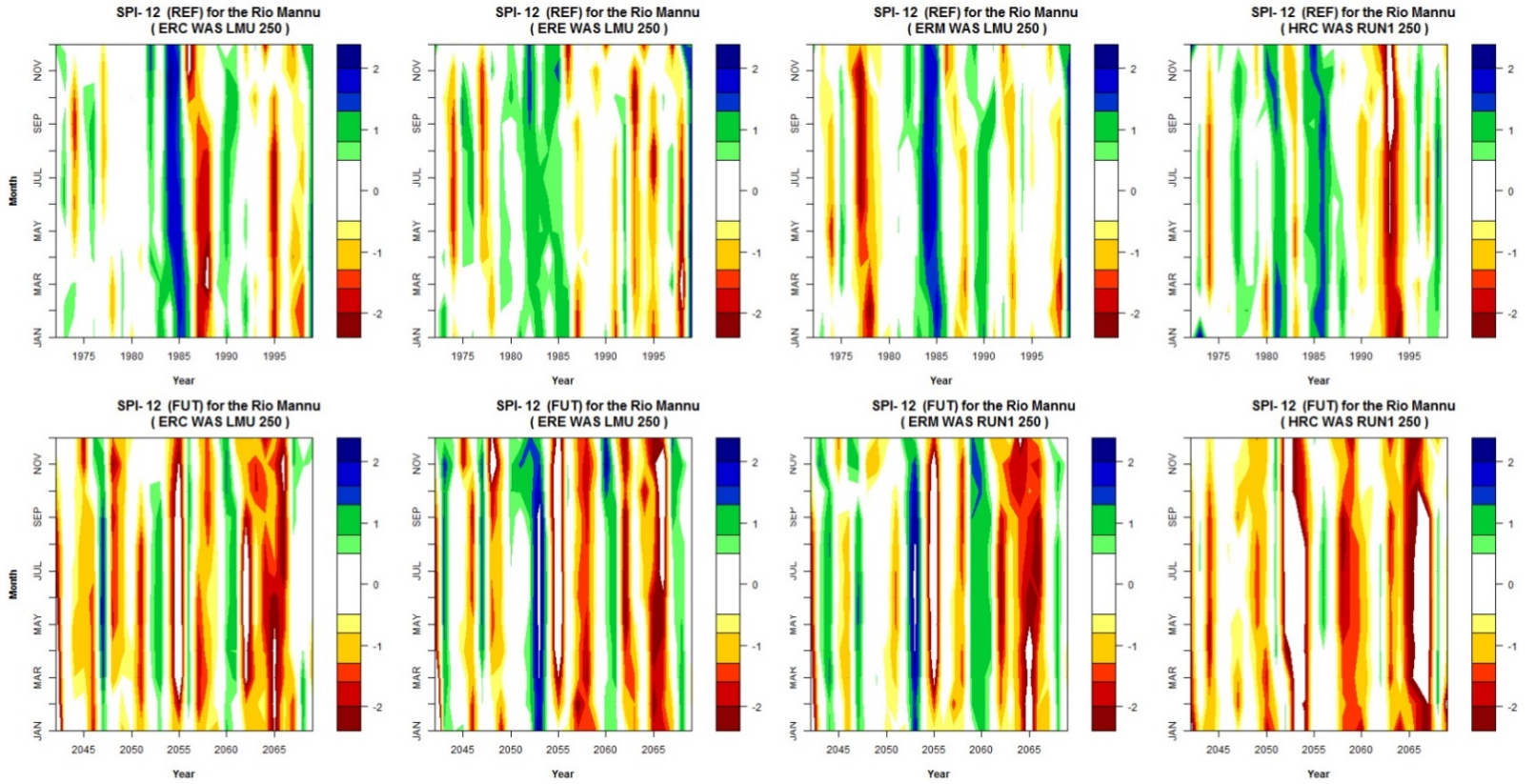

Figure 39: Standardized Precipitation Index for the 12 month interval (SPI 12) of the hydrological modeling for the FUT and REF. RCM abbreviation: ERC = ECHAM-5 RCA, ERE = ECHAM-5 REMo, ERM = ECHAM-5 RACMO and HRC = HadleyCM3 RCA. The values represent: +2 and above = (extremely wet), +1.5 to + 1.99 = very wet, +1.0 to +1.49 = moderately wet, -0.99 to +0.99 = near normal, -1.0 to -1.49 = moderately dry, -1.5 to -1.99 = severely dry and -2 and less = (extremely dry).

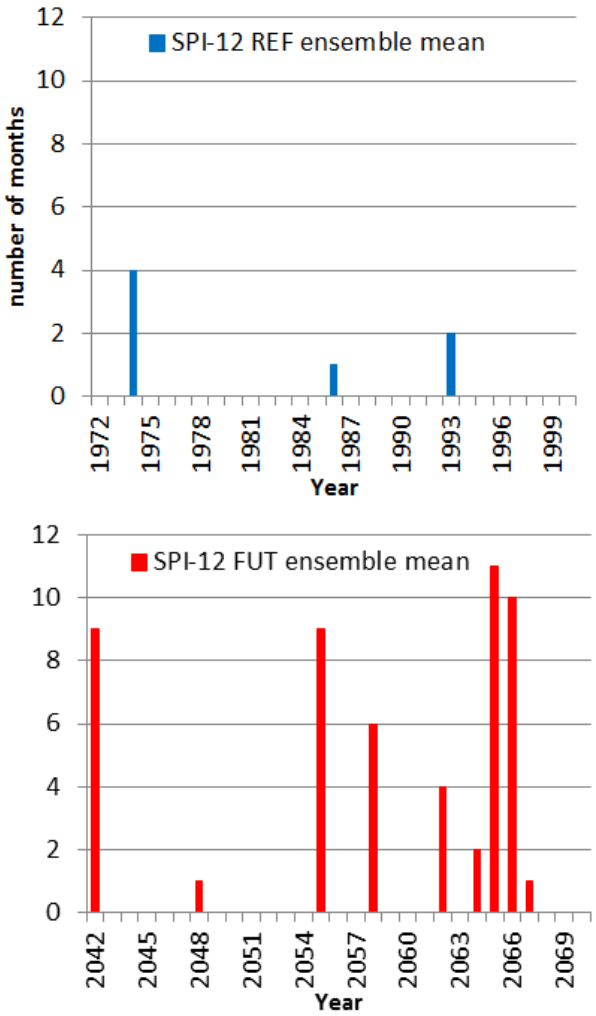

Figure 40: Number of months per year with Standardized Precipitation Index - 12 below -1.5 (severely dry) in the REF (blue) and FUT (red).

6.2.4 Soil moisture content

WaSiM-ARU and WaSiM-RKS soil moisture outputs are presented in Figure 41 and Figure 42 respectively on a long-term monthly mean basis for the REF and FUT. The SWC outputs of WaSiM-ARU reveal a plausible distribution within the course of the year, with low values in the dry summer season and a peak SWC in the winter season in February.

A very narrow range of hydrological model outputs is visible in autumn for all applied RCMs of the REF. The widest range on the other hand can be observed in the spring season in May. The range of model outputs of the FUT is for most months of the year higher compared to the REF. The long-term total ensemble mean is reduced in the FUT for all months of the year. SWC is, except for ECHAM-5 RACMO in January, reduced for all months of the year. WaSiM-ARU processes the highest reduction of SWC in the FUT when driven with HadCM3 RCA and lowest reduction when driven with ECHAM-5 RACMO. The strongest SWC reduction of the mean hydrological model ensemble can be observed in May.

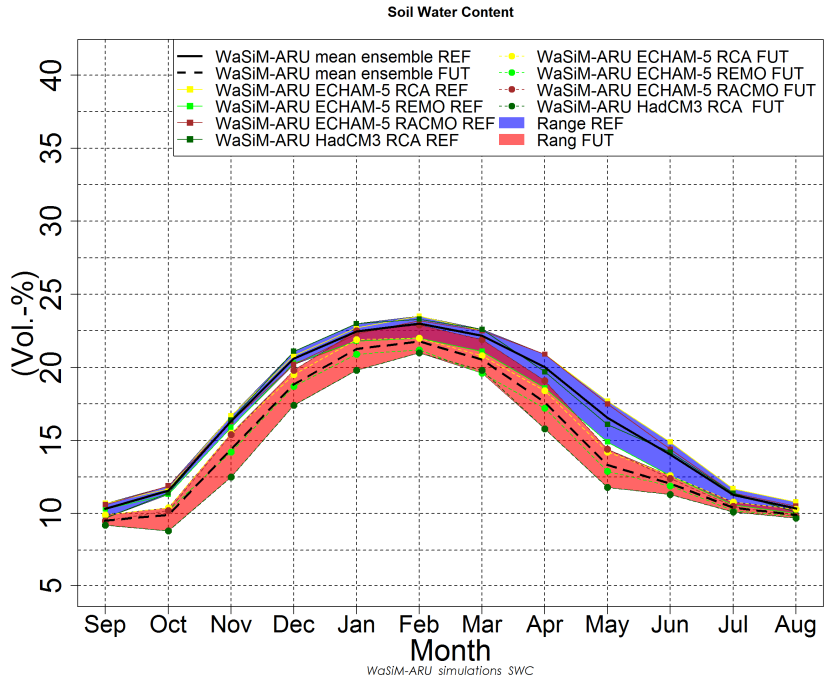

Figure 41: WaSiM-ARU outputs of long-term monthly mean SWC for the REF and FUT.

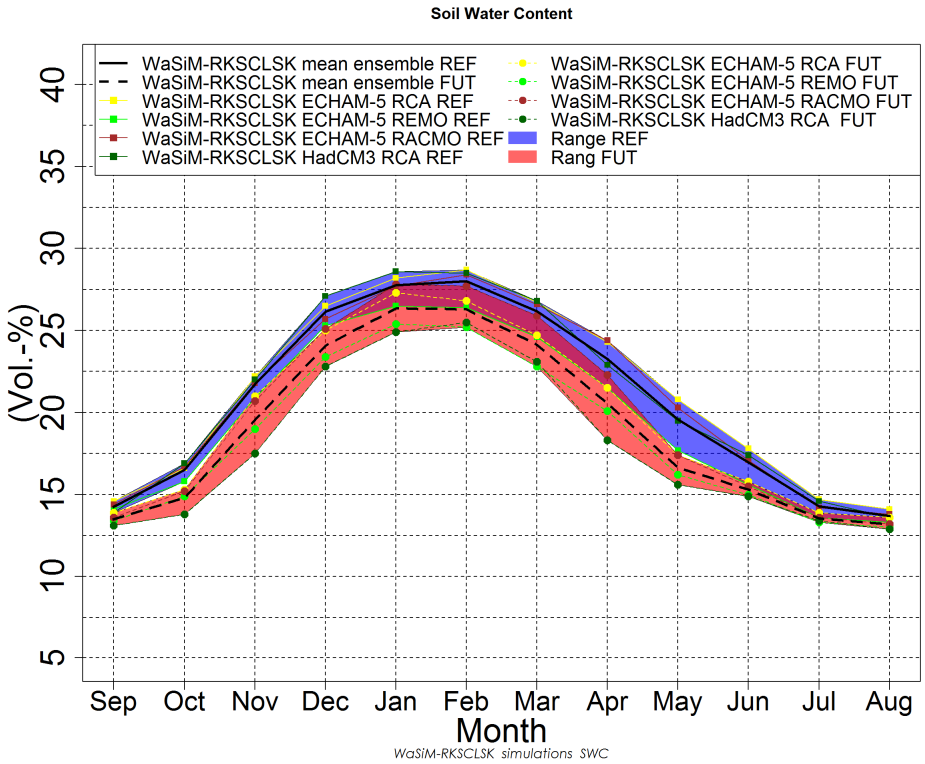

Figure 42: WaSiM-RKS outputs of long-term monthly mean SWC for the REF and FUT.

This behavior is the same for the WaSiM-RKS. The outline of the produced SWC outputs of both soil model setup look very similar over the course of the year. The major difference of the WaSiM-RKS setup is that SWC outputs are significantly higher compared to the WaSiM-ARU setup for the REF as well as for the FUT (Figure 34, Figure 41 & Figure 42).

While SWC outputs of the WaSiM-RKS are never below 12.9 vol.-% for all applied RCMs, very low SWC values below 10 vol.-% are processed in the summer season with WaSiM-RKS for the REF as well as for the FUT. The deviation of absolute SWC outputs between the two soil model setups is even higher in the wet winter season; here WaSiM RKS is processing about a 5 vol.-% higher SWC per month.

Table 10 reports the relative SWC changes of WaSiM-ARU and WaSiM-RKS for all applied RCMs as well as for the ensemble mean between REF and FUT. Except for January, relative soil moisture change in the future is negative for all SWC outputs of WaSiM-ARU

& -RKS. For January a slight increased trend of 1% is visible for ECHAM-5 RACMO applied to WaSiM-ARU and no change is processed when applied to WaSiM-RKS. The SWC outputs of both soil model setups show a significant mean ensemble reduction of -10% or more for the months of October, November, and April to May.

Table 10: Comparison of relative SWC change % of the WaSiM-ARU and WaSiM-RKS modeling outputs; Note the green upward arrow = 25 - 100%, green upward arrow tip = 1 - 24%, orange sideward arrow = 0%, downward red arrow tip = -1 - -24% and downward red arrow = -25 - -100% change.

	Change of atc. soil water content SWC (%)									
	ECHAM-5 RCA		ECHAM-5 REMO		ECHAM-5 RACMO		HadCM3-RCA		Ensemble Mean	
	ARU	RKS	ARU	RKS	ARU	RKS	ARU	RKS	ARU	RKS
Sep	▼ -7	▼ -5	▼ -8	▼ -5	▼ -10	▼ -6	▼ -5	▼ -6	▼ -8	▼ -6
Oct	▼ -11	▼ -8	▼ -10	▼ -6	▼ -14	▼ -9	▼ -23	▼ -18	▼ -15	▼ -10
Nov	▼ -7	▼ -5	▼ -11	▼ -9	▼ -6	▼ -5	▼ -24	▼ -20	▼ -12	▼ -10
Dec	▼ -6	▼ -6	▼ -8	▼ -8	▼ -2	▼ -2	▼ -18	▼ -16	▼ -9	▼ -8
Jan	▼ -4	▼ -3	▼ -4	▼ -4	▲ 1	⇨ 0	▼ -14	▼ -13	▼ -5	▼ -5
Feb	▼ -6	▼ -7	▼ -4	▼ -5	▼ -1	▼ -2	▼ -10	▼ -11	▼ -5	▼ -6
Mar	▼ -8	▼ -7	▼ -7	▼ -7	▼ -3	▼ -3	▼ -12	▼ -14	▼ -8	▼ -8
Apr	▼ -12	▼ -12	▼ -8	▼ -7	▼ -9	▼ -9	▼ -20	▼ -20	▼ -12	▼ -12
May	▼ -20	▼ -16	▼ -13	▼ -8	▼ -18	▼ -14	⇩ -27	▼ -20	▼ -20	▼ -15
Jun	▼ -15	▼ -11	▼ -6	▼ -4	▼ -14	▼ -9	▼ -20	▼ -14	▼ -14	▼ -10
Jul	▼ -8	▼ -5	▼ -4	▼ -2	▼ -8	▼ -4	▼ -11	▼ -8	▼ -8	▼ -5
Aug	▼ -5	▼ -4	▼ -2	▼ -2	▼ -7	▼ -4	▼ -4	▼ -5	▼ -5	▼ -4
	⇧ 25	▲ 1	⇨ 0	▼ -1	⇩ -25					

Spatially distributed long-term mean SWC outputs of WaSiM-ARU and WaSiM-RKS for the IPCC season are reported in Figure 43 and Figure 44, respectively. Distinct north-western and southeastern SWC pattern can be observed in the processed maps, which strongly follow the classified soil texture classes of the applied ARU soil texture map (Figure 18 a)). For the winter and spring season high soil SWC values are present in the northwestern pattern. This pattern is classified as pure clay in the ARU soil texture map. The southeastern pattern, which is mainly classified as sandy-loam in the ARU map, is characterized by much lower SWC. As soon as the SWC is dropping in the catchment, in the dry summer and autumn season, those very distinct patterns fade. This is especially true in the FUT projection, where the distributed pattern appear more random.

Figure 45 reports the relative climate change impact based on the relative SWC change (CSM) of the hydrological ensemble using WaSiM-ARU. CSM also follows patterns but

not as distinct as for the absolute SWC in Figure 43. The modeling results reveal a strong relative SWC reduction in the northwestern lower elevated areas for all applied RCMs and over all seasons. The strongest relative SWC reduction can be observed in the spring and autumn season, where SWC only reaches 91-81% and 90-80%, respectively of the REF level. A slight increase of soil moisture is visible for the all RCMs in the mountainous southeastern part of the RMB. Pixel covered by urban and pasture land are affected strongest by the SWC reduction.

WaSiM-RKS SWC and CSM results are presented in Figure 44 and Figure 46, respectively. The spatial distribution of SWC using WaSiM-RKS also follows strongly the applied soil texture map and its associated soil model parametrization (Figure 24), but this is less obvious compared to WaSiM-ARU. In general pixel in the WaSiM-RKS SWC outputs maps hold higher SWC compared to WaSiM-RKS. Low SWC values below 22 are present only in more elevated areas in winter and spring season. The summer and autumn season are characterized by significantly lower SWC values and pixel covered by urban and pasture land use hold the lowest SWC similar to WaSiM-ARU. In the FUT projection SWC is reduced for all IPCC seasons and all applied RCMs. The WaSiM-RKS CMS results are presented in Figure 46.

The strongest relative SWC reduction can be observed in the spring and autumn season, where SWC only reaches 93-82% and 94-86%, respectively of the REF level. While WaSiM-RKS CSM results reveal for all RCMs the strongest CC impact for the spring season, WaSiM-ARU driven with ECH-5 REMO, -RACMO and HadCM3 RCA projects this for the autumn season.

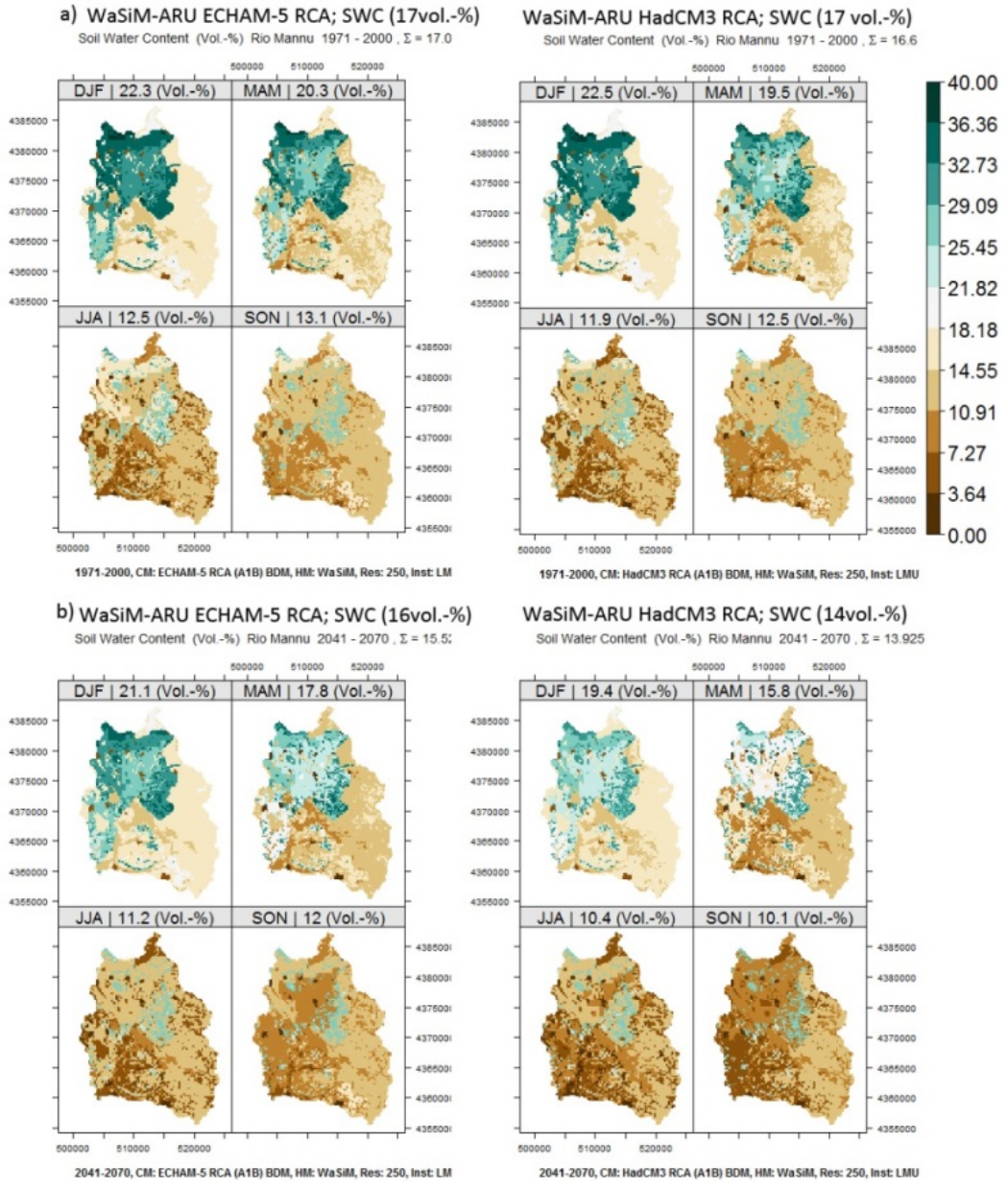

Figure 43: Spatially distributed soil water content (SWC) WaSiM-ARU driven with ECHAM-5 RCA and HadCM3 RCA for the IPCC seasons a) in the REF and b) in the FUT period.

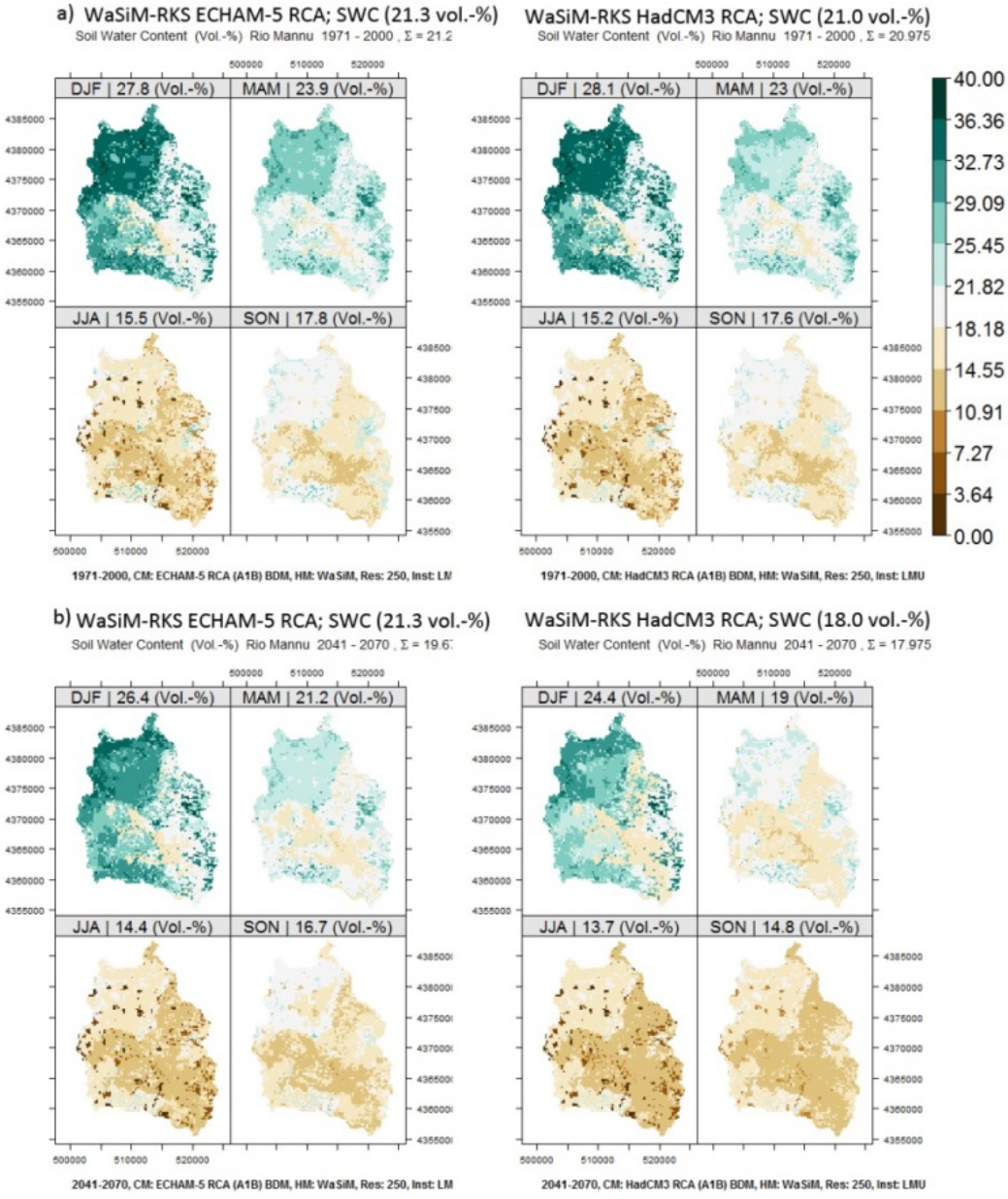

Figure 44: Spatially distributed soil water content (SWC) WaSiM-RKS driven with ECHAM-5 RCA and HadCM3 RCA for the IPCC season in the s a) REF and b) FUT period.

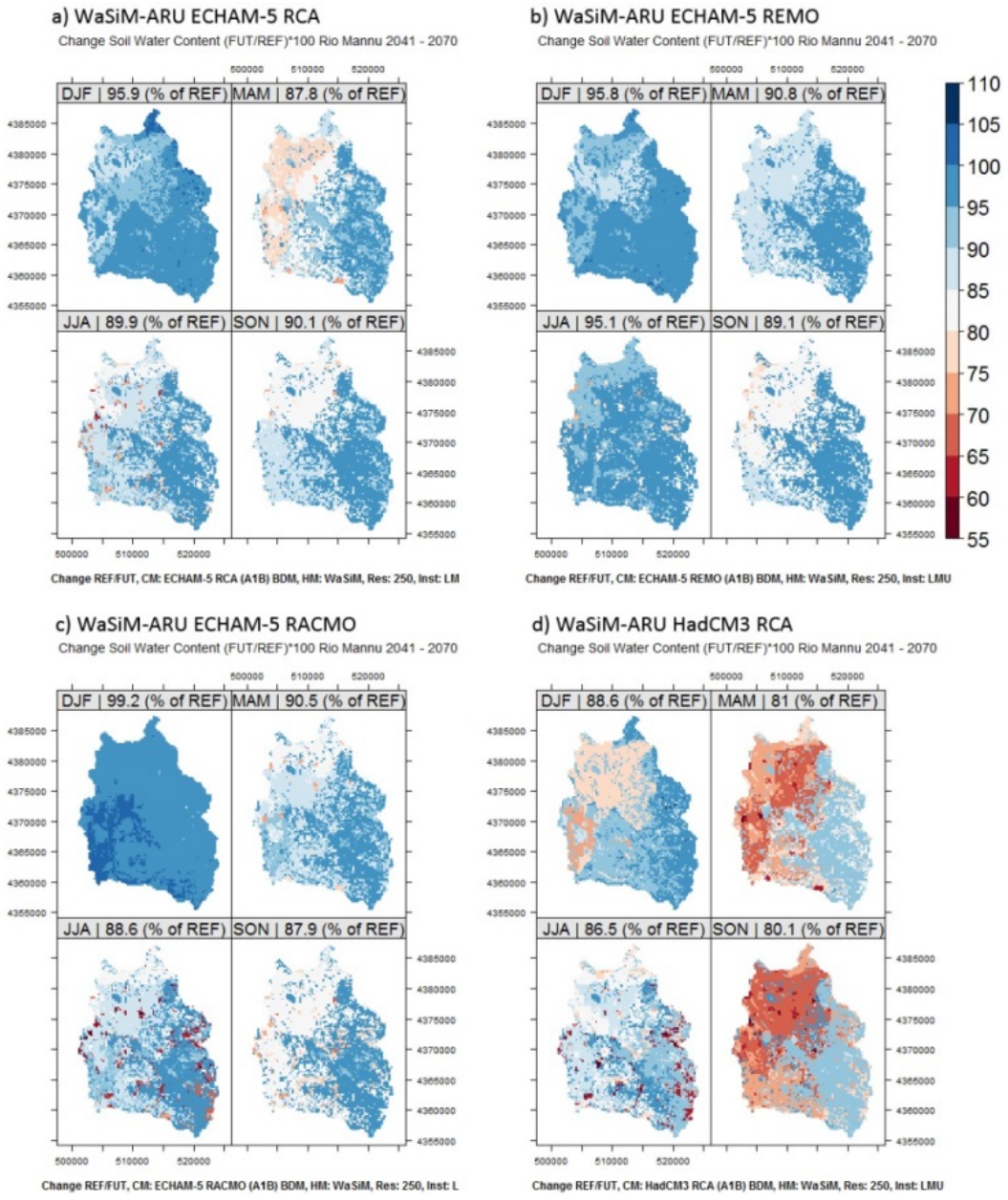

Figure 45: Spatially distributed soil moisture change [%] (CSM) using WaSiM-ARU driven with a) ECHAM-5 RCA, b) ECHAM-5 REMO, c) ECHAM-5 RACMO and d) HadCM3 RCA for the IPCC seasons of the FUT period.

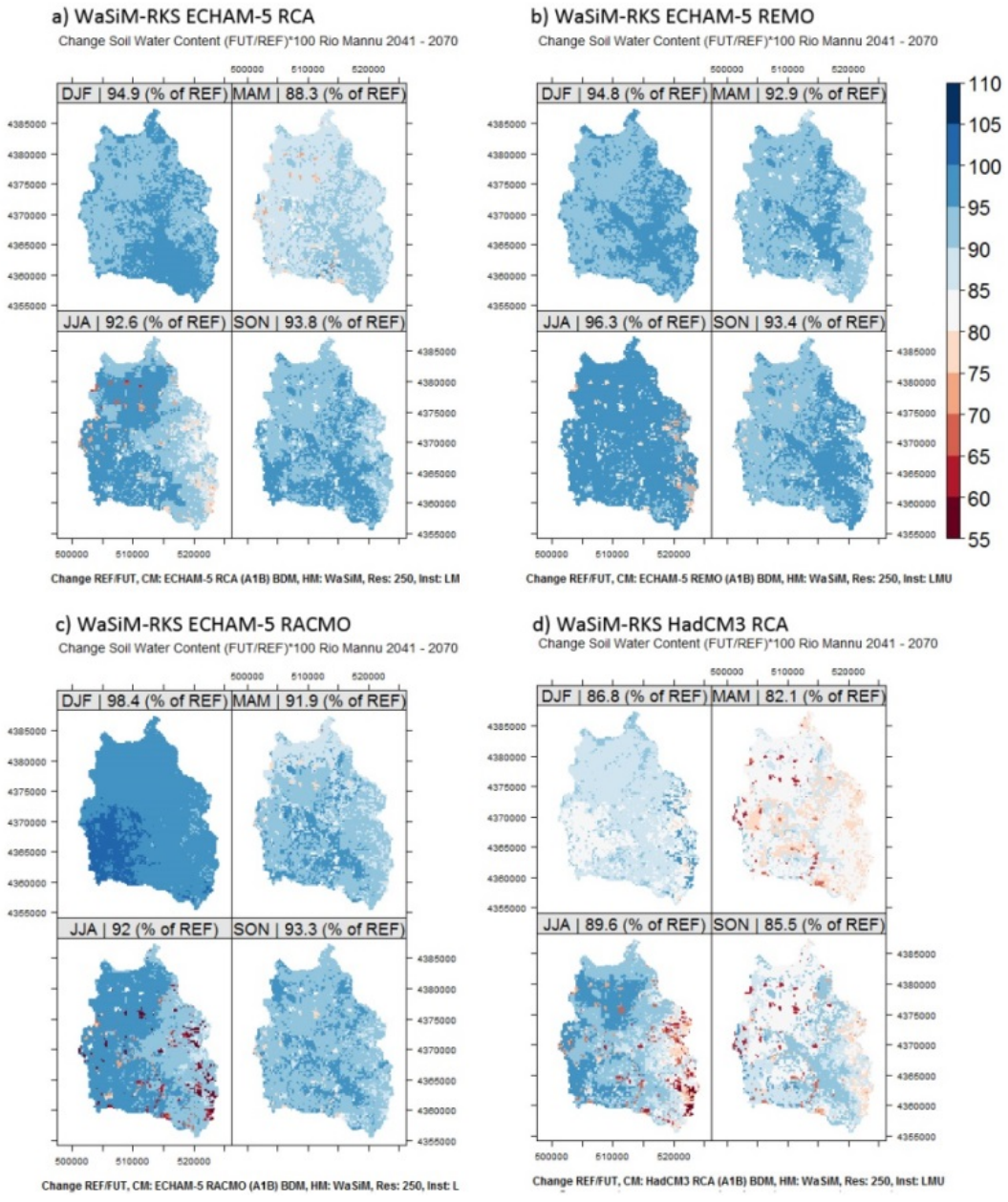

Figure 46: Spatially distributed soil moisture change (CSM) using WaSiM-RKS driven with a) ECHAM-5 RCA, b) ECHAM-5 REMO, c) ECHAM-5 RACMO and d) HadCM3 RCA for the IPCC seasons of the FUT period.

6.3 Actual evapotranspiration

In this section WaSiM's actual Evapotranspiration (ETR) outputs are compared for the ARU soil setup and the RKS soil setup and hydrological climate change impacts are assessed.

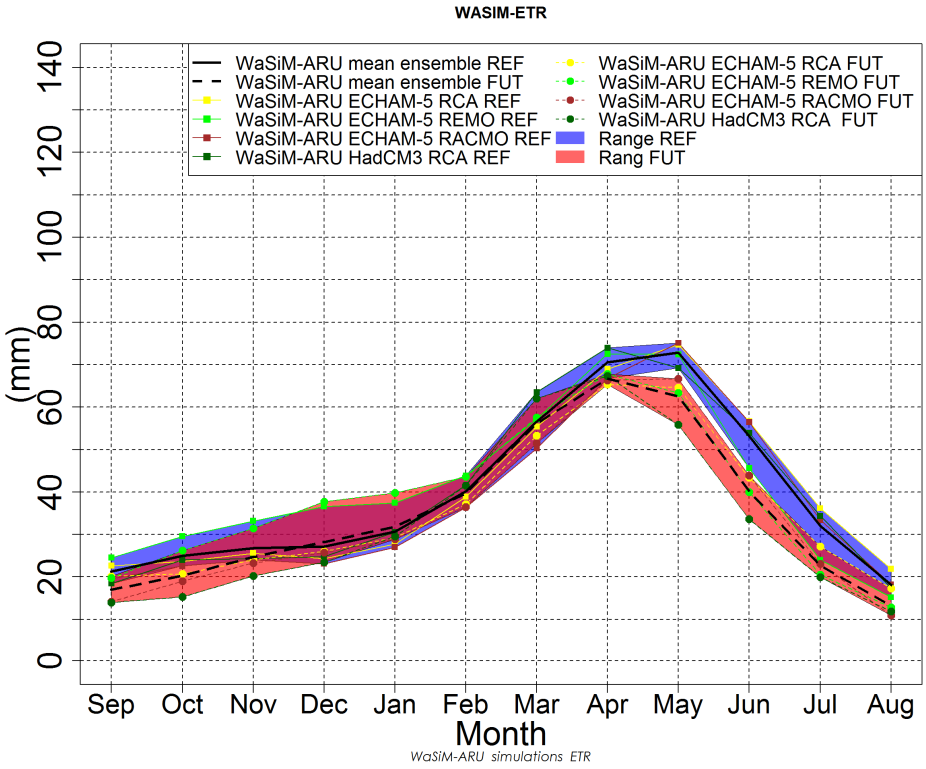

Figure 47: WaSiM-ARU outputs of long-term monthly mean ETR for the REF and FUT.

The ETR outputs using WaSiM-ARU driven with the climate ensemble for the REF and FUT are presented in Figure 47. The distribution of ETR outputs with in the course of the year shows lowest values in the summer months July to Octobert, peak values in the spring season March to June and moderate slowly increasing values from November to February. Deviations of the WaSiM-ARU model outputs are strongly dependent on the applied RCM. The range is not smiliar over the course of the year. The highest long-term mean deviations can be observed in December and January for the REF and FUT, while the range is smallest for the REF in May it is smallest in the FUT in April. This is indicating a higher confidence of the modelling outputs for those months.

The distribution of long-term monthly mean ETR results shows a very similar extent for the WaSiM-ARU and the WaSiM-RKS soil model setup (compare Figure 47 & Figure 48), but the ETR rates of the WaSiM-RKS setup are about 5-10mm higher per month compared to the WaSi-ARU setup.

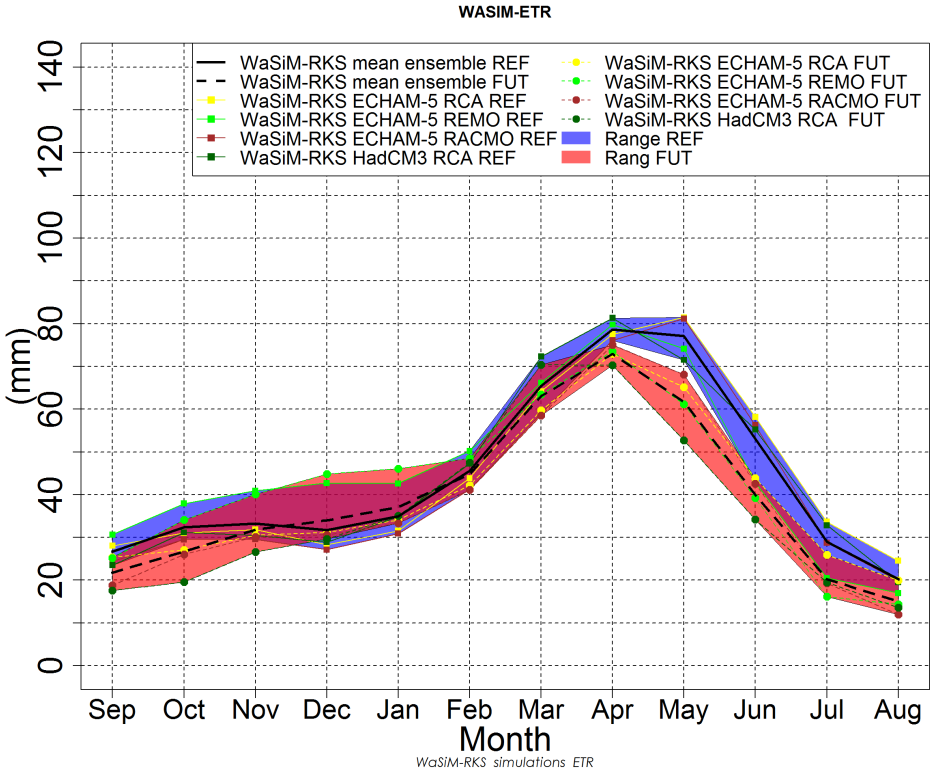

Figure 48: WaSiM-RKS outputs of long-term monthly mean ETR for the REF and FUT.

Also the peak month of the REF changed from May in the WaSiM-ARU to April in the WaSiM-RKS. Both WaSiM setups produce reduced ETR rates for the months of May to October, slightly increased rates for December and January and slightly decreased rates for November and February to April, when driven with the FUT climate projections. Table 11 reports the relative changes of WaSiM-Aru & WaSiM-RKS ETR outputs between the REF and FUT period for all applies RCMs. The model results reveal the strongest quantitative mean reduction of ETR in May (WaSiM-RKS; –15mm) and in June (WaSiM-ARU; -13mm). The relative change, presented in Table 11 on the other hand is strongest in July (-28% WaSiM-ARU & -30% WaSiM-RKS) for both model setups but this is repre-

senting a less strong total reduction of – 9mm for both hydrological model setups. WaSiM-RKS driven with HadCM3 RCA produces the lowest ETR rates of all applied FUT climate forcings over the year and for most of the month, with a relative reduction of up to 41% in July. The applied ECHAM-5 driven RCMs produce less negative ETR outputs. HadCM3 RCA produces an interesting deviation between the two soil setups for the months of December and January. Only WaSiM-ARU in combination with HadCM3 RCA shows a reduction of ETR for those months.

Table 11: Comparison relative ETR change in % of the WaSiM-ARU and WaSiM-RKS model outputs; Note the green upward arrow= 25 - 100%, green upward arrow tip = 1 - 24%, orange sideward arrow = 0%, downward red arrow tip = -1 - -24% and downward red arrow = -25 - -100% change.

	Change of act. Evapotranspiration ETR (%)									
	ECHAM-5 RCA		ECHAM-5 REMO		ECHAM-5 RACMO		HadCM3-RCA		Ensemble Mean	
	ARU	RKS	ARU	RKS	ARU	RKS	ARU	RKS	ARU	RKS
Sep	-11	-10	-19	-18	-27	-23	-24	-25	-20	-19
Oct	-13	-13	-11	-10	-16	-12	-36	-37	-19	-18
Nov	-6	-4	-5	-2	-3	2	-17	-13	-8	-4
Dec	7	10	3	5	11	13	-6	3	4	8
Jan	5	8	6	8	7	8	-3	1	4	6
Feb	-5	-4	-1	-3	0	0	0	0	-2	-2
Mar	-4	-7	1	-4	2	-1	-2	-3	-1	-4
Apr	-5	-6	-7	-8	-1	-1	-9	-14	-6	-7
May	-14	-20	-13	-18	-11	-16	-19	-26	-14	-20
Jun	-23	-25	-12	-9	-22	-24	-38	-38	-24	-24
Jul	-25	-23	-15	-21	-31	-33	-42	-41	-28	-30
Aug	-21	-19	-15	-15	-40	-40	-32	-30	-27	-26
	25	1	0	-1	-25					

Spatially distributed ETR modeling results of WaSiM driven with ECHAM-5 RCA and HaCNC3 RCA are presented in Figure 49 (WaSiM-ARU) and Figure 50 (WaSiM-RKS) for the IPCC seasons. The seasonal absolute results of WaSiM of both applied soil model setups follow roughly the ETR distribution presented in Figure 47 and & Figure 48. The ETR result maps of WaSiM-ARU show a similar spatial pattern like for the SWC, with high ETR rates (spring 241-276mm) in the northwestern part of basin and lower rates in the southeastern part (spring 172-206mm).

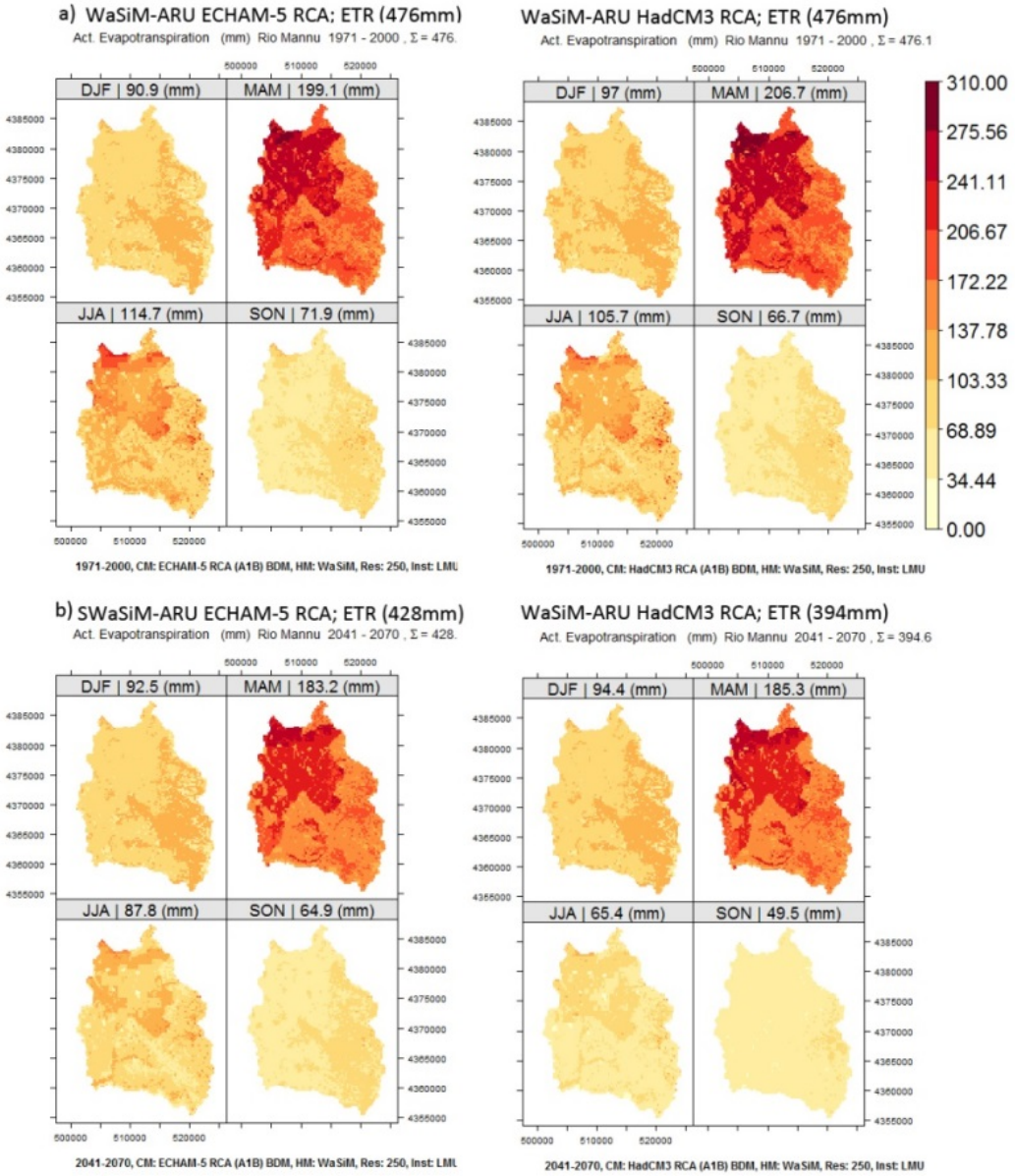

Figure 49: Modeled spatially distributed evapotranspiration outputs of WaSiM-ARU driven with ECHAM-5 RCA and HadCM3 RCA for the IPCC seasons in the a) REF and b) FUT period.

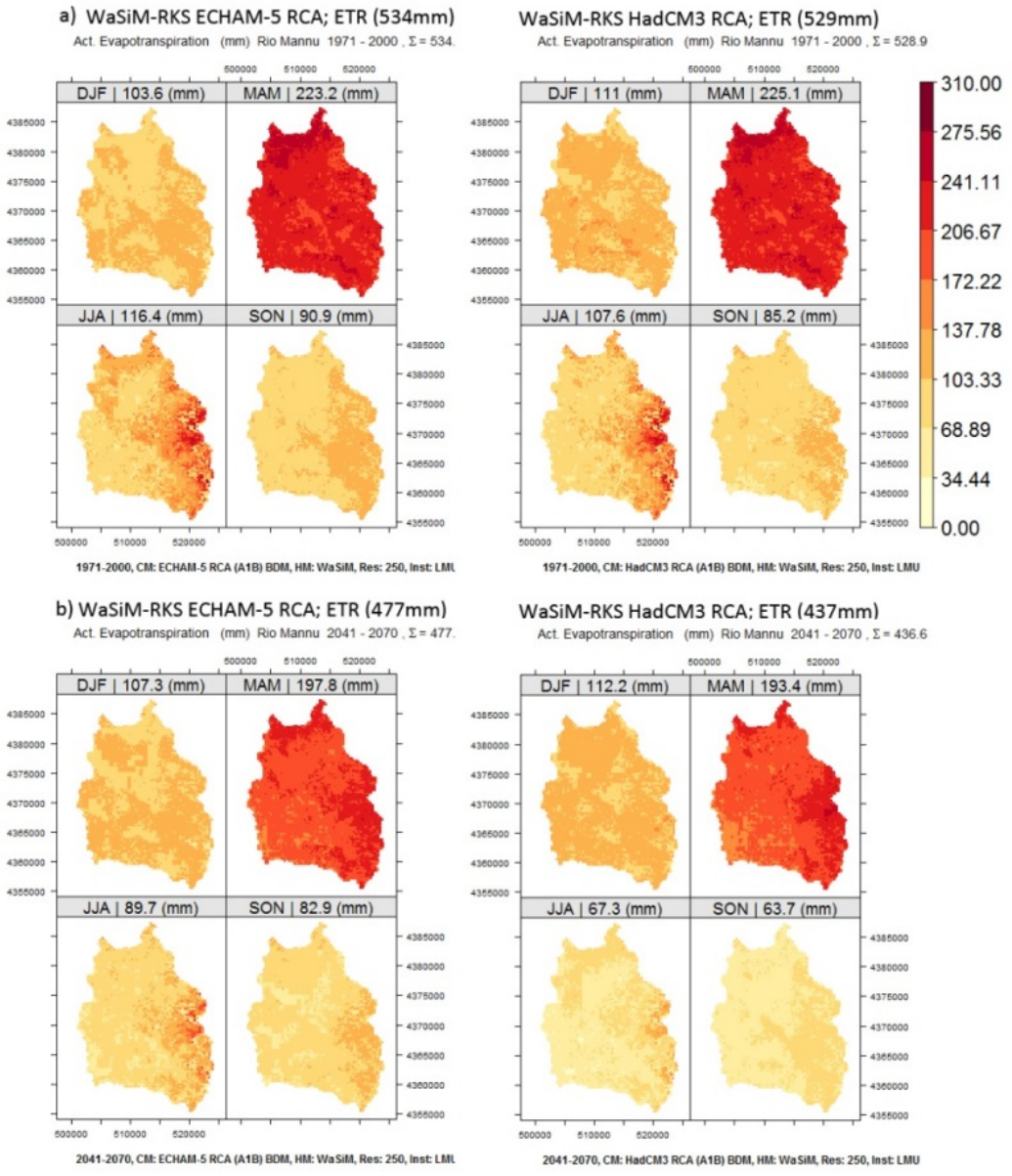

Figure 50: Modeled spatially distributed evapotranspiration outputs of WaSiM-RKS driven with ECHAM-5 RCA and HadCM3 RCA for the IPCC seasons in the a) REF and b) FUT period.

One can also observe for those outputs that the high values in the spring and summer season strongly follow the applied soil texture map. The WaSiM-RKS results on the other hand do not show this distinct distribution. ETR rates of WaSiM-RKS are more homogenously distributed in the basin and show a range of 206-241mm for most pixels in spring

season. WaSiM-RKS processes higher ETR rates compared to WaSiM-ARU in all seasons and for all applied RCMs.

Table 12: a) Difference of ETI results depending on the applied soil model. Comparison of WaSiM-ARU and WaSiM-RKS. b) Climate change impact on ETI results in the FUT by using WaSiM-ARU. c) Climate change impact on ETI results in the FUT by using WaSiM-RKS.

a)	**Difference of mean ETI results between WASIM-ARU and WaSiM-RKS**							
IPCC	ECHAM-5 RCA		ECHAM-5 REMO		ECHAM-5 RACMO		HadCM3 RCA	
SEASON	REF	FUT	REF	FUT	REF	FUT	REF	FUT
DJF	0.11	0.12	0.11	0.1	0.11	0.12	0.12	0.13
MAM	0.09	0.06	0.07	0.04	0.09	0.07	0.07	0.04
JJA	0.01	0.01	0.01	0	0	0	0.01	0.01
SON	0.09	0.08	0.09	0.07	0.09	0.1	0.1	0.06

b)				
IPCC	**Climate change impact on mean ETI results (FUT-REF) using WaSiM-ARU**			
SEASON	ECHAM-5 RCA	ECHAM-5 REMO	ECHAM-5 RACMO	HadCM3 RCA
DJF	-0.04	-0.04	-0.03	-0.08
MAM	-0.11	-0.09	-0.1	-0.16
JJA	-0.07	-0.03	-0.07	-0.09
SON	-0.05	-0.05	-0.06	-0.12

c)				
IPCC	**Climate change impact on mean ETI results (FUT-REF) using WaSiM-RKS**			
SEASON	ECHAM-5 RCA	ECHAM-5 REMO	ECHAM-5 RACMO	HadCM3 RCA
DJF	-0.03	-0.05	-0.02	-0.07
MAM	-0.14	-0.12	-0.12	-0.19
JJA	-0.07	-0.02	-0.07	-0.09
SON	-0.06	-0.07	-0.05	-0.16

The evapotranspiration index (ETI), which is the ETR share in the potential Evapotranspiration (ETP), is presented in Figure 51 (WaSiM-ARU) and Figure 52 (WaSiM-RKS). The ETI results of the hydrological ensemble for both WaSiM-ARU and WaSiM-RKS reveal maximum values in winter, moderate values in spring, low values in autumn and a minimum in summer. ETI is a drought stress indicator (Jasper et al. 2006) and defined by the thresholds 0.3 (severe) and 0.5 (moderate) of plant available water as a critical level.

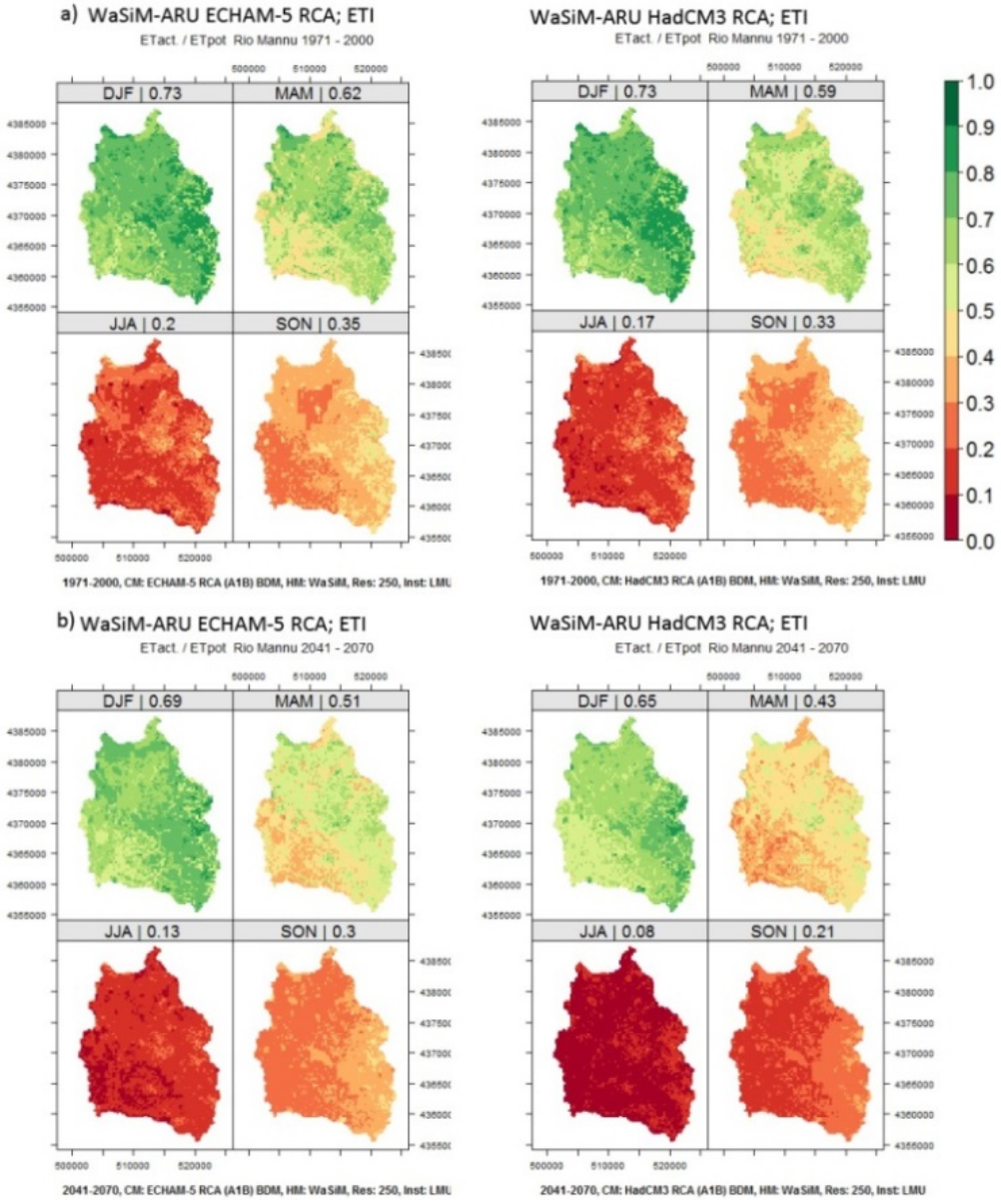

Figure 51: Modeled spatially distributed evapotranspiration index (ETI) outputs of WaSiM-ARU driven with ECHAM-5 RCA and HadCM3 RCA for the IPCC seasons in the a) REF and b) FUT period.

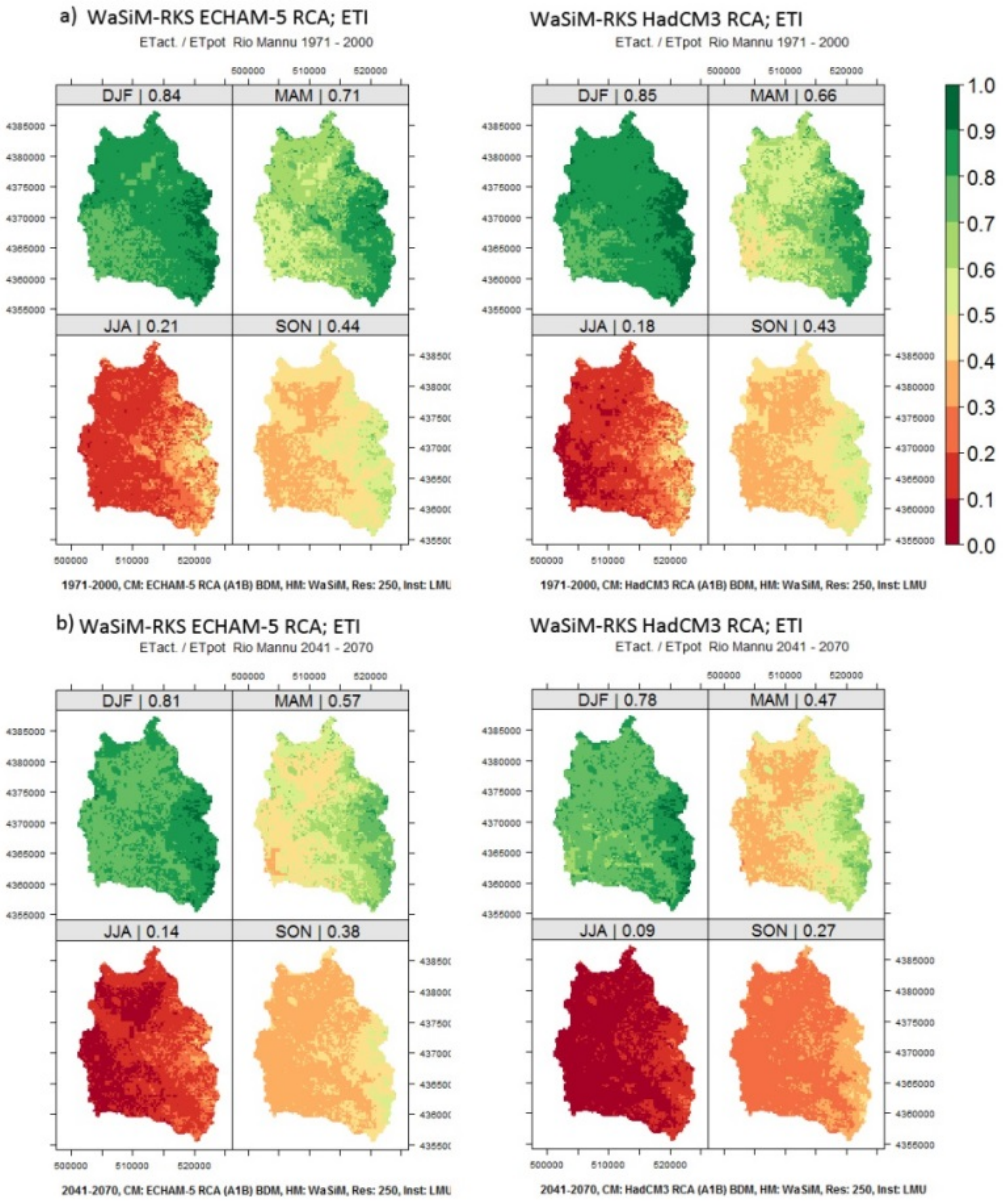

Figure 52: Modeled spatially distributed evapotranspiration index (ETI) output of WaSiM-RKS driven with ECHAM-5 RCA and HadCM3 RCA for the IPCC seasons in the a) REF and b) FUT period.

The FUT hydrological results reveal a decreasing ETI trend for all months of the year, with a maximum decrease in spring (-0.11 to -0.19) and minimum decrease in winter (-0.02 to -0.08) for both soil model setups (Table 12). The number of pixels having values below the critical 0.5 threshold is especially in the future spring season increased.

The absolute differences of WaSiM-ARU and WaSiM-RKS ETI results in winter are higher (+/- 0.11 to 0.13) than the CC impact signal (-0.04 to -0.08). This reveals that the soil model setup has a higher impact on the total modeling results than the applied RCM in winter when it's wet and minor impact in the dry summer season.

6.3.1 Ground water recharge

WaSiM's spatially distributed ground water recharge (GWR) results are shown in Figure 53 (WaSiM-ARU) and Figure 54 (WaSiM-RKS). GWR is positive for both soil model setups in the REF for the wet winter season and in the spring season and negative in the summer and autumn seasons. The catchment average positive GWR is for both WaSiM setups very similar. The patterns of increased GWR on the other hand are very different between the two WaSiM setups. The result maps of the WaSiM-RKS setup show increased GWR in a large area in the southwestern part of the catchment. The area of increased GWR in the WaSiM-ARU setup is smaller, but the total GWR rate for those pixels is higher. This is also true for the GWR reduction, which are caused by capillary uptake. The WaSiM-ARU results are in limited areas more extreme than the WaSiM-RKS. GWR is declining for all IPCC season and for all model setups in the FUT. The WaSiM-RKS results show a negative annual GWR for the REF when driven with ECHAM5 RCA and for all future scenarios. The WaSiM-ARU results on the other hand are positive for all REF and FUT scenarios. The relative change of GWR is strongly dependent on the applied soil texture information. For the applied HadCM3 RCA projection WaSiM-RKS results indicate a strong decrease in the northwestern part of the catchment, which is not present in the WaSiM-ARU GWR results. This result alone indicates that a precise future groundwater resource projection is highly dependent on high quality soil texture information.

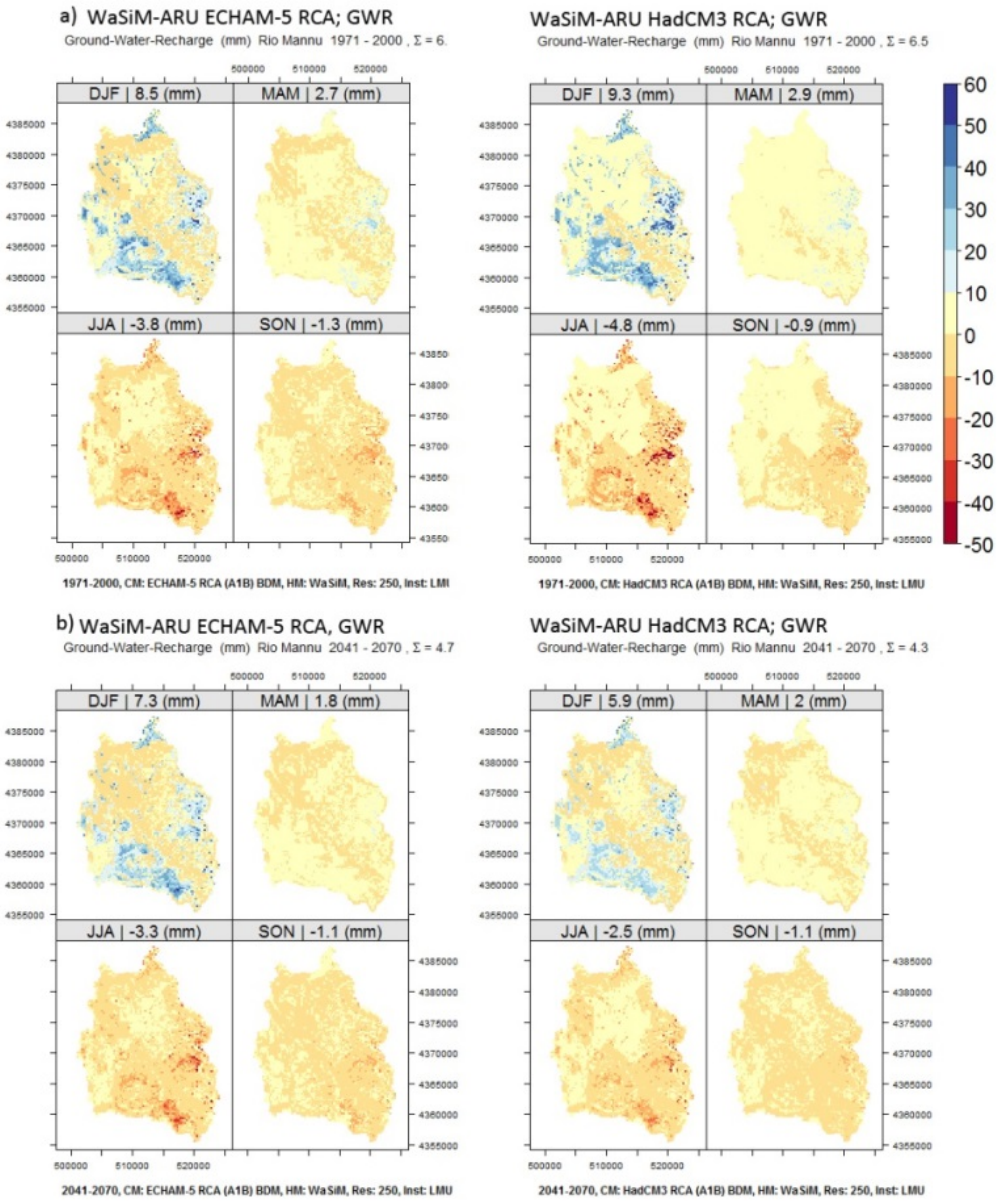

Figure 53: Modeled spatially distributed ground water recharge (GWR) using WaSiM-ARU driven with ECHAM-5 RCA and HadCM3 RCA for the IPCC seasons in the a) REF and b) FUT period.

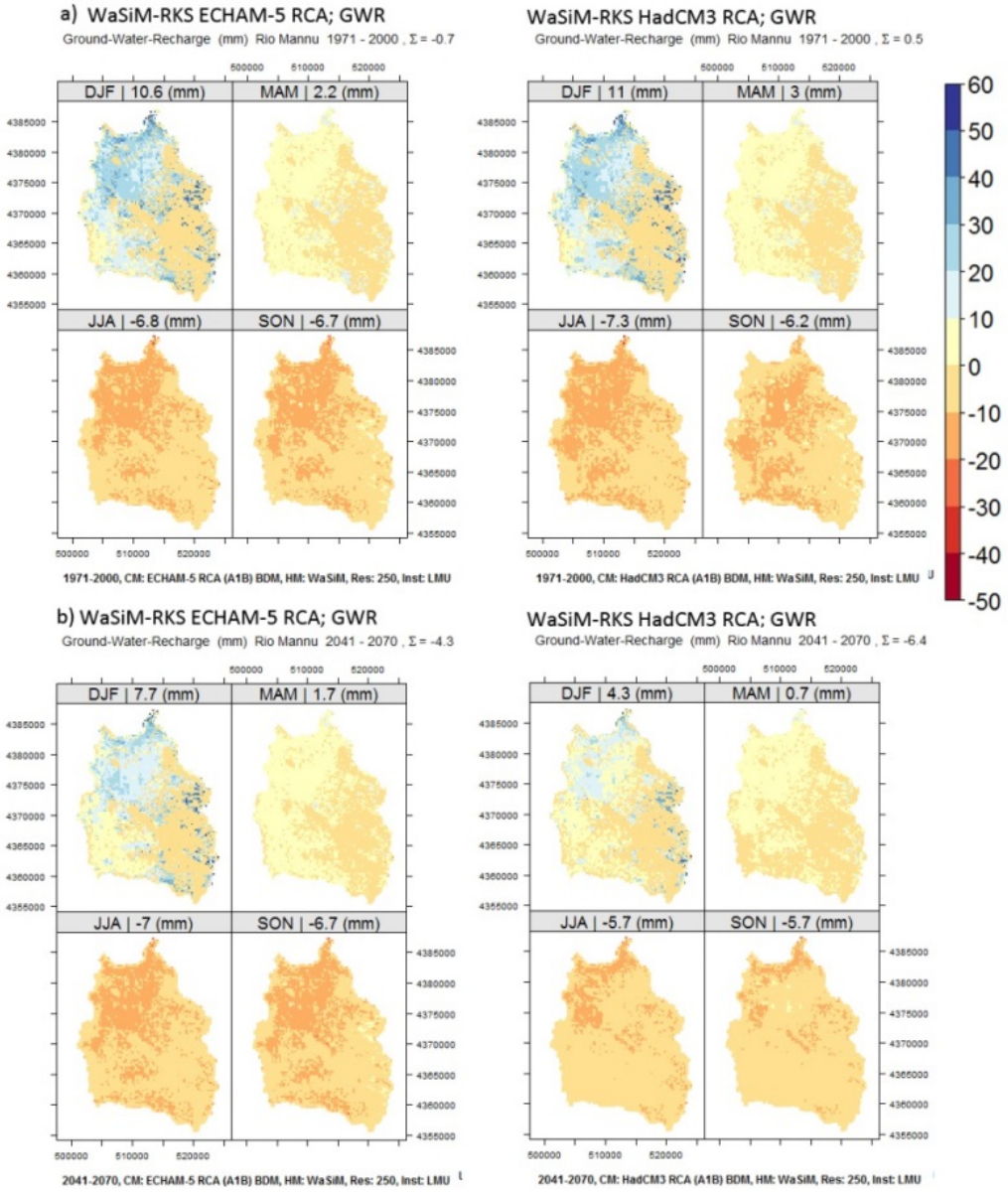

Figure 54: Modeled spatially distributed ground water recharge (GWR) using WaSiM-RKS driven with ECHAM-5 RCA and HadCM3 RCA for the IPCC seasons in the a) REF and b) FUT period.

6.3.2 Climate change impact on discharge and runoff

The long-term monthly mean Q modeling outputs of WaSiM-ARU are reported in Figure 55. All applied climate forcings of the REF are resulting in a modeled peak flow of Q in December. A second peak of Q in February in the results is visible for applied Hadley CM3 climate forcing. The modeling outputs reveal low flow conditions, with Q rates under 0.5 m^3/s, for the months June to September for all applied climate forcings in the REF and FUT. The ensemble average mean Q modeling results of the future scenarios reveal, a decrease of Q rates except for January and February for all months the year. The slightly increasing Q in January and February fit well the slight increase of precipitation rates in the FUT for those months.

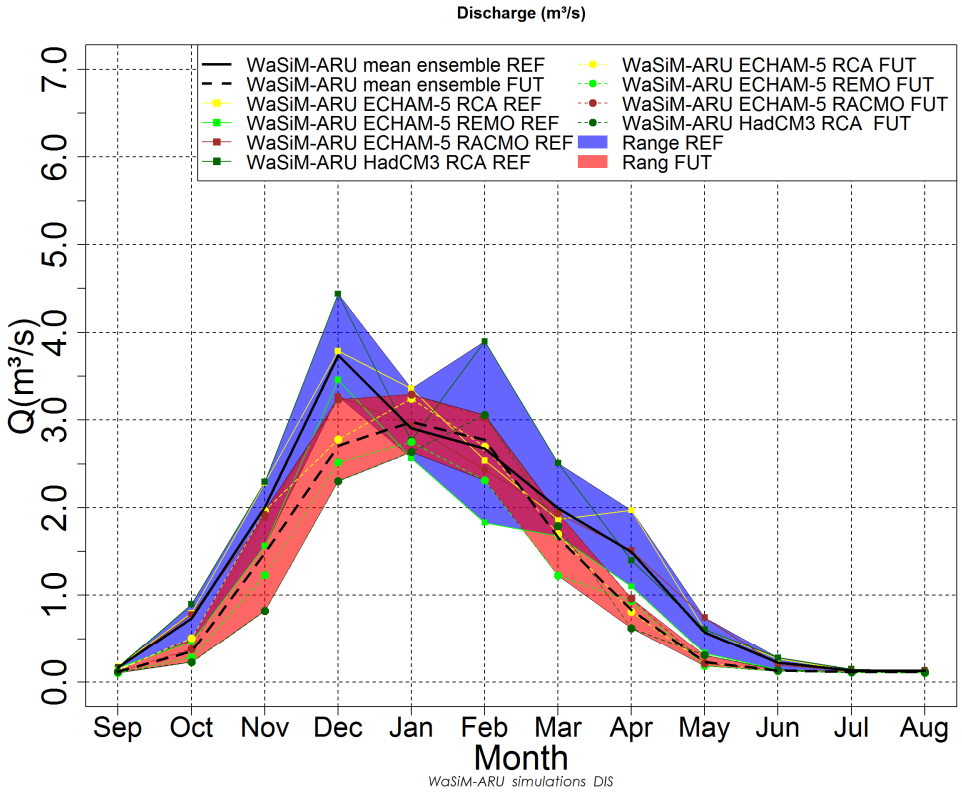

Figure 55: Long-term monthly mean Q outputs of the WaSiM-ARU.

A significant reduction of Q in the FUT outputs is visible for the months of April and May for all applied climate model forcings. A significant mean Q reduction is also noticeable

for the months of November and December, but this is only true for 3 of the for applied climate model forcings. WaSiM generates with the applied ECHAM-5 RACMO forcing, very similar Q outputs in the REF and FUT for those two months. The range of WaSiM model outputs show a much stronger deviation for the REF compared to the FUT from February to May. A similar difference in model output variation is visible for the WaSiM-RKS Q outputs in those months Figure 56.

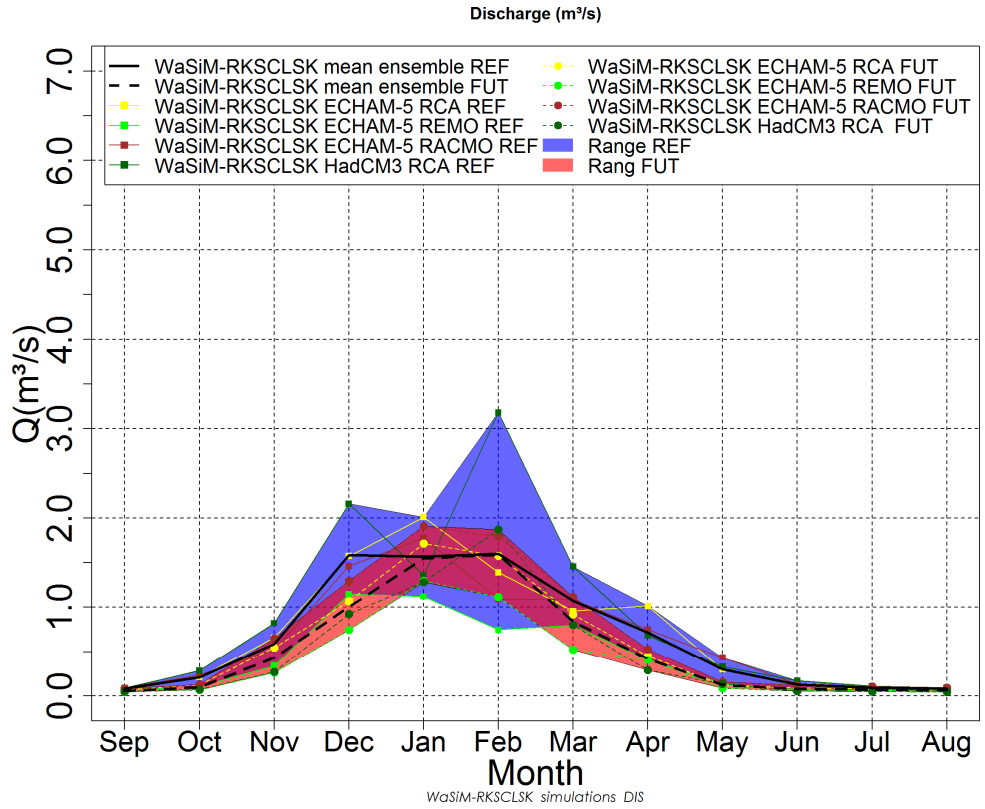

Figure 56: Long-term monthly mean Q outputs of the WaSiM-RKS.

But the WaSiM-RKS Q outputs reveal also strong differences compared to the WaSiM-ARU outputs. The Q outputs of WaSiM-RKS are strongly reduced for all months of the year compared to the WaSiM-ARU setup. Especially the mean peak flow in December is significantly lower compared to WaSiM-ARU. The mean Q peak of the WaSiM-RKS setup has nearly the same values of about 1.5 m^3/s for the months December to February in

the REF, this is about 2 m^3/s less than the long-term mean flow of the WaSiM-ARU setup in December.

The mean hydrological ensemble Q outputs reveal also for the WaSiM-RKS setup a reduction of Q for all months except for January and February. Since the WaSiM-RKS setup produces less total discharge, the reduction of the total quantities is less compared to the WaSiM-Aru setup. The model outputs reveal still a strong reduction in Figure 56 in the spring and autumn seasons, but the reduction appears not as dramatically as in the WaSiM-ARU results in Figure 55.

Table 13 reports the relative changes of the FUT modeling outputs compared to the REF for both hydrological modeling setups. For most months and applied climate forcings model results of WaSiM-ARU and WaSiM-RKS point into the same direction of change. The hydrological modeling outputs of both soil model outputs differ in the direction of change only for the ECHAM-5 RACMO climate forcing for the months of March, July, and August and for the ECHAM-5 REMO for the month of March. All modeling outputs project a decreasing Q trend for the months of September, October, December, May, and July with a strong negative gradient in October and May. The increasing mean ensemble Q trend for February is only visible for the ECHAM-5 driven RCMs, while the Hadley driven RCM shows a decreasing Q trend for all months of the year. Very interesting hydrological modeling results are visible for January, since modeling results of two different climate forcings show a negative trend (ECHAM-5 RCA & HADCM3-RCA) and two show a positive trend (ECHAM-5 REMO & ECHAM-5 RACMO).

The results reveal that the trend of the modeled future Q outputs are mainly controlled by the applied climate forcings, the strength of this trend on the other hand is for many months strongly influenced by the soil model parametrization. This is visible for example for the ECHAM-5 RCA in January, for the ECHAM-5 REMO for the months of January, June, and August, for the ECHAM-5 RACMO for the months of September, November, December, February, and June and for the HadCM3-RCA for the months of September, February, March, May to August, with deviations of 10% or more.

Table 13: Comparison of relative Q change in % of the WaSiM-ARU and WaSiM-RKS model outputs; Note the green upward arrow = 50 - 100%, green upward arrow tip = 1 - 49%, orange sideward arrow = 0%, downward red arrow tip = -1 - -49% and downward red arrow =-50 - -100% change.

	Change of discharge Q (%)									
	ECHAM-5 RCA		ECHAM-5 REMO		ECHAM-5 RACMO		HadCM3-RCA		Ensemble Mean	
	ARU	RKS	ARU	RKS	ARU	RKS	ARU	RKS	ARU	RKS
Sep	▼ -24	▼ -20	▼ -35	▼ -32	▼ -29	▼ -9	▼ -27	▼ -47	▼ -29	▼ -27
Oct	▼ -36	▼ -42	▼ -38	▼ -38	⇩ -52	▼ -46	⇩ -75	⇩ -75	⇩ -50	⇩ -50
Nov	▼ -14	▼ -17	▼ -21	▼ -23	▲ 2	▲ 23	⇩ -64	⇩ -67	▼ -24	▼ -21
Dec	▼ -27	▼ -32	▼ -27	▼ -35	▼ -1	▼ -11	▼ -48	⇩ -57	▼ -26	▼ -34
Jan	▼ -3	▼ -15	▲ 7	▲ 16	▲ 12	▲ 7	▼ -5	▼ -5	▲ 3	▲ 1
Feb	▲ 6	▲ 14	▲ 27	▲ 49	▲ 24	⇧ 65	▼ -22	▼ -41	▲ 9	▲ 22
Mar	▼ -9	▼ -4	▼ -27	▼ -34	⇨ 0	▲ 3	▼ -29	▼ -45	▼ -16	▼ -20
Apr	⇩ -59	⇩ -55	▼ -15	⇨ 0	▼ -36	▼ -30	⇩ -55	⇩ -58	▼ -41	▼ -36
May	⇩ -65	⇩ -59	▼ -44	▼ -38	⇩ -72	⇩ -63	▼ -49	⇩ -59	⇩ -58	⇩ -55
Jun	⇩ -50	▼ -41	▼ -15	▼ -25	▼ -32	▼ -10	⇩ -50	⇩ -68	▼ -37	▼ -36
Jul	▼ -9	▼ -23	▼ -13	▼ -20	▼ -5	▲ 5	▼ -25	⇩ -56	▼ -13	▼ -24
Aug	▼ -7	▼ -26	▼ -9	▼ -19	▼ -13	▲ 3	▼ -16	⇩ -53	▼ -11	▼ -24
	⇧ 50	▲ 1	⇨ 0	▼ -1	⇩ -50					

The spatially distributed runoff results are presented in Appendix 7 (WaSiM-ARU) and Appendix 8 (WaSiM-RKS), respectively. In the WaSiM-ARU setup runoff is generated in the southeastern part of the catchment, where sandy loam soil textures are present. The northwestern part which is covered by clay textures generates low runoff for all IPCC seasons (compare Figure 18). One can clearly recognize the unnatural appearing patterns of the ARU soil texture map in the runoff grids, for the wet season. The spatial patterns of the WaSiM-RKS setup appear differently. The runoff generation is in general lower, especially in the spring and autumn season. This lower runoff generation has a strong link to the high SWC of the generated by WaSiM-RKS. The runoff generation is low at locations where SWC is high in both soil model setups. The runoff generation seems to be improved in the WaSiM-RKS, based on the calibration results in section 3.8; Figure 33; Figure 34 and based on the more natural appearing spatial runoff patterns in Appendix 8.

Finally the number of low flow days (LF), days of dry conditions (DC), days of mid-range flows (MRF), moist conditions (MC) and high flows (HF) have been calculated (5.4.2).

Figure 57 compares those days of classified flow conditions for the REF and FUT as well as for the two applied WaSiM-ARU and WaSiM-RKS version. Furthermore the mean trend of an increase or decrease of each flow class is reported.

In the REF nearly no trend is visible for the number of high flow days, a decreasing trend is visible for the days with MC and MRF and the number is increasing for days with DC and LF. The highest decreasing trend is visible for the WaSiM-ARU results in the MRF, while for WaSiM-RKS days with MC decrease most. LF are increasing mostly in both WaSiM setups with a trend of +1.1 days/per year (WaSiM-ARU) to +2.2 days/per year (WaSiM-RKS) in the REF and those trends are strongly increasing to +3.9 days/per year (WaSiM-ARU) and +6.07 days per years (WaSiM-RKS) in the FUT.

The results of both WaSiM versions show a decreasing trend for all the other flow conditions in the FUT. Note that the trend of both WaSiM setups is reversed for the DC class in the FUT. The gain of days in the LF class using the WaSiM-ARU results in the FUT comes mainly from the DC, and the MDF classes, while they mainly come from MC and the MDF classes when using the WaSiM-RKS results. The two applied soil model setups are deviating especially in the extreme flows.

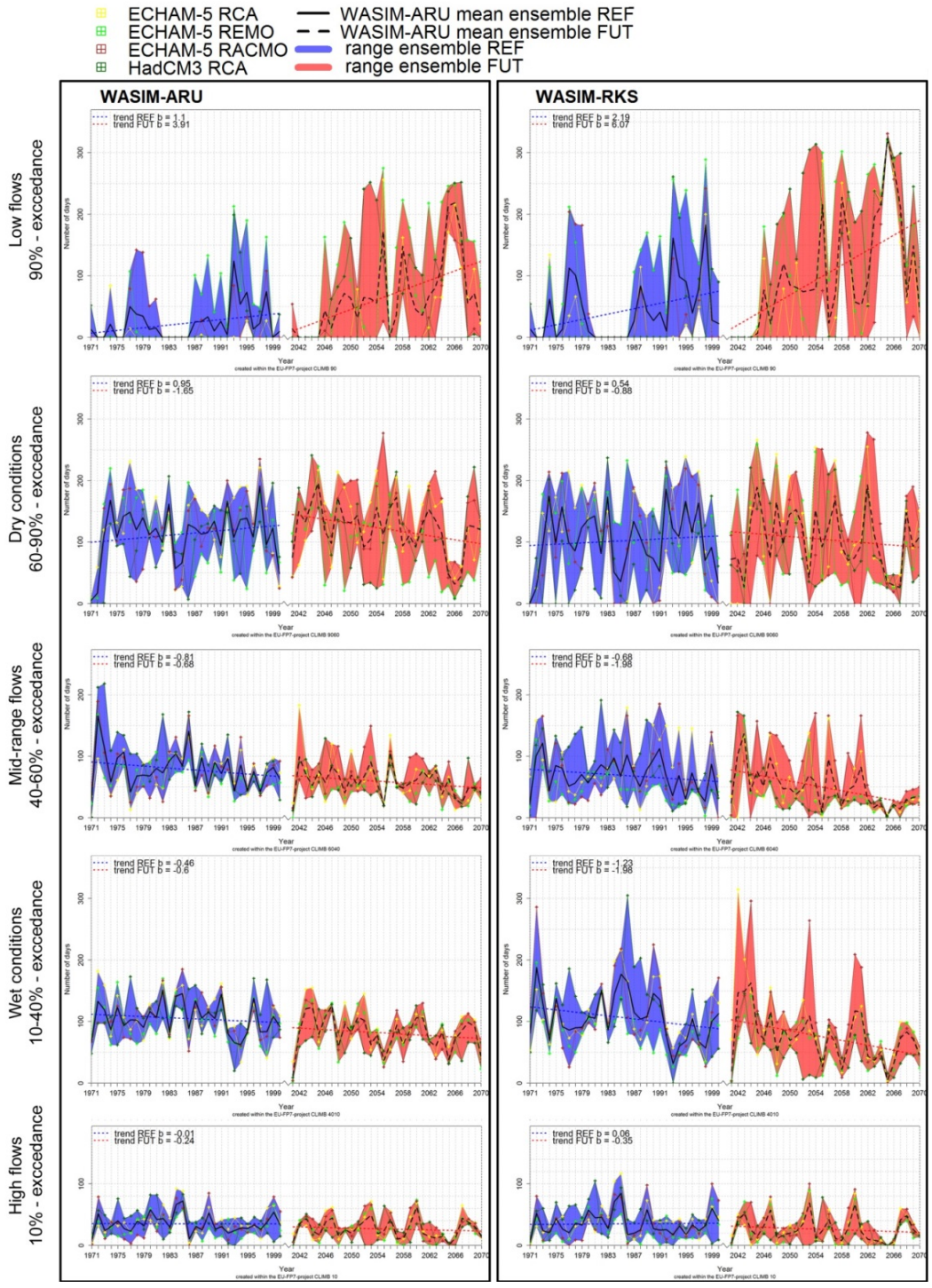

Figure 57: Number of days of low flows, dry, mid-range flow, wet and high flow conditions determined from WaSiM-ARU and WaSiM-RKS discharge outputs of the REF and FUT .

7. DISCUSSION

Model setup and calibration

In this study the physically based fully distributed hydrological model WaSiM was driven by a downscaled and bias-corrected regional climate model ensemble (RCM) to quantify climate change impacts on the water resources in the Mediterranean Rio Mannu catchment located on the island of Sardinia, Italy.

WaSiM had to be calibrated based on a historically recorded time series of discharge, derived Landsat evapotranspiration patterns and a short time series of record soil moisture, due to the scarce filed data situation in the catchment. All results of the applied calibration attempts have to be considered with caution. The available discharge time series was recorded from 1925-1935. The hydrological basin has been heavily modified since that time and a significant historical climate change impact already affected the basin as reported by Sannitu (2006). Thus the real hydrological situation of the considered reference time (1971-2000) might be significantly different compared to the available discharge record.

A solid soil model parametrization of WaSiM requires an enormous and reliable data collection and an intensive effort in pre-processing Rieger et al. (2010). These physically based parameters should be identified in a reasonable range before calibration Rieger et al. (2010).

Spatially distributed soil physical information was only available based on the presented Aru et al. (1990) map with nearly no mandatory information. Based on this map high ranges of different soil physical properties for each process pixel are possible, which leads to a very high spatial uncertainty in the model parametrization. But even after a very careful and precise soil parametrization using pedo-transfer functions, as conducted in this study, uncertainties in a range of 10% only based on the applied pedo-transfer function have to be expected (Rieger et al. 2010).

Ranges of even higher uncertainties might be expected for sub soil layers. Since the soil information was only collected for the top soil up to a depth of 30cm sub soil properties were parameterized based on the same soil physical properties, except for the saturated hydrological conductivity. This parameter was parameterized based on a recession constant.

This simplification does not consider changes in soil organic matter, bulk density and processes like clay leaching into sub soil layers. But those parameters can change significantly the hydrological properties of the soil layer, for example clay horizons based on clay leaching will increase the accumulation of soil water in the top soil layers, increase surface runoff and decrease the infiltration rate.

However, based on the available information the soil physical parametrization of both WaSiM setups in this study can be stated as solid. The physical and conceptual parameters of both WaSiM versions are the same except for the soil model. The significant differences in the outputs of both applied WaSiM versions show that the soil parametrization has a major impact on modeling results and also on the projected climate change impact.

The calibration outputs of soil moisture content and actual evapotranspiration of WaSiM-RKS setup outperform those of the WaSiM-ARU, while the WaSiM-ARU setup seems to better match the historical discharge. However, none of the applied calibration approaches are able to replace the quality of a calibration with a long-term record of discharge and the corresponding meteorology (air temperature, precipitation, global radiation, wind speed and rel. humidity) of the reference time series. In the conducted study calibration criteria with less accuracy have been applied since data scarcity like in the test side are common in the many Mediterranean catchments. But this unfortunate data situation should not detain hydrological climate change impact assessment research in those regions, since as shown in paragraph 1.3 climate change is already significantly affecting those regions. This means all available resources of calibration data sets need to be taken into account, even if they might also imply high uncertainties.

For example the applied ETR-TRI results must be handled with caution, as the remote sensing data shows only a snap shot of up to 4 different days in the RMB. Kalma et al. (2008) points out those measurement errors can reach levels of 15-30%. Compared to long-term point measurements this method has the disadvantage that the evapotranspi-

ration process is not recorded constantly and as soon as clouds are present in the catchment, measurements are strongly deteriorated. Constant point estimation, such as eddy covariance or Bowen ratio, has the disadvantage that it is only valid for the specific combination of land use and soil type. The Triangle method is advantageous when spatially distributed information is required for heterogeneous land use classes. Under these conditions, the ETR-TRI measurements can be a very attractive validation source for data scarce regions. By comparing the spatial pattern of the ETR-TRI results with the modeling outputs. The WaSiM-RKS setup shows a clear improvement compared to WaSiM-ARU setup.

The soil moisture calibration data set on the other hand is rather precise in terms of absolute values (±3 %), but this measurement is limited to one point of the catchment. In this study the point information was compared to a 250m*250m modeled pixel at the same location. The average soil physical properties of the 250m pixel and the point measure might be completely different. However, this available data should be considered at least in terms of plausibility. Here once again the WaSiM-RKS outputs outperform the WaSiM-ARU outputs and show that high quality soil information can improve certain modeled hydrological quantities SWC significantly.

The comparison of the ETR, soil moisture and discharge calibration results reveal a paradox situation in spring and summer time, since all modeled outputs in this time of the year are lower than the reference datasets. But here one needs to consider that none of the data sets covers the same time series, which means that every reference dataset is affected by a different meteorology. Furthermore the meteorology of each of the calibration dataset is different to the meteorology of the reference climate model data applied for the calibration. This problem for example can be observed in Figure 21. The recorded precipitation 1925-1935 is higher compared to the reference climate model precipitation for the months of May, June, and July. In this case it makes sense that the modeled reference discharge is lower than the recorded one of 1925-1935.

Climate change impact of the RCM input

In this section the WaSiM modeling results using the WaSiM-ARU and the WaSiM-RKS will be discussed with those of Piras et al. (2014), Piras (2013) and Ehlers (2014). In those studies the same climate model inputs were applied to the hydrological models TIN-based Real-time Integrated Basin Simulator (tRIBS) of Vivoni et al. (2000) and mGROWA,

of Kunkel & Wendland (2002), respectively. The parametrization of the tRIBS model and the mGROWA model are similar to the WaSiM-ARU set up. All three models where parametrized based on the CLIMB model harmonization strategy (section 5.2.3) and both models used the same climate model inputs and the Aru et al. (1990) soil texture map for the soil model parametrization.

The hydrological modeling results and climate change impact on the hydrology presented in section 6 draw a future picture of decreasing water resources in the Rio Mannu basin. The hydrological quantities, evapotranspiration, soil water content, discharge and ground water recharge are projected to decrease in the basin. This decrease is mainly related to the projected dropping of precipitation sums and rising air temperature in the future time series.

The annual and monthly mean relative changes are in good correspondence with the studies of Piras et al. (2014), Ehlers (2014) and the one conducted by Senatore et al. (2011) in southern Italy. The total modeled hydrological quantities on the other hand differentiate significantly compared to the other studies and seem to be more uncertain.

The comparison of climate model input data in the sections 6.2.1 and 6.2.2 show a decrease in annual precipitation of -7% (ECHAM-5 REMO) to -21% (HadleyCM 3 RCA) and an increase of air temperature of 1.8°C (ECHAM-5 REMO) to 3.1 °C (HadleyCM 3 RCA).

The average decrease of precipitation is similar to Piras et al. (2014), who pointed out that the uncertainty in this trend is low, since all climate change trends in all four climate projections are similar. Temperature is projected to increase for all climate forcings. Uncertainties in this trend are especially low since all RCMs indicate this trend. The degrees of change indicate that the RCM temperature change in the future is strongly influenced by the GCM, since all ECHAM-5 driven RCMs show a temperature increase of the region by 1.8°C while the HadleyCM3 driven RCM is increasingly stronger. Those results are also similar to Piras et al. (2014) and Ehlers (2014).

WaSiM's annual reference potential evaporation ETP (Table 9) fits well the ETP of Saadi et al. (2015) and Todorovic et al. (2013) (1300-1500mm/a) and is about 100-200mm/a higher compared to the results of Ehlers (2014). Based on the increased air temperature

in all future climate projections modeled ETP increased, too. The future relative ΔETP increase in the WaSiM outputs is up to 10% higher compared to Piras et al. (2014).

Actual Evapotranspiration (ETR)

The shape of the WaSiM-ARU and –RKS ETR results (Figure 47 & Figure 48) presented in section 6.3 are corresponding well to the results of Senatore et al. (2011) and Maselli et al. (2014), with peak ETR in May and with increasing water stress from August to September. ETR is dropping to the minimum value which lasting up to December. The harvesting date of the model was set in June and July, which is the common harvesting season in the catchment (Bird et al. 2015). The time between August and December is also characterized by limited vegetation growth, due to limited plant available water and most agricultural fields are free of crops. The presented monthly mean results of the reference time series (Figure 47, 46, 47 & 48) fit well those of Maselli et al. (2014) and Ehlers (2014). The results of Piras et al. (2014) on the other hand show a mismatch in the reference series and are significantly below the WaSiM results between December and May and are higher for the very dry months of July, August, and September.

The modeled evapotranspiration reduction in the future is in good correspondence with the results of Senatore et al. (2011), who also found a slight increase of evapotranspiration in the winter season and a decrease of up to 40% in summer and autumn. Results of Piras et al. (2014) project lower changes of up to 10%. The percentage change of ETR in future springtime might not seem to be as dramatic as in spring, but one should note that ETR reduction in terms of absolute quantities is largest in May and June. Especially changes in the months April to June indicate a high threat to the agricultural productivity, since an earlier reduction of ETR indicates that crops suffer earlier from water stress. This is also indicated by the fact that the peak ETR in the future changes from May in the reference to April. This assumption is further confirmed by the ETI results in Table 12, Figure 51, Figure 52 and the ground water recharge results presented in Figure 53 and Figure 54. ETI drops below the moderate threshold value of 0.5 in the spring season in the future scenario for most of the low land areas in the catchment. Those areas, mainly used for agricultural production, are affected by the strongest GWR reduction in the future scenario, but GWR results indicated a high uncertainty depending on the applied soil model setup. Note that those results have been processed with a very simplified groundwater modeling approach of WaSiM's unsaturated zone module. WaSiM's

groundwater module was not used due to missing GWR measurements for validation. Due to that results may imply a high error.

Modeled soil water content

Modeled monthly mean soil water content (SWC) results of WaSiM-ARU, WaSiM-RKS and tRIBS produce a similar shape over the course of the year, with high soil moisture values in the winter season and low values in the summer season. However, strong deviations are visible in the absolute values. The ensemble mean maximum SWC outputs of 27 vol.-% in tRIBS are processed in December and the minimum of 23 vol.-% are processed in August for the reference time series. The SWC of both WaSiM outputs show a much higher range over the course of the year with a maximum in February (WaSiM-ARU = 22.5 vol.-% and WaSiM-RKS = 27 vol.-%) and a minimum in August (WaSiM-ARU = 11 vol.-% and WaSiM-RKS = 13 vol.-%). The projected average decrease of SWC of WaSiM outputs (WaSiM-ARU = -10.75 vol.-% and WaSiM-RKS = -9.25%) is higher for tRIBS projection (tRIBS = -5.39%) and lower for the projection of Senatore et al. (2011) with a projected reduction of about ≈ -20%. Both WaSiM and tRIBS model outputs show the largest projected SWC decline in the spring time (WaSiM-ARU = -13%, WaSiM-RKS = -12%, tRIBS = -7%). The comparison of WaSiM and tRIBS results and the results of Senatore et al. (2011) shows that based on the applied climate model projections a decrease of plant available water in the future is confident.

Hydrological modeling results of Piras et al. (2014) further confirm the spatially distributed SWC change of WaSiM-ARU (Figure 45). Both modeling results show the strongest relative decrease of SWC in the northwestern part of the catchment. However, this pattern is less dominant in the WaSiM-RKS SWC output grids.

Very uncertain on the other hand is the total modeled soil water content. Here the tRIBS model produces significantly different total amounts of SWC than both WaSiM setups. Both WaSiM setups seem to produce more plausible SWC outputs, since SWC of the tRIBS outputs never drop under permanent wilting point even in the summer months and also do not fit well to the results of Senatore et al. (2011). Due to that the tRIBS SWC modeling result seems to be very unlikely for a semi-arid region. The soil textures of the WaSiM-RKS setup have in average a higher threshold of permanent wilting point and point of saturation compared to the WaSiM-ARU setup. This explains the total higher SWC values of the WaSiM-RKS outputs, since the soil water storage is higher and

release in dry conditions in terms of runoff and evaporation is less. The higher water content in wet and warm conditions (growing season WaSiM-RKS), increases the transpiration and evapotranspiration in this season. The WaSiM-ARU results of this study were used in the study of Bird et al. (2015) using the AquaCrop model to determine the threat of having lower yields in the future projection in the Rio Mannu basin. Based on the WaSiM-ARU results there is a 53% chance that the value of the wheat harvest is 75% of less of the current mean value in the future time series. This is a significant decrease in value (Bird et al. 2015). Plant available water mainly depends in the total soil water content in combination with the corresponding soil texture class at a given location. This value on the other hand is not similar for all locations in the catchment where wheat is grown, since it is heavily dependent on the given soil texture at each wheat location. This means a poor quality of soil information in a catchment increases the uncertainty of determining the climate change induced threats to agricultural production in the Rio Mannu. The higher SWC outputs of the WaSiM-RKS soil moisture outputs and the lower relative change in the modeled future results indicate that the probability of yield lost based on the WaSiM-RKS values is lower compared to the WaSiM-ARU results.

Modeled runoff and discharge

The simulation of projected Q changes involves the highest uncertainties, since it is depending strongly on the RCM input. Future Q changes range from an increase of 2% (ECHAM-5 RACMO) to a decrease of -46% (HadleyCM3 RCA). Furthermore, WaSiM's modeling results of the REF and FUT discharge and runoff show the largest response to the soil model parameterization. The WaSiM-RKS results for the REF and FUT are significantly lower compared to the WaSiM-ARU results. This shows that the soil physical setup has a strong influence on the modeled Q outputs as well as the climate change impact prediction of Q (Figure 55, Figure 56, Figure 57and Figure 58). Which of those two reference time series modeling results is more likely to represent the true hydrological situation in the catchment stays unclear. A satisfying answer to this question would need a long-term discharge record together with a sufficient record of WaSiM's meteorological inputs. The results in sections 6.2.1 and 6.3.2 proved that the soil inputs source and parameterization can have a major impact on the modeled Q outputs as well as on the spatial distribution of runoff generation in the catchment. Since now reliable Q record is available in the catchment WaSiM-ARU and –RKS Q outputs will be discussed

and compared in this section to the Q results of other hydrological models applied in the catchment.

Those four hydrological modeling results conducted with WaSiM, SWAT and tRIBS in the Rio Mannu catchment within the CLIB-Project are presented in Figure 58. All models were driven with the same climate model meteorology presented in section 5.2.1 and WaSiM-ARU, SWAT and tRIBS used the same land use, soil information and catchment setup based on the CLIMB model harmonization presented in section 5.2.3. Only WaSiM-RKS uses a different soil information input as presented in section 5.2.3.4. The applied models are all physically based and range from semi-distributed (SWAT) to fully distributed (tRIBS & WaSiM). The modeling results are very diverse for many months of the year. This is especially true for seasons (winter and spring) in which more Q is generated (Figure 58a). In December and January of the REF WaSiM-ARU processes a considerable higher amount of runoff compared to SWAT and tRIBS. From May to August WaSiM-ARU, -RKS and SWAT correspond well, while tRIBS processes higher Q from April to August in the REF and FUT. The hydrological models WaSiM-ARI, -RKS and SWAT respond to the REF annual precipitation peak in December with a peak flow for the same month, while tRIBS Q peak is in February. SWAT is the only model responding with a second Q peak to the second precipitation peak in February. This is indicating a higher sensitivity of the precipitation input for SWAT.

The Figure 59 compares the Q modeling outputs of the different models by standard deviation (SD). One graph show the SD of all models, one of all models using the Aru et al. (1990) soil information and one compares the results of WaSiM-ARU against WaSiM-RKS for each month of the year. The range of monthly mean Q and the SD presented in Figure 59 indicates a significant uncertainty related to the applied hydrological models. They confirm the findings of Velázquez et al. (2013) and Muerth et al.(2013), that not only climate model related uncertainties need to be considered, also the hydrological models apply a significant uncertainties to total Q generation.

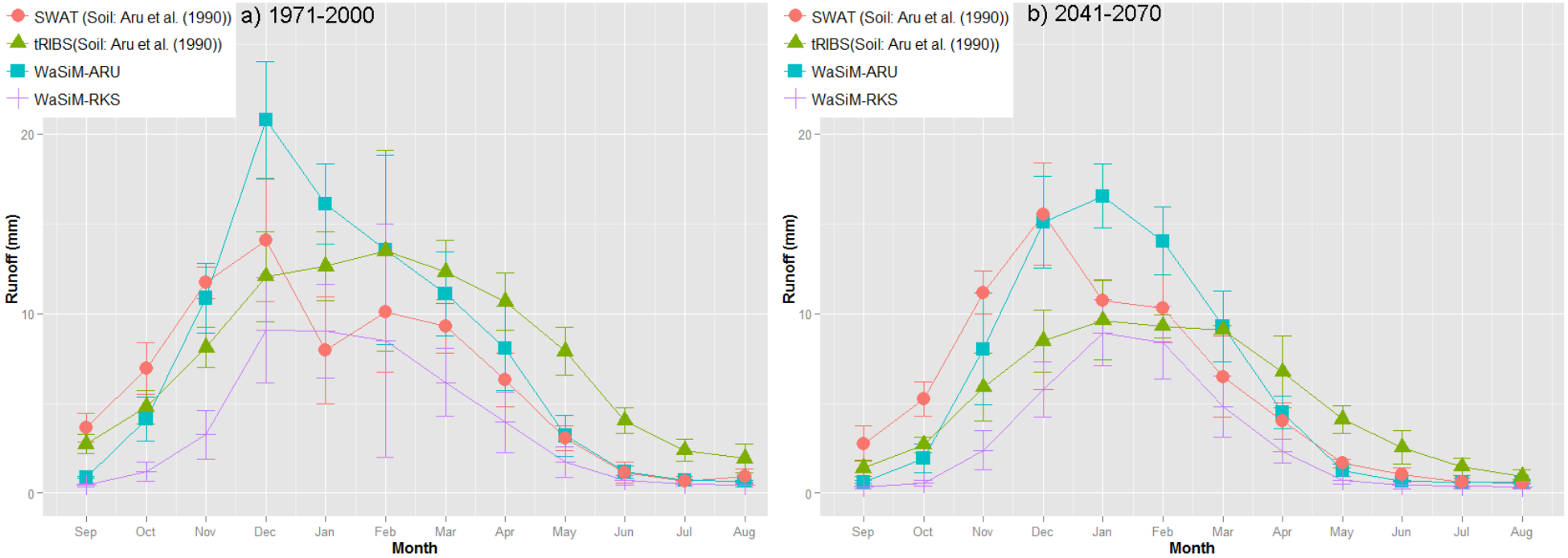

Figure 58: Comparison of modeled runoff [mm] of 4 different hydrological modeling results (WaSiM-ARU, WaSiM-RKS , SWAT conducted by the center for advanced studies, research and development in Sardinia CRS4 (SWA) and tRIBS conducted by Piras (2013) (TRI)) using the same climate model input meteorology and a harmonized model parametrization and applied in the Rio Mannu catchment for a) the reference time series (1971-200) and b) the future time series (2041-2070). The modeling was conducted within CLIMB.

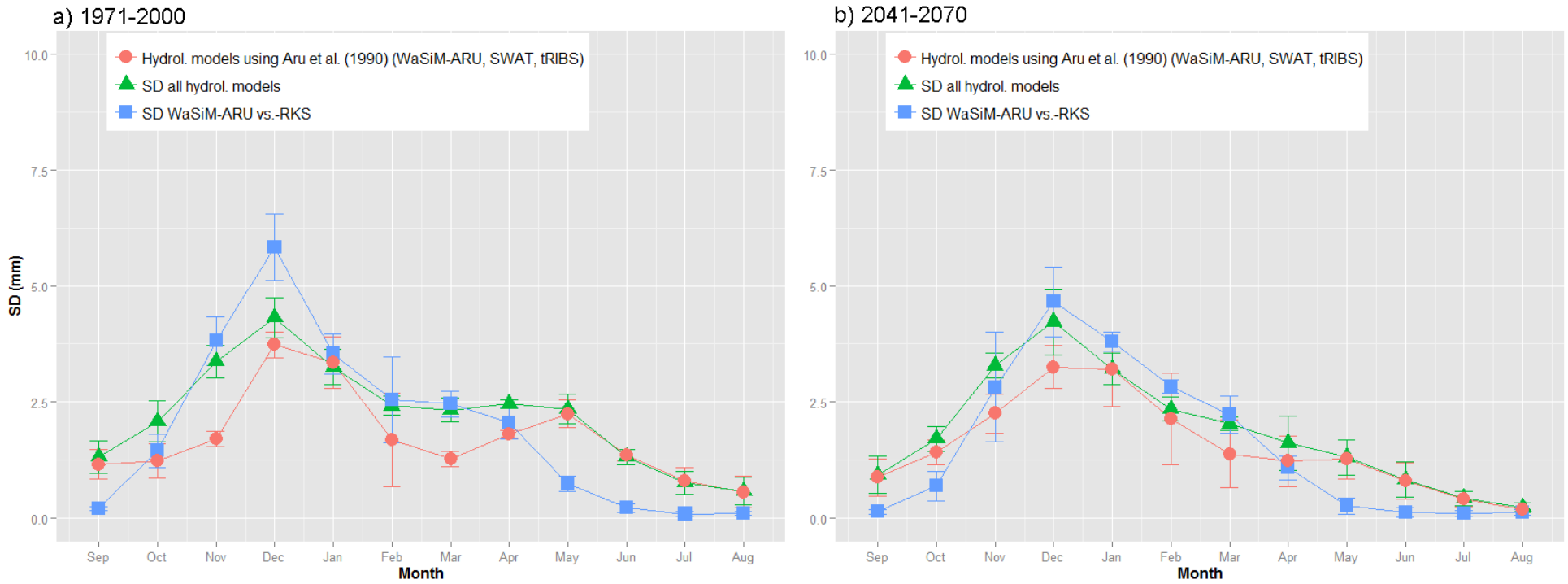

Figure 59: Standard Deviation (SD) of monthly mean runoff ensemble comparing all models (WaSiM-ARU, WaSiM-RKS, tRIBS, SWAT), WaSiM-ARU and WaSiM-RKS and the models with the Aru et al. (1990) soil texture information (WaSiM-ARU, tRIBS, SWAT).

Especially in ungauged catchment like the Rio Mannu those uncertainties need to be considered in the climate change impact assessment analysis, the resulting adaption strategies and for the policy decision making. However, findings also show that the quality of soil input and parametrization creates uncertainties when using WaSiM that are in the same range as the uncertainties produced by the different applied hydrological models. This is especially true for the wet months of December and January where the SD between the WaSiM-ARU and –RKS is higher than the SD between the hydrological model that are using the Aru et al. (1990) soil information (Figure 59).

Table 14: Projected annual runoff change in the Rio Mannu for the future time series using 3 different models with harmonized setup (WaSiM-ARU, SWAT, tRIBS) compared to the WaSiM-RKS setup.

Relative annual runoff change for the 2041-2070 period				
Hydrological model	Applied regional climate model			
	ECHAM-5 RCA	ECHAM-5 REMO	ECHAM-5 RACMO	HadleyCM3 RCA
WaSiM-ARU	-20%	-12%	-5%	-37%
WaSiM-RKS	-20%	-8%	2%	-46%
SWAT	-18%	2%	5%	-16%
tRIBS	-35%	-16%	-23%	-52%

The magnitude in uncertainty of average total modeled Q outputs for the different applied models as well as for the soil input increases for the high flow (winter) and wet conditions (spring), in this low flow dominated catchment. Those findings are contrary to those of Velázquez et al. (2013) who demonstrated an increasing uncertainty of hydrological model Q outputs for low flow conditions. However, their findings are based on a study made in catchments with humid and snowmelt dominated runoff regimes and due to that not fully comparable to the findings made in this study. Those uncertainties and the non-linear nature of hydrological modeling results are further reflected by the projected annual climate change impact on ΔQ as presented in Table 14. ΔQ is projected to decline for all WaSiM-ARU and tRIBS simulations, while for WaSiM-RKS & SWAT driven with ECHAM-5 RACMO and SWAT driven with ECHAM-5 REMO is projected to increase slightly. The most pessimistic ΔQ results are processed by WaSiM-ARU,

WaSiM-RKS and tRIBS when driven with HadleyCM3 RCA, while for SWAT this is the case when driven with ECHAM-5 RCA. The slightly positive increasing trend of ΔQ for WaSiM-RK (ECHAM-5 RACMO) compared to the negative trend of WaSiM-ARU (ECHAM-5 RACMO) and the more pessimistic negative trend of WaSiM-RKS (HadleyCM3 RCA) compared to WaSiM-ARU (HadleyCM3 RCA), shows the non-linear behavior of WaSiM to the combination meteorological and structural model inputs like soil texture information. Those results confirm on the one hand that in a climate change impact assessment uncertainties related to other aspects of the assessment procedure including the structural uncertainty of the hydrological model itself need to be taken into account (Honti et al. 2014) and on the other hand the findings of Ruelland et al. (2015) that,

I. "in non-stationary conditions, additional uncertainties arise from parameter instability due to possible changes in the physical basin characteristics and in the dominant processes"

II. "the hydrological uncertainty is very significant and that the lack of robustness of the hydrological model (due to its model structure and/or to the wrong estimate of its inputs) is a major source of variability among streamflow projections under future climate conditions."

Despite the propagation of those uncertainties, all applied hydrological modeling results agreed on a decrease ΔQ of -17% to -50% (WaSiM-ARU -25% to -39%; WaSiM-RKS -20% to -50%;) for the spring season (MAM) in future scenario. Also the SD of Q (Figure 59) between the different applied models is lower compared to the wet winter season and indicating a higher confidence in the hydrological impact projection for this season. This confirms the significant runoff reduction, based on CORDEX RCM projections found by Ruelland et al. (2015) for the same season. The reduction of Q indicates a major threat to water availability for the months with the highest agricultural productivity.

8. CONCLUSIONS

Climate change impacts were quantified by comparing models of water resources of the reference time series to those of the projection time series for the RMB. The available soil texture information needed to setup WaSiM and applied for the hydrological modeling within CLIMB appeared to be of poor quality. New soil information physical was surveyed in the catchment at 239 locations and regionalized by different deterministic, geo-statistic, and hybrid methods. The soil texture results maps of section 4 clearly confirms the hypothesis III in section 1.1 that "*Different regionalization methods applied to soil physical data will lead to different spatial distributions of soil textures in the catchment*". Regression kriging outperformed the other applied regionalization methods. The RMSE of the regression kriging results were found in the same range or better compared to other studies found in literature and discussed in section 4.6. However, the relation between co-variable and target variables was found to be low. This confirms the findings of Minasy & McBratney (2007) that RK appears to be robust to predict soil properties in various soil regions and suggest this method for practical applications, but has a major limitation, if the relationship between target and covariates is low. The assumed stationary condition across the space (Kumar 2015) is not always valid and a major limitation of this method. Despite the low relationship between target and co-variable regression kriging delivered the best performance and proved to be a solid and relatively easy to apply regionalization method. An improvement of those results might be possible by implementing different co-variables from airborne and infield remote sensing techniques, like synthetic aperture radar (Meyer 2009) or geophysical remote sensing like (gamma ray spectrometry, electromagnetic resistivity, or time domain reflectance) as used in Cassiani et al. (2012). In data scarce regions like the Rio Mannu Basin (RMB) this approach improves the knowledge of the soil physical setting in the catchment significantly and should be applied by hydrologists in the region with scarce soil texture information.

Simulated WaSiM results project a clear reduction of P, Q, ETR, and SWC, especially in the growing season (March to June). ETR rates are significantly reduced from April to October for the future time series in all simulation results. The reduction of ETR is caused by lower soil water content, where even the permanent wilting point is reached at an earlier time of the year in the future scenarios. Sufficient water availability for plants is crucial for the agricultural production in this season, being the main source of income in the RMB. The earlier onset of dry conditions in the catchment is a threat to agricultural production in the future, asking for the development of an adaptation strategy, such as a water resources management plan which takes such simulations into account. These findings clearly confirm hypothesis I in section 1.1 that "*Hydrological resources and the agricultural production are endangered by climate change impacts in the Mediterranean semi-arid area."* The quality quantification of future threats to agricultural productivity, as done by Bird et al. (2015), is highly dependent on solid hydrological modeling results. The study shows that in ungauged data scarce catchments the provision of certain hydrological climate change impact projections is strongly hampered and involves high uncertainties coming from different sources (e.g. climate model input, different hydrological model setups and architectures). Those uncertainties have to be assessed to quantify the full range possible future threats to water availability and agricultural productivity.

It is also visible that the total sums of modeled hydrological quantities show a noticeable dependency from the applied soil model parameterization. The WaSiM-ARU setup produces significantly higher amounts of runoff and low SWC outputs, while this observation is reversed for the WaSiM-RKS setup. The bias of modeled Q produced with the difference soil texture parametrizations (WaSiM-ARU & WaSiM-RKS) is in the range or even higher than the Q bias compared to other hydrological modeling results presented by Piras et al. (2014) using tRIBS and processed by CRS4 using SWAT, respectively. With those findings the two hypothesizes IV "*Setting up WaSiM's soil model with soil information coming from different sources will have a considerable impact on the hydrological modeling results*" and V "I.*The hydrological climate change impact assessment implies high uncertainties coming from different sources, like climate model input meteorology, the structural setup and the architecture of different hydrological models*" in section 1.1 can be confirmed.

Beside the climate model input related uncertainties, hydrological climate change impact assessment needs to consider the structural, parametrization, and hydrological model related uncertainties. This confirms hypothesis II in section 1.1, that "II. "*A solid soil physical parametrization of physically based fully distributed hydrological models hydrological models is crucial to simulate reliable modeling results for the spatial and temporal domain*". Accordingly, water planners and stakeholders should be very careful in managing water resources in ungauged basins based on the total modeled hydrological quantities.

The delta of the climate change impact on the hydrological quantities on the other hand implies lower model induced uncertainties and might give a better and reasonable orientation of future changes in the RMB. However, an improved management of water resources, adaptive to climate change impacts, will be strongly hampered as long as no reliable knowledge of the status quo of the total hydrological quantities in the catchment is available.

The spatially-explicit model outputs, as shown in the comparison to the derived ETR-TRI grids are better captured, when applying the WaSiM-RKS map. Even though correlations of the hydrological modeling ETR results of WaSiM-ARU and WaSiM-RKS with the ETR-TRI grids remain poor in both attempts, the WaSiM ETR results were adjusted from a negative correlation (WaSiM-ARU), to a positive correlation (WaSiM-RKS) for the month of June. It is noteworthy that the patterns of the WaSiM-RKS ETR grids appear plausible overall.

The combination of soil sampling, hybrid regionalization methods and ETR measurements, e.g. by means of the Triangle method, improves knowledge about spatially distributed key quantities of the hydrological cycle within a basin. This information can be obtained within a relatively short time, a clear advantage compared to long-time Q measurements, especially in data scarce regions.

The Mediterranean region is expected to be affected by climate change more negatively than other regions which leads to the controversial situation that,

I. based on the future climate projections the impact on the water resources is projected to be more negative than in other regions on the planet

II. based future climate projections water resource management and planning is more important than in other regions and needs to be very precise

III. due to the poor availability and quality of long-term hydrological quantity records, hydrological impact assessment is more affected by uncertainties especially in the structural model setup, parametrization and validation, than in catchments that are well monitored and sampled.

In order to reduce the massive prevailing uncertainties, especially in ungauged basins, any possible data source or validation method has to be taken into account to improve process understanding and the overall robustness of model results related to the assessment of future hydrological impact of climate change.

Especially in ungauged catchments hydrological climate change impact assessment is asking for a holistic approach, in which the close collaboration of the disciplines climatology, pedology, remote sensing, and hydrology reduces uncertainties as far as possible. The combination of sophisticated climate model downscaling and bias correction techniques, improved hydrological model parametrization with improved soil information, and validation with in-situ and remote sensing measurements, as shown in this study, has a high potential to improve environmental impact assessment in data scarce regions.

Acknowledgments

Funding for this research through the FP7-project CLIMB by the European Commission (GA: 244151) and contributions from CLIMB partners and local data providers are gratefully acknowledged.

9. REFERENCES

Adhikari, K., Kheir, R. B., Greve, M. B., Greve, M. H., 2013. Comparing kriging and regression approaches for mapping soil clay content in a diverse Danish landscape. In: Soil Science, 178(9), 505-517.

Alcamo, J., Moreno, J.M., Nováky, B.,Bindi, M., Corobov, R., Devoy, R.J.N., Giannakopoulos, C., Martin, E., Olesen, J.E. Shvidenko, , A. , 2007. Europe. Climate Change 2007: Impacts, Adaptation and Vulnerability. Contribution of Working Group II to the Fourth Assessment Report of the Intergovernmental Panel on Climate Change, M.L. Parry, O.F. Canziani, J.P. Palutikof, P.J. van der Linden and C.E. Hanson, Eds., Cambridge University Press, Cambridge, UK, 541-580.

Allen, R. G., Pereira, L. S., Raes, D., & Smith, M., 1998. Crop evapotranspiration-Guidelines for computing crop water requirements-FAO Irrigation and drainage paper 56. FAO, Rome, 300(9), D05109.

Arnell, N.W., 1999a. The effect of climate change on hydrological regimes in Europe: a continental perspective. Global Environmental Change, 9 ,5 – 2 .

Aru A., Baldaccini P., Barneschi P., Pietracaprina A., Arangino F., 1990. Carta dei suoli della Sardegna, in scala 1:250.000. Dipartimento Scienze della Terra Università di Cagliari, Assessorato Regionale alla Programmazione Bilancio ed Assetto del Territorio, SELCA, Firenze.

Batra, N., Islam, S., Venturini, V., Bisht, G., & Jiang, L. E., 2006. Estimation and comparison of evapotranspiration from MODIS and AVHRR sensors for clear sky days over the Southern Great Plains. Remote Sensing of Environment, 103(1), 1-15.

Beckers, J., Smerdon, B., & Wilson, M. (2009). Review of hydrologic models for forest management and climate change applications in British Columbia and Alberta. FORREX Forum for Research and Extension in Natural Resources, Kamloops, BC. FORREX Series No. 25. British Columbia, Canada.

Behrens, T., Förster, H., Scholten, T., Steinrücken, U., Spies, E. D., & Goldschmitt, M., 2005. Digital soil mapping using artificial neural networks. Journal of plant nutrition and soil science, 168(1), 21-33.

Beven, *K.J., Kirkby M.J., 1979. A physically based, variable contributing area model of basin hydrology. Hydrolog. Sci. J. 24 (1), 43-69.*

Blöschl, G., 2005. Rainfall-runoff modeling of ungauged catchments, Encyclopedia of Hydrological Sciences, John Wiley & Sons.

Blaschek, M., 2015. Digital soil mapping at different spatial scales using machine learning algorithms and multivariate geostatistics in a Mediterranean basin. Phd-thesis; Christian-Albrechts-Universität zu Kiel, Kiel 2015.

References

Blaschek, M., Duttmann, D., Meyer, S., Soddu, A., 2011. Spatial distribution of soil properties, report and maps of the study sites. CLIMB Report-Deliverable No. 3.2.4. URL: http://www.climb-fp7.eu/dissemination/deliverables/d_3_2_4_spatial_distribution_of_soil_properties_report_and_maps_of_study_sites.pdf (accessed 01.03.2015).

Böhner, J., McCloy, K.R., Strobl, J., 2006. SAGA – Analysis and Modeling Applications. Göttinger Geographische Abhandlungen, Vol.115, 130pp.

Browning, D.M., Duniway, M.C., 2011. Digital SoilMapping in the Absence of Field Training Data: A Case Study Using Terrain Attributes and Semiautomated Soil Signature Derivation to Distinguish Ecological Potential. In: Applied and Environmental Soil Science, Volume 2011, Article ID 421904, 12 pages doi:10.1155/2011/421904.

Carmignani, L., Oggiano, G., Funedda, A., Conti, P., & Pasci, S., 2015. The geological map of Sardinia (Italy) at 1: 250,000 scale. Journal of Maps, 1-10.

Carmignani, L., Carosi, R., Di Pisa, A., Gattiglio, M., Musumeci, G., Oggiano, G., & Carlo Pertusati, P., 1994. The hercynian chain in Sardinia (Italy). Geodinamica Acta, 7(1), 31-47

Cassiani, G., Ursino, N., Deiana, R., Vignoli, G., Boaga, J., Rossi, M., Perri, M. T., Blaschek, M., Duttmann, R., Meyer, S., Ludwig, R., Soddu, A., Dietrich, P., Verban, U., 2012. Noninvasive Monitoring of Soil Static Characteristics and Dynamic States: A Case Study Highlighting Vegetation Effects on Agricultural Land. In: Vadose Zone Journal *Vol. 11 No. 3.*

Casula, G., Cherchi, A., Montadert, L., Murru, M., & Sarria, E., 2001. The Cenozoic graben system of Sardinia (Italy): geodynamic evolution from new seismic and field data. Marine and Petroleum Geology, 18(7), 863-888.

Cermák, F., Gaspárek, J., De Lorenzi, F., Jones, H.G., 2007. Stand biometry and leaf area distribution in an old olive grove at Andria, southern Italy. Annals of Forrest Science, Volume 64, No. 5, 491-501.

Chai, T., & Draxler, R. R. (2014). Root mean square error (RMSE) or mean absolute error (MAE)?–Arguments against avoiding RMSE in the literature. Geoscientific Model Development, 7(3), 1247-1250.

Christensen, J. H**.**, Hewitson, B., Busuioc, A., Chen, A., Gao, X., Held, R., Jones, R., Kolli, R. K., Kwon, W. K., Laprise, R., Magana Rueda, V., Mearns, L., Menendez, C. G., Räisänen, J., Rinke, A., Sarr, A., Whetton, P., Arritt, R., Benestad, R., Beniston, M., Bromwich, D., Caya, D., Comiso, J., de Elia, R. and Dethloff, K., 2007. Regional climate projections , Climate Change, 2007. The Physical Science Basis. Contribution of Working group I to the Fourth Assessment Report of the Intergovernmental Panel on Climate Change, University Press, Cambridge.

Christensen, J.H., K. Krishna Kumar, E. Aldrian, S.-I. An, I.F.A. Cavalcanti, M. de Castro, W. Dong, P. Goswami, A. Hall, J.K. Kanyanga, A. Kitoh, J. Kossin, N.-C. Lau, J. Renwick, D.B. Stephenson, S.-P. Xie and T. Zhou, 2013: Climate Phenomena and their Relevance for Future Regional Climate Change. In: Climate Change 2013: The Physical Science Basis. Contribution of Working Group I to the Fifth Assessment Report of the Intergovernmental Panel on Climate Change [Stocker, T.F., D. Qin, G.-K. Plattner, M. Tignor, S.K. Allen, J. Boschung, A. Nauels, Y. Xia, V. Bex and P.M. Midgley (eds.)]. Cambridge University Press, Cambridge, United Kingdom and New York, NY, USA.

Ciampalini, R., Lagacherie, P., Monestiez, P., Walker, E., & Gomez, C., 2012. Co-kriging of soil properties with Vis-NIR hyperspectral covariates in the Cap Bon region (Tunisia). In: Digital Soil Assessments and Beyond (pp. 393-398). CRC Press.

Collins, M., R. Knutti, J. Arblaster, J.-L. Dufresne, T. Fichefet, P. Friedlingstein, X. Gao, W.J. Gutowski, T. Johns, G. Krinner, M. Shongwe, C. Tebaldi, A.J. Weaver and M. Wehner, 2013: Long-term Climate Change: Projections, Commitments and Irreversibility. In: Climate Change 2013. The Physical Science Basis. Contribution of Working Group I to the Fifth Assessment Report of the Intergovernmental Panel on Climate Change [Stocker, T.F., D. Qin, G.-K. Plattner, M. Tignor, S.K. Allen, J. Boschung, A. Nauels, Y. Xia, V. Bex and P.M. Midgley (eds.)]. Cambridge University Press, Cambridge, United Kingdom and New York, NY, USA.

Golmohammadi, G., Prasher, S., Madani, A., & Rudra, R. (2014). Evaluating Three Hydrological Distributed Watershed Models: MIKE-SHE, APEX, SWAT. Hydrology, 1(1), 20-39.

Conrad, O., 2006. SAGA - Program Structure and Current State of Implementation. In: Boehner, J., McCloy, K.R., Strobl, J. (Eds.), SAGA - Analysis and Modeling Applications. Vol. 115.

Cornelissen, T. Diekkrüger, B., Giertz, S., 2013. A comparison of hydrological models for assessing the impact of land use and climate change on discharge in a tropical catchment. In: Journal of Hydrology, Vol. 498, P. 221-236.

Cressie, N.A.C., 1993. Statistics for Spatial Data. Wiley, New York.

Daniel, E. B., Camp, J. V., LeBoeuf, E. J., Penrod, J. R., Dobbins, J. P., & Abkowitz, M. D., 2011. Watershed modeling and its applications: A state-of-the-art review. Open Hydrology Journal, 5(2).

Davies, J. A., 1967. A note on the relationship between net radiation and solar radiation. Quarterly Journal of the Royal Meteorological Society, 93(395), 109-115.

De Girolamo, A.M., Lo Porto, A., Oueslati, O., . 2010. MODELING NUTRIENT BALANCES IN THE RIO MANNU BASIN AND SCENARIO ANALYSIS OF THE IMPACT OF FERTILIZER REDUCTION. In: *FRESENIUS ENVIRONMENTAL BULLETIN* 19.9 (2010): 1854-1861.

De Gruijter, J.J., Brus, D.J., Bierkens, M.F.P., Knotters, M., 2006. Sampling for Natural Resource Monitoring. Springer, Berlin.

Deidda, R., Marrocu, M., Caroletti, G., Pusceddu, G., Langousis, A., Lucarini, V., Puliga, M., and Speranza, A. 2013. Regional climate models performance in representing precipitation and temperature over selected Mediterranean areas. In: Hydrology. Earth Syst. Sci., 17, 5041–5059.

Delitala, A.M.S., Cesari, D., Chessa, P.A., Ward, N., 2000. Precipitation over Sardinia (Italy) during the 1946-1993 rainy season and associated large-scale climate variations. In: International Journal of Climatology 20, 519-541.

Déqué, M., S. Somot, E. Sanchez-Gomez, C. M. Goodess, D. Jacob, G. Lenderink, and O. B. Christensen, 2012. The spread amongst ENSEMBLES regional scenarios: Regional climate models, driving general circulation models and interannual variability. In: Clim. Dyn., 38, 951–964.

Devia, G. K., Ganasri, B. P., & Dwarakish, G. S., 2015. A Review on Hydrological Models. Aquatic Procedia, 4, 1001-1007.

Doglioni, C., Flores G., 1997. An Introduction to the Italian geology. Lamisco

Duttmann, R. Sumfleth, K., 2007. Predictive mapping of soil characteristics in paddy rice landscapes of Central Eastern Jiangxi Province / China. In: Geoöko Vol. XXVIII, 72-103, Göttingen.

Durn, G., 2003. Terra rossa in the Mediterranean region: parent materials, composition and origin. Geologia Croatica, 56(1), 83-100.

References

EEA 2013: Water resources problems in Southern Europe, http://www.eea.europa.eu/publications/92-9167-056-1/page003.html.

EEA, 2007. Corine Land Cover 2006 technical guidelines. EEA Technical report No 17/2007. European Environment Agency. www.eea.europa.eu/publications/technical_report_2007_17.

Eldeiry, A. and Garcia, L., 2010. Comparison of Ordinary Kriging, Regression Kriging, and Cokriging Techniques to Estimate Soil Salinity Using LANDSAT Images. In: *J. Irrig. Drain Eng.*, 136(6), 355–364.

Ehlers, L., Herrmann, F., Blaschek, M., Duttmann, R., & Wendland, F., 2015. Sensitivity of mGROWA-simulated groundwater recharge to changes in soil and land use parameters in a Mediterranean environment and conclusions in view of ensemble-based climate impact simulations. In: Science of The Total Environment. Article in press.

Ehlers, L., 2014: Modeling past and future water balance in the Mediterranean: A case study for the Rio Mannu catchment on Sardinia. Master thesis, Chrisitan-Albrechts Universität zu Kiel

Falloon, P., Betts, R., 2010. Climate impacts on European agriculture and water management in the context of adaptation and mitigation—The importance of an integrated approach, Science of The Total Environment, Volume 408, Issue 23, 1 November 2010, Pages 5667-5687.

Fanni, S., Loddo,S., Manca, D., Puddu, R., 2004. I suoli della Sardegna, http://www.dista.unibo.it/aposa/soil/S18.pdf (Download, 10.08.2014).

Gädeke, A., Hölzel, H., Koch, H., Pohle, I. Grünewald, U. , 2013. Analysis of uncertainties in the hydrological response of a model-based climate change impact assessment in a subcatchment of the Spree River, Germany. In: Hydrol. Process., Vol. 28 Issu 12, p. 3978-3998.

Gampe, D., Ludwig, R., Qahman, K., & Afifi, S. (2015). Applying the Triangle Method for the parameterization of irrigated areas as input for spatially distributed hydrological modeling—Assessing future drought risk in the Gaza Strip (Palestine). Science of The Total Environment.

Gasch, Caley K., Snehalata V. Huzurbazar, and Peter D. Stahl, 2015. Small-scale spatial heterogeneity of soil properties in undisturbed and reclaimed sagebrush steppe. In: Soil and Tillage Research 153 (2015): 42-47

Ge, Y., Thomasson, J.A., Morgan, C.L., Searcy, S.W., 2007. VNIR DIFFUSE REFLECTANCE SPECTROSCOPY FOR AGRICULTURAL SOIL PROPERTY DETERMINATION BASED ON REGRESSION-KRIGING. In: American Society of Argicultural anfd Biological Engineers Vol. 50(3), p1081-1092.

Götzinger, J., Bárdossy, A., 2006. Comparison of four regionalisation methods for a distributed hydrological model. In: *Journal of Hydrology, 333*, 374-384.

Cragoa, R., & Brutsaert,, W. 1996. Daytime evaporation and the self-preservation of the evaporative fraction and the Bowen ratio. Journal of Hydrology, 178(1), 241-255.

Guo, P. T., Wu, W., Sheng, Q. K., Li, M. F., Liu, H. B., & Wang, Z. Y., 2013. Prediction of soil organic matter using artificial neural network and topographic indicators in hilly areas. Nutrient cycling in agroecosystems, 95(3), 333-344.

Guttmann, N.B., 1999. ACCEPTING THE STANDARDIZED PRECIPITATION INDEX: A CALCULATION ALGORITHM. In: Journal of the Amarican Water Resources Association, Vol. 35, No. 2.

Hayes, M. J., Svoboda, M. D., Wilhite, D. A., & Vanyarkho, O. V., 1999. Monitoring the 1996 drought using the standardized precipitation index. In: Bulletin of the American Meteorological Society, Vol. 80(3), p. 429-438.

Hengl, T., Heuvelink, G.B.M., Stein, A., 2004. A generic framework for spatial prediction of soil variables based on regression-kriging. Geoderma 120 (1-2), 75-93.

Hengl, T., 2009. A Practical Guide to Geostatistical Mapping. University of Amsterdam.

Herbst, M., Diekkrüger, B., Vereecken, H., 2006. Geostatistical co-regionalization of soil hydraulic properties in a micro-scale catchment using terrain attributes. In: *Geoderma*, *132*(1), 206-221.

Hiemstra, P.H., Pebesma, E.J., Twenhofel, C.J.W. and G.B.M. Heuvelink, 2008. Real-time automatic interpolation of ambient gamma dose rates from the Dutch Radioactivity Monitoring Network. Computers & Geosciences, accepted for publication.

Honti, M., Scheidegger, A., & Stamm, C., 2014. The importance of hydrological uncertainty assessment methods in climate change impact studies. Hydrology and Earth System Sciences, 18(8), 3301-3317.

Hrachowitz, M., Savenije, H. H. G., Blöschl, G., McDonnell, J. J., Sivapalan, M., Pomeroy, J. W., ... & Cudennec, C., 2013. A decade of Predictions in Ungauged Basins (PUB)—a review. *Hydrological sciences journal*, *58*(6), 1198-1255.

Hummel, F., Post, J., Prettenthaler, F., Bird, N., Köberl, J., 2013. CLIMB – Report-Deliverable 6.3.2. url: http://www.climb-fp7.eu/dissemination/deliverables/d_6_3_2_design_document_of_the_risk_analyses_and_implementation_with_a_risk_modeling_tool.pdf

Isaaks, E. & Srivastava, R., 1989. Applied Geostatistics. Oxford University Press.

Islam, Z., (2011). A Review on Physically Based Hydrologic Modeling. Literature Review on physically Based Hydrologically Modeling. Alberta

Jasper K., Calanca P., Fuhrer J., 2006. Changes in summertime soil water patterns in complex terrain due to climatic change. Journal of Hydrology 327, 550-563.

Jiang, L. & Islam, S., 1999. A methodology for estimation of surface evapotranspiration over large areas using remote sensing observations. In: *Geophysical research letters*, *26*(17), 2773-277.

Krige, D.G., 1951. A statistical approach to some basic mine problems on the Witwatersrand J. Chem. Metall. Min. Soc. S. Afr., 52 (1951), pp. 119–139

Kumar, S., 2015. Estimating spatial distribution of soil organic carbon for the Midwestern United States using historical database. In: *Chemosphere*, *127*, 49-57.

Kunkel, R. & F. Wendland, 2002. The GROWA98 model for water balance analysis in large river basins - the river Elbe case study. Journal of Hydrology, 259, 152-162.

Kutner, M.H., Nachtsheim, C.J., Neter, J., 2004. Applied Linear Regression Models. McGraw-Hill, Singapore.

Lark, R.M., Cullis, B.R., Welham, S.J., 2006. On spatial prediction of soil properties in the presence of a spatial trend: the empirical best linear unbiased predictor (E-BLUP) with REML. Eur. J. Soil Sci. 57, 787-799.

Leavesley, G. H., 1999. Overview of models for use in the evaluation of the impacts of climate change on hydrology. Impacts of Climate Change and Climate Variability on Hydrological Regimes, 107-122.

Lespinas. F., Ludwig, W., Heussner, S., 2014. Hydrological and climatic uncertainties associated with modeling the impact of climate change on water resources of small Mediterranean coastal rivers. Journal of Hydrology: 511, 403-422.

Liston, G. E. and Elder, K., 2006. A Meteorological Distribution System for High-Resolution Terrestrial ModModel (MicroMet), J. Hydrometeorol., 7, 217–234.

Lucke, B., Kemnitz, H., Bäumler, R., & Schmidt, M. 2014. Red Mediterranean Soils in Jordan: New insights in their origin, genesis, and role as environmental archives. *Catena*, *112*, 4-24

Ludwig, R., Soddu, A., Duttmann, R., Baghdadi, N., Benabdallah, S., Deidda, R., Marrocu, M., Strunz, G., Wendland, F., Engin, G., Paniconi, C., Prettenthaler, F., Lajeunesse, I.,Afifi, S., Cassiani, G., Bellin, A., Mabrouk, B., Bach H., Ammerl T., 2010a. Climate-induced changes on the hydrology of the Mediterranean Basins – A research concept to reduce uncertainty and quantify risk. In: Fresenius Environmental Bulletin, Volume 19 – No 10a. 2010.

Malone, B. P., McBratney, A. B., Minasny, B., & Laslett, G. M., 2009. Mapping continuous depth functions of soil carbon storage and available water capacity. Geoderma, 154(1), 138-152.

Melone, F., Barbetta, S., Diomede, T., Peruccacci, S., Rossi, M., & Tessarolo, A. (2005). Review and selection of hydrological models–Integration of hydrological models and meteorological inputs. Contract, (12).

McBratney, A. B., Odeh, I. O., Bishop, T. F., Dunbar, M. S., & Shatar, T. M., 2000. An overview of pedometric techniques for use in soil survey. In: Geoderma, 97(3), 293-327.

Mascaro, G., Piras, M., Deidda,R., Vivoni, E. R., 2013. Distributed hydrologic modeling of a sparsely monitored basin inSardinia, Italy, through hydrometeorological downscaling. Hydrology and Earth System Science 17, 4143-4158.

Mancosu, A., 2013. Taphonomy and palaeoecology of multi-element skeleton invertebrates: a genetic model for exceptional preservation. PhD-thesis. University of Cagliari.

Maselli, F., Papale, D., Chiesi, M., Matteucci, G., Angeli, L., Raschi, A., & Seufert, G. 2014. Operational monitoring of daily evapotranspiration by the combination of MODIS NDVI and ground meteorological data: Application and evaluation in Central Italy. Remote Sensing of Environment, 152, 279-290.

Mc Kee, T. B., Doeskin, N. J., and Kleist, J., 1993. The Relationship of Drought Frequency and Duration to Time Scales. Proc. 8th Conf. on Applied Climatology, January 17-22, 1993, American Meteorological Society, Boston, Massachusetts, pp. 179-184.

Mc Kee, T. B., Doeskin, N. J., and Kleist, J., 1995. Drought Monitoring with Multiple Time Scales. Proc. 9th Conf. on Applied Climatology, January 15-20, 1995, American Meteorological Society, Boston, Massachusetts, pp. 233-236.

Minasny, B., McBratney, A.B., 2007. Spatial prediction of soil properties using EBLUP with Matern covariance function. Geoderma 140, 324-336.

Meyer, S., Blaschek, M., Duttmann, R., & Ludwig, R. (2016). Improved hydrological model parametrization for climate change impact assessment under data scarcity—The potential of field monitoring techniques and geostatistics. Science of The Total Environment, 543, 906-923.

Meyer, S., 2009. Regionalisierung von Bodeneigenschaften unter Anwendung digitaler Geländemodelle und des L-band Synthetic Aperture Radar auf der Feldskale. Diploma thesis, CAU Kiel.

Mohamed, Y. A., Savenije, H. H. G., Bastiaanssen, W. G. M., & Van den Hurk, B. J. J. M., 2005 . New lessons on the Sudd hydrology learned from remote sensing and climate modeling. In:*Hydrology and Earth System Sciences Discussions Discussions*, *2*(4), 1503-1535.

Molina-Navarro, E., Trolle, D., Martínez-Pérez, S., Sastre-Merlín, A., Jeppesen, E., 2014. Hydrological and water quality impact assessment of a Mediterranean limno-reservoir under climate change and land use management scenarios. In: Journal of Hydrology, Volume 509, 13.

Moonjun, R., Farshad, A., Shrestha, D.P.,Vaiphasa, C., 2010: Artifical Neural Network and Decision Tree in Predictive Soil Mapping of Hoi Num Rin Sub-Watershed, Thailand. In: Boettinger, J.L., Howell, D.W., Moore, A.C., Hartemink, A.E., Kienast-Brown, S., (Hrsg).: Digital Soil Mapping – Bridging Research, Environmental Application, and Operation. , Wageningen.

Moore, I.D., Gessler, P.E., Nielsen, G.A., Peterson G.A., 1993. Soil attribute prediction using terrain analysis. Soil Sci. Soc. Am. J. 57, 443-452.

Moradkhani, H., & Sorooshian, S., 2008. General review of rainfall-runoff modeling: model calibration, data assimilation, and uncertainty analysis. In Hydrological modeling and the water cycle (pp. 1-24). Springer Berlin Heidelberg.

Muerth, M. J., Gauvin St-Denis, B., Ricard, S., Velázquez, J. A., Schmid, J., Minville,, M., Ludwig, R., Turcotte, R., 2013. On the need for bias correction in regional climate scenarios to assess climate change impacts on river runoff. In: *Hydrology and Earth System Sciences*, 17(3), 1189-1204.

Murru, M., Bassi, D., & Simone, L., 2015. Displaced/re-worked rhodolith deposits infilling parts of a complex Miocene multistorey submarine channel: A case history from the Sassari area (Sardinia, Italy). Sedimentary Geology, 326, 94-108.

Nakićeović, N., Alcamo J., Davis G., de Vries H.J.M., Fenhann J., Gaffin S., Gregory K., Grubler A., Jung T. Y., Kram T., La Rovere E. L., Michaelis L., Mori S., Morita T., Papper W., Pitcher H., Price L., Riahi K., Roehrl A., Rogner H.-H., Sankovski A., Schlesinger M., Shukla P., Smith S., Swart R., van Rooijen S., Victor N., Dadi Z., 2000. Emissions Scenarios. A Special Report of Working Group III of the Intergovernmental Panel on Climate Change. Cambridge University Press: Cambridge; 559.

Neter, J., Kutner, M.H., Nachtsheim, C.J., Wasserman, W. (Eds.), 1996. Applied Linear Statistical Models. McGraw-Hill/Irwin, Chicago.

Odeh, I.O.A., McBratney, A.B., Chittleborough, D.J., 1995. Further results on prediction of soil properties from terrain attributes: heterotopic cokriging and regression-kriging. Geoderma 67 (3-4), 215-226.

Odeh, I. O., & McBratney, A. B., 2000. Using AVHRR images for spatial prediction of clay content in the lower Namoi Valley of eastern Australia. In: Geoderma, 97(3), 237-254

Olaya, V., 2004. A gentle introduction to SAGA GIS. http://dfn.dl.sourceforge.net/project/saga-gis/SAGA%20-%20Documentation/SAGA%20Documents/SagaManual.pdf (26.03.12).

Oliver, M.A., Webster, R., 2014. A tutorial guide to geostatistics: Computing and modeling variograms. In: Catena 113 (2014): 56-69.

Ott, I., Duethmann, D., Liebert, J., Berg, P., Feldmann, H., Ihringer, J., Kunstmann, H., Merz, B., Schaedler, G., Wagner, S., 2013. High resolution climate change impact analysis on medium sized

river catchments in Germany: An ensemble assessment. In: Journal of Hydrometeorology, Vol. 14, 1175–1193.

Patil, S., and Stieglitz, M., 2011. Hydrologic similarity among catchments under variable flow conditions. In: Hydrol. Earth Syst. Sci., 15, 989-997.

Pebesma, E.J., 2004. Multivariable geostatistics in S: The gstat package. Comput. Geosci. 30 (7), 683-691.

Peckham, S.D., 2011. Profile, Plan and Streamline Curvature: A Simple Derivation and Applications. In: Proceedings of Geomorphometry (2011): 27-30

Perrin, C., Oudin, L., Andreassian, V., Rojas-Serna, C., Michel, C., & Mathevet, T., 2007. Impact of limited streamflow data on the efficiency and the parameters of rainfall—runoff models. In: Hydrological sciences journal, 52(1), 131-151.

Piccini, C., Marchetti, A., Francaviglia, R., 2014. Estimation of soil organic matter by geostatistical methods: Use of auxiliary information in agricultural and environmental assessment. In: Ecological Indicators, 36, 301-314.

Piras, M., Mascaro, G., Deidda, R., and Vivo, E. R., 2014. Quantification of hydrologic impacts of climate change in a Mediterranean basin in Sardinia, Italy, through high-resolution simulations. In: Hydrology and Earth System Science 18, 5201-5217.

Priestley, C. & Taylor, R., 1972. On the assessment of surface heat flux and evaporation using large-scale parameters. Monthly Weather Review, 100(2):81-92.

Raposo, J. R., Dafonte, J., & Molinero, J., 2013. Assessing the impact of future climate change on groundwater recharge in Galicia-Costa, Spain. *Hydrogeology Journal*, *21*(2), 459-479.

Rezaee, H., Asghari, O., & Yamamoto, J. K.,2012. On the reduction of the ordinary kriging smoothing effect. In: Journal of Mining and Environment, 2(2), 102-117

Roedel, W., 2013. Physik unserer Umwelt: Die Atmosphäre. Springer-Verlag.

Rossi, P., Oggiano, G., Cocherie, A., 2009. A restored section of the "southern Variscan realm" across the Corsica–Sardinia microcontinent. In: Comptes Rendus Geoscience, Volume 341, Issues 2–3, 224-238.

Rötzer, K., Montzka, C., Bogena, H., Wagner, W., Kerr, Y. H., Kidd, R., & Vereecken, H., 2014. Catchment scale validation of SMOS and ASCAT soil moisture products using hydrological modeling and temporal stability analysis. Journal of hydrology, 519, 934-946.

Ruelland, D., Hublart, P., & Tramblay, Y., 2015. Assessing uncertainties in climate change impacts on runoff in Western Mediterranean basins. Proc. IAHS, 371, 75-81.

Rochester, R. E. L., 2010. Uncertainty in hydrological modeling: a case study in the Tern catchment, Shropshire, UK (Doctoral dissertation, UCL (University College London)).

SAGA User Group Association, 2011. System for Automated Geoscientific Analysis (version 2.0.7). (software). http://www.saga-gis.org/ (26.03.12).

Saadi, S., Todorovic, M., Tanasijevic, L., Pereira, L. S., Pizzigalli, C., & Lionello, P. 2015. Climate change and Mediterranean agriculture: Impacts on winter wheat and tomato crop evapotranspiration, irrigation requirements and yield. Agricultural Water Management, 147, 103-115.

Sannitu, S., 2006. The integrated water cycle in the context of water management systems: the Sardinian experience. WATER RESOURCES FOR THE FUTURE

Schauppenlehner, T., 2008. Geostatistische Analysen zur Integration von Geländemodellen und Bodenschätzungsdaten für verbesserte digitale Bodenkarten am Beispiel einer alluvialen Landschaft. na.

Schulla, J., 2015. Model Description WaSiM, Water balance Simulation Model. Completely revised version 2012 with 2013-2015 extentions, last change: June, 11, 2015, Hydrology Software Consulting J. Schulla, Zurich, Switzerland.

Schulla, J., 2012. Model Description WaSiM, Water balance Simulation Model. Completely revised version 2012, last change: June, 19, 2012, Hydrology Software Consulting J. Schulla, Zurich, Switzerland.

Schulla, J., & Jasper, K., 2007. **"**MODEL DISCRIPTION WASIM (Water balance Simulation Model "ETH).

Searcy, J., 1959. Flow Duration Curves. In: Manual of Hydrology Part 2. Low-Flow Techniques, Washington

Senatore, A., Mendicino, G., Smiatek, G., & Kunstmann, H. 2011. Regional climate change projections and hydrological impact analysis for a Mediterranean basin in Southern Italy. Journal of Hydrology, 399(1), 70-92.

Seo, Y., Kim, S., Singh, V.P., 2015. Estimating Spatial Precipitation Using Regression Kriging and Artificial Neural Network Residual Kriging (RKNNRK) Hybrid Approach. In Water Resources Managemant Vol.1 2015 p. 1-16

Sivapalan, M., 2003. Prediction in ungauged basins: a grand challenge for theoretical hydrology. Hydrological. Processes 17, 3163–3170.

Sood, A., & Smakhtin, V., 2015. Global hydrological models: a review. Hydrological Sciences Journal, 60(4), 549-565.

Sørensen, R., Zinko, U., Seibert, J., 2006. On the calculation of the topographic wetness index: evaluation of different methods based on field observations. In: *Hydrology and Earth System Sciences* **10**: 101–112.

Sponagel, H., (Ed.), 2005. Ad-Hoc-Arbeitsgruppe Boden der Staatlichen Geologischen Dienste und der Bundesanstalt für Geowissenschaften und Rohstoffe (2005). *Bodenkundliche Kartieranleitung:[KA 5];* H. Schweizerbart.

Stisen, S., Sandholt, I., Nørgaard, A., Fensholt, R., & Jensen, K. H., 2008. Combining the triangle method with thermal inertia to estimate regional evapotranspiration—Applied to MSG-SEVIRI data in the Senegal River basin. Remote Sensing of Environment, 112(3), 1242-1255.

Stockmann, U., Malone, B. P., McBratney, A. B., & Minasny, B., 2015. Landscape-scale exploratory radiometric mapping using proximal soil sensing. In: *Geoderma*, *239*, 115-129.

Sun, W., Minasny, B., MCBratney, A., 2012. Analysis and prediction of soil properties using local regression-kriging. In: Geoderma, 171-172(2012), 16-23

Sumfleth, K., 2008. Predictive mapping of soil characteristics in paddy rice landscapes of Central Eastern Jiangxi Province / China. – Kiel.

Tang, R., Li, Z-L., Tang, B., 2009. An application of the Ts–VI triangle method with enhanced edges determination for evapotranspiration estimation from MODIS data in arid and semi-arid regions: Implementation and validation. In: Remote Sensing of Environment 114 (2010) 540–551.

Todorovic, M., Karic, B., & Pereira, L. S. 2013. Reference evapotranspiration estimate with limited weather data across a range of Mediterranean climates. Journal of Hydrology, 481, 166-176.

United States Department of Agriculture (USDA), 2015. "Soil Formation Factors". 02.03.2015 <http://www.nrcs.usda.gov/wps/portal/nrcs/detail/wa/soils/?cid=nrcs144p2_036333>

United States Environmental Protection Agency (USEPA), 2011. An Approach for Estimating Stream Health Using Flow Duration Curves and Indices of Hydrologic Alteration. Texas

Vacca, A., Loddo, S., Ollesch, G., Puddu, R., Serra, G., Tomasi, D. and Aru, A., 2000. Measurement of runoff and soil erosion in three areas under different land use in Sardinia (Italy). Catena 40, 69-92.

Van Gnuchten, M.T., 1976. A Closed-Form Equation for Predicting the Hydraulic Conductivity of Unsaturated Soils. Soil Sience Society of American Journal, Vol. 44(5), 892-898.

Velázquez, J. A., Schmid, J., Ricard, S., Muerth, M. J., Gauvin St-Denis, B., Minville, M., Chaumont, D., Caya, D., Ludwig, R., Turcotte, R., 2013. An ensemble approach to assess hydrological models' contribution to uncertainties in the analysis of climate change impact on water resources. In: Hydrol. Earth Syst. Sci., 17, 565-578.

Verheye, W., de la Rosa, D., 2006. Mediterranean Soils. In: Land Use, Land Cover and Soil Sciences. Ed. by W. H. Verheye. UNESCO-EOLSS Publishers. url: http://www.eolss.net/

Villalobos, F.J., L. Testi, J. Hidalgo, M. Pastor, F. Orgaz, 2006. Modeling potential growth and yiel of olive (Olea europea L.) canopies. European Journal Agronomy, Volume 24, Issue 4, 296-303.

Vivoni, E.R., Ivanov, V.Y., Bras, R.L., Entekhabi, D., 2000. The tRIBS (TIN-based Real-Time Integrated Basin Simulator. Department of Civil and Environmental Engineering of the Massachusetts Institute of Technology

Wang, K., Li,Z., Cribb, M., 2006. Estimation of evaporative fraction from a combination of day and night land surface temperatures and NDVI: A new method to determine the Priestley-Taylor parameter, Remote Sensing of the Environment, 102, 293-305.

Winsemius, H. C., Savenije, H. H. G., & Bastiaanssen, W. G. M., 2008. Constraining model parameters on remotely sensed evaporation: justification for distribution in ungauged basins?. In: Hydrol. Earth Syst. Sci., 12, 1403-1413, 2008.

Waseem, M., Ajmal, M., Kim, T-M., 2015. Development of a new composite drought index for multivariate drought assessment. In: Journal of Hydrology Vol. 527 (2015) P. 30–37.

Wheater, H., Sorooshian, S., & Sharma, K. D. (Eds.)., 2007. Hydrological modeling in arid and semi-arid areas. Cambridge University Press.

Webster, R., Oliver, M.A., 2007. Geostatistics for Environmental Scientists. Wiley.

Winkel, T. and S. Rabal, 1993. Influence of Water Stress on Grapevines Growing in the Field: From Leaf to Whole Plant Response. Australian Journal of Plant Physiology 29(2) 143-157.

World Meteorological Organization (WMO), 2012. Standardized Precipitation Index User Guide. Geneva, Switzerland.

Wösten, J.H.M., Lilly, A., Nemes, A., Le Ba, C.,1999. Development and use of a database of hydraulic properties of European soils. Geoderma 90, 169-185

Xu, C., Widen, E., and Halldin, S., 2005. Modeling hydrological consequences of climate change – Progress and challenges, Adv. Atmos. Sci. 22, 789-797, 2005.

Yaalon, D. H., 1997. Soils in the Mediterranean region: what makes them different?. Catena, 28(3), 157-169.

Yaalon, Dan H. "Soils in the Mediterranean region: what makes them different?." Catena 28.3 (1997): 157-169.

Yao, X., Fu, B., Lü, Y., Sun, F., Wang, S., Liu, M., 2013. Comparison of Four Spatial Interpolation Methods for Estimating Soil Moisture in a Complex Terrain Catchment.In: PLoS ONE, 8(1).

Zhao, Y., Han, H., Cao, L., & Chen, G. 2012. Study on Soil Nutrients Spatial Variability in Yushu City. In *Computer and Computing Technologies in Agriculture V* (pp. 1-7). Springer Berlin Heidelberg.

Zollo, A., Mercogliano, P., Turco, M., Vezzoli, R., Guido, R., Bucchignani, E. & Montesarchio, M., 2012. Architectures and tools to analyse the impact of climate change on hydrogeological risk on Mediterranean area. *CMCC.*

10. APPENDIX

a. Additional figures

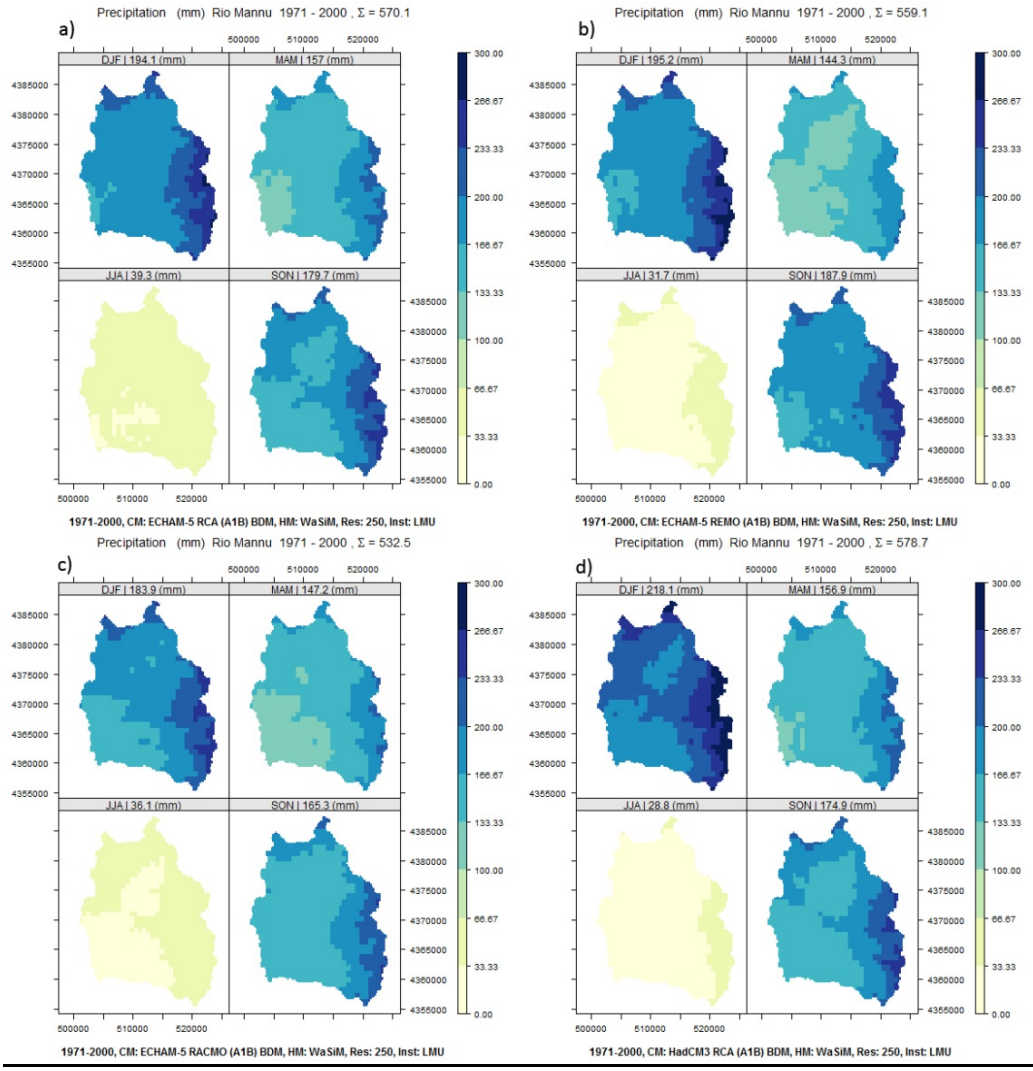

Appendix 1: Spatially distributed precipitation (PRC) WaSiM-ARU outputs driven with ECHAM-5 -RCA, -REMO, RACMO and HadCM3 RCA respectively for the IPCC seasons for the REF projection.

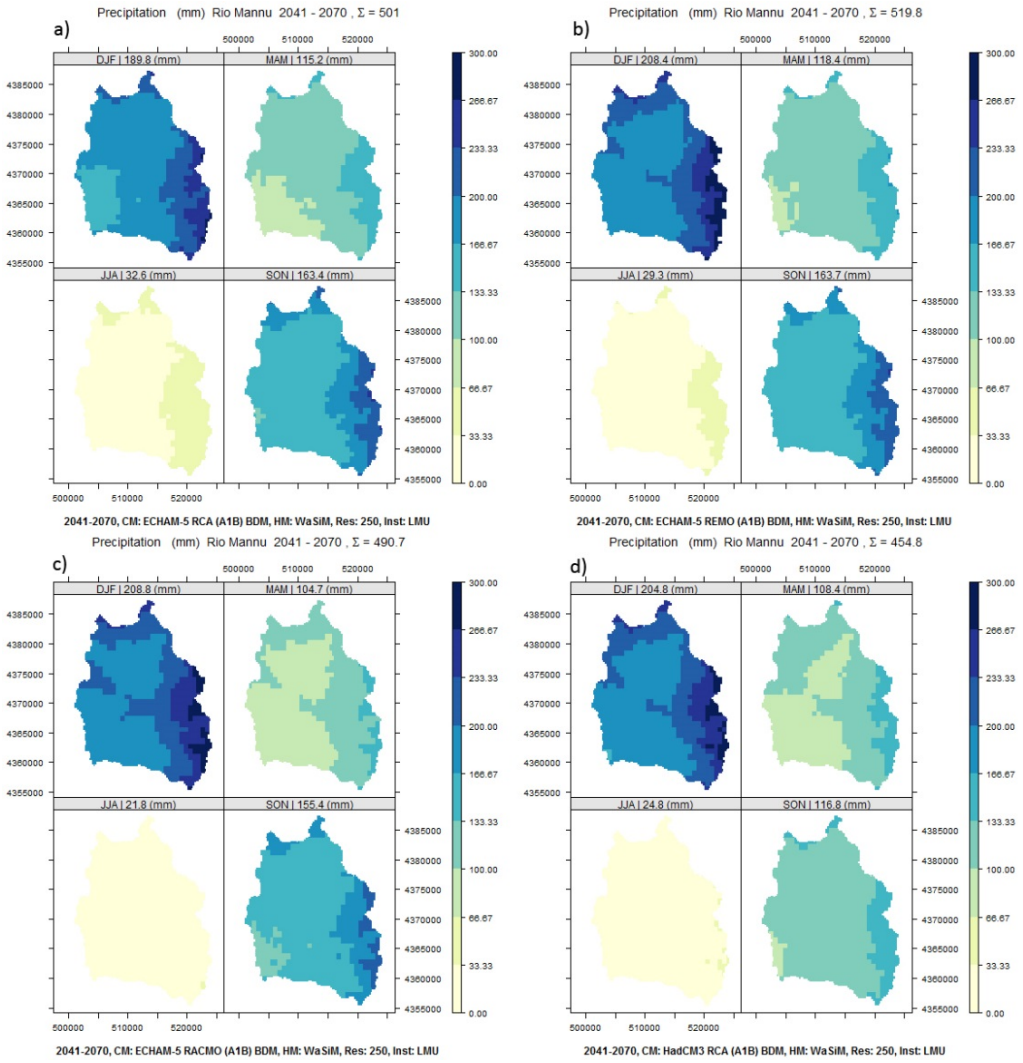

Appendix 2: Spatially distributed precipitation (PRC) WaSiM-ARU outputs driven with ECHAM-5 -RCA, -REMO, RACMO and HadCM3 RCA respectively for the IPCC seasons for the FUT projection.

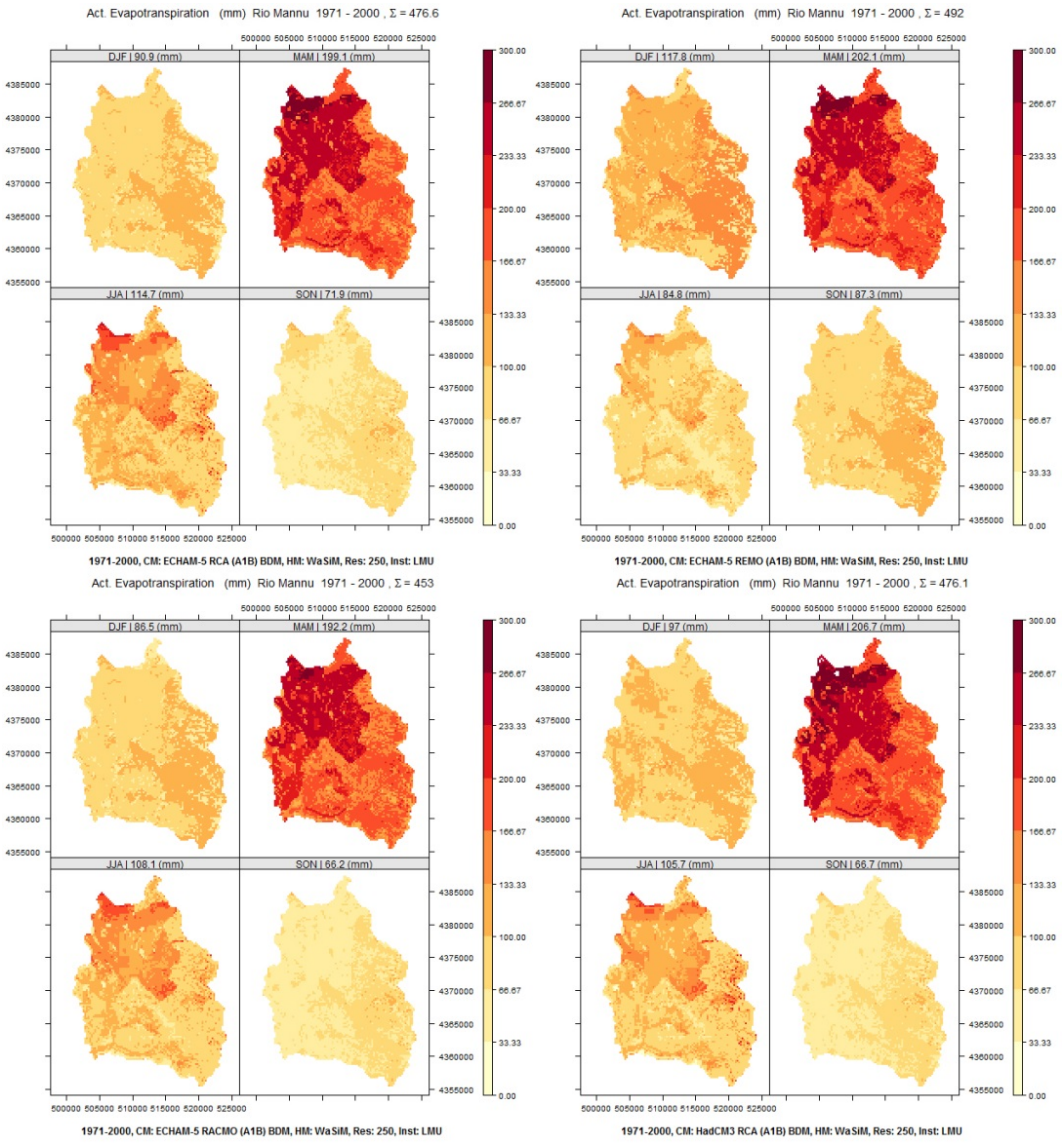

Appendix 3: Spatially distributed evapotranspiration (ETR) WaSiM-ARU outputs driven with ECHAM-5 -RCA, -REMO, RACMO and HadCM3 RCA respectively for the IPCC seasons for the REF projection.

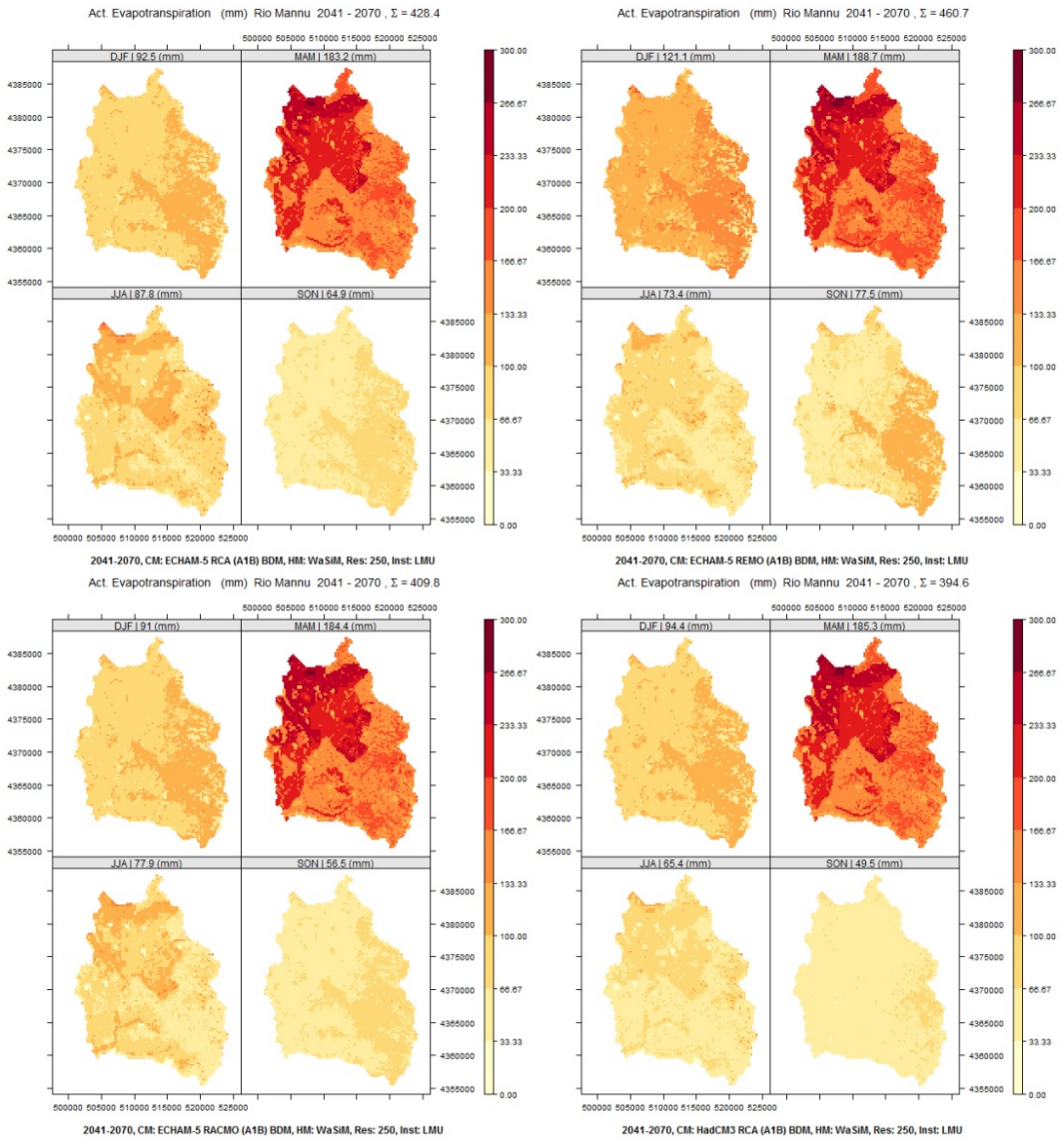

***Appendix* 4: Spatially distributed evapotranspiration (ETR) WaSiM-ARU outputs driven with ECHAM-5 -RCA, -REMO, RACMO and HadCM3 RCA respectively for the IPCC seasons for the FUT projection.**

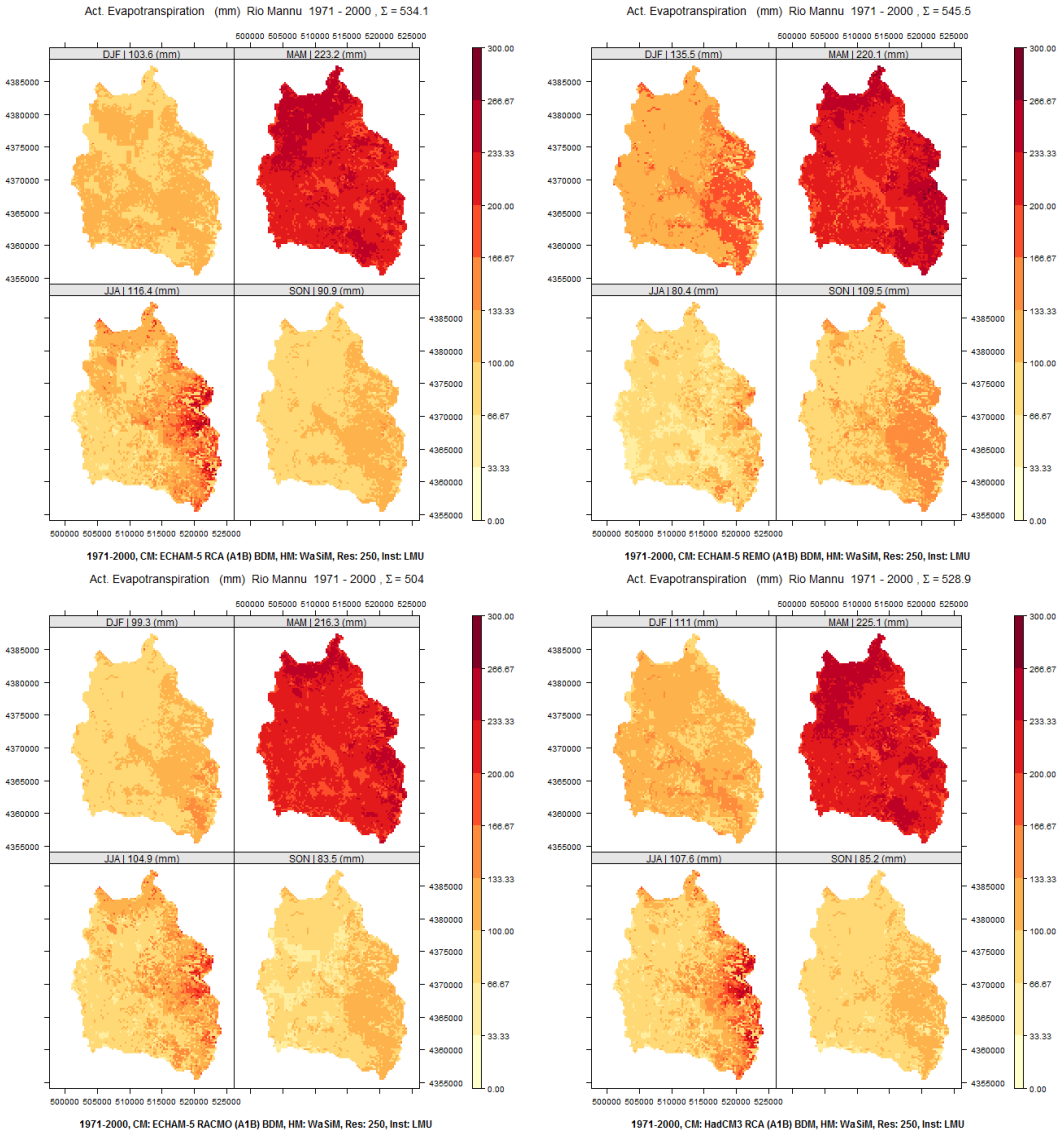

Appendix 5: **Spatially distributed evapotranspiration (ETR) WaSiM-RKS outputs driven with ECHAM-5 -RCA, -REMO, RACMO and HadCM3 RCA respectively for the IPCC seasons for the REF *projection.***

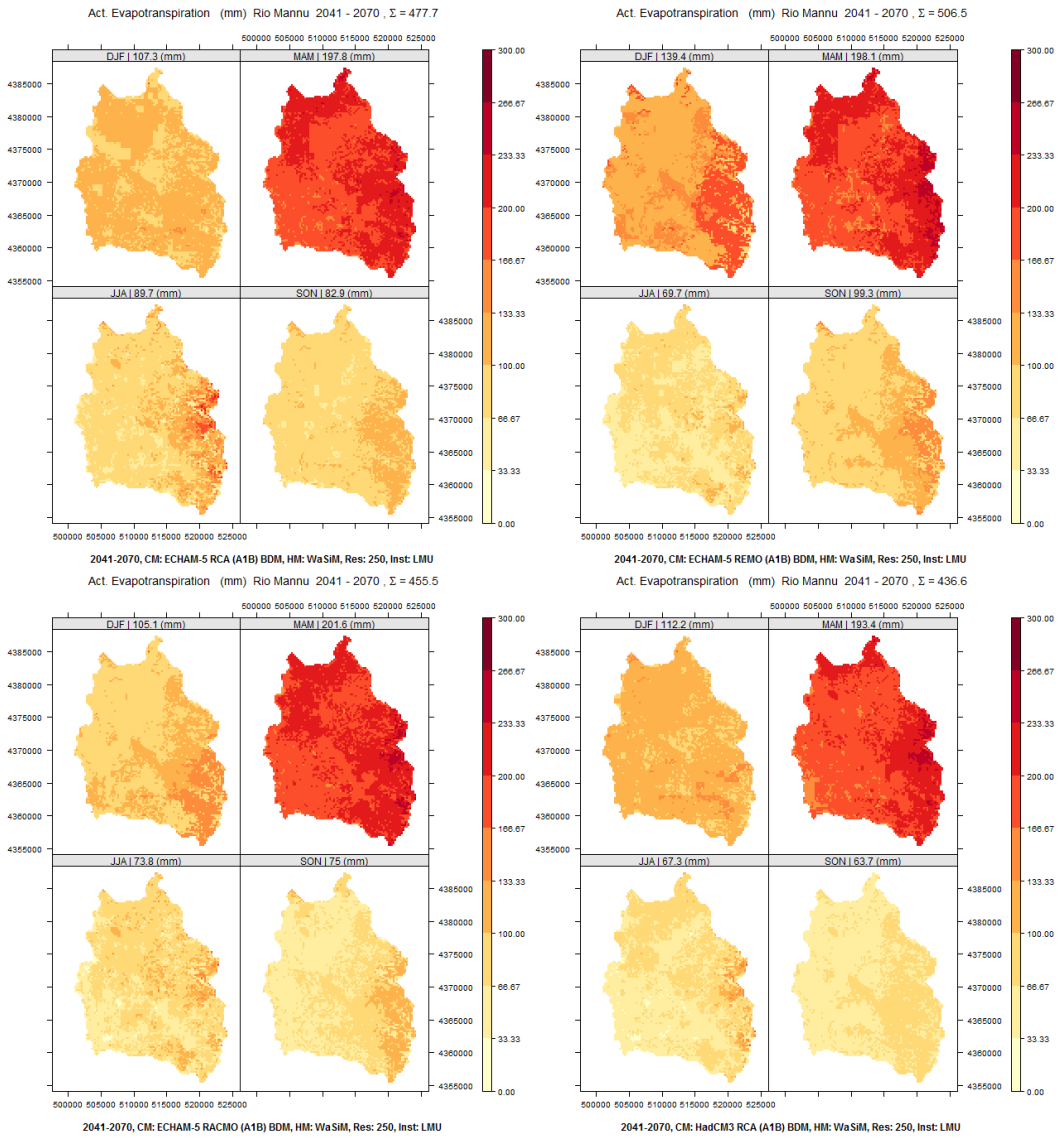

Appendix 6: Spatially distributed evapotranspiration (ETR) WaSiM-RKS outputs driven with ECHAM-5 -RCA, -REMO, RACMO and HadCM3 RCA respectively for the IPCC seasons for the FUT projection.

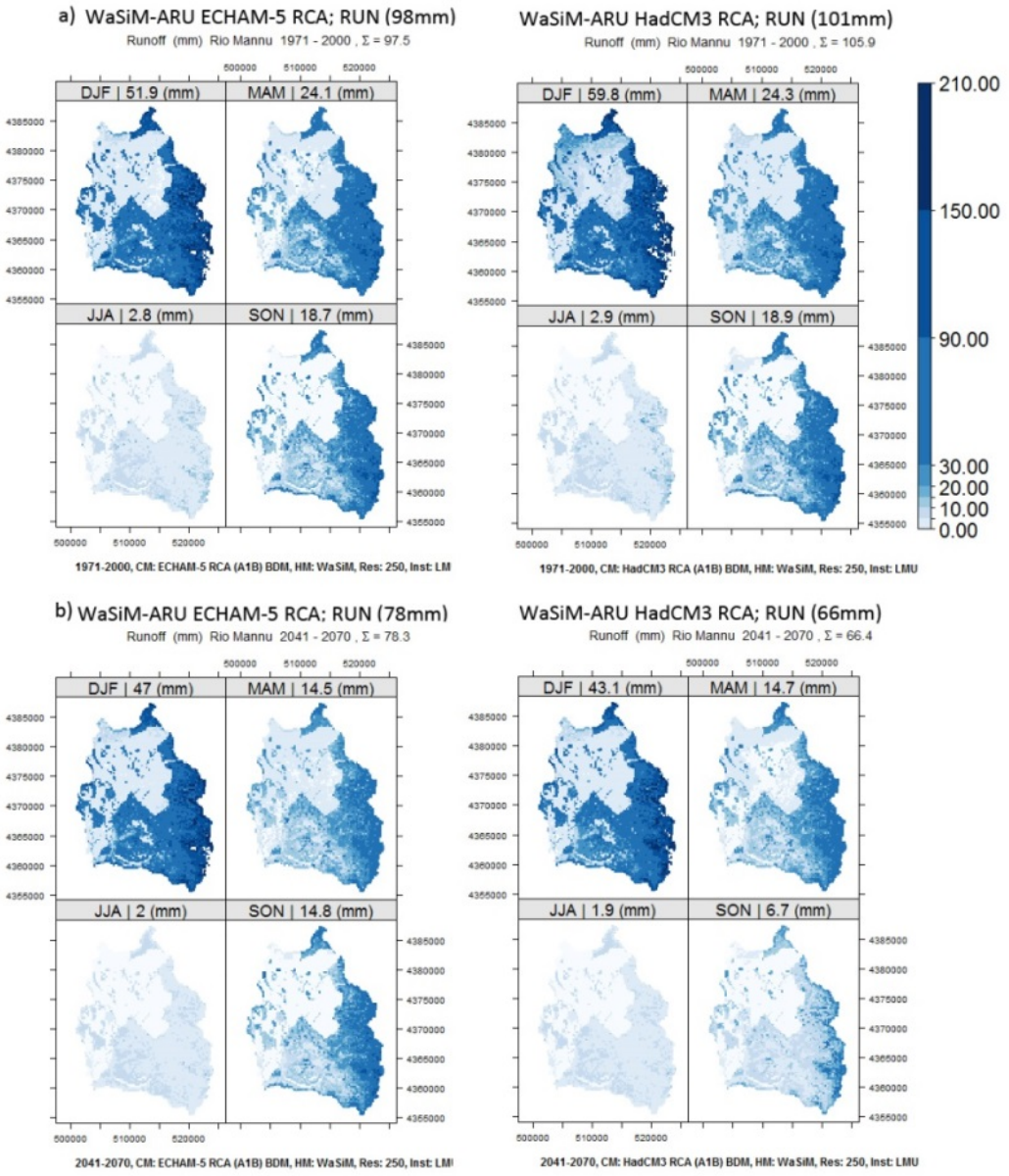

***Appendix 7*: Spatially distributed runoff (RUN) WaSiM-ARU driven with ECHAM-5 RCA and HadCM3 RCA for the IPCC seasons a) REF and b) FUT period.**

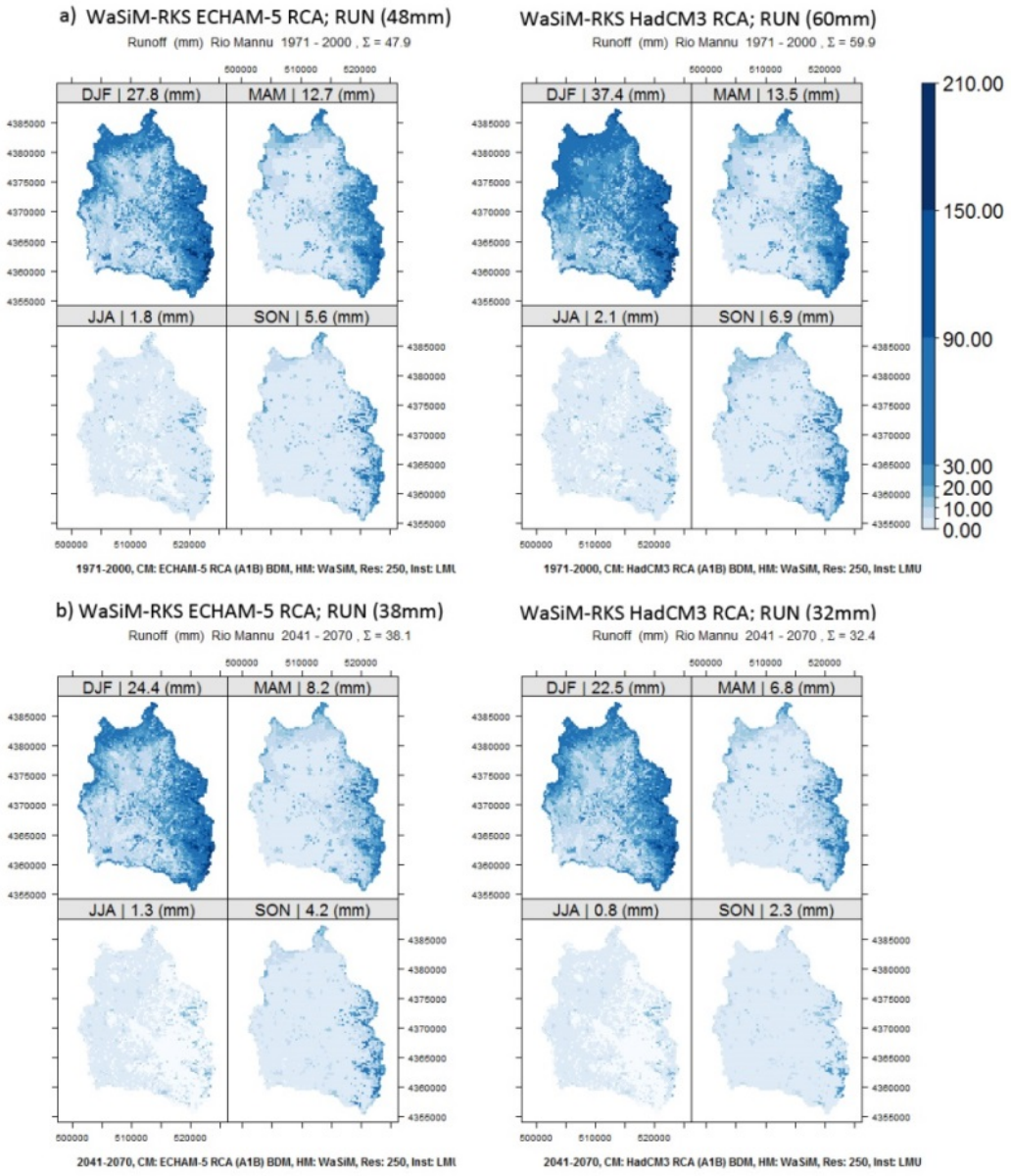

Appendix 8: Spatially distributed runoff (RUN) WaSiM-ARU driven with ECHAM-5 RCA and HadCM3 RCA for the IPCC seasons a) REF and b) FUT period.

b. List of important abbreviations

1. Climate modeling related abbreviations

GCM =	General Circulation Model
RCP =	Representative Concentration Pathway
RCM =	Regional Climate Model
ECHAM-5 RCA & ECH-RCA =	Regional Climate Model RCA of the Swedish Meteorological and Hydrological Institute (SMHI) driven with General Circulation Model ECHAM-5 of Max-Planck-Institut für Meteorologie (MPI)
ECHAM-5 REMO & ECH-REM =	Regional Climate Model REMO Max-Planck-Institut für Meteorologie (MPI) driven with General Circulation Model ECHAM-5 of Max-Planck-Institut für Meteorologie (MPI)
ECHAM-5 RACMO & ECH-RMO =	Regional Climate Model RACMO of the Koninklijk Nederlands Meteorologisch Instituut (KNMI) driven with General Circulation Model ECHAM-5 of Max-Planck-Institut für Meteorologie (MPI)
HadCM3-RCA & HCH-RCA=	Regional Climate Model RCA of the Swedish Meteorological and Hydrological Institute (SMHI) driven with the coupled atmosphere-ocean general circulation model Hadley Centre Coupled Model, version3.
IPCC =	Intergovernmental Panel on Climate Change

IPCC seasons

DJF =	Winter season (December, January, February)
MAM =	Spring season (March, April, May)
JJA =	Summer season (June, July, August)
SON =	Fall season (September, October, November)

IPCC Emission Scenarios IPCC - Fourth Assessment Report (uncomplete)

A1 =	*The A1 scenarios are of a more integrated world. Characterized by: Rapid economic growth. A global population that reaches 9 billion in 2050 and then gradually declines. The quick spread of new and efficient technologies. A convergent world - income and way of life converge between regions. Extensive social and cultural interactions worldwide.*
A1B =	*Subset of scenario A1. A balanced emphasis on all energy sources.*

A2 =	*The A2 scenarios are of a more divided world. Characterized by: A world of independently operating, self-reliant nations. Continuously increasing population. Regionally oriented economic development.*
B1 =	*The B1 scenarios are of a world more integrated, and more ecologically friendly. Characterized by: Rapid economic growth as in A1, but with rapid changes towards a service and information economy. Population rising to 9 billion in 2050 and then declining as in A1. Reductions in material intensity and the introduction of clean and resource efficient technologies. An emphasis on global solutions to economic, social and environmental stability.*
B2 =	*The B2 scenarios are of a world more divided, but more ecologically friendly. Characterized by: Continuously increasing population, but at a slower rate than in A2. Emphasis on local rather than global solutions to economic, social and environmental stability. Intermediate levels of economic development. Less rapid and more fragmented technological change than in A1 and B1.*

2. Soil survey and soil regionalization related abbreviations

A =	*Aspect*
β =	*Slope*
CDI =	*Convergence Divergence Index*
Ch =	*Plan Curvature*
Cv =	*Profile Curvature*
DEM =	*Digital Elevation Model*
LS =	*Slope length factor*
SCA =	*Specific Catchment Area*
Ω & SPI =	*Stream Power Index*
SWI =	*Saga Wetness Index*
TWI =	*Topographic Wetness Index*
CSM =	*Change of Soil Moisture*
CV =	*Coefficient of Variation*
DEM =	*Digital Elevation Model*
IDW =	Inverse Distance Weighting
Max =	Maximum
Min =	Minimum
MLR =	Multi-Linear Regression
NSR =	Nugget to Sill Ratio
OK =	Ordinary Kriging
OLS =	Ordinary Least Squares
RK =	Regression Kriging
RMSE =	Root Mean Square Error
SD=	Standard Deviation
SOC =	Soil Organic Carbon
EMI =	Electromagnetic Induction

3. Hydrological modeling related abbreviations

ETI =	Evapotranspiration Index
ETP =	Potential Evaporation
ETR =	Actual Evapotranspiration
ETR-TRI =	Actual Evapotranspiration derived by the Triangle Method
FDC =	Flow Duration Curve
FP-7 =	EU 7th Framework Programme for Research
FUT=	Projected time series 2041-2007
USDA =	U.S. Department of Agriculture
Q =	Discharge
REF =	Reference time series 1971-2000
SWAT =	Soil Water Assessment Tool
tRIBS =	TIN-based Real-time Integrated Basin Simulator of Vivoni et al. (2000)
WaSiM =	Water Flow and Balance Simulation Model
WaSiM-ARU =	WaSiM setup with the soil information of the Aru et al. (1990) soil map
WaSiM-RKS =	WaSiM setup with the soil information derived in a field servey within CLIMB and regionalized by applying regression kriging.